"MASS TRANSFER BETWEEN SINGLE BUBBLES AND NEWTONIAN AND

NON-NEWTONIAN LIQUIDS"

by

Dwight Spencer L. Johnson, B.Sc. (Hons.)

Thesis presented for the Degree of Doctor of Philisophy of the

University of Edinburgh in the Faculty of Science

July, 1969.

To my family

and to my alma mater,

Wolmer's Boys' School, Kingston Jamaica.

Banquo:

"The earth hath bubbles, and so has the sea"

William Shakespeare.

CONTENTS

C O N T E N T S (Contd.)

C O N T E N T S (Contd.)

C O N T E N T S (Contd.)

C O N T E N T S (Contd.)

A C K N O W L E D G E M E N T S

The author would like to express his gratitude to:

Professor P. H. Calderbank, D.Sc., for his readily given guidance and advice during the course of this research work.

Dr. M. A. S. Ross, Ph.D., of the Department of Physics, for her helpful discussions on certain aspects of theoretical Fluid Dynamics.

Dr. J. R. Loudon, Ph.D., of Shell U.K. Ltd., for the characterisation of the viscous properties of the non-Newtonian liquid used in this work.

The Workshop Staff of the Chemical Engineering Department for assistance in the construction of experimental equipment.

The Photographic Department of the School of Engineering Science for developing and printing the bubble photographs.

The Edinburgh Regional Computing Centre for providing computing facilities.

Glaxo Laboratories Ltd., for providing a research grant during the course of this work.

SUMMARY

Instantaneous values of bubble volume, shape, rise velocity, overall mass transfer product, surface area and overall mass transfer coefficient for single carbon dioxide bubbles in free rise through liquids contained in a 10.16 cm I.D. column were experimentally evaluated.

In the experimental investigations, a novel data processing technique was used which allowed accurate measurement of the instantaneous rate of change of pressure of the constant volume system, consisting of a liquid contained in the mass transfer column and isolated from the atmosphere, as a bubble rose through the liquid and dissolved in it.

A wide range of bubble sizes (0.2 - 6.0 cm diameter) was investigated in three Newtonian liquids - distilled water and two aqueous Glycerol solutions - and a non-Newtonian viscoelastic aqueous Polyox solution, which exhibited pseudoplastic behaviour in steady shear. Detailed comparisons of the collected data with existing theoretical models relating to bubble rise velocity and overall mass transfer coefficient were carried out.

In the carbon dioxide-distilled water system, bubble shape was seen to go from spherical to oblate spheroidal to spherical cap with increasing bubble size. Bubble shapes observed in the two aqueous Glycerol solutions were similar to those observed in water, with an additional > hemisphere shape and the occurrence of spherical cap bubble skirting in the more concentrated Glycerol solution.

The/

The shapes and terminal rise velocities of large bubbles in the Newtonian liquids were found to be influenced by the proximity of the column walls. The terminal rise velocity data for bubbles in the non-Newtonian Polyox solution was lower than for distilled water; and exhibited an abrupt increase by a factor in excess of 4 at a critical bubble size. Bubbles in the Polyox solution exhibited tailing over the size range 0.27 cm $\leqslant D_e <$ 2.2 cm. Bubble tailing is known to be peculiar to non-Newtonian fluid fields. In the Polyox solution suitable bubble sizes adopted spherical, prolate spheroidal, oblate spheroidal and spherical cap shapes. A previously unreported spherical cap bubble rear configuration was observed for large bubbles in the Polyox solution.

Instantaneous overall mass transfer coefficients based on actual bubble surface areas were evaluated. The transfer coefficients of small bubbles in all four solutions investigated were closely predicted by theoretical equations for circulating spheres and for rigid spheres in creeping flow. The transfer coefficient data for carbon dioxide bubbles in the Polyox solution confirmed the suggestion (A7) that at the critical bubble size in viscoelastic pseudoplastic liquids a transfer from rigid to circulating body behaviour in creeping flow occurred. Certain bubble shape transitions were found to result in maxima in the transfer coefficient versus diameter plots for the solutions investigated.

The overall mass transfer coefficients of sufficiently large bubbles in all four solutions studied were approximately predicted by an/

an existing theoretical equation for circulating spheres in potential flow. As these large bubbles adopted a spherical cap shape, the transfer over the noses of these spherical caps was more accurately given by another theoretical equation for spherical cap frontal area transfer under conditions of potential flow. An approximate theoretical solution was developed in the present work for mass transfer from the rear of spherical cap shaped bubbles, and this, when combined with the theoretical equation for spherical cap frontal area transfer, more accurately predicted instantaneous overall mass transfer coefficients around spherical cap bubbles than the equation for circulating spheres in potential flow.

INTRODUCTION

There is a variety of engineering operations and processes in which gas or liquid as a dispersed phase plays an important part. Thus bubbles and drops occur in atomisers, scrubbers, dryers, absorbers, combustors, evaporators, air lift pumps, homogenizing and emulsifying systems, fermentation, flotation, and gas cooling.

Gas-liquid contact carried out for the purpose of mass transfer in systems where heat effects are absent or of secondary importance has many applications in chemical engineering since absorption, scrubbing, stripping, fermentation, waste disposal and sewage treatment are embraced.

The problem involving absorption of a gas by a liquid within which the solute gas undergoes diffusion with reaction is of increasing importance in the chemical and allied industries as a result of the development of liquid phase catalysts and the sustained importance of slurry reactions. A particularly striking example in this field is the liquid phase catalysed oxidation of absorbed ethylene to yield acetaldehyde in the Wacker process.

The contacting of a gas with a liquid is normally carried out by subdividing one or both of the phases. This phase subdivision leads to an increase in the interfacial area and produces relative motion between the phases, both these effects contributing to an increase in overall mass transfer rate. If only one phase is subdivided, that phase in which the major resistance to transfer lies is/

is made the continuous phase, since the velocity gradient due to relative motion between the phases is produced mainly in the continuous phase. Gas-liquid contacting equipment in which subdivision of both phases occurs includes plate columns with bubble cap, sieve or valve trays. Packed and wetted wall columns are used for gas-liquid mass transfer processes in which the liquid phase is subdivided, while bubble columns and stirred bubble absorbers are used when the gas phase is subdivided.

In industrial gas-liquid contacting equipment in which the gas phase is dispersed in the liquid, it is usual that the gas is subdivided to form a swarm of numerous small bubbles of varying size, a bubble swarm or cloud, thereby producing a high interfacial area and enhanced relative motions between the phases.

Bubbles in dilute turbulent dispersions behave independently and their rates of dissolution are little affected by turbulence or mutual proximity (C4). Also rapid desorption of gas, and bubble coalescence can result in large bubbles ascending through the liquid in virtual isolation of their neighbours. Hence in this work the motion and mass transfer of single isolated bubbles ascending in pure quiescent liquids is studied. In the majority of industrial bubble columns and stirred bubble absorbers complex interactions occur between the neighbouring small bubbles of the bubble swarm. The experimental correlations contained in the literature for gas bubble swarms in liquids give relationships between the physical and mass transfer properties of dispersions and the system variables, from which/

which predictive process design calculations can be made. These correlations also provide some identification of the important variables affecting equipment performance. The study of single isolated bubbles eliminates many of the complications associated with bubble swarms, such as bubble interactions and coalescence, random distribution of bubble size and residence times, turbulence and contamination of liquid or gas. Thus the single isolated bubble lends itself to theoretical analysis. The ultimate aim of the single bubble approach is extension to the case of bubble swarms in an analogous manner. The work of Marrucci (M4), who presented a cellular spherical model for the velocity of rising swarms of spherical bubbles and obtained an expression for the ratio of velocity of rise of the swarms to velocity of a single spherical bubble, provides an example of the extension of single particle dynamics to a multiple particle system.

The phenomena met with in the study of a gas bubble in a liquid are not unique to it, since the behaviour of gas bubbles has certain similarities with that of liquid droplets in a liquid, gas bubbles in fluidised beds and vapour bubbles in boiling liquids.

The behaviour of single freely rising bubbles has been extensively studied. Theoretical models have been developed for certain idealised situations, many of which are realised in practice, though the existing theories fall short in several respects and throw little light on the problems of mass transfer in bubble wakes. Experimental data relating to apparently identical systems have sometimes/

times been conflicting, and comparatively little attention has been paid to the study of single bubbles in viscous Newtonian liquids, and little work has been done on bubble motion and mass transfer in the various types of non-Newtonian liquids, though chemical engineers in industry are often concerned with non-Newtonian and viscous Newtonian liquids.

In the present investigations, a novel data processing technique was used which allowed accurate measurement of the instantaneous rate of change of pressure of a constant volume system, consisting of a liquid contained in a column and isolated from the atmosphere, as a bubble rose through the liquid and dissolved in it. This permitted measurement of instantaneous values of liquid film controlled dissolution rates of single gas bubbles in free rise through quiescent liquids. A complementary study of the rising velocities of gas bubbles was also carried out. Bubble diameter was varied over a ten to twenty-five fold range and studies were carried out using three Newtonian liquids covering a wide range of liquid viscosity, and one non-Newtonian liquid which was viscoelastic and exhibited pseudoplastic behaviour in steady shear. This permitted an investigation of the effect of Newtonian liquid viscosity on bubble motion and mass transfer, and extended the limited experimental data relating to non-Newtonian liquids. Detailed comparisons of the data collected and the existing theoretical models relating to bubble motion and mass transfer were carried out, and an approximate theoretical solution for mass transfer from the rear of spherical cap shaped bubbles was derived.

C H A P T E R 1

L I T E R A T U R E S U R V E Y

1. INTRODUCTION

The rates of solution of gas bubbles depend on the inter-relationships that exist between shape, turbulence, boundary layer and velocity of rise. A knowledge of bubble motion is thus of importance in understanding the mass transfer process from the rising bubble to the surrounding liquid.

The first section of this survey contains a discussion on Newtonian and non-Newtonian fluids - their general classification and the existing flow models. This will be followed by a brief summary of previous work on bubble motion in liquids. Drag coefficients and rise velocities (including the effects of gas solubility on rise velocities), bubble shapes, stability in motion, and wake structure are considered separately; though it is the interaction of these various factors which determine mass transfer rates in any given situation. The third and final section of this survey will deal with mass transfer in Newtonian and non-Newtonian liquids.

1.1 SECTION I

1.1.1 GENERAL CLASSIFICATION OF FLUIDS

As a fluid is deformed because of flow and applied external forces, frictional effects are exhibited by the motion of molecules relative to each other. These frictional effects are due to the fluid viscosity.

For a thin layer of Newtonian fluid subject to a shear stress τ, the shear rate (or velocity gradient) $\dot{\gamma}$ resulting across the fluid layer is given by (F5, W9)

$$\tau = \mu \dot{\gamma} \qquad (1)$$

An ideal fluid is one which is incompressible and has zero viscosity. All real fluids have finite viscosity.

Non-Newtonian fluids are those in which the viscosity at a given temperature and pressure is a function of the rate of shear. Non-Newtonian liquids include solutions of polymers, proteins, carbohydrates in aqueous and non-aqueous solvents, soaps of the alkali and heavy metals in toluene and xylene, dilute suspensions of clays, water-oil emulsions, paints, inks and so on (P8).

There are three broad classifications of non-Newtonian fluids

(i) Time-independent non-Newtonian fluids

(ii) Time-dependent non-Newtonian fluids

(iii) Viscoelastic non-Newtonian fluids

(i) Time-independent non-Newtonian Fluids

For these fluids the shear rate $\dot{\gamma}$ is a function of shear stress

τ/

τ alone (W9). They include:

(a) Bingham (ideal) plastics, which can withstand a certain amount of shearing stress, but once the shearing stress has attained a certain yield value they exhibit a constant viscosity independent of the rate of shear. Bingham plastics are thus characterised by the equation

$$\tau - \tau_o = \mu \dot{\gamma} \qquad (2)$$

where τ_o is the yield stress.

(b) Real plastics, for which the viscosity does not become constant until fairly high rates of shear are reached, as is indicated by curve C in Fig. (1).

(c) Pseudoplastic fluids, which constitute the majority of time-independent non-Newtonian fluids (W9), and are typified by an apparent viscosity, μ_a, which decreases with increasing rate of shear. Pseudoplasticity is attributed to a variety of mechanisms: the alignment of colloidal particles along the lines of flow, the de-kinking and uncoiling of long-chain molecules, the change in the shapes of suspended elastic particles when they are under the influence of shear and so on (P8).

(d) Dilatant fluids, in which the apparent viscosity increases with increasing shear rate. Dilatancy appears to arise from the change in volume occupied by the solid or semi-solid material in the system when it is being subjected to shear. As it commences to flow, the solid particles in it move out of their close-packed state into a more open arrangement, thereby trapping liquid in the voids between them. This has the effect of drying out the system, which then returns to its fluid/

FIG. 1. ARITHMETIC FLOW CURVES OF SOME FLUIDS

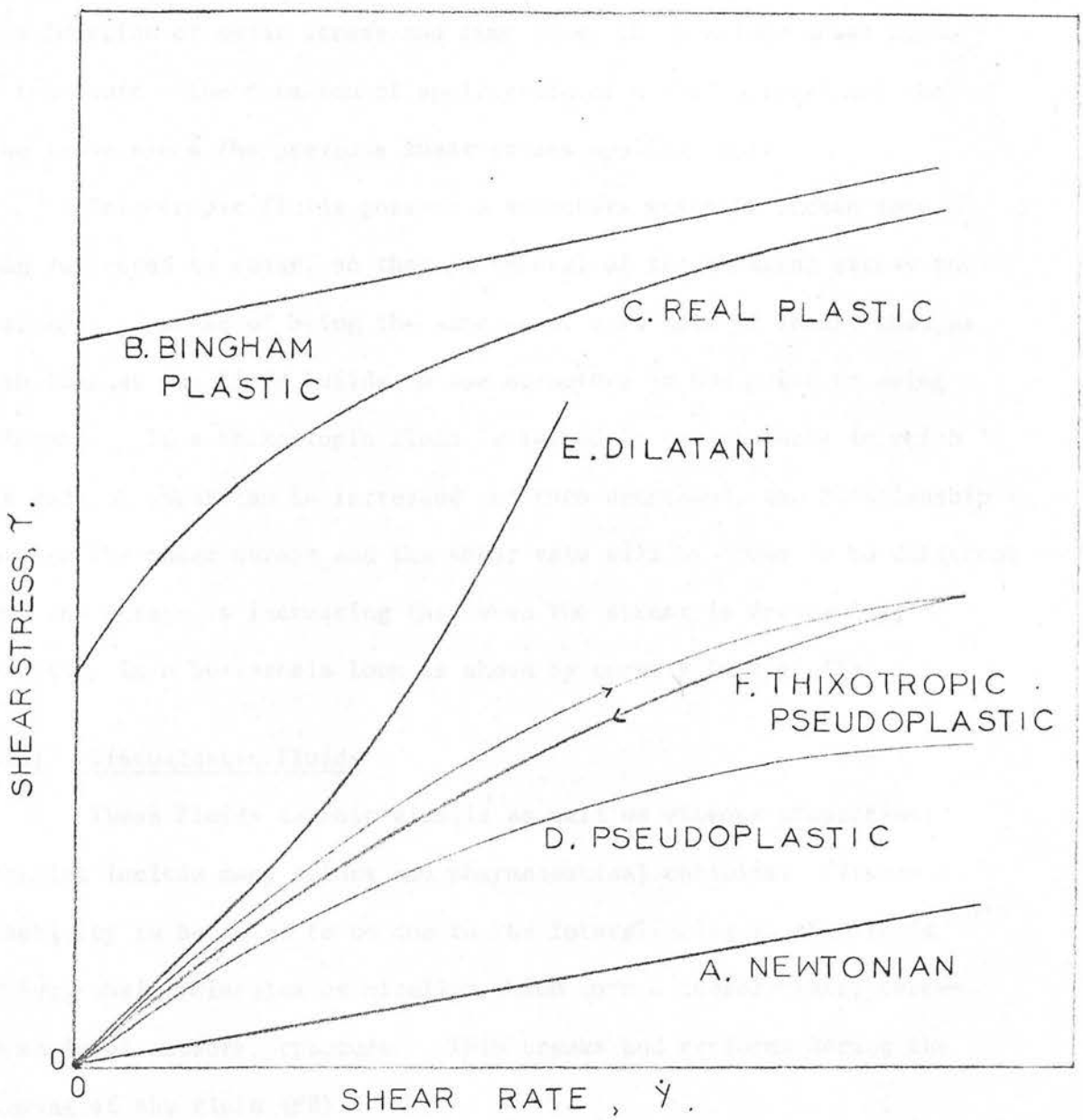

fluid condition when the shear is subsequently withdrawn (P8).

(ii) Time-Dependent non-Newtonian Fluids

For these fluids, termed Thixotropic fluids, the shear rate is a function of shear stress and time (i.e. the previous shear history of the fluid - the duration of application of a shear stress and the time lapse since the previous shear-stress application).

Thixotropic fluids possess a structure which is broken down when subjected to shear, so that on removal of the shearing stress the viscosity, instead of being the same as at zero rate of shear, changes with time as the fluid builds up the structure it had prior to being deformed. If a thixotropic fluid is tested in an apparatus in which the rate of shear can be increased and then decreased, the relationship between the shear stress and the shear rate will be found to be different when the stress is increasing than when the stress is decreasing, resulting in a hysteresis loop as shown by curve F in Fig. (1).

(iii) Viscoelastic Fluids

These fluids exhibit elastic as well as viscous properties; examples include many paints and pharmaceutical colloids. Visco-elasticity is believed to be due to the interlinking in the liquid of long-chain molecules or micelles which form a loosely-knit, three-dimensional network structure. This breaks and re-forms during the flowing of the fluid (P8).

1.1.2 NON-NEWTONIAN FLOW MODELS

Empirical/

Empirical power functions of the type

$\tau = K \dot{\gamma}^{n}$ ($n < 1$ pseudoplastic, $n = 1$ newtonian, $n > 1$ dilatant) (3)

have been widely used to approximately characterise non-Newtonian fluids of the pseudoplastic and dilatant type. K is a measure of the consistency of the fluid, the higher the K, the more viscous the fluid.

The Ellis model has been used to characterise the flow behaviour of pseudoplastic fluids:

$$\dot{\gamma} = K_1 \tau + K_2 \tau^{\alpha'} \qquad (4)$$

K_1, K_2 and α' are constant at a particular temperature and pressure for a given fluid. This model has sometimes proved more successful in correlating experimental measurements than equation (3) (A6, B4, S11).

The equations of Einstein (E1), Sibree (S5) and Smoluchowski (S13) are particular examples of the following general equation for the viscosity of many visco-inelastic emulsions and dispersions at a particular rate of shear:

$$\mu = \mu_o (1 + 2.5 \phi' + a''' \phi'^2 + b''' \phi'^3 + \ldots) \qquad (5)$$

where μ_o is the viscosity of the continuous phase and ϕ' is the volume concentration of the disperse phase - a''', b''' etc. are numerical constants. Equation (5) results from considerations on the connection between non-Newtonian viscosity and the microscopic and macroscopic liquid structure.

Further empirical models are summarised in (F5, P8, W9).

The rheological properties of viscoelastic liquids can be expressed/

expressed in various ways. For some purposes equations of the power law type (Eqn. (3)) are reasonably satisfactory (P8).

Tanner (T2) suggests that the equation of state of a viscoelastic fluid should show:

(i) Typical relaxation spectrum when subjected to small sinusoidal strains,

(ii) Apparent viscosity decreasing monotonically with increasing shear rate,

(iii) Normal forces which develop in the liquid when it is subjected to a shear stress (determined by using an instrument known as the Roberts-Weissenberg rheogoniometer (W6)).

Tanner concluded that these requirements where satisfied, at least in a qualitative way, by the model for the so-called Oldroyd bodies (O2)

$$\tau + K_3 \dot{\tau} = \mu (\dot{\gamma} + K_4 \ddot{\gamma}) \qquad (6)$$

where μ is the viscosity determined at low shear rates under steady state conditions, i.e. when $\dot{\tau} = \ddot{\gamma} = 0$, and the constants K_3 and K_4 are the relaxation time, (the time constant of the exponential decay of stress on the sudden cessation of shear), and the retardation time, (the time constant of the exponential decay of strain on the removal of all stresses), respectively. Oldroyd derived Eqn. (6) theoretically after investigating the elastic and viscous properties of emulsions and suspensions of one Newtonian liquid in another. Fröhlich and Sack (F8) derived the same equation for a dilute suspension of solid elastic particles in a viscous liquid.

For Maxwellian viscoelastic liquids, the following equation due/

due to Maxwell (M5) holds:

$$\tau + K_5 \dot{\tau} = \mu \dot{\gamma} \qquad (7)$$

where $K_5 = {}^{\mu}/_{G}$, the ratio of a constant Newtonian viscosity coefficient to the rigidity modulus of the fluid. K_5 represents the relaxation time.

1.2 SECTION II

1.2.1 DRAG COEFFICIENTS AND VELOCITIES OF RISE

Drag is an energy loss resulting from the resistance to the movement of an object in a fluid, and may be further subdivided into deformation drag, friction drag and pressure drag. It is usual to introduce an arbitrarily defined drag coefficient combining the individual contributions of all three components. The coefficient of drag is defined in the same way as the friction factor for circular tubes, i.e.

$$C_D = \frac{2F}{\rho_o U^2 A'_C} \qquad (8)$$

where F is the total fluid retarding force and is given by $V\Delta\rho g$, where V is the volume of the moving body. A'_C is the cross-sectional area of the body in the direction of rise or fall. Thus for a spherical bubble,

$$C_D = \frac{4g D_e (\rho_o - \rho_i)}{3 U^2 \rho_o} \qquad (9)$$

(a) Theoretical Work

Small Re

Stokes Regime

A gas bubble moves in this regime when the bubble is spherical and the interface rigid (i.e. zero surface velocity). For sufficiently small/

small bubble volumes, this condition is attained for any liquid (A5, B8).

By neglecting the inertial terms appearing in the Navier-Stokes equation, i.e. Re < 1, Stokes (S16) found for a Newtonian liquid that

$$C_D = 24/Re \qquad (10)$$

The velocity of the bubble in the gravitational field is then given by

$$U = \frac{84}{\nu} V^{2/3} \qquad (11)$$

Oseen (O3) proposed that for Re < 2,

$$C_D = \frac{24}{Re} (1 + \frac{3}{16} Re) \qquad (12)$$

Ladenburg (L1) proposed the following relation for the drag coefficient for flow past a sphere in a cylinder of diameter D_c:

$$C_D = \frac{24}{Re} (1 + 2.4 \frac{D_e}{D_c}) \qquad (13)$$

For the analogous problem for power law fluids the definition of a modified Reynolds Number

$$Re' = \frac{(D_e)^n \rho U^{2-n}}{m} \qquad (14)$$

allows the drag coefficient to be given by

$$C_D = \frac{X_n}{Re'} \qquad (15)$$

where X_n is a function of the flow index n (A7). The function is

not/

not known rigorously - only an upper and a lower bound have been calculated (W4). The two bounds coincide at the value 24 when n = 1.

The velocity-volume relationship is

$$U = \left(\frac{\rho_o}{m} \right) \frac{2^{1+n}}{X_n} \left(\frac{4\pi}{3} \right)^{\frac{2-n}{3}} \Bigg)^{\frac{1}{n}} V^{\frac{(1+n)}{3n}} \qquad (16)$$

Hadamard/Rybczynsky regime

This regime is encountered by a gas bubble or liquid drop when the surrounding liquid is in creeping flow (Re < 1), the bubble or drop is spherical and the interface is free. Thus a finite velocity exists at the interface and this is specified to be equal for the continuous and the dispersed phase at a given latitude of the spherical bubble.

Hadamard (H2) and Rybczynsky (R13) independently solved the equations of motion for this case and found that

$$C_D = \frac{24}{Re} \frac{(2\mu_o + 3\mu_i)}{(3\mu_o + 3\mu_i)} \qquad (17)$$

For a gas bubble in a liquid, $\mu_i << \mu_o$; and so

$$C_D = \frac{16}{Re} \qquad (18)$$

The bubble velocity is given by

$$U = \frac{126}{\nu} V^{2/3} \qquad (19)$$

For the analogous problem for non-Newtonian power-law fluids (A7)

C_D /

$$C_D = \frac{X'_n}{Re'} \qquad (20)$$

where X'_n is a function of n. The velocity is again given by Eqn. (16) with X'_n substituted for X_n.

It is presumable that for pseudoplastic fluids

$$n < 1, \quad X'_n < 16 = (X'_n)_{n=1} \qquad (21)$$

Hence presumably,

for $n < 1$, $X_n / X'_n > 1.5$ (the value for n = 1).

Intermediate Re

In the range $10 < Re < 100$ and $Pe \gg 1$, Hamielec and Johnson (H3) obtained functional approximations for the velocity field by assuming a trial stream function in the Navier-Stokes equations and evaluating the undetermined coefficients from the boundary conditions using the method of residuals. They found that

$$C_D = \frac{(16)}{(3)} \frac{(-24A_2 - 70A_3 - 144A_4)}{Re}$$

$$+ \frac{(16)}{(15)} (1 - A_1 - 2A_2 - 3A_3 - 4A_4)(B_1 + 2B_2 + 3B_3 + 4B_4) \qquad (22)$$

Recurrence formulae relate the higher coefficients A_2, A_3 ... and B_2, B_3 ... to their first coefficients A_1 and B_1, these latter being given as a function of Re. The tabulated data of Hamielec and Johnson enabled Redfield and Houghton (R2) to calculate C_D up to Re = 30, the range being extended from Re = 30 to Re = 70 by Baird and Hamielec (B3).

At/

At higher intermediate Re, $100 < Re < 1000$, by applying boundary layer theory to flow around circulating fluid spheres the following result is arrived at

$$C_D = \frac{48}{Re}\left(1 + \frac{\mu_i}{\mu_o} - 0.314\, Re^{-\frac{1}{2}}\left(\frac{4}{3} + 2\,\frac{\mu_i}{\mu_o}\right)\right) \qquad (23)$$

This boundary layer approach was first used by Chao (C5) who, due to an error in his analysis, arrived at an incorrect conclusion. Lochiel (L16) and Moore (M12) noticed the error and the above equation was derived by Lochiel. Moore assessed the drag contributed by the boundary-layer and by the thin wake behind the bubble and his expression for the total drag is

$$C_D = \frac{48}{Re}\left(1 - 2.2\, Re^{-\frac{1}{2}} + 0\,(Re^{-5/6})\right) \qquad (24)$$

High Re

Levich Regime

A bubble or drop moves in this regime when Re is high, the bubble is spherical and the interface is free. The problem is solved by equating the viscous energy dissipation rate connected with the flow field calculated from inviscid flow theory to the rate of positional energy loss due to the motion of the gas bubble (M12). The drag coefficient is given by

$$C_D = \frac{48}{Re} \qquad (25)$$

and/

and hence the velocity

$$U = \frac{42.0}{\nu} V^{2/3} \qquad (26)$$

The same conclusion was reached by Siemes (S6) by using the velocity distributions of Boussinesq (B9) for potential flow.

The solution has been extended to power-law fluids by Astarita and Marrucci (A8), the drag coefficient in this case being given by

$$C_D = \frac{K_n}{R'_e} \qquad (27)$$

where $K_n = \frac{2^{n+3}\, 3^{n+1}}{1 + 4n} \int_0^1 (1 + 2x^2)^{\frac{(n+1)}{2}}\, dx \qquad (28)$

The function $K_n(n)$ takes values, which, for $n < 1$, are always smaller than 48.

Substituting K_n for X_n in Eqn. (16) gives the expression for the velocity U.

Taylor Regime

This regime corresponds to a high Re, and the bubble having a spherical cap shape and a free interface. In this regime C_D is constant.

Using a value of 50 degrees for Θ, the half-angle of the spherical cap, it is found (A7) that

$$C_D = 2.6 \qquad (29)$$

Davies and Taylor (D7) and Moore (M11) have shown that for this regime

U/

$$U = \frac{2}{3}(gR'')^{\frac{1}{2}} \qquad (30)$$

and again using a value of 50 degrees for Θ,

$$U = 25.0\, V^{1/6} \qquad (31)$$

Rippin and Davidson (R3) postulated the existence of a wake of stagnant liquid extending to infinity below a spherical cap bubble, such that the boundary of the wake and the nose of the bubble formed a continuous free streamline. They modified this free boundary by successive perturbations so as to satisfy the boundary conditions derived from Bernouilli's theorem on the assumption of irrotational flow. They found that

$$U = 0.952\, g^{\frac{1}{2}}\, V^{1/6} \qquad (32)$$

This result for U is about 20% higher than that of Davies and Taylor, and Rippin and Davidson suggest that this is due to the pressure rise in the turbulent wake giving a higher drag coefficient in reality.

Collins (C14) by satisfying the constant pressure on the curved bubble nose requirement to a higher order than did Davies and Taylor - $(d^4p/d\Theta^4)_{\Theta = 0} = 0$ as opposed to

$(d^2p/d\Theta^2)_{\Theta = 0} = 0$ - found that

$$U = 0.652\, (gR')^{\frac{1}{2}} \qquad (33)$$

Mendelson (M7) has suggested that the terminal velocity of ellipsoidal and spherical cap bubbles in low viscosity liquids of infinite extent may be represented by the equation

U/

$$U = \sqrt{\frac{2\sigma}{D_e \rho_o} + \frac{gD_e}{2}} \qquad (34)$$

The first term on the r.h.s. corresponds to the surface tension and the second to the buoyancy - dominated regimes of the inviscid flow regime. The equation was derived intuitively by applying the equation from Wave theory giving the velocity for waves of small wavelength compared to the depth of liquid, and substituting for the wavelength (λ) the equivalent spherical bubble circumference (πD_e).

For large bubbles $\frac{gD_e}{2} >> \frac{2\sigma}{D_e \rho_o}$, and the Mendelson equation becomes

$$U = 22.2\sqrt{D_e} \qquad (35)$$

which corresponds to $C_D = 2.67$ in agreement with the derivations of Davies and Taylor (D7).

Dumitrescu (D9) and Davies and Taylor (D7) considering slug flow in a stationary liquid, (i.e. very long and thus wakeless bubbles in inertial flow), showed that

$$U = C_1 \sqrt{gD_c} \qquad (36)$$

C_1 has been assigned values of 0.35 (D9) and 0.33 (D7). Griffith and Wallis (G12) demonstrated that U depended on the shape of the liquid profile and the resulting equation was

$$U = C_1 C_2 \sqrt{gD_c} \qquad (37)$$

C_1 having the value 0.35. C_2 is a function of bubble velocity and the velocity profile of the liquid.

(b)/

(b) Experimental Work

Numerous experimental observations have been carried out on the drag coefficients and terminal velocities of solid spheres, drops and bubbles in motion through fluids (A2, A3, A5, A7, B4, B8, B12, C3, D3, D4, D5, D7, G4, G5, G6, G9, H1, H13, J2, K1, L15, L19, M8, N3, O1, P4, R2, R5, T1, T7, U1, W2, W8).

Newtonian Liquids

Datta (D3) demonstrated experimentally that the effect of the walls of the container in reducing bubble velocity by drag at the walls became increasingly important when $\frac{D_e}{D_c} \geqslant 0.1$. Uno and Kintner (U1) measured terminal rise velocities of air bubbles in four liquids contained in vertical cylindrical tubes of different diameters and proposed the following equation for wall effect correction,

$$\frac{U}{U_{(\infty)}} = \left(\frac{1}{b''} \left(1 - \frac{D_e}{D_c}\right) \right)^{0.765} \qquad (38)$$

b" is a constant which depends upon tube diameter and liquid surface tension. Uno and Kintner (U1) also indicated a ratio of $\frac{D_e}{D_c} < 0.1$ for wall effects to be negligible.

Angelino's terminal rise velocity measurements (A3) for air in water ($\mu_o = 1.6 \times 10^{-2}$ P), dipropylene/tripopylene glycol, D/TPG, ($\mu_o = 1.05$ P), and oil ($\mu_o = 7.40$ P), contained in tubes of different diameters agree with Eqn. (38) proposed by Uno and Kintner (U1). His measurements using glycerol ($\mu_o = 14.40$ P), however show better agreement with the experimentally determined correlations proposed by Fidleris/

Fidleris and Whitmore (F2) when the liquid is contained in tubes with $D_c > 10.16$ cm.

Fidleris and Whitmore (F2) collected experimental data on the drag exerted by the walls of a cylindrical vessel on a solid sphere falling axially down it through a liquid. The experiments were carried out with 60 solid spheres (covering a range of diameters and densities), four cylinders of different diameters, and fifteen Newtonian liquids of various viscosities and densities. The range $0.054 < Re < 20000$ was covered. Fidleris and Whitmore (F2) presented curves showing the factors $\frac{U_{(\infty)}}{U}$ by which readings taken in a cylindrical vessel must be multiplied to give the terminal velocity in an infinite medium.

Peebles and Garber (P4) measured bubble velocities in sixteen liquids and deduced the following empirical correlations for drag coefficients in the four regimes into which they divided their results:

$$C_D = \frac{24}{Re} \quad ; \quad Re \leqslant 2 \tag{39}$$

$$C_D = \frac{18.7}{Re^{0.68}} \quad ; \quad 2 \leqslant Re \leqslant 4.02M^{-0.214} \tag{40}$$

$$C_D = 0.0275\, MRe^4; \quad 4.02M^{-0.214} \leqslant Re \leqslant 3.10M^{-0.25} \tag{41}$$

$$C_D = 0.82M^{0.25}\, Re; \quad 3.10M^{-0.25} \leqslant Re \tag{42}$$

M is a dimensionless group dependent on liquid properties only, such that

$$M = g\mu_o^4/\rho_o\sigma^3 \tag{43}$$

However/

However Datta (D3) and Uno and Kintner (U1) have both shown that wall effects are important for a ratio of tube diameter to bubble diameter of less than ten. The tube used by Peebles and Garber being only 1.03" (2.62 cm.) internal diameter means that the value of their results for bubble diameters greater than 0.25 cm. is limited. Thus only the first two equations, Eqns. (39) and (40), are satisfactory.

Tadaki and Maeda (T1) measured terminal velocities of bubbles in the size range 0.25 cm. $< D_e <$ 1.8 cm. in fourteen different liquids and concluded that

$$C_D = 0.076\ (\text{Re. } M^{0.23})^{1.82} \quad ; \quad 8M^{0.068} < \text{Re. } M^{0.23} < 6 \qquad (44)$$

$$C_D = 1.25\ (\text{Re. } M^{0.23})^{0.26} \quad ; \quad 6 < \text{Re. } M^{0.23} < 16.5 \qquad (45)$$

$$C_D = 2.6 \quad ; \quad 16.5 < \text{Re. } M^{0.23} \qquad (46)$$

Haberman and Morton (H1) studied the motion of air bubbles in eight test liquids, (with water at three different temperatures), using three test tanks, all of which were large enough to prevent the presence of the walls from affecting the bubble velocities. Their results for C_D vs Re in the air-water system is shown in Fig. (2). They carried out a dimensional analysis of the motion of rising bubbles using eight physical variables and found that

$$f\ (C_D, \text{Re}, \text{We}, M) = 0 \qquad (47)$$

Considering gas density and viscosity to be negligible, the number of dimensionless groups reduced to three. For the particular case in which/

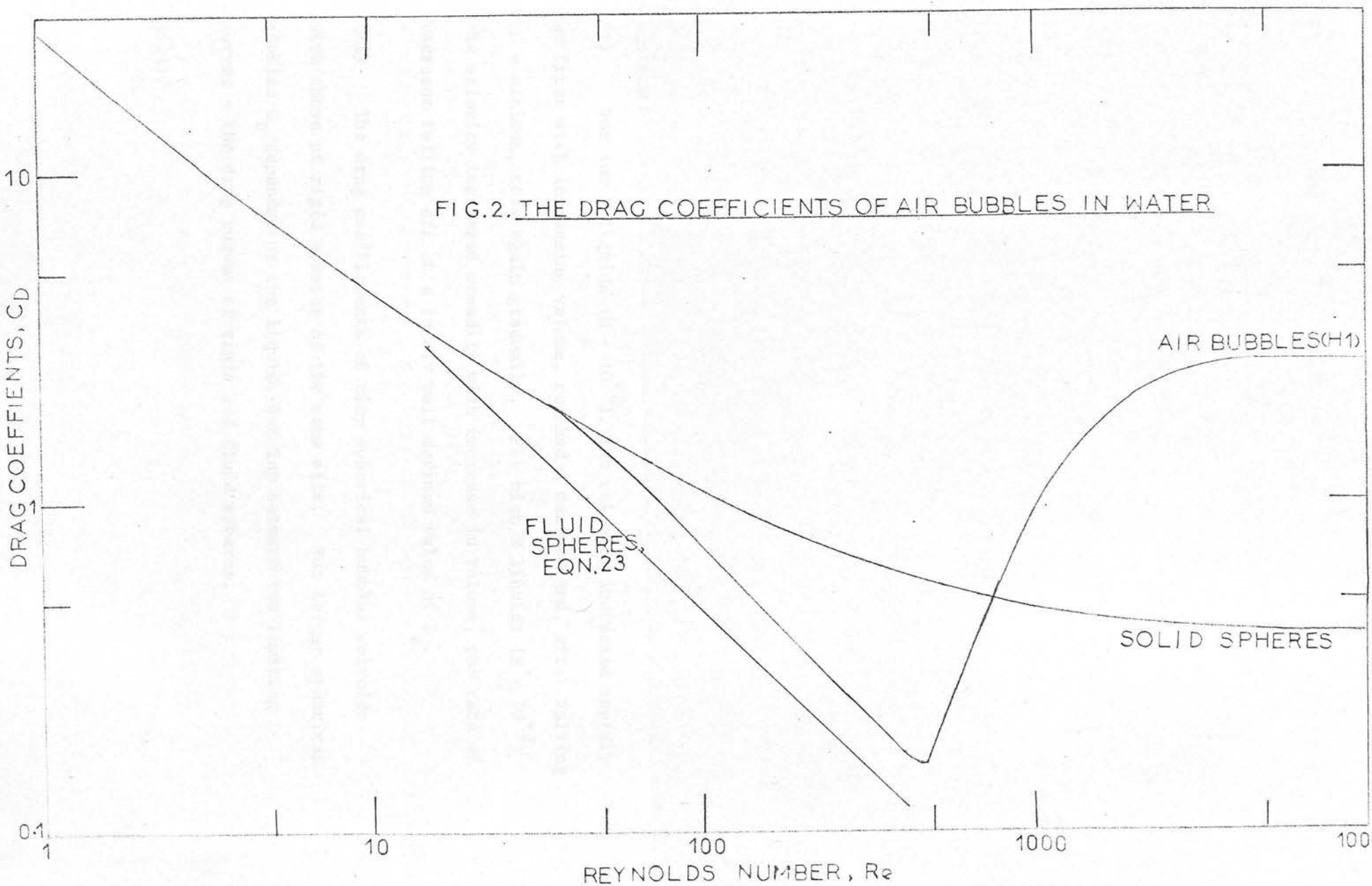
FIG.2. THE DRAG COEFFICIENTS OF AIR BUBBLES IN WATER
DRAG COEFFIENTS, C_D
10
1
0.1
1
10
100
1000
10000
REYNOLDS NUMBER, Re
AIR BUBBLES(H1)
FLUID SPHERES, EQN.23
SOLID SPHERES

which only the velocity, the acceleration due to gravity, the liquid density and the bubble equivalent spherical diameter are considered, one dimensionless parameter was obtained -

$$C_D = \text{constant} \qquad (48)$$

Haberman and Morton (H1) plotted C_D vs. Re and We with M as an additional parameter. Their plots showed no systematic arrangement of the curves relative to the change in the parameter M, which was constant for a specific liquid. It was therefore concluded that the six variables, (velocity, acceleration due to gravity, density and viscosity of the liquid, surface tension and equivalent spherical diameter), were insufficient for the complete description of bubble motion. Other important conclusions from the results of Haberman and Morton (H1) were:

(i) For low M liquids ($M < 10^{-8}$), the velocity increased rapidly at first with increasing volume, reached a maximum and, after falling to a minimum, rose again gradually. For high M liquids ($M > 10^{-3}$) the velocity increased steadily with increase in volume, the rate of increase falling off at a fairly well defined value of D_e.

(ii) The drag coefficients of tiny spherical bubbles coincide with those of rigid spheres of the same size. For larger spherical bubbles C_D depended on the liquid, but lay between two limiting curves - the drag curves of rigid and fluid spheres.

(iii)/

(iii) For low M liquids, a minimum in C_D was reached at Re ≃ 250, the minima occurring near the diameter for transition from spherical to ellipsoidal shapes. Such minima were not found for liquids of high M value.

(iv) The drag coefficients of large spherical cap bubbles have a constant value of 2.6.

(v) Impurities and surfactants increased the drag on small bubbles in water. Beyond a certain critical concentration of the surface-active substances, an increase in concentration had relatively little influence on the drag of the bubbles.

The data for the five low viscosity liquids used by Haberman and Morton, (water, methyl alcohol, Varsol, turpentine and a 13 per cent solution of ethyl alcohol in water), and in particular the two pure compounds, water and methyl alcohol, are correlated well by Eqn. (34) proposed by Mendelson (M7).

Liquid metals differ hydrodynamically from other liquids by their considerably higher surface tensions. Schwerdtfeger (S4) measured the rise velocities of ellipsoidal and spherical cap argon bubbles rising in the liquid metal mercury, and found that the data could be correlated within their experimental precision by the Mendelson equation (34).

Cole (10) collected velocity and drag coefficient data for vapour bubbles ($0.1 \leq D_e < 1.3$ cm.), rising through a variety of saturated liquids under pressures ranging from 48 to 540 mm. Hg. Although /

Although considerable scatter of the data was evident, it was apparent that the mean of the data was in agreement with Mendelson's analysis.

Davenport, Richardson and Bradshaw (D5) noted that additions of up to 4.5 per cent polyvinyl alcohol (PVA) to water, which increased the viscosity from that for water, 1.11 cP, to that for the aqueous solution, 54 cP, had no appreciable effect on the terminal rise velocity of air bubbles. Further additions of PVA to 115 cP caused some reduction in velocity, and this was even more marked when the viscosity was increased to 216 cP. This effect was especially noticeable for bubbles of $D_e < 2$ cm. Angelino (A3) also noticed a similar reduction in bubble terminal velocity as the viscosity of the Newtonian liquid used increased.

For $D_e/D_c \geq 0.75$, Datta et al (D4) showed that bubbles adopt a cylindrical shape with rounded nose, forming slugs of finite length, and, in the limit, long bubbles for which wake effects may be neglected.

White and Beardmore (W8) studied rise velocities of single cylindrical bubbles in nineteen different liquids and arrived at the following empirical correlation based on tube diameter,

$$(Fr)^{\frac{1}{2}} = f(Eo) \qquad (49)$$

where M is an additional parameter. White and Beardmore (W8) also concluded that

$gD^3/\mu_o^2 > 3 \times 10^5$; viscous effects negligible

Eo/

$Eo > 70$; interfacial effects negligible

$Fr < 3 \times 10^{-3}$; inertial effects negligible

Goldsmith and Mason (G6), in a similar investigation on cylindrical bubbles rising through twelve different air-liquid and liquid-liquid systems, observed that under inertial flow conditions, part of the bubble nose assumed a spherical shape and agreement with theory relating terminal rise velocity to tube diameter was obtained. In viscous flow regimes they found that the bubble nose and rear assumed respectively prolate and oblate forms, and agreement with a theory relating terminal rise velocity to liquid film thickness resulted.

Nicolitsas and Murgatroyd (N3) using water as the liquid phase measured air slug velocities; the time taken for the slug to pass between two photocell stations being automatically recorded with a maximum overall electronic jitter of ±2 m sec. The value of the constant C_1 in Eqn. (36) was determined by a least squares fit to give the value 0.35. Nicolitsas and Murgatroyd (N3) found that the dispersions in transit times were much greater than could be accounted for by electronic jitter. Thus their measured values of C_1 ranged between 0.350 and 0.358. They concluded that the transit time dispersions probably represent random fluctuations in the slug flow conditions.

Finally, a selection of smoothed experimentally measured terminal rise velocities for single bubbles in free rise through different Newtonian liquids as obtained by various investigators is shown/

shown in Fig. (2) of reference (L19). Loudon (L19) points out that in the absence of any wall effect and for corresponding liquids, good agreement among different investigators is reached only in the extreme regions of very small (spherical - Stokes regime) and large (spherical cap - Taylor regime) bubbles. Various proposals concerning the observed discrepancies in the intermediate range have been put forward, including the effects of system contamination by surfactants, irregularities of motion caused by turbulence and wake effects and, for different gases, bubble solubilities.

Non-Newtonian Liquids

Loudon (L19) working with water and aqueous solutions of CMC, sodium carboxymethylcellulose, (which exhibit non-Newtonian pseudoplastic behaviour), found that for CMC concentrations in excess of 1 per cent wt., the rising velocities of carbon dioxide bubbles were generally lower than in distilled water. This effect was most noticeable at small bubble diameters and became more pronounced with increasing CMC concentration (see Fig. (3)).

Barnett et al (B4) studied the drag coefficients of small carbon dioxide bubbles and small glass spheres moving through dilute aqueous solutions of pseudoplastic carboxymethylcellulose, thereby obtaining a comparison for solid vs. fluid sphere behaviour. They were unable to correlate the drag coefficient data in terms of the generalised Reynolds Number, Re', defined in Eqn. (14), which had successfully been used by Fararoui and Kintner (F1) to correlate data for drops. Barnett et al (B4) thus defined a new Reynolds Number, Re" /

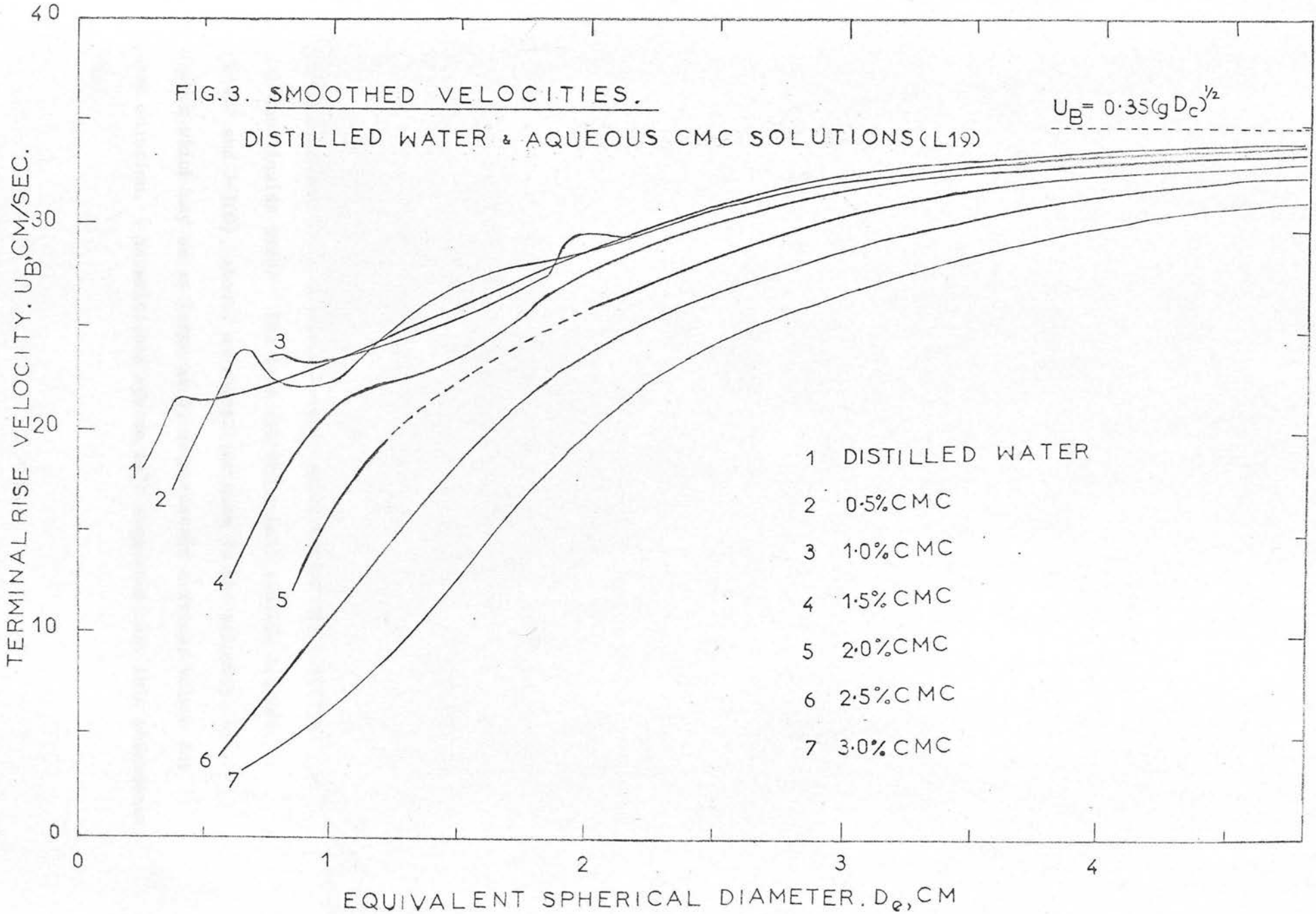
FIG. 3. SMOOTHED VELOCITIES.
DISTILLED WATER & AQUEOUS CMC SOLUTIONS (L19)
$U_B = 0{\cdot}35(g D_c)^{1/2}$
TERMINAL RISE VELOCITY, U_B, CM/SEC.
EQUIVALENT SPHERICAL DIAMETER, D_e, CM
0
10
20
30
40
1
2
3
4
1 DISTILLED WATER
2 0·5% CMC
3 1·0% CMC
4 1·5% CMC
5 2·0% CMC
6 2·5% CMC
7 3·0% CMC

Re", for non-Newtonian fluids which follow the Ellis model (Eqn. (4)),

$$Re'' = K_1 D U \rho + K_2 U^{2\alpha' - 1} \rho^{\alpha'} \qquad (50)$$

Solid and fluid sphere drag coefficient data were successfully correlated in terms of Re" for Re" < 400, as were the experimental data of Slattery (S10) and Slattery and Bird (S11) for solid sphere drag in CMC solutions. With increasing pseudoplasticity, the solid sphere drag coefficient increases, in qualitative agreement with the calculations of Bizzell and Slattery (B6). Both the solid sphere drag coefficient data and the bubble drag coefficient data approach the curve for solid spheres in Newtonian fluids, (Eqn. (10)) at Re" < 1.

Astarita and Apuzzo (A7) measured the terminal velocities of air bubbles in four types of non-Newtonian solutions - aqueous solutions of Carbopol (purely viscous, highly pseudoplastic liquids), aqueous solutions of CMC (slightly elastic, pseudoplastic liquids), aqueous solutions of ET497 (highly elastic, pseudoplastic liquids), aqueous solutions of J-100 (highly elastic, pseudoplastic liquids). Bubble sizes over the range 10^{-4} cc to 10 cc were investigated.

The data of Astarita and Apuzzo (A7) show that at large enough volumes the conditions of the Taylor regime are satisfied for all the liquids used. The data for the highly elastic liquids, (Et497 and J-100), showed an abrupt increase in the velocity, by a factor which may be as large as 6, at a certain critical volume for each solution. Astarita and Apuzzo (A7) suggested that this phenomenon was/

was due to a transition from the Stokes to the Hadamard regime, and that viscoelasticity was responsible for the abruptness of the transition.

Sato et al (S2) measured the terminal velocities of falling spheres, (steel bearing balls), in three synthetic rubber-organic solvent solutions, all of which exhibited pseudoplastic behaviour, contained in cylindrical containers of various diameters. They found that the apparent rate of shear around a sphere for the non-Newtonian fluids was given by

$$\dot{\gamma}_a = 0.6 \left(\frac{U_{(\infty)}}{D_e}\right) , \quad \dot{\gamma}_a < 2.0 \qquad (51)$$

where $U_{(\infty)}$ is the terminal velocity of the sphere corrected for wall effect and D_e is the diameter of the falling sphere. Sato et al (S2) also found that the wall effect on the falling spheres in non-Newtonian fluids were less than that in Newtonian fluids.

Effect of Gas Solubility on Bubble Rise Velocities

With two exceptions, (D4, L8), the assumption that mass transfer does not influence instantaneous bubble rise velocities has been borne out by several investigators (B2, G13, H1, H5, L12, L16, S17, Z1).

Datta et al (D4) investigated experimentally rise velocities of air and carbon dioxide bubbles in water, and noted that mass transfer resulted in velocity retardation.

Leonard and Houghton (L8) compared terminal rise velocities

of/

of nitrogen and carbon dioxide bubbles in water and reported that rise velocities were strongly dependent upon mass transfer for small bubbles in the bubble size range $0.2 \leqslant D_e \leqslant 0.6$ cm. Leonard and Houghton (L9) suggested that this velocity retardation may be due to electrokinetic effects induced by mass transfer. However Lochiel (L16), in investigating carbon dioxide bubbles in water finds good agreement between his velocity measurements and those of Leonard and Houghton for carbon dioxide bubbles, and of Uno and Kintner for air bubbles in the size range $0.5 < D_e < 0.8$ cm., though these velocities fall below those of Haberman and Morton (H1) using air bubbles in water. Lochiel (L16) suggests that a more likely explanation than surface effects for the velocity difference is that point velocities such as Haberman and Morton's (made over a short vertical displacement of about 6 cm. so that the bubble size is essentially constant), differ from average velocities found over large pool depths when the bubble size is changing constantly, (as is the case for Leonard and Houghton's results and those of Uno and Kintner and Lochiel).

1.2.2 BUBBLE SHAPES

It is usual to assign simple geometric configurations to approximately describe the shape of drops and bubbles in motion through fluids.

Newtonian Liquids

In/

In liquids of low M, small gas bubbles are spherical. As the bubble size is increased a continuous progression to oblate spheroid then through irregular ellipsoid to spherical cap occurs (D4, D7, D8, H1, L19, M8, R5, S1, S6, T1, U1).

There is a certain amount of disagreement about the precise bubble sizes at which these shape transitions occur in a particular liquid, though in the air-water system, (M for water is approx. 3×10^{-7}), the average of experimental findings (L16) gives the following approximate shape regions:

Spheres	$D_e < 0.12$ cm.
Oblate spheroids	$0.12 < D_e < 0.60$ cm.
Irregular ellipsoids	$0.60 < D_e < 1.8$ cm.
Spherical caps	$D_e > 1.8$ cm.

A number of investigators (D4, D8, P3) have presented photographic evidence of the upper surface of the oblate spheroid bubbles being flatter than the lower surface, and spherical cap bubbles have been shown to be truly spherical only over part of the frontal surface extending out from the apex (C11, D7). The shapes of the irregular ellipsoids are known to fluctuate rapidly (H1).

Tadaki and Maeda (T1) correlated their data on the bubble shapes obtained in various liquids, ($2.52 \times 10^{-4} \geqslant M \geqslant 3.94 \times 10^{-11}$), in terms of a shape ratio $D_e/_{2a}$, thus

Spheres/

Spheres	$D_e/_{2a} = 1$	$Re_M^{0.23} < 2$	(52)
Oblate spheroids	$D_e/_{2a} = 1.14\ (Re._M^{0.23})^{-0.176}$	$2 < Re_M^{0.23} < 6$	(53)
Irregular ellipsoids	$D_e/_{2a} = 1.36\ (Re._M^{0.23})^{-0.28}$	$6 < Re_M^{0.23} < 16.5$	(54)
Spherical caps	$D_e/_{2a} = 0.62$	$Re_M^{0.23} < 16.5$	(55)

The range of bubble diameters studied was $0.25 < D_e < 1.8$ cm. and the experiments were carried out in a square column of side 10 cm.

Defining an additional shape ratio, the bubble eccentricity, as

$$E = {}^{2a}/_{2b} \qquad (56)$$

C(3), equations (51) - (54) may be expressed in the forms,

Spheres	$E = 1$	$Re_M^{0.23} < 2$	(57)
Oblate spheroids	$E = 0.675\ (Re_M^{0.23})^{0.528}$	$2 < Re_M^{0.23} < 6$	(58)
Irregular ellipsoids	$E = 0.4\ \ (Re_M^{0.23})^{0.84}$	$6 < Re_M^{0.23} < 16.5$	(59)
Spherical caps	$E = 3.5$	$Re_M^{0.23} > 16.5$	(60)

Siemes' results (S6) were in substantial agreement with Eqns. (58) and (59), though Rosenberg's results (R5) for the same regions were approximately 50 per cent higher. Spherical cap eccentricities found by Rosenberg (R5) were in agreement with Eqn. (60), though the results of Davies and Taylor (D7) ranged between 3.23 and 4.65, those of Lochiel (L16) between 2.5 and 4 and those of Loudon (L19) between 2.5/

2.5 and 4.5. For D_e > 3.5 cm using a 10.16 cm diameter column, Loudon's results (L19) indicated that wall proximity was influencing bubble shape, and the smoothed curve drawn through the E vs. D_e data showed a downward trend. The results mentioned in this paragraph all refer to the air or carbon dioxide-water system, except for those of Davies and Taylor (D7) which refer to the air-nitrobenzene system.

The shapes of larger bubbles rising through viscous liquids tend to remain stable andnot to fluctuate about a mean form as in liquids of low M. Also in viscous liquids the bubble size range spanned by the ellipsoid regimes seem to be reduced (A3, D5). Thus the photographs of Angelino (A3) show that air bubbles in glycerol (μ_o = 14.4 P, σ = 63.72 dynes/cm., i.e. M = 1.33 x 10^2) were spherical for D_e up to 2.7 cm., though the larger bubbles in this region would better be described by a 'greater than hemispherical' shape. For D_e up to 4.7 cm. E for the bubbles rose to a value of about 2 (i.e. an approximately hemispherical shape). For D_e > 4.7 cm., the photographs suggest that the bubbles developed a trailing gas envelope or skirt, though this is not stated explicitly by Angelino. In oil (μ_o = 7.4 P, σ = 31.85 dynes/cm., i.e. M = 1.03 x 10^2) hemispherical bubbles were observed up to D_e = 2.8 cm. From D_e = 2.8 cm to D_e = 3.6 cm the bubbles adopted a spherical cap shape, skirting appearing to commence thereafter. For D/TPG, (μ_o = 1.05 P, σ = 34.15 dynes/cm., i.e. M = 2.93 x 10^{-2}), the spherical cap shape was adopted over the entire 1.08 < D_e < 3.86 cm size range investigated. In Angelino's experiments, the minimum air bubble size used in glycerol was 1.20 cm. and in oil 1.08/

1.08 cm.

Shoemaker and Marc de Chazal (S19) have observed skirting and dimpling, the existence of concave rear surfaces on large spherical cap drops, for drops of 2-butanone, acetone, hexane, 2-ethyl-1-hexanol, and 145 c.p. paraffin oil in glycerol. Photographs of single drops in free rise and of two drops undergoing coalescence are presented in ref. (S19). Shoemaker and Marc de Chazal attribute the dimples and skirts formed in the trailing end of the drops to stable vortices in the wakes of the drops, and to circulation within the drops.

Davenport, Richardson and Bradshaw (D5) determined the shapes of gas bubbles, (gases used were air,nitrogen and carbon dioxide), rising through various liquids, (liquids used were water, aqueous solutions of polyvinyl alcohol (PVA) with viscosities up to 216 cP and ethyl alcohol), in a 15 cm. diameter column. Their results re shape and stability are shown in Table 1, though only the various shapes encountered will be discussed in this sub-section.

TABLE 1

Liquid	Bubble volume (cm^3)	D_e (cm)	Remarks
Tap water and distilled water	0.04-4.5	0.42-2.04	Ellipsoidal bubbles - marked oscillation. Helical rise.
	4.5 - 40	2.04-4.2	Spherical cap bubbles. Rippling evident both on rear and front surfaces.
Ethyl alcohol	< 1	< 1.24	Ellipsoidal bubbles with marked oscillation.
	1 - 40	1.24-4.2	Spherical cap bubbles as for water. Rippling slightly more pronounced.
½ per cent PVA	< 1	< 1.24	Ellipsoidal bubbles with no oscillation.
(μ = 2 cP, σ = 49.7 dyn cm^{-1})	1 - 3.5	1.24-1.90	Ellipsoidal bubbles. Oscillations evident but less noticeable than with ethyl alcohol or water.
	3.5 - 40	1.90-4.2	Spherical cap bubbles - rectilinear rise. Rippling much less pronounced than with water.
4.2 per cent PVA	< 1	< 1.24	Ellipsoidal - no oscillation
(μ = 54 cP, σ = 47.0 dyn cm^{-1})	1 - 3	1.24-1.78	Transition region. Ellipsoidal with slight oscillation.
	3 - 40	1.78-4.2	Spherical cap bubble. Rectilinear motion. Apart from initial release rippling very slight. Lower surface slightly concave.
5.4 per cent PVA	< 1	< 1.24	Ellipsoidal. No surface instability.
(μ = 115 cP, σ = 46.9 cyn cm^{-1})			

TABLE 1 (Contd.)

Liquid	Bubble volume (cm^3)	D_e (cm)	Remarks
	1 - 1.5	1.24-1.42	Slight surface instability. Gradual change of shape to spherical cap.
	1.5-40	1.42-4.2	Spherical cap. Rectilinear rise. No rippling. Lower surface concave.
6.1 per cent PVA (μ = 216 cP, σ = 46.2 cyn cm^{-1})	0.2 - 15	0.72-3.0	Spherical cap. Rectilinear rise. No rippling or oscillation. No shape transition in this range.
	15 - 40	3.0 - 4.2	Bubble tends to form thin skirts of trailing gas. Length of skirt increasing with bubble size, up to approx. 30 cm. long.

Fig. (4) shows the measured heights and basal radii for bubbles rising in water and the PVA solutions. Davenport et al (D5) noted that the large bubbles were of the spherical cap shape observed by previous investigators (D7, H1, T1). Photographs showed the curvature of the front surface of bubbles of $D_e > 2.7$ cm. to be very nearly spherical.

Davenport et al (D5) suggest that for gas bubbles in Newtonian liquids, the gas properties are unimportant and so dimensional analysis yields

$$f\left(E, Re, M, \frac{D_e}{D_c}\right) = 0 \qquad (61)$$

Since neither the surface tension nor the viscosity are likely to be important for large bubbles, E should be constant for low values of D_e/D_c. Davenport et al point out, however, that though their results show less scatter than those of Davies and Taylor (D7), there is still some doubt about the constancy of the value of E, which for $D_e < 2$ cm appears to be influenced by liquid properties. With larger bubbles ($D_e > 4$ cm), E decreases with size as would be expected from the influence of wall proximity on bubble shape. Figure 4 also indicates that with increasing PVA concentration (and hence viscosity), E decreases; the effect being most noticeable with small bubbles in the 216 cP solution. Table 1 shows that the size at which transition to the spherical cap shape occurs decreases with increasing viscosity.

Grace and Harrison (G10) investigated the influence of bubble shape on the rising velocities of large bubbles. They derived

equations/

FIG. 4. BUBBLE DIMENSIONS vs. EQUIVALENT DIAMETER (D5)

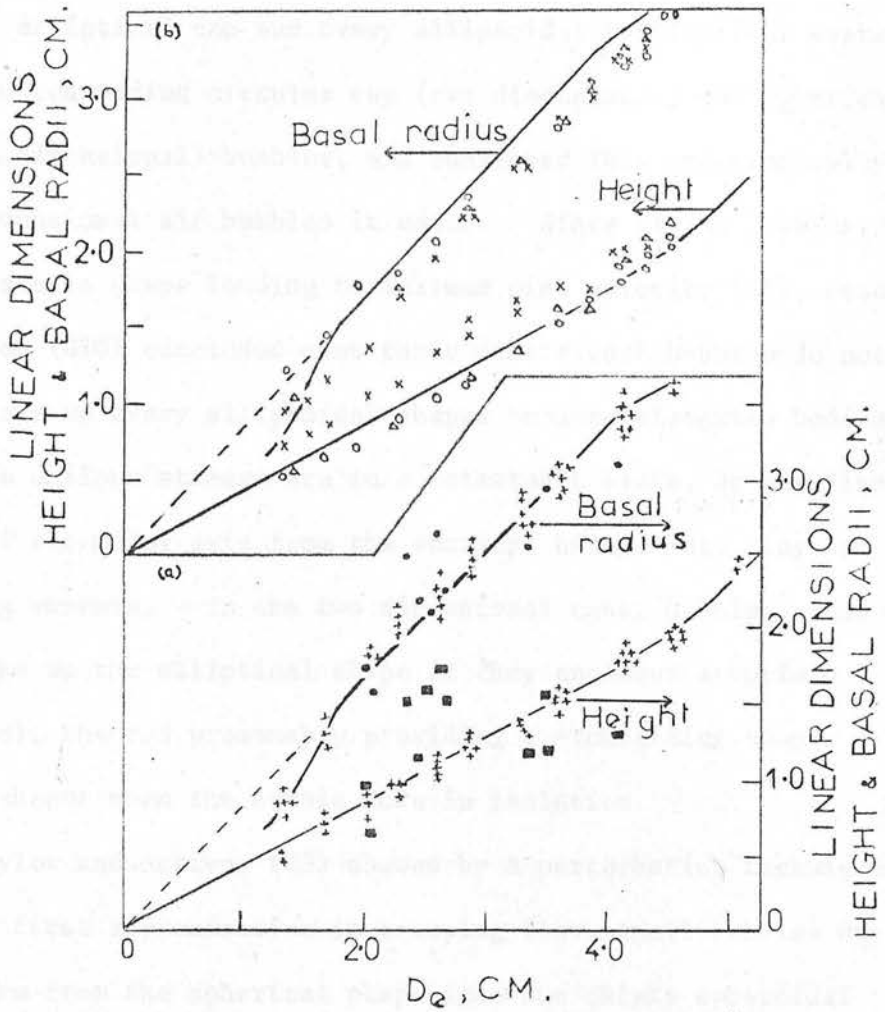

LOWER GRAPH (a) Bubbles in water : + , height ▪ , basal radius •

UPPER GRAPH (b) Bubbles in PVA solutions : 54 cP ○ , 115 cP △ , 216 cP × , lines as for water

equations in two and three dimensions which related the rising velocity of a large bubble in an inviscid liquid to its size and to the radius of curvature of its leading edge. Grace and Harrison (G10) found that elliptical cap and ovary ellipsoidal bubbles rose faster than the corresponding circular cap (two dimensional) and spherical cap (three dimensional) bubbles, and confirmed this experimentally for two dimensional air bubbles in water. Since rising bubbles adopt the stable shape leading to maximum rise velocity (G1), Grace and Harrison (G10) concluded that three dimensional bubbles do not normally take up ovary ellipsoidal shapes because elongated bodies immersed in uniform streams are in a metastable state, as any disturbance of the major axis from the vertical brings into play destabilizing moments. In the two dimensional case, bubbles could be made to take up the elliptical shape if they enclosed a surface (e.g. a rod), the rod presumably providing a stabilizing couple which was absent when the bubble rose in isolation.

Taylor and Acrivos (T3) showed by a perturbation technique that, to a first approximation in creeping flow, small bubbles or drops deform from the spherical shape into the oblate spheroidal shape. In their analysis Re and We of both phases were small and of the O(1) or less, and the effects due to surface active agents were ignored. Pan and Acrivos (P1) extended the Taylor-Acrivos solution to the more general case when Re pertaining to motion inside the bubble was unrestricted. Thus Pan and Acrivos (P1) determined theoretically the shapes of bubbles or liquid drops in steady translation through an unbounded, quiescent, and viscous fluid medium for the/

the cases where the Reynolds and Weber numbers of the continuous phase were both small, and the interface clean. The inertia forces of the internal circulation did not affect the shape of a gas bubble, and contributed in a minor, but significant way to the deformation of a liquid drop; and so for bubbles the result of Taylor and Acrivos (T3) was found to be applicable even when $Re_g >> 1$; and so

$$r(\mu) = 1 - 0.21\ We\ P_2(\mu) - 0.09\ \frac{We^2}{Re}\ P_3(\mu) \qquad (62)$$

Experimental observations were carried out by Pan and Acrivos (P1) with air bubbles, ($0.52 < D_e < 0.94$ cm.), in zerolene. The Taylor-Acrivos, Pan-Acrivos analysis showed good agreement with shapes of bubbles at the lower end of the bubble size range investigated, but agreement became progressively worse with increasing bubble size. Wellek et al (W7) found that the Acrivos and Taylor analysis for liquid drops accurately predicted their experimentally determined drop eccentricities for drop Reynolds numbers less than about 10.

Non-Newtonian Liquids

Similar bubble shapes have been observed in non-Newtonian liquids to those found in Newtonian liquids, (i.e. spheres, oblate spheroids, irregular ellipsoids, spherical caps); but a notable addition in the case of non-Newtonian fluids is the onset of bubble tailing resulting in the lower pole of the ascending gas bubble being cuspidal. This phenomenon has been observed in non-Newtonian fluid fields/

fields by Philopoff (P7) using thixotropic solutions, Astarita and Apuzzo (A7) using elastic pseudoplastic aqueous solutions of ET497 and J-100, Barnett et al (B4) using pseudoplastic aqueous CMC solutions, and Loudon (L19) using pseudoplastic aqueous CMC solutions for ascending gas bubbles; and by Warshay et al (W2), Mhatre and Kintner (M10), and Fararoui and Kintner (F1) for liquid drops.

The onset of bubble tailing results in top shapes, or oblate spheroids with protruding rear tip, or spherical caps with protruding rear tip, depending on bubble size.

The most extensive work on bubble shapes in non-Newtonian liquids has been carried out by Loudon (L19) for carbon dioxide bubbles in pseudoplastic aqueous CMC solutions ranging from 0.5% wt to 3% wt concentration in increments of 0.5% wt. In addition to bubble tailing in the more concentrated CMC solutions (occurring over the size range $0.8 < D_e < 2$ cm in the 2% wt, $0.8 < D_e < 2.4$ cm in the 2.5% wt, and $0.9 < D_e < 3.5$ cm in the 3% wt), the spherical caps were observed to develop a lip around the lower extremity of the frontal surface in the range $1.9 < D_e < 3.2$ cm for the 1% wt solution. Loudon (L19) also observed that large bubbles ($D_e > 4$ cm) rising in the 2.5% wt and 3% wt CMC solutions possessed a concave indentation in the centre of the bubble floor.

A tentative explanation of bubble and drop tailing in pseudoplastic and thixotropic fluids has been proposed by Philopoff (P7) and Warshay et al (W2) in terms of the fluid displaced by the motion of the bubble or drop failing to recover rapidly enough, resulting in/

in a 'hole' to the rear of the bubble which is filled by the bubble tail. Barnett et al (B4) suggested, further, that the hole sets up an adverse pressure gradient resulting in flow separation. For a Newtonian fluid, a wake would develop but for a pseudoplastic fluid the development of the wake would require more energy than its Newtonian counterpart, slowing down the bubble. If this energy were not supplied, the pressure gradient itself would act as a brake on the bubble. Barnett et al (B4) concluded that either condition would result in a greater drag coefficient for the pseudoplastic fluid than for the Newtonian which was in agreement with their experimental findings.

Loudon (L19) summed up that the appearance of unusual bubble shapes in liquids must be the result of a highly complex interaction between internal and external flows, both of which are strongly influenced by the physical properties of the continuous phase.

1.2.3 BUBBLE STABILITY IN MOTION

The path followed by a single gas bubble of given size and shape rising freely in a liquid is a characteristic of the liquid properties (C15, D3, G9, H1, H8, H12, M8, S1, T1). The four main classifications of bubble path are,

(a) Rectilinear

(b) Zig-zag

(c) Spiral

(d) Rectilinear with rocking

Saffman/

Saffman (S1) investigated the motion of small air bubbles in water ($0.1 < D_e < 0.8$ cm) and observed that

$D_e < 0.14$ Rectilinear rise

$0.14 < D_e < 0.2$ cm Zig-zag rise

$D_e > 0.2$ cm Zig-zag or spiral rise

Saffman treated zig-zag and spiral motions theoretically by assuming inviscid flow near the bubble front, and obtained reasonable agreement between predicted and observed rise velocities and shapes for given bubble sizes. His theoretical treatment of zig-zag motion yielded the criterion

$$We_{crit} = 1.03 \qquad (63)$$

for the stability of rectilinear motion. Experimental investigation yielded the criterion

$$We_{crit} = 1.7 \qquad (64)$$

Saffman concluded that the interaction between periodic wake oscillation and instability of motion near the front of a bubble, which occurred when the bubble was sufficiently oblate, resulted in zig-zag motion.

The experimental investigation of Hartunian and Sears (H8) into the instability of bubble motion in twelve different liquids yielded two separate criteria for the onset of instability,

$Re_{crit} = 202$ for impure or viscous liquids (65)

$We_{crit} = 1.26$ for pure, low viscosity liquids (66)

Approximate/

Approximate theoretical considerations involving only hydrodynamic pressure and surface tension and including the effects of bubble deformation gave, for moderate We,

$$We_{crit} = 1.23 \qquad (67)$$

Hartunian and Sears concluded that the main factors determining the stability of bubble rise were surface tension and hydrodynamic pressure forces.

Haberman and Morton (H1) and Davenport et al (D5), (see Table 1), both observed that increasing liquid viscosity damped out bubble rise path instability, the former investigators reporting only rectilinear motion in viscous liquids with Re < 150. Haberman and Morton (H1) suggested that for all liquids

Re < 300	Rectilinear motion
300 < Re < 3000	Spiral motion
Re > 3000	Rectilinear motion with rocking

They also noted that the helical path of the bubbles followed either a clockwise or a counterclockwise direction, depending on conditions of generation.

Rippling has been observed on the surfaces of large bubbles ($1.5 < D_e < 4$ cms) rising through liquids of low viscosity (D5, L19), though, as noted by Davenport et al (D5), (see Table 1), increasing liquid viscosity damped out rippling. Sternling and Scriven (S14) pointed out that there are ever present, small, random fluctuations about/

about any fluid-fluid interface. These random fluctuations touch off bubble surface rippling in relatively inviscid liquids when there is hydrodynamic instability at the surface.

Chou and Charles (C7) investigated the onset of interfacial wave formation in co-current gas-liquid stratified flow and derived a criterion for interface instability. Chou and Charles (C7) and Hanratty and his co-workers (C9, H7) both observed that in co-current gas-liquid stratified flow transition to a disturbed interface, (rippling), took place with the less viscous phase in turbulent motion and the more viscous phase in laminar motion. Hanratty and Engin (H7) noted a qualitative agreement between their experimental results and observations of the effect of wind velocity upon the surface of a large body of liquid.

Avetisyan and Trapeznikov (A9) obtained data on the relationship between intensity of damping out of waves by monolayers of insoluble substances and the degree of compression of the monolayer, i.e. on the two-dimensional pressure F' and the area occupied by a molecule. They studied the action of monolayers differing widely in two-dimensional viscosity. Avetisyan and Trapeznikov (A9) obtained graphs of the increase in logarithmic damping decrement $\Delta\phi$ plotted against F' for seven different monolayers on water. They found that (1) in all instances the intensity of damping passed through a maximum which occurred at relatively low values of F'; (2) at the oscillation frequency of 20 c/sec monolayers which differed in two-dimensional viscosity by many orders of magnitude nevertheless possessed roughly/

roughly the same ability to damp out waves. It was noted that the position of the maxima on the $\Delta\phi$ curves corresponded roughly to the position of the maxima for stability of bubbles in the same monolayers.

Bubbles in low viscosity liquids, particularly those classified as irregular ellipsoids (see Section 1.2.2), are known to pulsate or oscillate around a mean shape (D5, H1, L16). Pulsations are reduced and eventually eliminated by increasing liquid viscosity (D5, H1). Zieminski and Raymond (Z2) investigated carbon dioxide bubbles ($0.26 < D_e < 0.38$ cm) rising through water and found that the stability in motion of these small bubbles was dependent on the bubble release time. Long release times resulted in increased oscillation and a high degree of randomness in the motion of the bubble, which persisted almost to the top of the liquid column (82 cm. high).

1.2.4 BUBBLE WAKES

At present there is no adequate mathematical description of the wake region of a fluid with a free interface, although certain phenomena associated with bubble motion, in particular bubble instability, have been attributed to wake effects (H1, S1).

Very small gas bubbles in the Stokes regime (see Section 1.2.1) behave like rigid spheres, as do larger bubbles when contaminated by surfactants (see "Experimental Work" Section 1.3.1). The wakes formed/

formed behind solid bluff bodies will therefore be described by following the discussion of Goldstein (G7), before considering the wakes formed behind fluid bodies.

The first stage in the development of a wake behind a solid body appears in the broadening out behind an obstacle (e.g. a sphere or a circular cylinder) of the streamlines calculated by the method of Stokes or Oseen (see Section 1.2.1). As the Reynolds number is increased, the streamlines widen out more and more. They form a closed region behind the obstacle within which there is an inflow along the axis of the wake and a flow in the general direction of motion in the outer portions; this circulatory motion constituting a vortex pair. The vortices become more and more elongated in the direction of flow, eventually above some critical Reynolds number (depending on the obstacle shape, the degree of turbulence in the main stream and the proximity of the channel walls) the vortices become asymmetrical shortly after the beginning of the motion, leave the obstacle and move downstream. At moderately high Reynolds number the vortex layers which spring from the surface of the solid body are unstable, and roll up in such a way that vortices are formed at their ends and are shed alternately. An eddying motion of definite frequency is set up, and downstream the double row appears again. At still higher Reynolds numbers the vortices diffuse so rapidly after their formation that it is no longer possible to speak of the formation of a double row. No definite value can be assigned to this upper limit, but from an investigation of the records of various experimenters, Goldstein/

Goldstein (G7) concluded that no double row had been seen or photographed above Re = 2500. At the back of the solid body, however, vortices continued to be shed with unfailing regularity until Re = 4×10^5 or 5×10^5. Beyond this upper limit the flow was turbulent.

The mechanism of the motion may be explained in terms of the boundary layer and vortex layers. Separating the fluid in the wake from the main flow are layers of vorticity (the vortex layers), which left the surface at the separation points. At moderately small Reynolds numbers the vortex layers come together downstream and vorticity diffuses from the layers into the bulk fluid, but is also generated in the boundary layer and added to the vortex pair. At small Reynolds numbers a state of equilibrium is set up between the rates of generation and diffusion of vorticity, and the vortex pair is stationary relative to the solid body. As the Reynolds number increases so does the rate of generation of vorticity. In order to counteract this the vortex layers become longer in the direction of flow, thereby providing a larger area from which vorticity can diffuse; at the same time the strength of the individual vortices in the vortex pair increases. The vortex layers are unstable, and at some critical Reynolds number one or other is shed. As overall horizontal momentum is conserved the liquid still directly associated with the solid body has a velocity in the direction opposite to that of the discharged vortex. Hence a periodic instability is set up with the vortices discharging alternately from side to side.

Magarvey/

Magarvey and Maclatchy (M2) investigated the wake phenomena associated with a single liquid drop falling through a quiescent liquid phase. The stream surfaces associated with the field responsible for the transfer of vorticity were made visible by means of dye trails. At some point on the downstream side of the drop equator the boundary layer was observed to separate from the drop surface and to continue as a free vortex sheet. Magarvey and Maclatchy (M2) noted that the asymmetrical reactive forces associated with the build up and detachment of vortex elements combined with the dynamic forces over the leading surface to give the freely falling drop a rocking motion, the frequency of this motion being identical to that at which vortex elements were shed.

Magarvey and Bishop (M1) observed and classified wakes behind liquid drops falling through quiescent water into the approximate regions shown in Table 2.

TABLE 2

Class	Range of Re	Nature of Trail
1	0 - 210	Single trail
2	210 - 270	Double trail
3	270 - 290	Double trail with waves
4	290 - 410	Procession of vortex loops
5	410 - 700	Double row of vortex rings
6	700 - 2500	Irregular wake

The/

The Class 1 wake appeared to be the only one in which the configurations behind freely falling drops and rigidly held solid spheres were identical. In Class 2 wakes there was a continuous backflow which contacted the back surface of the drop before escaping the near wake region by way of the vortex trails. The arguments for the buildup of the periodic shedding of vorticity, finally ending with the irregular wake, as Reynolds number was increased (Classes 2 - 6) were as for wakes behind solid bodies.

The wakes behind bubbles have also been investigated photographically. Hartunian and Sears (H8), using a vegetable dye tracer, showed that wakes behind small bubbles existed only in impure or viscous liquids. In pure liquids, bubbles were trailed by a small closed vortex pair immediately after bubble release, after which bubble oscillation set in and the dye was dispersed. It was concluded that the dye itself had caused liquid contamination and that a wake existed only until the bubble had shed the dye, after which motion of the small bubble through the pure liquid was not associated with a wake of appreciable extent.

Lochiel (L16) further assumed that there were no appreciable wakes behind larger, oblate bubbles, since oblate bubbles moved essentially under potential flow conditions for which wakes did not exist.

Due to an optical anistropy of nitrobenzene, Davies and Taylor (D7), in photographing spherical cap air bubbles in nitrobenzene, revealed a three-dimensional wake which approximately completed the spheroid/

spheroid of which the bubble cap formed a part; though there did not appear to be any indication of disturbances downstream of the spheroidal region.

Crabtree and Bridgwater (C16) photographed two-dimensional air bubbles (10 cm^3 to 35 cm^3) rising through five water-glycerol solutions having kinematic viscosities from 8.34 cm^2/sec to 1.02 x 10^{-2} cm^2/sec and contained in a 8 ft. x 3 ft. x $\frac{1}{2}$ in. (244 cm x 91.5 cm x 1.27 cm) tank. They found that in the most viscous liquid no vortex formation was observed, the boundary layer from around the bubble meeting and continuing downstream of the bubble. As the liquid viscosity was reduced, the meeting of the boundary layer moved further downstream from the bubble rear, a weak systematic vortex pattern being eventually obtained. Further reduction of the liquid viscosity resulted in the vortices getting stronger and larger. After the passage of a bubble the shed vortices increased in radius and decayed in strength at a rate dependent on the kinematic viscosity of the liquid (S3). Crabtree and Bridgwater (C16) found that the discussion of Goldstein (G7) for the wakes behind solid bluff bodies qualitatively explained their observed wake phenomena. It was noted that clockwise rotation of the bubble release cap caused the first vortex to be shed to the left and anticlockwise to the right, in the liquids in which vortex shedding was observed.

Collins (C12, C13) photographed the wake behind a large two-dimensional cylindrical cap bubble (Re $\simeq$ 2.5 x 10^4) rising through water contained in a 3 ft. x 3 ft. x $\frac{1}{4}$ in. (91.5 cm x 91.5 cm x 0.64 cm) tank/

tank with the aid of dyed polystyrene particles suspended in the water. Collins (C12, C13) showed the cylindrical cap bubble to move with a certain body of liquid (present as a trailing vortex pair), the combined air and vortex pair system being approximately circular. The photographs of Crabtree and Bridgwater (C16) for the air-water system, however, showed that alternate vortex shedding occurred in the wake behind two-dimensional bubbles. Crabtree and Bridgwater's photographic information (C16) is in agreement with that of Maxworthy (M6) for a 2.5 cm^3 three-dimensional bubble in water and Loudon for large three-dimensional air bubbles in water. Maxworthy (M6), using a simple flow dye visualization technique, showed that as a large air bubble rose through a quiescent liquid it produced a well-defined wake. It was also shown that the drag on the bubble appeared as a momentum defect within the wake.

Moore (M11) and Rippin and Davidson (R3), in their theoretical analyses, rejected closed wake models on the ground that they have no drag and hence, presumably, infinite terminal velocity by d'Alembert's paradox (B5). Collins (C13) pointed out that it was not necessary to assume that the fluid was inviscid; what was assumed was that the flow over the bubble cap was irrotational because viscous and surface tension forces were negligible in that region. Collins (C13) noted that d'Alembert's paradox dealt with an inviscid fluid and thus had no relevance to the method used by Davies and Taylor (D7) and Collins (C14) in deriving Eqns. (30) and (33) respectively.

Slaughter and Wraith (S12), using a shadow-graph arrangement, presented/

presented an excellent photograph of an air bubble (D_e = 2.40 cm) rising through 87 per cent wt/wt aqueous glycerol (ν = 1.43 cm^2/sec), and this is shown in Fig. (5). The wake appears to consist of a toroidal vortex moving with the bubble, and a streaming cylindrical tail extending along the rise path. Slaughter and Wraith (S12) found the wakes of successive bubbles to be similar in form and to retain their axiality. The outline of the vortex part of the wake suggested an attached spheroidal section similar to that observed by Davies and Taylor (D7), the lower tailing section extending along the rise path corresponded to the downstream disturbances discussed by Maxworthy (M6). Slaughter and Wraith (S12) noted the similarity between the wake in their photograph and the wake observed behind a partially immersed solid cylinder at the same order of Reynolds number (G8) and the wakes behind the two-dimensional cap bubbles of references (C4, C12, C16, L19).

Loudon (L19) photographed the wakes of air bubbles rising in two and three-dimensional columns containing water or aqueous solutions of CMC. Finely ground perspex or small metallic silver flakes, dispersed in the liquid, enabled the visualization of the flow patterns. It was found that the extent of wake and wake turbulence progressively decreased with increasing pseudoplastic viscosity.

1.2.5 SUMMARY. Bubble Motion in Liquids

The/

FIG. 5. PHOTOGRAPH OF SPHERICAL CAP BUBBLE AND WAKE (S12)

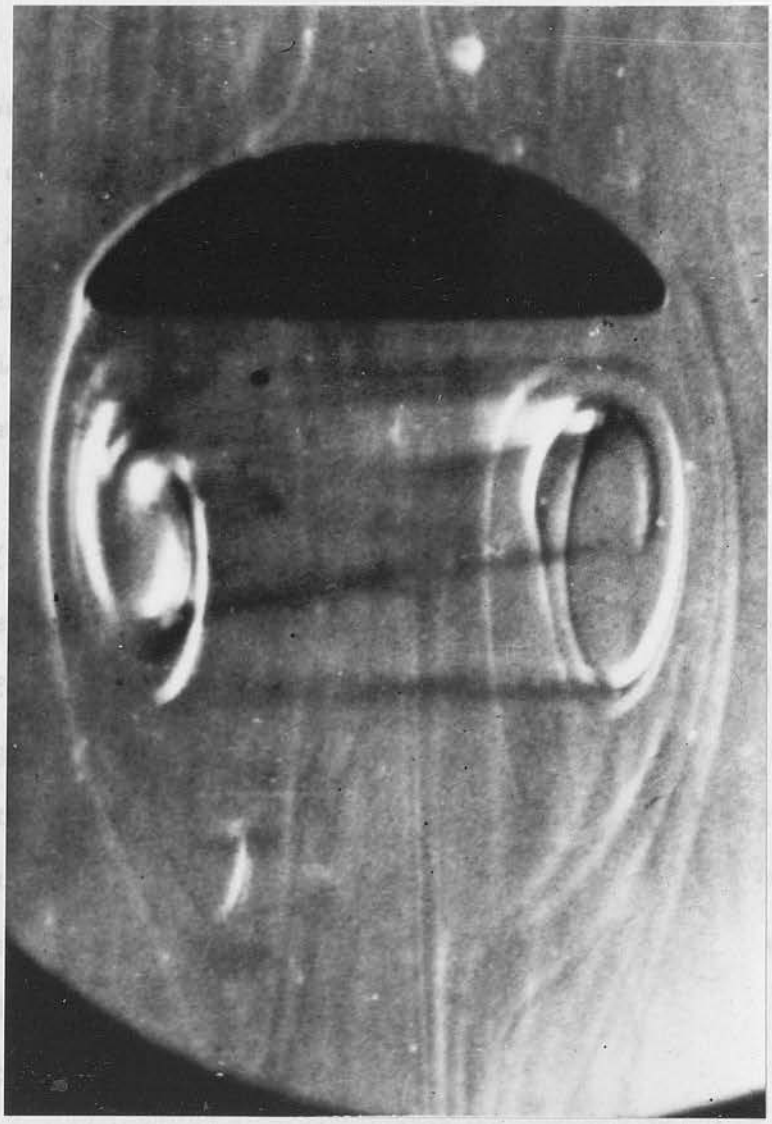

AIR BUBBLE: D_e = 2.40 cm in 87 per cent wt/wt AQUEOUS GLYCEROL SOLUTION, ν = 1.43 cm^2/sec.

U_B = 33.5 cm/sec. 2a = 4.22 cm.

The theoretical analyses of Stokes and Hadamard/Rybczynsky for rigid and circulating spheres in creeping flow provide respectively lower and upper limits to rise velocity data. The purity of the liquid continuous phase governs the transition from solid to fluid sphere behaviour, this being most important in the case of low viscosity liquids.

For large spherical cap bubbles, the Davies-Taylor and Mendelson equations give good agreement with experimental results when wall effects are absent, and for spherical caps subjected to wall effects the Dumitrescu equation provides an upper limit for rise velocity data. There is good agreement between the Mendelson equation and velocity of rise data for bubbles in the ellipsoidal regime in low viscosity liquids, particularly for ellipsoids rising in pure, (i.e. single component), liquids.

Generally, in the Reynolds number range intermediate between creeping flow and potential flow over the bubble nose, (Davies-Taylor regime), there is appreciable disagreement among various investigators. This is due to the fact that theories concerning bubble motion in this intermediate Reynolds number range are on the whole based on simplified models which ignore observed shape irregularities, bubble instability and wake effects.

For bubbles rising through non-Newtonian liquids, theoretical approaches are limited to solid and fluid spheres obeying the empirical power law relationship, and the solutions are in most cases incomplete. For non-spherical bubbles in non-Newtonian fluids no theoretical/

theoretical analyses have been carried out, though the Davies-Taylor and Dumitrescu equations are applicable for large spherical cap bubbles. The success of C_D vs Re correlations depend on the choice of a suitable definition of Reynolds number which in turn is dependent on the liquid non-Newtonian properties.

Peculiarities in bubble and drop shapes, (such as tailing), in non-Newtonian liquids have only been qualitatively explained.

1.3 SECTION III

1.3.1 MASS TRANSFER BETWEEN SOLID AND FLUID BODIES AND FLUIDS

All drops and bubbles may be taken to be axisymmetric about the axis in the direction of rise, so that transfer around them can be analysed using equations for an axisymmetric body of revolution (L18).

(a) Theoretical Work

Solid and Fluid Spheres

Langmuir (L3) considered the case of pure radial diffusion from a sphere into an infinite quiescent fluid and concluded that

$$Sh = 2 \qquad (68)$$

This equation agrees with the experimental findings of several investigators (L21, M13, T5, W11).

When the fluid flows past bodies undergoing transfer, i.e. under forced convection conditions, the continuous phase transfer rate increases markedly above the value predicted by Eqn. (68).

Several investigators (A1, B3, B11, F7, F6, L11, L16, R9) have theoretically derived the following equation for forced convection transfer from rigid spheres in the Stokes regime (S16) ($Re < 1$, $Pe \gg 1$),

$$Sh = k\, Pe^{1/3} \qquad (69)$$

where k is a constant being assigned values 0.89 (F6), 0.978 (B11), 0.99/

0.99 (B3, L16), 1.01 (L11) and 1.037 (A1, R9).

Griffith (G11) and Ward (W1) investigated the case of a fluid sphere with internal circulation in the same flow regime and, for example, Ward (W1) found that

$$Sh = 0.98 \left(\frac{\mu_i + 1.33\,\mu_o}{\mu_i + \mu_o} \right)^{1/3} Pe^{1/3} \qquad (70)$$

Using an interpolation method Ruckenstein (R10) derived the following equation for a fluid sphere with intermediate interfacial mobility moving at Re << 1,

$$0.849 \frac{U_o}{U} Sh^{-2} + 0.662 \left(\frac{3}{2} - \frac{2U_o}{U} \right) Sh^{-3} = Pe^{-1} \qquad (71)$$

where $\frac{U_o}{U}$ is a dimensionless equatorial velocity.

For Re >> 1 and intermediate surface mobility, Ruckenstein (R10) derived

$$0.849 \frac{U_o}{U} Sh^{-2} Re + 0.278 \left(\frac{3}{2} - \frac{U_o}{U}\right)\left(\frac{3}{2} + \frac{U_o}{U}\right)^{\frac{1}{2}} Re^{3/2} Sh^{-3} = Sc^{-1} \qquad (72)$$

Ruckenstein (R10) pointed out that the prediction of $\frac{U_o}{U}$ for Re >> 1 was very difficult.

At the intermediate and high Reynolds numbers, the only rigid sphere models available are semi-empirical, such as those due to Frössling (F9),

Sh/

$$Sh = 2 + 0.55\ Re^{0.5}\ Sc^{0.33} \qquad (73)$$

and Griffith (G11),

$$Sh = 2 + 0.57\ Re^{0.5}\ Sc^{0.35} \qquad (74)$$

The mass transfer of a fluid sphere moving uniformly in a continuous fluid medium are affected by the motion inside the sphere.

Using the Hadamard-Rybczynski (H2, R13) velocity distributions for a bubble or drop moving at $Re < 1$ with $Pe \gg 1$ and with free interface, Levich (L11) obtained

$$Sh = 0.65\ Pe^{\frac{1}{2}} \qquad (75)$$

The same equation was derived by Lochiel and Calderbank (L18) and Stewart, Angelo and Lightfoot (S15). Ruckenstein (R12), Griffith (G11) and Ward (W1) obtained similar equations but with the multiplying constants ranging between 0.61 and 0.67. The constant 0.65 appears to be the most reliable, as, unlike the others, it was arrived at without any assumption being made about the form of the concentration distribution around the sphere.

Lochiel (L17) presented equations which predicted the effect of trace surface-active impurities on mass transfer across a mobile spherical interface at creeping flow. The equations indicated that transfer in the bulk phase surrounding the spheres decreased on increasing the surfactant concentration, and also that the influence of surface-active contaminants on drag and transfer decreased as the viscosity of the bulk phase was increased.

In/

In the intermediate Reynolds number range $10 < Re < 100$ and $Pe >> 1$, Hamielec and Johnson (H3) obtained

$$Sh = 1.13 \left(\frac{5}{6} + \frac{A_1}{6}\right)^{\frac{1}{2}} Pe^{-\frac{1}{2}} \qquad (76)$$

the values of the coefficient A_1 being found in references (H3) and (B3).

At higher Reynolds numbers, $100 < Re < 1000$, and using the modification of the boundary conditions of Chao (C5) due to Lochiel and Calderbank (L18), the resulting equation is

$$Sh = 1.13 \left(1 - \frac{2 + 3\mu_i/\mu_o}{1 + (\rho_i\mu_i/\rho_o\mu_o)^{\frac{1}{2}}} \cdot \frac{1.45}{Re^{\frac{1}{2}}}\right)^{\frac{1}{2}} Pe^{\frac{1}{2}} \qquad (77)$$

which for a gas bubble in a liquid, $\mu_i << \mu_o$ and $\rho_i \mu_i << \rho_o \mu_o$, yields

$$Sh = 1.13 (1 - 2.90 Re^{-\frac{1}{2}})^{\frac{1}{2}} Pe^{\frac{1}{2}} \qquad (78)$$

Hamielec, Johnson and Houghton (H4) used finite-difference methods to obtain steady state solutions of the Navier-Stokes equation for Reynolds numbers of 0.1, 1, 50, 100 and 200. The results showed a steady trend from Hadamard-Rybczynski (H2, R13) flow to boundary-layer flow after Levich-Chao-Moore (L11, C5, M12).

Finally, for very high Reynolds numbers, potential flow exists (i.e. the flow of the continuous fluid is irrotational), where viscous effects are negligible compared with inertial effects, and the solution of Boussinesq (B9) is

$$Sh = 1.13\ Pe^{\frac{1}{2}} \qquad (79)$$

Equation (79) has been derived in a more accessible reference by Ruckenstein (R12).

To predict overall mass transfer coefficients with the above equations, flow separation has to be assumed to be negligible.

Sih and Newman (S8) investigated mass transfer to a sphere in Stokes flow at high Peclet numbers. By using the singular-perturbation technique, they found six distinct regions of different mass transfer mechanisms. One of these regions, the diffusion layer, has already been solved by the boundary-layer method (L11), and Sih and Newman (S8) solved the region at the rear of the sphere finding that

$$Sh = 1.192 \qquad (80)$$

at the rear stagnation point.

It should be noted that in the case of a solid sphere, flow separation occurs near the rear of the sphere and so the diffusion layer region covers most of the surface of the sphere. For a spherical bubble with a mobile interface, an even larger portion of the surface area is occupied by unseparated flow (L11). For deformed bubbles, the region of separation, which encloses the wake, may occupy an appreciable percentage of the bubble surface area. As Section 1.2.2 of this survey has shown, there are many situations in which the bubbles undergoing transfer are not spherical.

Oblate Spheroids, Prolate Spheroids and Spherical Caps

For fluid oblate spheroids in potential flow through liquids (large Re and Pe), Lochiel and Calderbank (L18) have shown that

$$\frac{Sh_{os}}{Sh_s} = \left(\frac{2}{3}(1 + k)\right)^{\frac{1}{2}} \times \frac{2E^{1/3}(E^2 - 1)^{\frac{1}{2}}}{E(E^2 - 1)^{\frac{1}{2}} + \ln\left(E + \sqrt{(E^2 - 1)}\right)} \qquad (81)$$

where subscript os means oblate spheroid, and subscript s, sphere. Thus, Sh_s is the Sherwood number for a mobile sphere of the same volume and is given by Eqn. (79).

For transfer around prolate spheroids in potential flow they derived the following equation,

$$\frac{Sh_{ps}}{Sh_s} = \left(\frac{2}{3}(1 + k)\right)^{\frac{1}{2}} \times \frac{2E^{1/3}(1 - E^2)^{1/2}}{E(1 - E^2)^{\frac{1}{2}} + \sin^{-1}(1 - E^2)^{\frac{1}{2}}} \qquad (82)$$

where subscript ps means prolate spheroid.

Values of Sh_{os}/Sh_s and Sh_{ps}/Sh_s calculated from Eqns. (81) and (82) by Lochiel and Calderbank (L18) are shown in Fig. (6), from which it may be seen that flattening does not influence the transfer coefficient to an important degree.

Sy and Lightfoot (S18) considered the behaviour of drops and bubbles at low Re (< 20) and We < 1 in systems free from surfactants, when the departures from sphericity are small. They used the surface-stretch model of Angelo et al (A4) to show that for oblate spheroids

Sh_{os} /

FIG.6. POTENTIAL FLOW TRANSFER RATIO Sh_{ps}/Sh_s & Sh_{os}/Sh_s vs E (L16, L18)

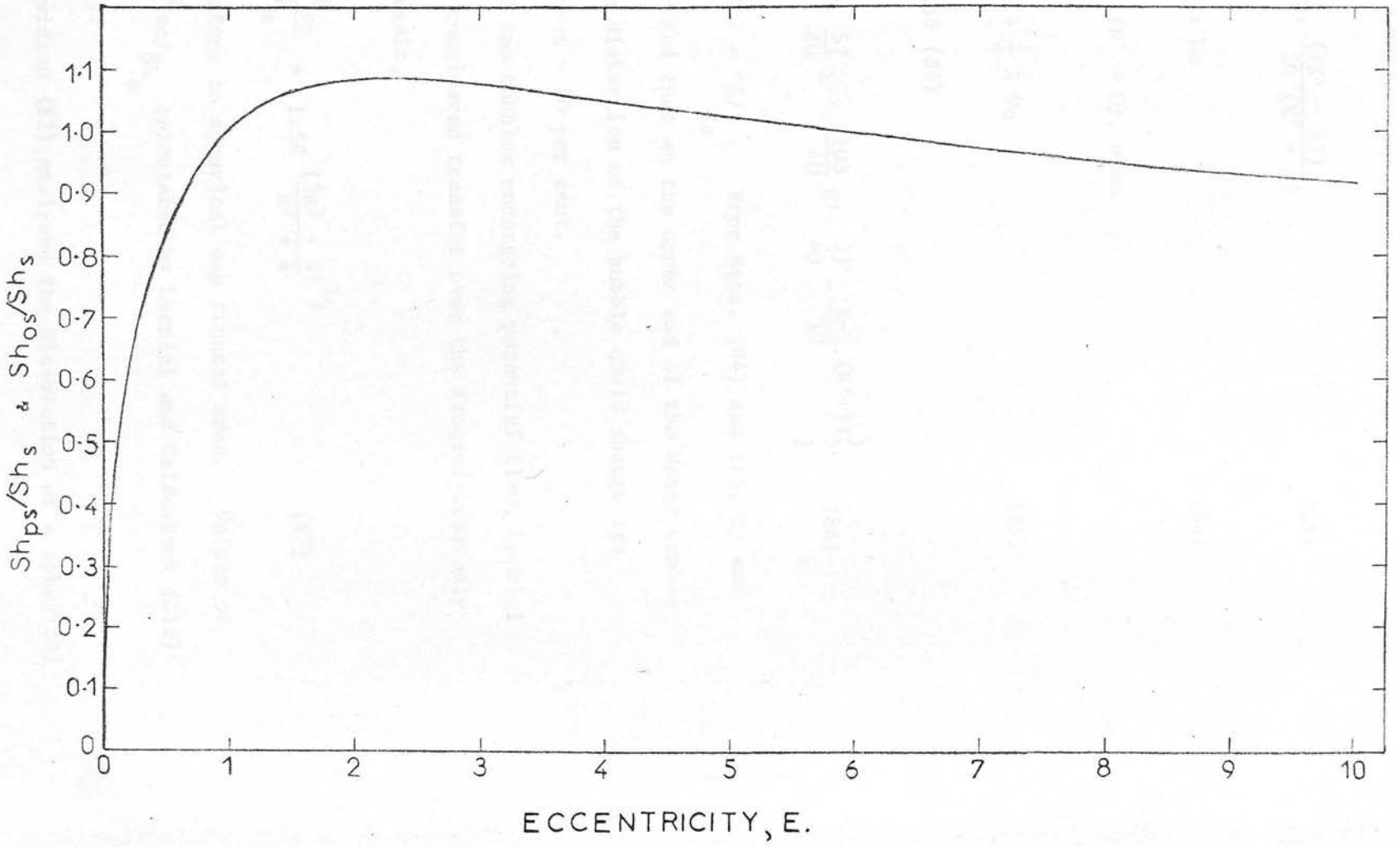

$$\frac{Sh_{os}}{Sh_s} = 1 + \lambda\ We\ \frac{(7K' - 17)}{20\ (K' + 1)} \qquad (83)$$

$$= 1 - \frac{17}{20}\ \lambda\ We \qquad (84)$$

for small gas bubbles ($K' \to 0$), when

$$\frac{A_{os}}{A_s} = 1 + \frac{1}{4}\ \lambda\ We \qquad (85)$$

In Eqns. (82), (83) and (84)

$$\lambda = \frac{1}{4(K'+1)^3}\left(\left(\frac{81}{80}\ K'^3 + \frac{57}{20}\ K'^2 + \frac{103}{40}\ K' + \frac{3}{4}\right) - \frac{\ell-1}{12}\ (K'+1)\right) \qquad (86)$$

where $K' = \mu_i/\mu_o$ and $\ell = \rho_i/\rho_o$. From Eqns. (84) and (85) Sy and Lightfoot (S18) estimated that at the upper end of the Weber number range considered, the distortion of the bubble could change its Sherwood number by about - 20 per cent.

For spherical cap bubbles undergoing potential flow, Lochiel and Calderbank (L18) considered transfer over the frontal area only and arrived at the result,

$$\frac{Sh_{sc}}{Sh_s} = 1.58\ \frac{(3E^2 + 4)^{2/3}}{E^2 + 4} \qquad (87)$$

where subscript sc refers to spherical cap frontal area. Values of the transfer ratio Sh_{sc}/Sh_s calculated by Lochiel and Calderbank (L18) are shown in Fig. (7).

Baird and Davidson (B2) analysed the dissolution of a spherical cap/

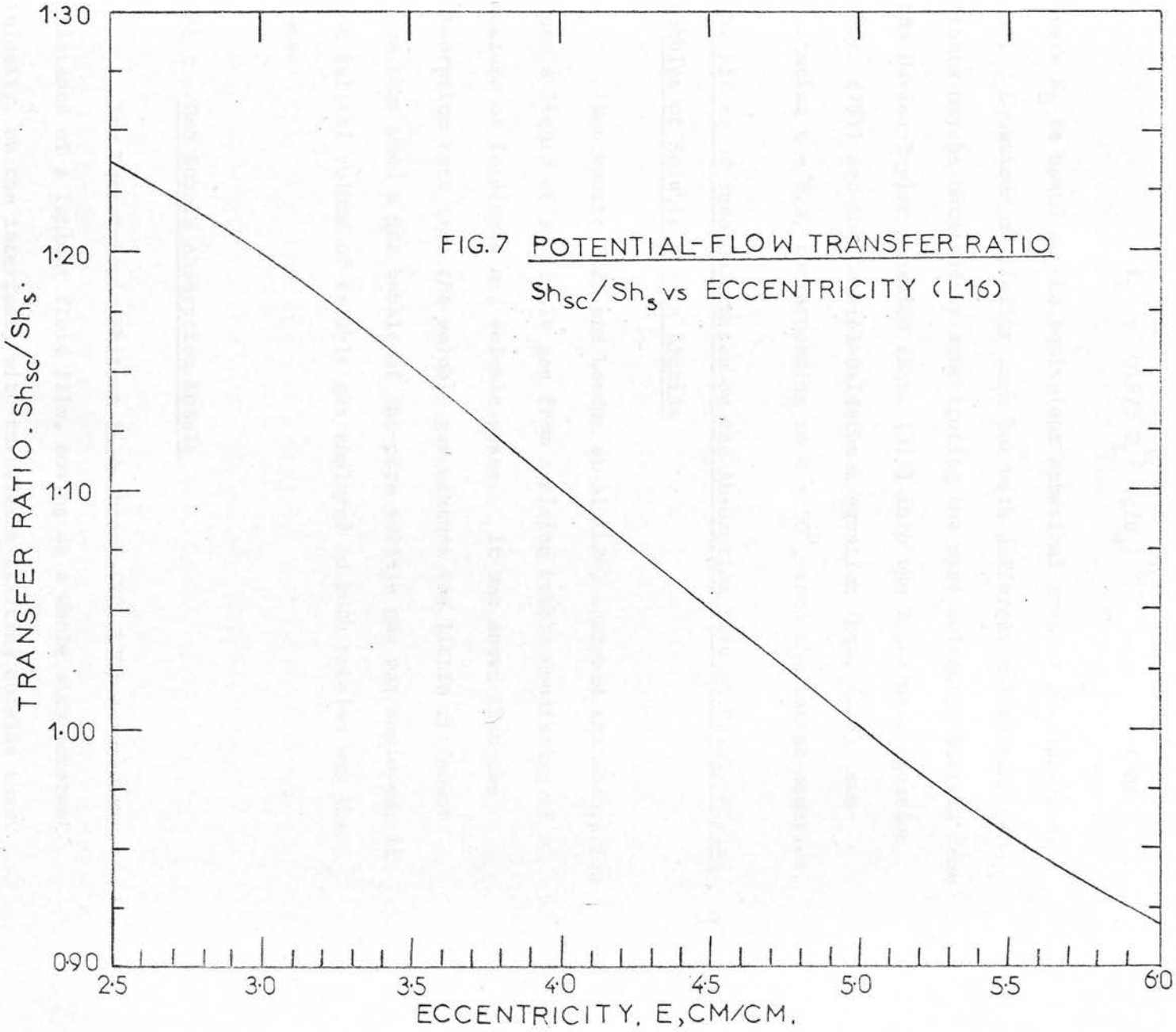

FIG. 7 POTENTIAL-FLOW TRANSFER RATIO
Sh_{sc}/Sh_s vs ECCENTRICITY (L16)

cap with an included angle of 100^{o} moving in an infinite liquid medium and found that

$$K_L = 0.975\, D_L^{1/2}\, (g/D_e)^{1/4} \qquad (88)$$

where K_L is based on the equivalent spherical area of the spherical cap. Equations of similar form but with different multiplying constants may be obtained by substituting the rise velocity obtained from the Davies-Taylor equation (Eqn. (31)) into the Boussinesq equation (Eqn. (79)) and the Lochiel-Calderbank equation (Eqn. (87)), substituting $E = 4.3$, corresponding to $\Theta = 50^{o}$, into the latter equation.

The Effect of Insoluble Gases on the Absorption Rate of Freely Rising Bubbles of Soluble Gas in Liquids

Danckwerts (D2) and Loudon et al (L20) analysed the absorption into a liquid of a soluble gas from a rising bubble consisting of a mixture of insoluble and soluble gases. It was shown that the absorption rate from the soluble gas mixture was little different from that when a gas bubble of the pure soluble gas was employed, if the initial volume of soluble gas employed in both bubbles was the same.

(b) Gas Bubble Absorption Models

The Nernst-Lewis-Whitman film theory (N2, L10) assumed the existence of a laminar fluid film, moving as a whole with constant velocity, on the interface, with turbulence existing outside these films/

films, and concluded that the coefficient of mass transfer was linearly dependent on the coefficient of molecular diffusion and inversely proportional to film thickness.

Higbie (H10) considered the film theory incorrect because the short phase contact in the superficial layer would not permit a stationary distribution of concentration to be successfully established, and so concluded that mass transfer was accomplished by unsteady-state molecular diffusion, (termed penetration by Higbie). Neglecting the influence of the real geometry of the interface, and the influence of convective transfer, Higbie (H10) obtained the equation

$$K_L = 1.13 \sqrt{\frac{D}{t_e}} \qquad (89)$$

where t_e is the phase contact time which Higbie took to be equal to De/U for a bubble in motion. The exact agreement of Eqn. (89) with the Boussinesq solution, (Eqn. (79)), seems to be purely coincidental (H6, R8). Eqn. (89) is simply the expression for molecular diffusion into an infinite liquid with the boundary conditions of uniform concentration at $t_e = 0$ and a constant surface concentration for $t_e > 0$.

Danckwerts (D1) proposed a model based on renewal of the surface, resulting from continuous replacement of liquid (or gas) elements adjacent to the interface by new elements reaching the surface. An exponential distribution of residence times of liquid elements on the surface results, and the average transfer coefficient is given by

K_L/

$$K_L = \sqrt{D_L S'} \qquad (90)$$

where S' was the fractional rate of surface renewal. The surface renewal parameter is, however, not measurable.

The hydrodynamic conditions close to the interface were correctly taken into consideration in Levich's diffused boundary layer theory (L11). This theory gave a new meaning to the film thickness of the film theory - considering it not as an immobile layer (or, what is equivalent, to be moving as a single whole with a constant velocity), but as the thickness of the diffused boundary layer, (the region of sharpest change of concentration), amenable to strict calculation.

Stewart, Angelo and Lightfoot (S15) used a generalization of the penetration and surface-renewal theories, surface stretch effects being included, to derive equations for heat and mass transfer at mobile interfaces. Stewart et al (S15) pointed out that for a circulating bubble, the penetration and surface-renewal theories failed, since the exposure time of the surface elements was unlimited. The surface elements were not renewed, but were simply stretched out from the front of the sphere and crowded in at the rear. Thus the earlier theories which ignored the changes in size of the surface element failed to predict the pseudo-steady behaviour, (i.e. steady when viewed from some external non-deforming coordinate frame). From their theory, Stewart et al (S15) derived the Levich equation (Eqn. (75)), and obtained the results of the diffusional analyses of Baird and Hamielec (B3), Winnikow (W10) and Cheh and Tobias (C6) for/

for circulating bubbles in non-creeping flow.

(c) Experimental Work

Newtonian Liquids

Liquid film controlled mass transfer rates from soluble gas bubbles rising freely in liquids has been extensively investigated by experimenters using a variety of methods. Most of the investigations have been concerned with multibubble systems. Those experimenters who did work with single bubbles generally obtained their data averaged over the life of the bubble. In many cases the results were influenced by the wake of the preceding bubble.

Thus Pasveer (P2), Pattle (P3), Bowman and Johnson (B10), Coppock and Meiklejohn (C15), Guyer and Pfister (G13), Li et al (L13), and von Bogdandy et al (V1), determined average transfer coefficients around bubbles rising in a continuously generated bubble stream through a liquid pool, by measuring overall volume or liquid phase solute concentration changes with time.

Various methods have been used to determine the rate of change of volume of a single bubble and hence its mass transfer coefficient. Ledig and Weaver (L5) and Ledig (L4) determined average transfer coefficients by using a closed system open to the air through a capillary tube, a photographic technique being used to record the motion of the meniscus produced by the change in bubble volume. A similar technique with minor modifications was later used by Clarke (C8), Hammerton (H5), Hammerton and Garner (H6), Leonard (L7), Leonard and Houghton/

Houghton (L9) and Redfield and Houghton (R2).

Baird and Davidson (B2) obtained instantaneous transfer data by measuring the rate of volume change by cinephotography of a stop-watch and a sensitive soap-film meter connected to the absorption column. Deindorfer and Humphrey (D8) employed a photographic technique to determine volume changes and hence instantaneous mass transfer rates for individual bubbles in liquids. This technique has been criticised by Calderbank and Lochiel (C3) and Zieminski and Raymond (Z2) especially when used for larger and deformed bubbles; since as the bubble volume was determined indirectly from the linear bubble dimensions the accuracy of such measurements was questionable. Calderbank and Lochiel (C3) and Loudon (L19) estimated instantaneous transfer rates from bubbles. The first-named investigators recorded pressure changes occurring in the gas space above the liquid surface; while the latter recorded, by way of a pressure transducer, pressure changes at a point in a closed, constant volume liquid column containing the gas bubble, from which the mass transfer rate was being measured, as the only gas space in the column. Nate and Himmelblau (N1) obtained instantaneous transfer rates by using an apparatus designed to set up steady state rates of transfer from a stationary gas bubble to a flowing liquid film which surrounded the bubble. Zieminski and Raymond (Z2) determined instantaneous mass transfer coefficients by employing a method of measurement similar to that of Ledig and Weaver (L5). They used high speed photography to follow the motion of the bubble simultaneously with the change in volume as indicated /

indicated by the capillary of a dilatometer.

A representative selection of experimental data obtained by various investigators for mass transfer coefficients of freely rising gas bubbles in water is to be found in Fig. (3) of Ref. (L19). From Fig. (3) of Ref. (L19), Loudon (L19) noted that the highest values of K_L were for dissolution rates determined by continuous bubbling methods, where bubbles rose through a central core of turbulent liquid and were subject to mutual proximity effects. Thus the extrapolation of data to zero bubbling rate by Bowman and Johnson (B10) resulted in K_L decreasing towards transfer data for Single isolated bubbles.

Zieminski and Raymond (Z2) measured transfer rates around small carbon dioxide bubbles, ($0.26 < D_e < 0.38$ cm.), rising through water and their results are shown in Fig. (8). The curve shows a sharp rise in the K_L value with decrease in bubble size to a diameter of 0.3 cm., and then a gradual drop. Zieminski and Raymond (Z2) pointed out that analysis of their high speed photographs revealed that in the bubble size region $D_e < 0.3$ cm., the helical motion of the bubble gradually disappeared and the bubble began to rise vertically, which suggested a decay of circulation. Thus Zieminski and Raymond concluded that the occurrence of the maximum in K_L could be explained by the transition from the circulating bubbles to rigid spheres. The results of Hammerton and Garner (H6) for ethylene, oxygen, carbon dioxide and hydrogen bubbles in water, and those of Baird and Davidson (B2) for carbon dioxide bubbles in water also show maxima of K_L values at a diameter/

FIG.8. OVERALL MASS TRANSFER COEFFIENTS(Z2)
CARBON DIOXIDE – DISTILLED WATER

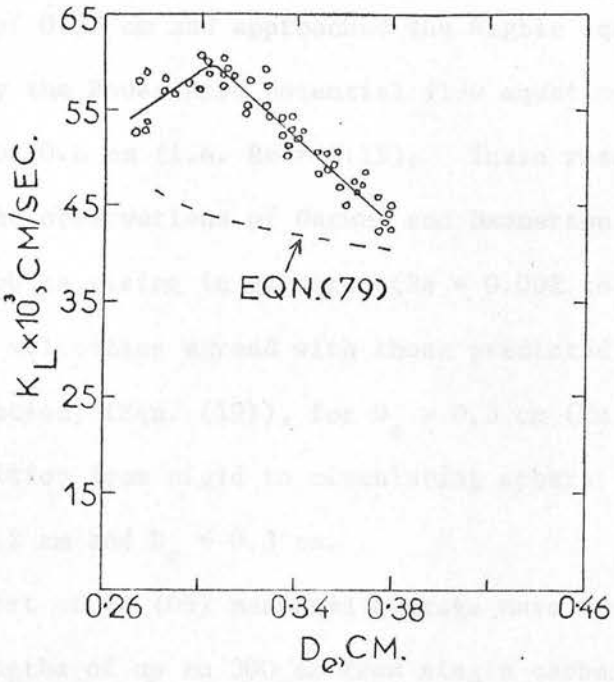

diameter of about 0.3 cm. Zieminski and Raymond's conclusions (Z2) are also in agreement with the findings of von Bogdandy et al (V1), Hammerton (H5), and Hammerton and Garner (H6), whose experimental results show a downward trend at small bubble diameters towards solid sphere predictions (Eqn. (73) or (74)).

Hammerton and Garner (H6) took a few results for carbon dioxide bubbles, ($0.2 < D_e < 0.6$ cm), rising through glycerol, and these are shown in Fig. (9). They observed that the rate of dissolution of carbon dioxide bubbles increased from a value above that indicated by the Frössling equation for solid spheres, (Eqn. (73)), at a diameter of 0.25 cm and approached the Higbie equation, (i.e. more accurately the Boussinesq potential flow equation (Eqn. (79)), at a diameter of 0.6 cm (i.e. $Re \simeq 0.15$). These results are in keeping with the observations of Garner and Hammerton (G2) who investigated small bubbles rising in glycerol ($Re = 0.002$ to $Re = 1$) and found that the velocities agreed with those predicted by the Hadamard-Rybczynsky equation, (Eqn. (19)), for $D_e > 0.3$ cm ($Re \simeq 0.023$), and that the transition from rigid to circulating sphere took place between $D_e = 0.2$ cm and $D_e = 0.3$ cm.

Davenport et al (D5) measured average mass transfer coefficients over column lengths of up to 300 cm from single carbon dioxide bubbles to water, (distilled and tap), aqueous solutions of polyvinyl alcohol (PVA), and ethyl alcohol, with an accuracy of approximately ± 20 per cent. The transfer coefficients for tap water were on average 15 per cent below those for distilled water. Davenport et al (D5) expressed/

FIG. 9.

CO_2 BUBBLES IN GLYCEROL (H6)

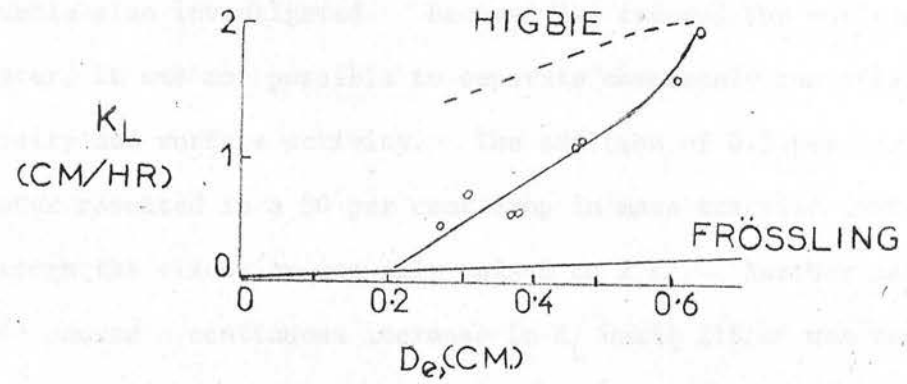

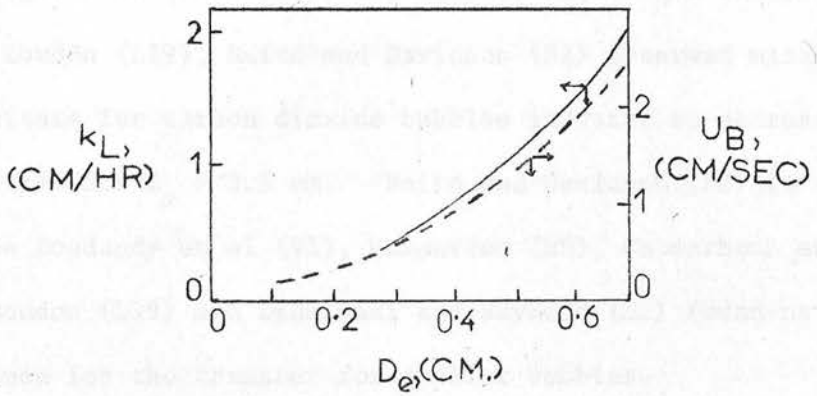

expressed some doubt about the purity of the distilled water used in their work, and the presence of impurities may explain the fall off in transfer coefficient as D_e decreased from 2 cm to 0.8 cm, the smallest bubble size investigated. Because PVA reduced the surface tension of water, it was not possible to separate completely the effects of viscosity and surface activity. The addition of 0.5 per cent PVA to water resulted in a 50 per cent drop in mass transfer coefficient though the viscosity was only raised to 2 cP. Further additions of PVA caused a continuous increase in K_L until 216 cP was reached, in which large bubbles, $D_e > 3.6$ cm, developed skirts and the resulting transfer coefficients were 30 per cent higher than for bubbles without skirts.

Several investigators (C8, D4, D8, L3, L7, L9, R2) found the transfer rate around single rising bubbles to decay with increasing bubble age. In contrast to the data of Calderbank and Lochiel (C3) and of Loudon (L19), Baird and Davidson (B2) observed mass transfer coefficients for carbon dioxide bubbles in water to decrease throughout rising time for $D_e > 2.5$ cm. Baird and Davidson (B2) in agreement with von Bogdandy et al (V1), Hammerton (H5), Calderbank and Lochiel (C3), Loudon (L19) and Zieminski and Raymond (Z2) found no time-dependence for the transfer for smaller bubbles.

Barnett et al (B4) suggested that the observed time-dependence of the transfer coefficients of Deindoerfer and Humphrey (D8) was due to imperfections in the bubble release mechanism resulting in initial wild bubble oscillations. Baird and Davidson (B2) attributed their/

their time-dependent transfer rates around large spherical cap bubbles to gradual wake saturation. Leonard and Houghton (L9) postulated that mass transfer might induce electrokinetic potentials at the interface leading to the formation of a thin layer of stagnant liquid around the bubble surface. It was further proposed that the volume of the film would remain constant so that its thickness would increase on dissolution of the bubble. Lochiel (L16) noted that this mechanism implied eventual interfacial stagnation, (i.e. rigid sphere transfer), and for gas bubbles in low viscosity liquids, Eqns. (73) and (74) for solid spheres underestimated transfer rates by five to ten times. Lochiel (L16) summarised a substantial amount of evidence supporting the contention that transfer rate decay with increasing bubble age was due to progressive interfacial contamination by surfactants, which diffused towards a freshly-found interface and retarded interfacial flow. For large interfacial shear rates caused by the external liquid flow, surface-active agents would not be expected to reduce interfacial movement to an important degree. Thus Clarke (C8) investigated mass transfer from carbon dioxide and ethylene bubbles, ($0.1 < D_e < 0.4$ cm), to distilled water and aqueous solutions of glycerol, and noted that though in water transfer from the bubbles was highly time dependent, for concentrations in excess of 12.5 per cent wt/wt of glycerol the transfer coefficients were time-independent.

Leibermann (L6), Manley (M3) and Houghton et al (H12) have shown that even the most carefully purified water may contain contaminants that inhibit the dissolution rates of small bubbles, though the contaminant/

contaminant concentration may be too low to detectably affect the physical properties of the gas-liquid system. Deliberate addition of surfactants to the continuous liquid phase (B2, H5, L9, S7, T4) has resulted in decrease in K_L by reduction of interfacial flow (G3, G14, L17, L22), by damping of interface ripples (B2), or by formation of a stagnant cap over the bubble rear (C17).

Ruckenstein (R11) demonstrated theoretically that solute concentration variation in the boundary layer around a soluble bubble in laminar motion through a pure liquid phase, would, as a result of the Marangoni effect, influence the liquid velocity distribution in the vicinity of the interface leading to a dependence of the mass transfer coefficient on the direction of the transfer.

Non-Newtonian Liquids

Timson and Dunn (T4) studied the mechanism of gas absorption into distilled water and 0.5 per cent aqueous Carbopol, (a highly pseudoplastic liquid), from oxygen bubbles existing under shear in the annulus between two cylinders, the inner of which was rotated. Over rates of shear in the range 0 to 250 sec^{-1} it was found that the absorption coefficient of the oxygen in distilled water to which was added 15 p.p.m. of pentapropylbenzene-sulphonate surfactant decreased by as much as 67 per cent compared to the absorption coefficient in distilled water. Over the same range of shear in the contaminant-free Carbopol solution, the mass transfer coefficient fell up to 50 per cent below that in distilled water, and on addition of the surfactant

K_L /

K_L was further depressed to fall between 20 and 30 per cent of that in distilled water.

Barnett et al (B4) obtained instantaneous transfer data for the absorption of small carbon dioxide bubbles (D_e < 0.5 cm) rising through 0.1055 per cent wt and 0.272 per cent wt aqueous CMC solutions. They used the same photographic technique of Deindoerfer and Humphrey (D8) to measure bubble volume changes and hence mass transfer coefficients. Transfer rates were found to be high initially and to tail off rapidly with bubble age, although there were some exceptions when the trend was reversed and K_L rose to a maximum before falling off. These exceptions occurred at specific diameters where the bubble shape went through a transition. Thus at a diameter of about 0.2 cm Barnett et al (B4) observed a transition from oblate spheroidal to spherical shape, and at a diameter of approximately 0.4 cm a change from top to oblate spheroidal shape.

Loudon (L19) measured instantaneous mass transfer coefficients for carbon dioxide bubbles (0.5 < D_e < 5 cm) rising through aqueous CMC solutions of solute concentrations 0.5 - 3.0 per cent wt contained in a 4 in (10.16 cm) I.D. column, and his results are shown in Fig. (10). It was found that the decay rate was highest in the 0.5 per cent wt aqueous CMC solution at only 3-4 per cent/sec over a bubble age difference of up to six seconds. This time dependence diminished with increasing pseudoplastic viscosity until in the 3.0 per cent wt aqueous CMC solution there was no appreciable age effect. Loudon (L19) noted that the dependence of K_L upon bubble diameter became generally/

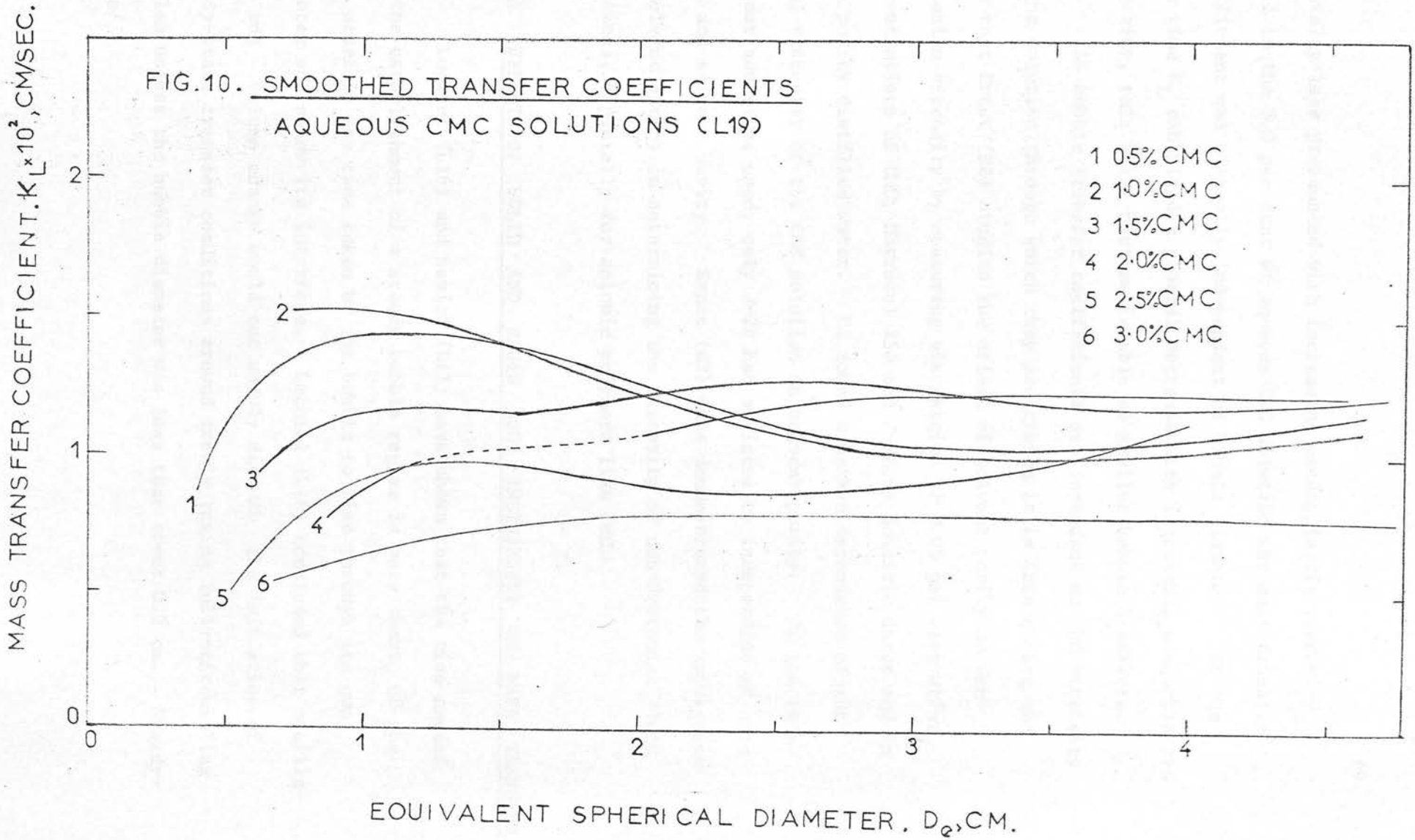
FIG.10. SMOOTHED TRANSFER COEFFICIENTS
AQUEOUS CMC SOLUTIONS (L19)
1 0·5% CMC
2 1·0% CMC
3 1·5% CMC
4 2·0% CMC
5 2·5% CMC
6 3·0% CMC
MASS TRANSFER COEFFICIENT. $K_L \times 10^2$, CM/SEC.
EQUIVALENT SPHERICAL DIAMETER, D_e, CM.
0
1
2
3
4

generally less pronounced with increasing pseudoplastic viscosity until in the 3.0 per cent wt aqueous CMC solution the mass transfer coefficient was virtually independent of bubble diameter. At the same time K_L exhibited a general decrease with increasing pseudoplastic viscosity, this being most noticeable at smaller bubble diameters.

As bubble transfer coefficients are dependent on the viscosity of the solution through which they are rising it is interesting to note that Ernst (E2) studied the effect of solvent purity on non-Newtonian viscosity by measuring viscosities of 0.05 per cent wt/wt concentrations of CMC, Natrosol 250 and J-2P in domestic water and in high purity distilled water. He found a marked dependence of the final viscosity of the CMC solution on solvent purity. Of the three polymer additives used, only J-2P had a viscosity independent of both time and solvent purity. Ernst (E2) thus demonstrated the importance of solvent purity in determining the viscosity of non-Newtonian fluid solutions, especially for anionic polymers like CMC.

1.3.2 EFFECT OF SOLID AND FLUID BODY INSTABILITY ON MASS TRANSFER

Lochiel (L16) and Levich (L11) have shown that the time needed for the establishment of a steady bubble regime is very short, of the same order as the time taken by the bubble to rise through its own diameter and renew its interface. Lochiel (L16) concluded that oscillation and volume change would not unduly disturb the initiation of steady-state transfer conditions around freely rising fully-circulating bubbles unless the bubble diameter was less than about 0.2 cm. Steady-

state equations could therefore be used to express instantaneous transfer rates at which bubble dissolution occurred with reasonable accuracy.

Rose and Kintner (R4) developed a mass transfer model for vigorously oscillating single liquid drops moving in a liquid field utilising the concept of interfacial stretch and internal droplet mixing. The model took into account both amplitude and frequency of drop oscillation. Experimental values of fraction extracted (C1, G3, J3, L14, S9) were predicted with an average deviation of 15 per cent - these results being an order of magnitude greater than calculated extraction rates based on Hadamard-Rybczynsky streamlines (H2, R13) existing within the drop. The oscillations broke up internal circulation streamlines and resulted in a type of turbulent internal mixing being achieved. Harriott (H9) suggested that the vigorous drop oscillations observed in some cases were set up as the drop formed, the oscillations being slowly damped as the drop fell.

Lochiel (L16) showed that steady state around a solid sphere of fixed size applied after the sphere had moved through a distance approximately equal to ten times its diameter. Thus for a rapidly dissolving solid sphere steady conditions could not be attained and the steady-state equations only approximately described the transfer rates. Lochiel (L16) pointed out that heat and mass transfer studies have shown that vibration and rotation has no effect on transfer coefficients when the vibrational and rotational velocities were less than the main-stream velocity. Noordsij and Rotte (N4) have recently measured average mass transfer coefficients to a rotating and to a vibrating/

vibrating sphere in a stagnant liquid using an electrochemical method. Semi-empirical equations for the mass transfer coefficient were presented for the rotating sphere and for the vibrating sphere.

1.3.3 SUMMARY. Mass Transfer Between Gas Bubbles and Liquids

Theoretical predictions of forced convection mass transfer rates around rising rigid or circulating spherical bubbles at low Reynolds numbers and in potential flow have been carried out. For non-spherical bubbles, the theoretical analyses, (with the exception of the work of Sy and Lightfoot (S18) for slightly deformed oblate bubbles at low Reynolds numbers), have been restricted to potential flow transfer, for spherical cap bubbles the potential flow transfer predictions applying over the frontal surface only. For ideal fluids where the Reynolds number is infinite or for viscous fluids where the flow of the continuous fluid is irrotational, the potential flow solutions are applicable. The complex nature of bubble wakes has meant that no adequate theoretical analysis of wake transfer has been carried out, though a knowledge of wake transfer is of importance in determining overall transfer rates around large deformed bubbles, particularly those bubbles adopting the spherical cap shape. In the Reynolds number range intermediate between the creeping flow regime and the potential flow regime, theoretical analyses have dealt with only spherical bubbles; and as pointed out by Redfield and Houghton (R2) /

(R2) these spherical models represent only gross approximations because of the complicated changes in shape, motion and the effects of boundary layer separation (the wake).

Many early investigators measured average transfer coefficients, often in multibubble systems, and their data is of limited value (L16). The weight of recent experimental work suggests that the disagreement between the values obtained for liquid film controlled mass transfer coefficients by various investigators is connected with the purity of the gas-liquid system used, since progressive interfacial contamination by surfactants results in K_L being time-dependent. Increasing liquid viscosity would be expected to reduce the effect of surfactants present and thus eventually to eliminate the time-dependence of K_L. Bubble oscillation and volume change are not expected to unduly affect the initiation of steady-state transfer conditions around fully-circulating bubbles in free rise, except in the case of very small bubbles (D_e < 0.2 cm) (L16).

C H A P T E R 2

E X P E R I M E N T A L P R I N C I P L E S

2. INTRODUCTION

The aims of the experimental programme were to determine near instantaneous diameter, rise velocity, shape, surface area, overall mass transfer product and hence mass transfer coefficient, for single gas bubbles in free rise through both Newtonian and non-Newtonian liquids.

The method employed in determining the rate of bubble dissolution was to record pressure changes at a point in a constant volume system as the bubble rose and dissolved in the system. The gas bubble rose through a liquid pool filling a column isolated from the atmosphere. This technique is identical to that used by Loudon (L19).

In choosing the gas-Newtonian liquid systems, it was necessary to have in bulk, pure transparent liquids of well defined physical properties and covering a wide range of liquid viscosity; and a high purity gas of solubility such that conveniently measurable rates of pressure change during absorption runs were possible. For these reasons the carbon dioxide-water and carbon dioxide-aqueous glycerol solutions systems were selected. Carbon dioxide was also chosen for use in a non-Newtonian liquid - an aqueous solution of polyethylene oxide (polyox) of concentration 1% by weight. Polyox solutions are known to be elastic and to exhibit pseudoplastic behaviour in steady shear/

shear (B1).

As pointed out above, the experimental technique employed is identical to that used by Loudon - so the derivation of the relationships allowing the interpretation of pressure measurements during the ascent and dissolution of a gas bubble in the liquid is similar to that found in ref. (L19). It is given below for the sake of completeness.

In the system considered, the gas bubble constitutes the only gas space existing in the system bounded by the column walls.

Assuming: $P_B V_B = n'RT$ Ideal Gas Law (91)

$P_B = M'.He.C^*$ Henry's Law (92)

$\frac{dn'}{dt} = -K_L A(C^* - C_o)$ Fick's Law (93)

$T = \text{constant}$ Isothermal conditions

then if after time t, the bubble is at height h above the pressure recording station situated in the liquid, then differentiating the ideal gas law with respect to t,

$$\frac{d}{dt}(P_B V_B) = RT \frac{dn'}{dt} \quad (94)$$

$$\text{i.e.} \quad \frac{dn'}{dt} = \frac{1}{RT}\left(P_B \frac{dV_B}{dt} + V_B \frac{dP_B}{dt}\right) \quad (95)$$

Introducing Fick's Law,

$$-K_L A(C^* - C_o) = \frac{1}{RT}\left(P_B \frac{dV_B}{dt} + V_B \frac{dP_B}{dt}\right) \quad (96)$$

Assuming/

Assuming the concentration of solute in the bulk liquid phase, C_o, to be zero, and using Henry's Law to give the interfacial solute concentration C^*,

$$- K_L A = \frac{1}{S} \left(\frac{dV_B}{dt} + \frac{V_B}{P_B} \cdot \frac{dP_B}{dt} \right) \qquad (97)$$

where S is a solubility term defined by

$$S = \frac{RT}{M' He} \qquad (98)$$

The bubble internal pressure P_B, and the liquid pressure P_T at the pressure recording station situated at depth h below the bubble are related by

$$P_B = P_T - \frac{\rho_o}{\rho_{H_2O}} .h + P_A \qquad (99)$$

As all experimental runs were carried out with the liquid in the column maintained at 25°C, the unit of pressure employed in this work was cm H_2O at 25°C.

Equation (99) assumes that pressure equilibrium exists across the bubble wall. Atmospheric pressure P_A is introduced to allow for measurement of P_T on a gauge pressure recording instrument.

Differentiating Eqn. (99) with respect to t and replacing the resulting term $\frac{dh}{dt}$ by the bubble rise velocity U_B,

$$\frac{dP_B}{dt} = \frac{dP_T}{dt} - \frac{\rho_o}{\rho_{H_2O}} U_B \qquad (100)$$

Further/

Further, by direct measurement, a specific compressibility, α, of the experimental system may be determined, such that,

$$\alpha = \frac{\Delta V_S}{\Delta P_T} \tag{101}$$

As the bubble volume constitutes the only gas space in the otherwise completely liquid-filled column, any change in volume of the liquid system bounded by the column walls will be reflected in an equal change in bubble volume. If at time t = 0 the initial bubble volume is V_{B1} and the corresponding liquid pressure at the pressure recording station is P_{T1}, then from Eqn. (101)

$$\alpha = \frac{V_{B1} - V_B}{P_{T1} - P_T} \tag{102}$$

$$\text{i.e.} \quad V_B = V_{B1} + \alpha\,(P_T - P_{T1}) \tag{103}$$

Differentiating with respect to t,

$$\frac{dV_B}{dt} = \alpha \frac{dP_T}{dt} \tag{104}$$

Combining Eqns. (99), (100), (103), (104) with Eqn. (97) gives

$$-K_L A = \frac{1}{S}\left(\alpha \frac{dP_T}{dt} + \frac{(V_{B1} + \alpha\,(P_T - P_{T1}))\left(\frac{dP_T}{dt} - \frac{\rho_o U_B}{\rho_{H_2O}}\right)}{P_T - \frac{\rho_o}{\rho_{H_2O}} h + P_A}\right) \tag{105}$$

By/

By photographing a bubble at height h, thus enabling a decision on bubble shape to be made, and calculating the instantaneous bubble volume from the photographic measurements, the assumed analytical equations defining the bubble surface may be verified by comparison with V_B obtained from equation (103).

Summarising, instantaneous values of the following parameters may be determined:

(i) bubble volume V_B (and hence equivalent spherical diameter De)

(ii) overall mass transfer product $K_L A$

(iii) bubble surface area, A

(iv) overall mass transfer coefficient K_L.

2.1 EQUIPMENT

2.1.1 Mass Transfer Column

The column in which the absorption experiments were carried out is shown schematically in Fig. (11) and is essentially the same as that used by Loudon (L19). The main features of the equipment will be described briefly - a complete description can be found in (L19); and then the modifications to the equipment of Loudon will be dealt with in more detail.

The main column consisted of a 3 ft. (91.4 cm) vertical length of Q.V.F. glass pipe of 4 in. (10.16 cm) I.D., around which were mounted three photoelectric cell units P_1, P_2 and P_3. P_1 and P_3 rested on rubber O-rings mounted around the column and were used in connection with bubble terminal rise velocity measurements, and unit P_2 was mounted in a 6 in. (15.2 cm) cubical Perspex optical block (B) which surrounded the outer wall of the column, and on opposite sides of which were mounted a camera (C) and a photoflood (P). The photoelectric cell unit P_2 served to actuate a solenoid (S) operating on the camera shutter cable release, thus automatically photographing a rising bubble midway between photoelectric cell units P_1 and P_3. Illumination for each of the three photoelectric cell units was provided by a 60 watt striplight.

The column main section was supported on a Q.V.F. glass equal tee of 4 in. (10.16 cm) I.D., in which was situated the bubble release mechanism consisting of a transparent plastic hemispherical dumping cup/

FIG.11. MASS TRANSFER COLUMN

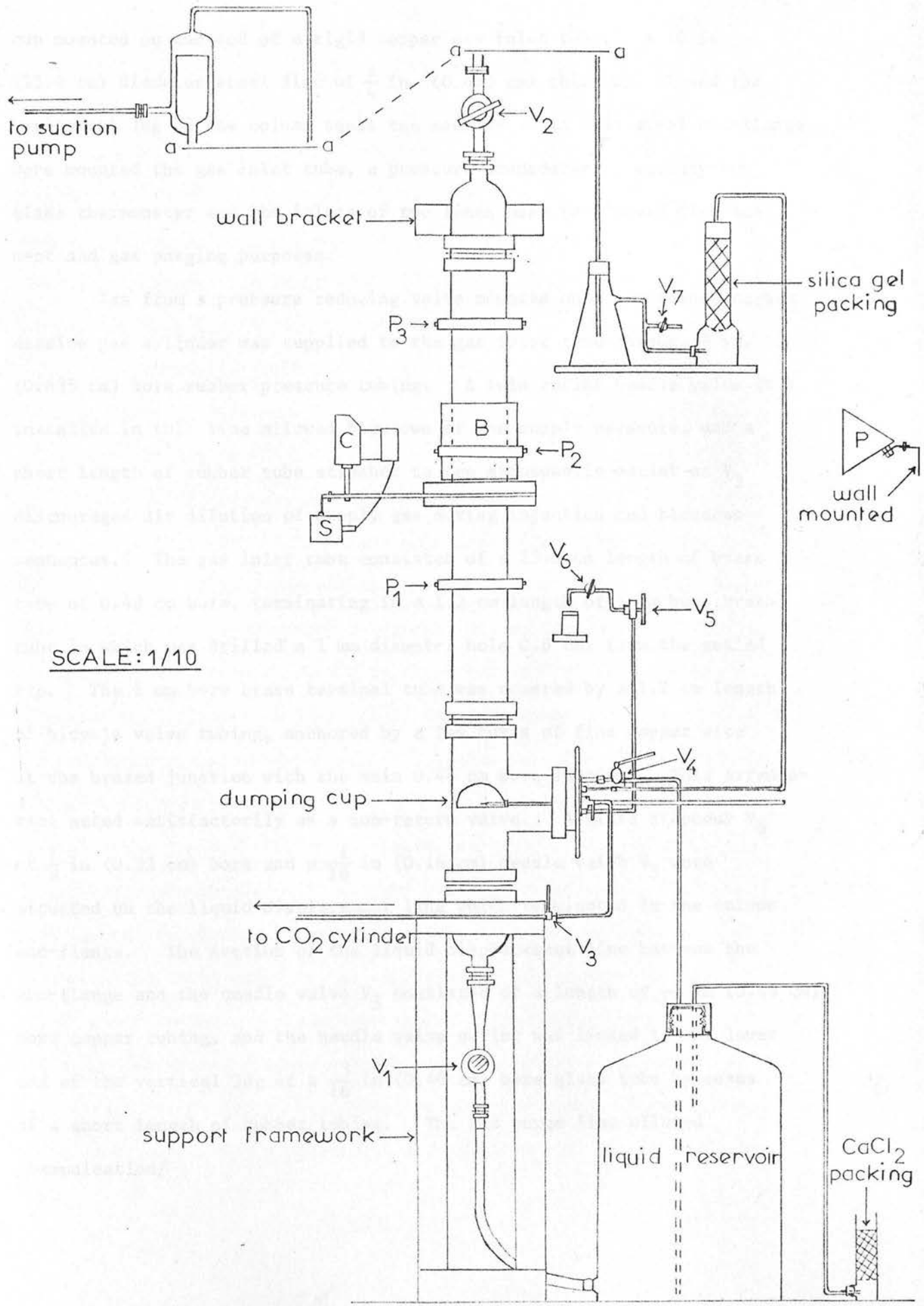

cup mounted on the end of a rigid copper gas inlet tube. A 10 in. (25.4 cm) diameter steel disc of $\frac{1}{4}$ in. (0.635 cm) thickness closed the horizontal leg of the column equal tee section. In this steel end-flange were mounted the gas inlet tube, a pressure transducer, a mercury-in-glass thermometer and the inlets of two lines used for liquid displacement and gas purging purposes.

Gas from a pressure reducing valve mounted on a compressed carbon dioxide gas cylinder was supplied to the gas inlet tube through $\frac{1}{4}$ in. (0.635 cm) bore rubber pressure tubing. A twin outlet needle valve (V_3) installed in this line allowed blowdown of gas supply pressure, and a short length of rubber tube attached to the atmospheric outlet of V_3 discouraged air dilution of supply gas during injection and blowdown sequences. The gas inlet tube consisted of a 23.5 cm length of brass tube of 0.48 cm bore, terminating in a 1.2 cm length of 1 mm bore brass tube in which was drilled a 1 mm diameter hole 0.6 cm. from the sealed tip. The 1 mm bore brass terminal tube was covered by a 1.2 cm length of bicycle valve tubing, anchored by a few turns of fine copper wire at the brazed junction with the main 0.48 cm bore section. This arrangement acted satisfactorily as a non-return valve. A glass stopcock V_6 of $\frac{1}{8}$ in (0.32 cm) bore and a $\frac{1}{16}$ in (0.16 cm) needle valve V_5 were situated on the liquid displacement line which terminated in the column end-flange. The section of the liquid displacement line between the end-flange and the needle valve V_5 consisted of a length of $\frac{3}{16}$ in (0.48 cm) bore copper tubing, and the needle valve outlet was linked to the lower end of the vertical leg of a $\frac{3}{16}$ in (0.48 cm) bore glass tube by means of a short length of rubber tubing. The gas purge line allowed communication/

communication between the liquid in the column and residual liquid in the Polythene liquid reservoir. A Klinger AB10 brass stopcock fitted with a $\frac{1}{8}$ in. (0.32 cm) bore Teflon bush (V_4) was coupled to a $1\frac{3}{4}$ in. (4.45 cm) length of $\frac{3}{8}$ in. (0.95 cm) bore brass tubing screwed into the column end-flange, and also communicated with the main liquid reservoir by means of a length of $\frac{1}{4}$ in. (0.635 cm) bore rubber tubing terminating in a length of $\frac{1}{4}$ in. (0.635 cm) bore glass tubing which dipped into residual liquid contained in the reservoir. The purge line permitted displacement by liquid of any gas pockets trapped in the horizontal leg of the column equal tee section.

Two Q.V.F. glass reducing sections reduced the column diameter from 4 in. (10.16 cm) I.D. to 1 in. (2.54 cm) I.D. at the top and bottom. A stainless steel adaptor section further reduced the column diameter to $\frac{1}{4}$ in. (0.635 cm) I.D. at the bottom, thereby permitting the attachment of a $\frac{1}{4}$ in. (0.635 cm) bore Hone valve (V_1) at the bottom of the column. A $\frac{1}{2}$ in. (1.27 cm) bore Sabal ball plug valve (V_2) was located at the upper end of the column. The lower valve V_1 was connected via a length of $\frac{1}{2}$ in. (1.27 cm) bore rubber tubing to a 40 litre capacity Polythene liquid reservoir. The upper stopcock V_2 communicated with a liquid disengagement space, which in turn was connected through a drying flask containing calcium chloride to a reducing valve and suction pump by means of a length of $\frac{1}{4}$ in. (0.635 cm) bore rubber pressure tubing. By applying a partial vacuum to the liquid disengagement space, the column could be filled with liquid drawn through V_1; and, further, the liquid in the column could be degassed with V_1 closed. A length of $\frac{1}{4}$ in. (0.635 cm) bore/

bore rubber tubing allowed communication between the liquid disengagement space and the pressure transducer tailpipe, via a Buchner filter flask acting as a liquid trap, and a small drying tower packed with silica gel. This line could be opened to atmosphere by means of a $\frac{1}{2}$ in. (1.27 cm) bore glass stopcock V_7. Installation of this line was necessary to prevent too large a pressure difference being developed across the pressure transducer diaphragm during column filling and liquid degassing sequences.

Column sections were flanged and bolted together with standard Q.V.F. alloy flanges which gripped the tapered glass section ends via rubber compression rings, and all glass to glass joints as well as that joint between the steel end-plate and the horizontal leg of the glass equal tee section were rendered airtight by means of rubber gaskets. A framework with a support section, (2 ft. 6 in. ($\simeq$ 76 cm) in height and approximately 10 in. (25 cm) square), for the column, and carrying a horizontal wooden surface and a vertical wooden surface was constructed from angle-mild steel for the equipment. The entire column structure was supported by bolting the lowermost $4\frac{1}{2}$ in. (11.43 cm) I.D. alloy flange to the support section of the mild steel framework. Additional stability was obtained by bolting the uppermost $4\frac{1}{2}$ in. (11.43 cm) I.D. alloy flange to a steel bracket which was screwed to a vertical steel plate screwed at its lower end to the support section of the steel framework. The tape recorder, amplifier and microsecond stopclock were placed on the horizontal wooden surface, while the instrument dials and switches, and the two 0-260 v/

0-260 v slide regulators were mounted on the vertical surface. The equipment was housed in a room, the temperature of which was controlled.

2.1.2 Modifications to Equipment

(1) The mild steel disc used in the equipment described in ref. (L19) had its face that was in communication with the column chromium plated and further coated with 'Britect', a transparent lacquer, due to difficulties encountered in the rusting of that part of the disc in contact with the liquid contained in the column. In view of this, the mild steel disc was replaced by a $\frac{1}{4}$ in. (0.635 cm) thick stainless steel disc of the same dimensions and with the gas inlet tube, pressure transducer, mercury-in-glass thermometer and inlets of the two lines for liquid displacement and gas purging mounted in exactly corresponding positions in the disc.

(2) In the equipment used in this work, a stainless steel adaptor section and a Hone valve (V_1) replaced the glass reducing section and glass stopcock at the lower end of the column, whereas a Sabal ball plug valve (V_2) replaced the glass adaptor section and stopcock at the top of the column. Although the glass stopcocks were lubricated at points displaced as far as possible from the stopcock bores, spreading of the petroleum jelly lubricant over the glass plugs after a few turns of the plugs to allow opening and closing of the stopcocks, means that the lubricant constituted a potential source of liquid surfactant/

surfactant contamination. Consequently it was desirable to replace the glass stopcocks by valves requiring no lubrication. A stainless steel adaptor section was made which reduced the column diameter from 1 in. (2.54 cm) to $\frac{1}{4}$ in. (0.635 cm) I.D. A diagram of this section is shown in Fig. (12). The larger end of the adaptor section was soldered into a flange, thus allowing it to be bolted to theQ.V.F. alloy flange surrounding the glass section of column immediately above this steel adaptor section. The other end of this adaptor section was externally threaded for a distance of ½ in. (1.27 cm) to permit it to be screwed into an internally threaded opening of the Hone valve (V_1). The Chromium-Nickel Hone needle valve of $\frac{1}{4}$ in. (0.635 cm) I.D. required no lubrication. The other opening of the Hone valve was externally threaded so that a small brass adaptor section could be screwed onto it. Over the end of this adaptor section, (external diameter $\frac{5}{8}$ in. (1.59 cm)),was fitted a ½ in. (1.27 cm) bore rubber tubing which was connected with the Polythene liquid reservoir.

The Sabal G type ball plug valve ASA 150 (V_2) at the upper end of the column was of ½ in. (1.27 cm) bore and constructed of a P.T.F.E. bush with steel barrel and end flanges. Thus this stopcock required no lubrication and at the same time could be quickly opened and closed. The end flanges of valve V_2 were suitably bored to permit it to be bolted into place.

(3) The 150 Watt 240 v A.C. photoflood used in the work of Loudon (L19) was replaced by a 55 Watt 12 v D.C. Lucas Tungsten Iodine fog-spot/

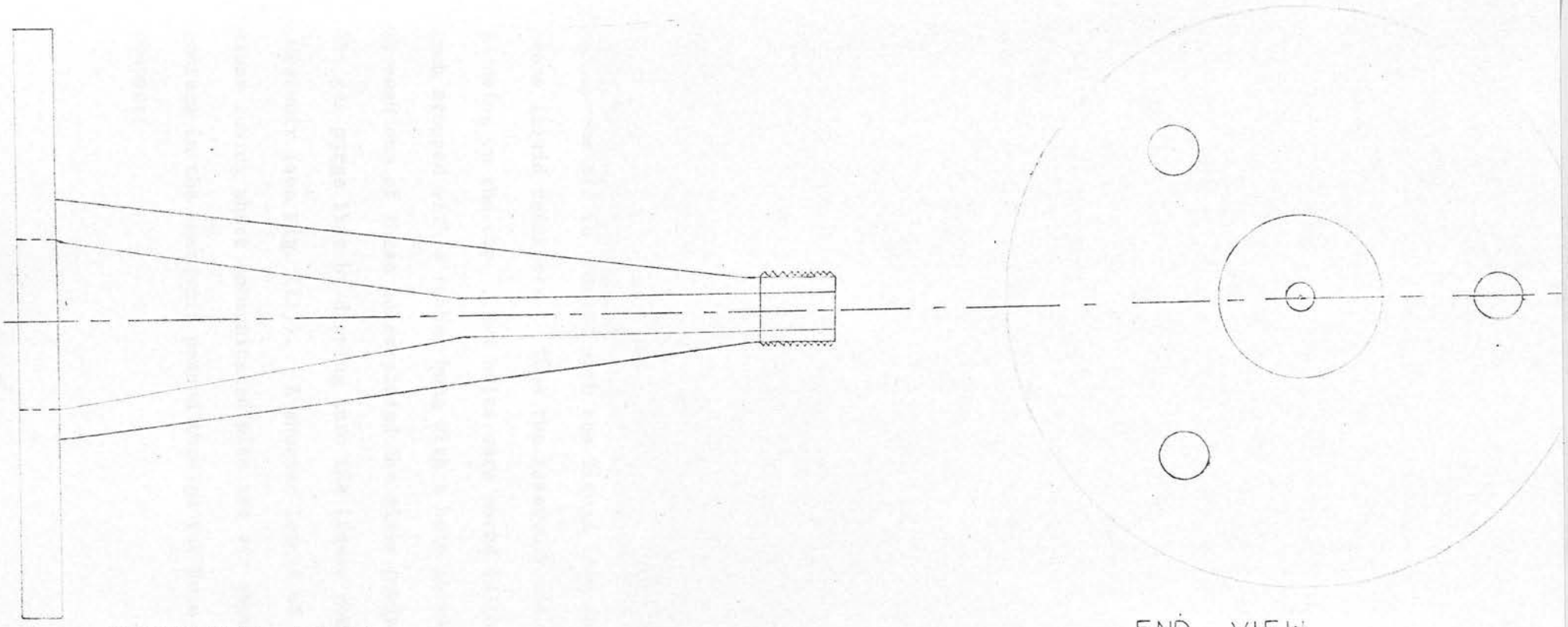

FIG. 12. STAINLESS STEEL ADAPTOR SECTION

SCALE: 1/1

spot lamp housed in a Lucas Headlamp with a chrome plated reflecting surface. The entire photoflood assembly was mounted 85 cm. away from the column on a Dexion bracket which was bolted onto a steel bracket which in turn was screwed into the wall of the room containing the experimental equipment. The Tungsten Iodine lamp provided approximately the same amount of light for the photographing of the gas bubbles as the 150 Watt photoflood, but at the same time gave out appreciably less heat. This reduced the problem of creating hot spots in the liquid contained in the column - noting that the equations derived for processing the experimental measurements assume an isothermal system.

The camera used for taking the bubble photographs was an Exacta Varex IIb single lens reflex 35 mm camera fitted with a Pancolar 2/50 f 2 lens, the same camera used by Loudon.

(4) Glycerol is a hygroscopic liquid (F3) and as aqueous solutions of glycerol were used in the experimental programme, it was necessary to dry the air in contact with the liquid free surface in the polythene liquid reservoir. Thus the reservoir was made air tight by screwing on the cap. Two holes were bored in the top of the cap and each stopped with a rubber bung with a hole through its centre. Through one of these holes passed the glass tubing which terminated the gas purge line by dipping into the liquid contained in the reservoir (see Fig. (11)). A shorter length of $\frac{1}{4}$ in(0.635 cm) bore glass tubing which communicated with the air above the liquid free surface in the reservoir passed through the hole in the other rubber stopper/

stopper. This glass tube was connected by means of a $\frac{1}{4}$ in. (0.635 cm) bore rubber tubing to a drying tower containing calcium chloride and open at its other end to the stmosphere.

(5) The water ejector system used for applying a partial vacuum to the liquid disengagement space was replaced by an electrically driven Speedivac High Vacuum Single Stage Pump made by Edwards and Co. (London) Ltd. This pump was connected in series with a reducing valve supplied by Edwards High Vacuum Ltd. and a drying flask containing calcium chloride. It was necessary to use a vacuum pump in place of a water ejector vacuum system as the water pressure from the tap in the room in which the experimental equipment was housed was too small to permit the required column filling and liquid degassing operations to be carried out.

(6) It was decided to control the temperature of the room in which the equipment was housed so that all experimental measurements could be carried out on an isothermal system at 25°C. A bimetallic thermostat controlled the switching on and off of the 1 kilowatt heating element of an electric fan heater situated 100 cm above floor level. A fan was situated on the floor of the room and a window 200 cm above the floor was kept slightly open. The thermostat could be set to control at various temperatures by adjusting a dial situated above its bimetallic stem. A mercury-in-glass thermometer hanging in the air near the thermostat gave a quick indication of the temperature at which the thermostat was controlling, while a red warning light indicated/

indicated whether or not the heating element of the fan heater was on. The temperature of the liquid in the column was obtained from the mercury-in-glass thermometer located in the end-flange and projecting into the liquid (see Fig. (11)).

(7) To improve the accuracy of measurement of the instantaneous pressure, P_T, and the rate of change of pressure, dP_T/dt, it was decided to alter the means of recording the pressure variations in the constant volume column as the gas bubble rose through the liquid and dissolved. Consequently instead of recording the pressure trace generated by the transducer on a Visicorder as in the work of Loudon (L19), the trace was amplified by a mains powered Rocher Electronique Amplifier and recorded on Channel 1 of the magnetic tape of a mains powered Elliot Tanberg Tape Recorder, Model 64E2. The tape recorded pressure trace was then digitised with the aid of an analogue-digital converter and a PDP-8 digital computer.

The pulses, 0, 1, 2 and 3, marking locations corresponding to the bubble in the cup just after injection and just prior to release, and to the bubble at photo-electric cell stations P_1 and P_3, were recorded on Channel 2 of the tape recorder. A circuit was constructed so that a 'manual' pulse could be generated by pressing a button to complete the circuit consisting of a $4\frac{1}{2}$ v dry cell battery in series with a 50 K Ω potentiometer. The live and earth leads for the 'manual' pulses, pulses 0 and 1, and the triggered pulses, pulses 2 and 3, were brought together into a single coaxial plug which was plugged into the input to Channel 2 of the tape recorder. To prevent cross interference/

interference of the pulses, a 1-1 3 way switch (SW6), was placed in series with the pulse triggers and just before the leads were brought together into the single coaxial plug, (see Fig. (13)).

Details of the specifications of instruments used, and circuit diagrams are given in Appendix I.

FIG. 13. MANUAL & TRIGGER PULSES TO TAPE RECORDER

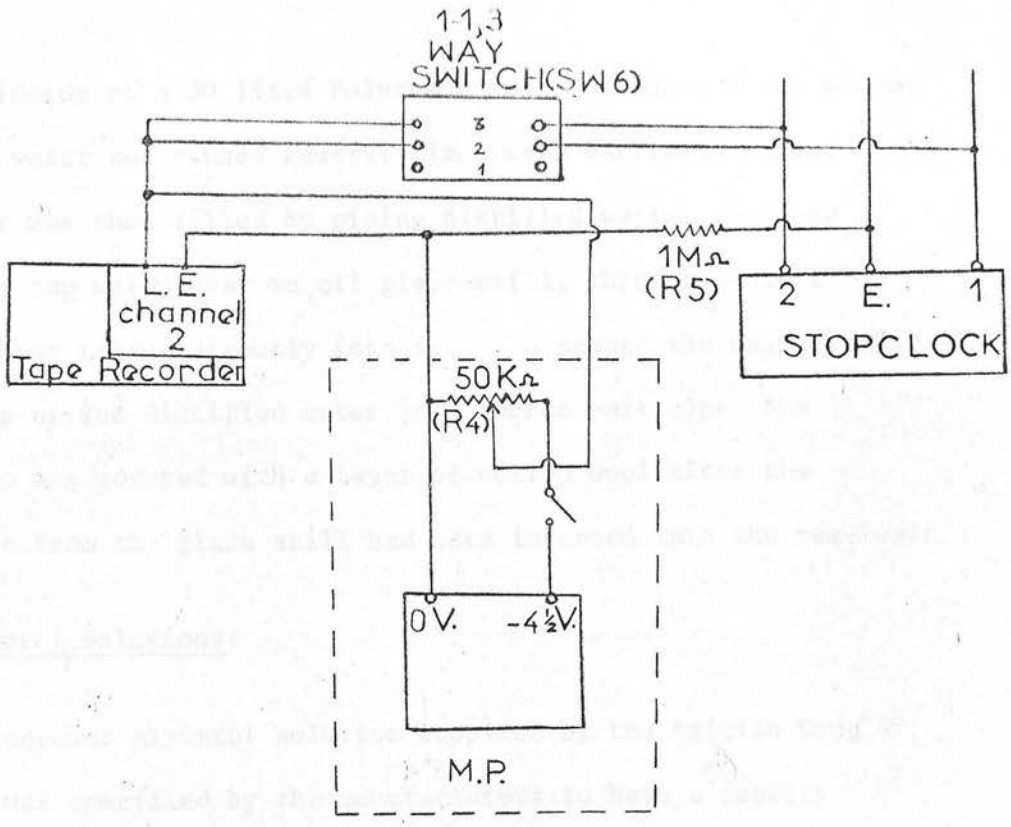

L. LIVE
E. EARTHY
M.P. 'MANUAL' PULSE CIRCUIT

SW6 POSITIONS:—

1 'MANUAL' PULSE
2 START STOPCLOCK
3 STOP STOPCLOCK

2.2 OPERATION

2.2.1 Preparation of Liquids

Water:

The inside of a 30 litre Polythene reservoir bottle was washed with hot tap water and rinsed several times with distilled water. The reservoir was then filled by piping distilled water, obtained by distilling tap water over an all glass still, through a short length of rubber tubing directly into it. To reduce the chances of contamination of the distilled water by airborne particles, the reservoir top was covered with a layer of cotton wool after the delivery line from the glass still had been inserted into the reservoir.

Aqueous Glycerol Solutions:

The aqueous glycerol solution supplied by the British Drug Houses Ltd. was specified by the manufacturers to have a density lying between 1.252 gm/cc and 1.257 gm/cc at $25^{o}C$, and to contain not less than 98 per cent wt/wt glycerol. Density measurements carried out with a 50 cc specific gravity bottle, specified the supplied aqueous glycerol solution as being a 99.0 per cent wt/wt solution of glycerol in water (see Appendix IV, section A.IV.i).

To prepare the 90.6 per cent wt/wt aqueous solution of glycerol, 18160 gm of the 99.0 per cent solution were weighed out, and 1690 gm of distilled water added. The mixture was placed in a mixing vessel, a large plastic container equipped with a Kestner Evaporator and Engineering Co. Ltd. $\frac{1}{4}$ H.P. turbine stirrer. The stirrer was set in/

in motion at 440 R.P.M. and stirring continued at ambient temperature for 45 minutes before transferring the solution to the 40 litre Polythene reservoir connected to the base of the mass transfer column.

Aqueous Polyox Solution:

The plastic mixing vessel was washed with hot tap water and rinsed several times with distilled water. 17250 gm of distilled water were weighed out in the plastic mixing vessel and to this was added 174 gm of polyethylene oxide, (Polyox WSR 301 supplied by Union Carbide Ltd.). Because of the high degree of polymerisation, polyox is subject to degradation by the shearing action of high speed mixing (B1), and so the turbine stirrer could not be used for mixing the solution. Instead the mixing vessel was covered and allowed to stand for 7 days, each day it was subjected to mild agitation for ½ an hour by hand stirring using a clean glass rod.

To prevent contamination of the liquids used in the experimental program all the vessels used in the solution preparation, (the 30 litre Polythene reservoir used for collecting distilled water from the all glass still, the 40 litre Polythene reservoir connected to the base of the mass transfer column, and the approximately 100 litre plastic mixing vessel), were thoroughly washed with hot tap water and rinsed with distilled water prior to use.

2.2.2 Column Filling and Liquid Degassing

The procedure described below was used for all four liquids employed in the experimental investigations, (distilled water, 99.0 per cent and 90.6 per cent wt/wt aqueous glycerol solutions, 1.0 per cent wt/wt aqueous polyox solution).

Referring to Fig. (11), after the liquid being used had been transferred to the 40 litre Polythene reservoir, the reservoir was connected to the lower stopcock V_1 and the cap of the reservoir, through which passed the glass tubing terminating the gas purge line and the glass tubing linked by way of a drying tower to the atmosphere, screwed onto its top. Valves V_1 and V_2 at the lower and upper ends of the mass transfer column were fully opened while all other valves and stopcocks were closed. To start column filling with liquid drawn from the reservoir, a partial vacuum was applied to the liquid disengagement space at the top of the column by means of an electrically driven Speedivac Vacuum Single Stage Pump. Column filling was stopped by closing valve V_1, slowly opening valve V_7 and switching off the vacuum pump.

To cause liquid degassing, the column was filled to about three-quarters of its capacity and valve V_1 then closed. This resulted in a progressive reduction in column internal pressure until a state of near vacuum was attained. Degassing was initiated by momentarily opening and closing stopcock V_4 to allow entry into the column of a slug of liquid from the Polythene reservoir at substantially atmospheric pressure. The sudden pressure reduction imposed on the entering liquid/

liquid slug resulted in the formation of a large number of small bubbles in the vicinity of the entry region. Gas desorption into these small nucleus bubbles commenced, and liquid degassing was thus initiated. Liquid slug introduction was repeated at intervals until the liquid level in the column had risen into the liquid disengagement space above the upper stopcock V_2. Liquid degassing was allowed to continue for about ten minutes, after which the column vacuum was released by slowly opening valve V_7 and then switching off the vacuum pump. Time was allowed for any remaining gas bubbles to rise to the liquid surface and leave the column. As pointed out by Loudon (L19), it was considered unwise to make the length of time devoted to liquid degassing too long, as in the case of the aqueous solutions lengthy degassing might result in a significant evaporation of the water solvent.

Air trapped in the liquid displacement line was purged to atmosphere by opening valves V_5 and V_6, when the liquid head in the column resulted in liquid flowing through the liquid displacement line to the terminal nozzle. Valves V_5 and V_6 were closed on termination of the gas purging from the liquid displacement line.

A pocket of gas generally remained in the column equal tee section at a location adjacent to the end-flange, and this was removed by temporarily opening stopcock V_4. The ensuing flow of liquid through V_4 displaced the gas pocket into the Polythene liquid reservoir.

A careful visual inspection was carried out to ensure that no gas/

gas spaces remained in the liquid filled column. To test the system for leaks all valves and stopcocks were closed except valve V_2 which was opened fully. A partial vacuum was applied to the liquid surface in the liquid disengagement space by switching on the vacuum pump. Any imperfect gaskets or seals would clearly be shown up by the entry of air into the liquid filled column.

The transducer tailpipe line limited the pressure difference applied across the transducer diaphragm to that of the head of column liquid above the transducer location, and so prevented the 0 - 10 p.s.i.g maximum pressure differential range of the transducer from being exceeded.

In the present work, experimental runs were carried out first with distilled water and then with the 99.0 per cent aqueous glycerol solution, followed by the 90.6 per cent aqueous glycerol solution, and finally the 1.0 per cent aqueous polyox solution. Column glassware, the end-flange and all rubber gaskets were washed with hot water and rinsed several times with distilled water before commencing the experimental program. After experimental runs had been completed with a given liquid and the column emptied, the column was rinsed with distilled water and allowed to stand filled with distilled water until time to fill the column with the next liquid to be investigated.

2.2.3 Column Compressibility Measurement

The system compressibility was determined by employing the column/

column pressure drop technique described in ref. (L19). This method depends on the fact that if the column is filled with liquid and valves V_1, V_4, V_5 and V_6 are closed while Valve V_2 is open, the pressure in the region of valve V_2 is essentially atmospheric. Subsequent closing of valve V_2 and opening of valves V_5 and V_6 in the liquid displacement line results in a drop in column liquid pressure equal to the head of liquid between valve V_2 and the terminal nozzle of the liquid displacement line. A volume of liquid issues from the liquid displacement line terminal nozzle equal to the column system volume change accompanying this pressure drop.

Thus the pressure transducer circuit was switched on and the supply voltage adjusted to 5.0 v D.C. Valve V_2 was opened and the calibrated amplified transducer output voltage, giving $\Delta 1$, recorded on Channel 1 of the tape recorder, pulses on Channel 2 noting the location of the recording. Valves V_6 and V_5 were opened in that order and the displaced liquid collected in a weighing bottle of known weight. The recorded amplified transducer voltage output was monitored with a digital voltmeter until a steady value, corresponding to a steady pressure, Δ_2, was reached, when the location of the transducer recording was marked off by pulses on Channel 2 of the tape recorder. Any liquid remaining in the form of a droplet on the liquid displacement line terminal nozzle was wiped off into the weighing bottle which was then weighed (giving M_L). Knowing the liquid density, (ρ_o), the volume of displaced liquid, ΔV_S, was calculated, and since the difference between initial and final column pressures/

pressures at the pressure transducer location, $(\Delta_1 - \Delta_2)$, gave ΔP_T, the column compressibility α could be calculated from Eqn. (101).

2.2.4 Terminal Rise Velocity and Mass Transfer Runs

It was first necessary to focus the camera and to determine the extent of photographic distortion for the liquid system being used. Consequently the column was filled with liquid to a level slightly above the upper photoelectric cell unit P_3. The top section of the column, including the 4 in. (10.16 cm) to 1 in. (2.54 cm) upper reducing section, was removed and a perspex graticule, which had been thoroughly washed with distilled water and on which were drawn a series of concentric circles (1 cm, 2 cm, 3 cm, 4 cm and 6 cm diameters), was lowered along the column central axis. The graticule was glued to a 35.4 cm length of perspex, which in turn was centrally glued to a circular perspex slab which was machined to fit over the top of the 4 in. (10.16 cm) I.D. column walls, and so on lowering, the graticule took up a position along the column vertical axis in a plane at right angles to the camera-photoflood direction. The camera which had been loaded with a 36 exposure cassette of Kodak Tri-X Pan (27 DIN) 35 mm film was screwed into position. The flood lighting was switched on and the camera was focused on the concentric circles of the graticule and the position and focal setting of the camera noted. The camera shutter speed was set to 1/1000 sec and a Weston Master III lightmeter placed just in front of the/

the camera lens determined the lens aperture to be used. This was found to vary between f4 (water) and f2.5 (1% aqueous polyox solution). The camera lens aperture was set and the graticule photographed. The ratio of the vertical to the horizontal dimensions of the photograph of the concentric circles on the graticule provided a measure of the photograph magnification, M_R, in the vertical plane when the photograph was printed with horizontal dimensions magnified to full size.

After the setting up of the photographic equipment, the top section of the column was again bolted into position and the filling of the column with liquid completed. The liquid was degassed and the liquid filled column left to attain temperature equilibrium with the room, the final temperature of the liquid (25°C) being checked by means of the thermometer mounted in the column stainless steel end-flange. In order to make maximum use of the voltage range capable of being recorded (+ 2.5 v to -2.5 v), the amplifier and the tape recorder potentiometers, (one for each channel), were suitably adjusted. It was found that for the systems used, setting the recorded voltage at between 0 v and 0.5 v for water and the aqueous polyox solution, and at between -1.0 v and -1.5 v for the aqueous glycerol solutions with valves V_5 and V_6 open and valves V_1, V_2 and V_4 closed, and at between 1.5 v and 2.0 v for water and the aqueous polyox solution, and at approximately 1.5 v for the aqueous glycerol solutions with valve V_2 open and valves V_1, V_4, V_5 and V_6 closed, suitably covered the range of pressures encountered during bubble rise and/

and dissolution. The recorded voltages were monitored with a digital voltmeter. The system specific compressibility was measured using the column pressure drop technique described in Section 2.2.3.

The gas injection line from the carbon dioxide cylinder was purged free of air by injecting and releasing into the column liquid several large carbon dioxide bubbles which were allowed to leave the column via upper valve V_2. The blowdown valve V_3 was closed to discourage entry of air into the gas injection line.

Following a careful visual check to ensure the absence of any air pockets in the liquid filled column, all instrument circuits and lighting were switched on. The trigger levels of the photoelectric cell units P_1, P_2 and P_3 were set to threshold level with the aid of the adjusting potentiometers, the monitor meter and the indicating meter associated with the camera solenoid. A small beaker was placed under the liquid displacement line terminal nozzle, the upper valve V_2 was closed and the liquid displacement line valves V_6 and V_5 were opened in that order. On establishment of pressure equilibrium the beaker was used to wipe off any surplus liquid remaining on the tip of the liquid displacement line terminal nozzle before it was replaced by a weighing bottle of known weight. Bubble injection was immediately commenced by opening the carbon dioxide cylinder valve and adjusting gas injection line blowdown valve V_3 so that a stream of small bubbles rose into the inverted dumping cup. Bubble injection was terminated by opening fully the blowdown valve V_3 and closing the reducing valve of the carbon dioxide cylinder/

cylinder. During the time required for the total coalescence of gas under the dumping cup and the re-establishment of column pressure equilibrium, (as indicated by the recorded voltage as monitored by the digital voltmeter attaining a constant value, and by the cessation of liquid issuing from the displacement line terminal nozzle), photo-electric cell units P_1, P_2 and P_3 were rechecked for proximity to trigger level, the camera shutter cocked and the camera solenoid switch set to the 'operate solenoid' position. A check was made to see that the amplifier was switched on and the tape recorder was then started. A 'manual' pulse, pulse 0, was recorded on Channel 2 of the recorder and valves V_6 and V_5 were closed in sequence. Upper valve V_2 was then opened momentarily and again closed. The momentary opening and closing of valve V_2 resulted in a pressure head of the order of 120 cm of liquid at the transducer station and served as a safeguard against the imposition of sub-atmospheric pressures on the pressure transducer diaphragm during bubble ascent. A 'manual' pulse, pulse 1, was recorded on Channel 2 of the tape recorder with switch SW6 in position 1, (see Fig. (13)), and the bubble released by smoothly rotating the dumping cup. SW6 was manually switched to position 2 before the bubble reached photoelectric cell unit P_1, and to position 3 while the bubble was between P_1 and P_3.

When the bubble reached the top of the column, the tape recorder was stopped. Any liquid remaining on the terminal nozzle of the displacement line was carefully wiped into the weighing bottle before the latter was sealed to prevent evaporation losses. The reading on the/

the electronic stopclock, which was started and stopped by the pulses generated by P_1 and P_3 respectively, was noted before resetting the stopclock to zero. The bubble trapped below the upper valve V_2 was released by opening V_2. Atmospheric pressure was noted.

Runs were performed in the manner described above until a set of twelve weighing bottles contained displaced liquid. These bottles were then weighed, emptied and reweighed in preparation for the next set of twelve runs. After each set of twelve runs the constancy of the recorded voltage for a given head of liquid, H, above the transducer station, (100 cm liquid pressure head was usually chosen), was checked with the digital voltmeter on lowering the column liquid level to the chosen mark. The column was refilled, and prior to commencing the next set of twelve runs the system compressibility rechecked.

Approximately three dozen runs were carried out before the entire film cassette was exposed. The film was removed from the camera and placed in a sealed container and the camera loaded with a fresh film. The liquid in the column was again degassed. Further runs were carried out until sufficient data had been collected for the gas-liquid system being investigated.

At the end of a series of runs the transducer output was calibrated by recording the amplified transducer output voltage corresponding to different column liquid heights above the transducer station. These liquid heights were measured against a meter rule running parallel to the column vertical axis. For each liquid six to ten/

ten calibration points were taken. Solartron Ltd. claim that the pressure transducer voltage output, (a maximum of approximately 20.5 mV at a pressure of 10 p.s.i.g.), is linear to an accuracy of approximately 1 per cent of the full scale reading. All calibrations carried out indicated that the pressure transducer output was a substantially linear function of the differential pressure imposed across the diaphragm.

For the column used in the experimental work, the photoelectric cell units P_1 and P_3 were situated 50.0 cm apart, L, with the midpoint between the two where the bubble was photographed at a height of 66.5 cm above the pressure transducer location, h_2.

It was found that in the aqueous glycerol and aqueous polyox solutions the photoelectric cell units were not sensitive enough to guarantee the detection of the passage of small bubbles. Consequently the negative pulses corresponding to a bubble at the positions of photoelectric cells P_1 and P_3 were generated by pressing a button to complete the manually operated circuit containing a $4\frac{1}{2}$ v dry cell battery and a potentiometer in series. For these cases photographs were taken by manually operating the camera shutter.

As polyox solutions are subject to degradation on prolonged exposure to light (M8), the 1.0 per cent aqueous polyox solution was stored in the dark during preparation and the column filling and liquid degassing operations were also carried out in the dark. The photoflood and striplights for the photoelectric cell units P_1, P_2 and P_3 were switched on just prior to bubble introduction and switched off/

off immediately after each run, so that the total exposure time to light of the aqueous polyox solution after the completion of the experimental runs was only of the order of three hours.

To limit as far as possible the introduction of impurities into the liquid phase, the column was kept filled with freshly prepared distilled water during the non-operational intervals between the experimental runs carried out with the different liquids.

C H A P T E R 3

D A T A P R O C E S S I N G

3. INTRODUCTION

In the evaluation of $K_L A$ using Eqn. (105), the crucial measurement determining the accuracy of the calculated value of $K_L A$ is the rate of change of pressure, $dP_{T/dt}$. Consequently it was felt to be necessary to utilise more sensitive equipment to measure this quantity than the Visicorder used by Loudon (L19), with its pen and chart method of recording the pressure variations in the constant volume column as a bubble rose through its contained liquid and dissolved.

Thus a novel data processing system was developed which consisted of an amplifier for the voltage output from the transducer, the 2-channel tape recorder, and two analogue-digital converters, (Type 189 and Type 139E supplied by Digital Equipment Corporation).

The transducer output, recording pressure changes in the constant volume column, was recorded on Channel 1 of the tape recorder, and four pulses, (pulses 0, 1, 2 and 3), to locate certain positions while a bubble was in the column, on Channel 2. Pulses 0 and 1 were produced by the manually operated circuit (MP) (see Fig. (13)). Pulse 0 located the position when the bubble was in the cup just after injection, and pulse 1 when the bubble was in the cup just prior to its/

its release to rise through the column. Pulse 2 and pulse 3 resulted as the bubble passed photoelectric cell stations P_1 and P_3 respectively.

The recorded traces on Channels 1 and 2 were fed through the analogue-digital converters, Types 139E and 189 respectively, into the Programmed Data Processor-8 (PDP-8), a high speed, stored program, digital computer manufactured by the Digital Equipment Corporation. Samples were taken off the continuous pressure trace on Channel 1, digitised and punched out on paper tape with a simultaneous printed output. By utilising the storage facility of the PDP-8 it was possible to sample at rates greater than the speed of the output punch, by storing and punching out later at the normal rate. The sampling rate used was 50 samples/second at tape speed $3\frac{3}{4}$ i.p.s., which after the tape recorder had been slowed by a factor of two (to $1\frac{7}{8}$ i.p.s.) was equivalent to a sampling rate of 100 samples/second.

The maximum recorded voltage range of the recorder was +2.5 v to -2.5 v. This was biased so that it lay between 0 v and -5 v, the input range of the analogue digital converters being 0 v to -10 v. The maximum noise level from the transducer on amplification and output from the recorder (< 0.05 volts) was small compared to the recorded signal levels.

The output from the PDP-8 was equal parity binary coded punched tape and simultaneously printed decimal integers. The print out of the output from the computer had a scale from 0 to 4095 and an accuracy of ± 0.025% of full scale.

The transducer output was calibrated by recording the transducer voltage output corresponding to various measured liquid heights above/

above the transducer station, and hence to various pressures. These recordings were printed and punched out.

When pulse 1 was sensed on Channel 2, 100 samples were taken from the recording on Channel 1. After pulse 2, sampling recommenced at 100 samples/second and stopped when pulse 3 was sensed. The first 100 samples were then simultaneously printed and punched out, followed by the number of samples taken between pulses 2 and 3, and finally by the samples taken between pulses 2 and 3.

The liquid pressure, P_{T1}, when the bubble was in the cup prior to release was found by taking the mean of the first 100 samples. The 50 samples immediately before the point midway between photo-electric cell units P_1 and P_3 and the 50 samples immediately after it were taken, and smooth 1st and 2nd order polynomial curves fitted using the least squares method of Legendre (T6).

From the smoothed data, the gradient, giving $dP_{T/dt}$, and the liquid pressure, P_T, at the central measuring point were found.

100 samples were taken off periodically at marker pulse 0 to check P_{TO}, the liquid pressure after bubble injection when pressure equilibrium had been re-established with the atmosphere - noting that valves V_5 and V_6 were still open at that point.

Computer programs written in Atlas Autocode and run off on the Edinburgh University KDF9 computer performed the above calculations.

P_{T1}, P_T, and $dP_{T/dt}$, along with the other necessary physical quantities, (see Eqn. (105)), were fed into the main program (also written in Atlas Autocode) for calculating K_LA and K_L, the instantaneous mass/

mass transfer product and mass transfer coefficient respectively, and for applying the Uno-Kintner correction for wall effect (U1) to the measured bubble terminal velocities.

The data for K_LA and K_L vs D_e (the equivalent spherical diameter of the bubble), and U (measured terminal rise velocity of gas bubble) and $U(\infty)$ (Uno-Kintner corrected U) vs D_e were smoothed by the least squares method.

Programs in Atlas Autocode were also written for evaluating the theoretical comparisons for the experimental data found for $U(\infty)$ and K_L.

A schematic diagram of the data processing method employed is shown in Fig. (14).

FIG.14. DATA PROCESSING METHOD

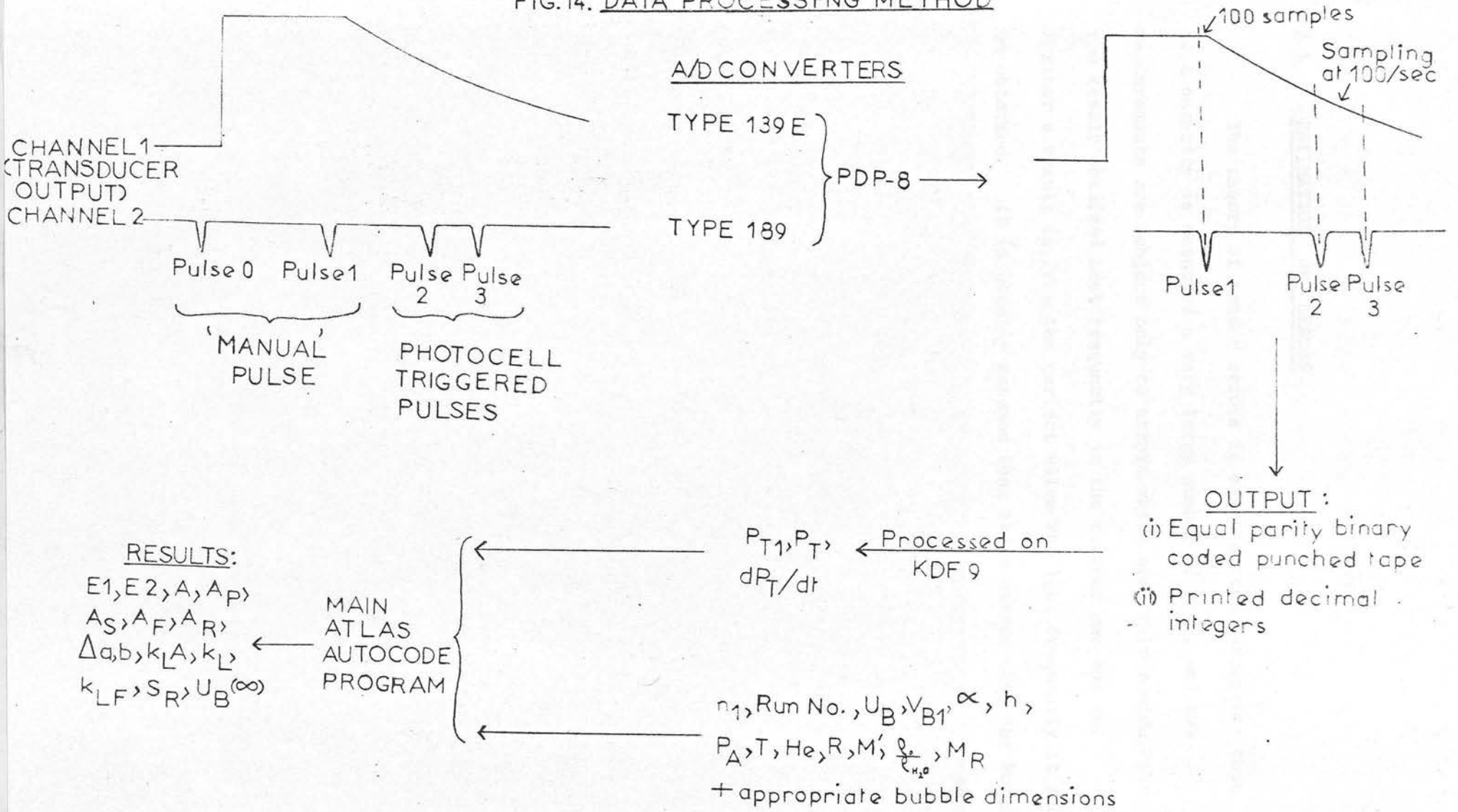

3.1 ESTIMATION OF ERRORS

The theory of random errors is based on the assumption that if a quantity is measured a very large number of times and the measurements are subject only to errors which are truly random, then the result obtained most frequently is the correct one and the further a result is from the correct value the less frequently it should be obtained. It is usually assumed that these errors obey the Normal (or Gaussian) frequency distribution i.e. the random error is equally likely to be positive or negative.

The standard deviation (β) is the most commonly used index of precision. The standard deviation or root-mean-square error is derived from the root-mean-square of the errors in an infinite number of measurements.

The probability that the	($-\beta$ to β)		(0.3173)
error of any observation	(-2β to 2β)		(0.0457)
chosen at random shall be	(-3β to 3β)	is	(0.0027)
outside the range	(-3.09β to 3.09β)		(0.0020)

Thus an error as great as 3.09 times the standard deviation is only to be expected about once in 500 observations.

The principle of least squares was first formulated by Legendre and states that the most probable value of any observed quantity is such that the sum of the squares of the deviations of the observations from this value is least. Applying the principle of least/

least squares it may be shown (T6) that the most probable value of a measured quantity is the arithmetic mean of the observations.

If n observations a_1, a_2, ..., a_k, ..., a_n are made of a physical quantity, then their arithmetic mean is

$$\bar{a} = \frac{1}{n} \Sigma a_k \qquad (106)$$

If the residuals are denoted by U_k where

$$U_k = a_k - \bar{a} \qquad (107)$$

then the standard deviation of the most probable true value of the physical quantity, the arithmetic mean, is given by

$$\beta = \frac{\Sigma U_k^2}{n(n-1)} \qquad (108)$$

There is one class of observation where repetition of measurement is unnecessary. This class includes the simple reading of a scale or measurement of length. In such cases, the maximum error of measurement can be estimated from the accuracy with which the scale can be read. The standard deviation, β, will therefore be 68% of the maximum error.

To estimate the standard deviation of a compound quantity the following rules are applied (T6):

If a number of measured quantities have means m_1, m_2, ..., m_n with standard deviations β_1, β_2, ..., β_n respectively then the standard deviation of

(i) /

(i) the sum $m_1 + m_2$ is $\sqrt{(\beta_1^2 + \beta_2^2)}$ (109)

(ii) the difference $m_1 - m_2$ is $\sqrt{(\beta_1^2 + \beta_2^2)}$ (110)

(iii) the product $m_1 m_2 m_3$ is β where

$$\left(\frac{\beta}{m_1 m_2 m_3}\right)^2 = \left(\frac{\beta_1}{m_1}\right)^2 + \left(\frac{\beta_2}{m_2}\right)^2 + \left(\frac{\beta_3}{m_3}\right)^2 \quad (111)$$

(iv) the power m_1^p is β where

$$\frac{\beta}{m_1^p} = \frac{p\beta_1}{m_1} \quad (112)$$

$$\text{or } \beta = (pm_1^{p-1})\ \beta_1 \quad (113)$$

(v) any function of $m_1, m_2, \ldots, m_n$, namely

$f(m_1, m_2, \ldots, m_n)$ is β where

$$\beta^2 = \left(\frac{\delta f}{\delta m_1}\right)^2 \beta_1^2 + \left(\frac{\delta f}{\delta m_2}\right)^2 \beta_2^2 + \ldots + \left(\frac{\delta f}{\delta m_n}\right)^2 \beta_n^2 \quad (114)$$

(i) and (iv) are special cases of (v).

Eqns. (109) to (114) were used to determine standard deviations in the measured values of:

(a) Column Compressibility, α

From Section 2.2.3,

$$\Delta V_S = M_{L/\rho o} \quad (115)$$

$$\Delta P_T = \Delta_1 - \Delta_2 \quad (116)$$

Therefore from Eqn. (101) it is seen that α was calculated from four variables,

α/

$$\alpha = f(M_L, \rho_L, \Delta_1, \Delta_2) \qquad (117)$$

(b) Equivalent Spherical Diameter, D_e

On the cessation of liquid flow from the liquid displacement line terminal nozzle, bubble volume, V_{BO}, at a bubble internal pressure of P_{BO} was given by,

$$V_{BO} = M_L/\rho_o \qquad (118)$$

where M_L was the mass of displaced liquid collected in a weighing bottle.

When the liquid displacement line valves V_6 and V_5 were closed and the column upper stopcock V_2 was momentarily opened, the increase in pressure was reflected by an increase in bubble internal pressure to P_{B1}. For isothermal conditions, the volume of the bubble, V_{B1}, just prior to its release from the dumping cup was therefore given by,

$$V_{B1} = \frac{V_{BO}\, P_{BO}}{P_{B1}} \qquad (119)$$

Both P_{BO} and P_{B1} were obtained from Eqn. (99),

$$P_B = P_T - \frac{\rho_o}{\rho_{H_2O}} h + P_A \qquad (99)$$

by substituting P_{TO} and P_{T1} for P_T when P_{BO} and P_{B1} were, respectively, substituted for P_B. h, the vertical displacement of the injected bubble above the pressure transducer location, was 1 cm.

The/

The bubble volume, V_B, at the point in the column at which it was photographed, (i.e. just after photoelectric cell P_2 and midway between P_1 and P_3), was obtained from Eqn. (103),

$$V_B = V_{B1} + \alpha\ (P_T - P_{T1}) \qquad (103)$$

where P_T and P_{T1} were the liquid pressures at the pressure transducer location when the bubble volumes were V_B and V_{B1} respectively.

Bubble instantaneous equivalent spherical diameter, D_e, was given by

$$D_e = (^{6V_B/\pi})^{1/3} \qquad (120)$$

From Eqns. (120), (103), (119), (118) and (99) it is seen that

$$D_e = f\ (\alpha,\ P_T,\ P_{T1},\ M_L,\ \rho_o,\ P_A,\ h,\ P_{TO}) \qquad (121)$$

(c) Bubble Terminal Rise Velocity, U_B

The pulses generated by the photoelectric cell units P_1 and P_3 when a bubble passed those stations acted as markers on the column internal pressure record, and also served to start and stop an electronic stopclock which then displayed a timed interval, τ', corresponding to the distance L between P_1 and P_3 through which the bubble had risen. Bubble terminal rise velocity averaged over the distance L and pertaining to the point midway between the units P_1 and P_3, which was also the point where the bubble was photographed, was given by,

U_B /

$$U_B = L/_{\tau'} \qquad (122)$$

U_B is therefore expressed as a function of two variables only,

$$U_B = f\ (L,\ \tau') \qquad (123)$$

(d) Instantaneous Mass Transfer Product, $K_L A$

From Eqn. (105) it is seen that,

$$K_L A = f\ (\frac{1}{S},\ \alpha,\ {}^{dP}T/dt,\ V_{B1},\ P_T,\ P_{T1},\ \rho_o,\ U_B,\ h,\ P_A) \qquad (124)$$

The errors involved in the measurement of bubble eccentricity, E_1, bubble surface area, A, and hence instantaneous overall mass transfer coefficient, K_L, are largely systematic, i.e. they vary in a regular manner. Thus bubble tilting and rippling affected the eccentricity measurements, and bubble surface area determinations were carried out on the basis of a shape fitting procedure and bubble dimension adjustment technique (see Appendix III). As a result error estimations were not carried out on the measured values of these quantities.

The values assigned to the different experimental errors and used to evaluate the standard deviations of α, D_e, U_B and $K_L A$ are given in Appendix II.

3.2 COMPUTER PROGRAMS

(a) Sampling from Tape Recorded Pressure Trace

This program was written in PDP-8 programming language.

Flow Diagram

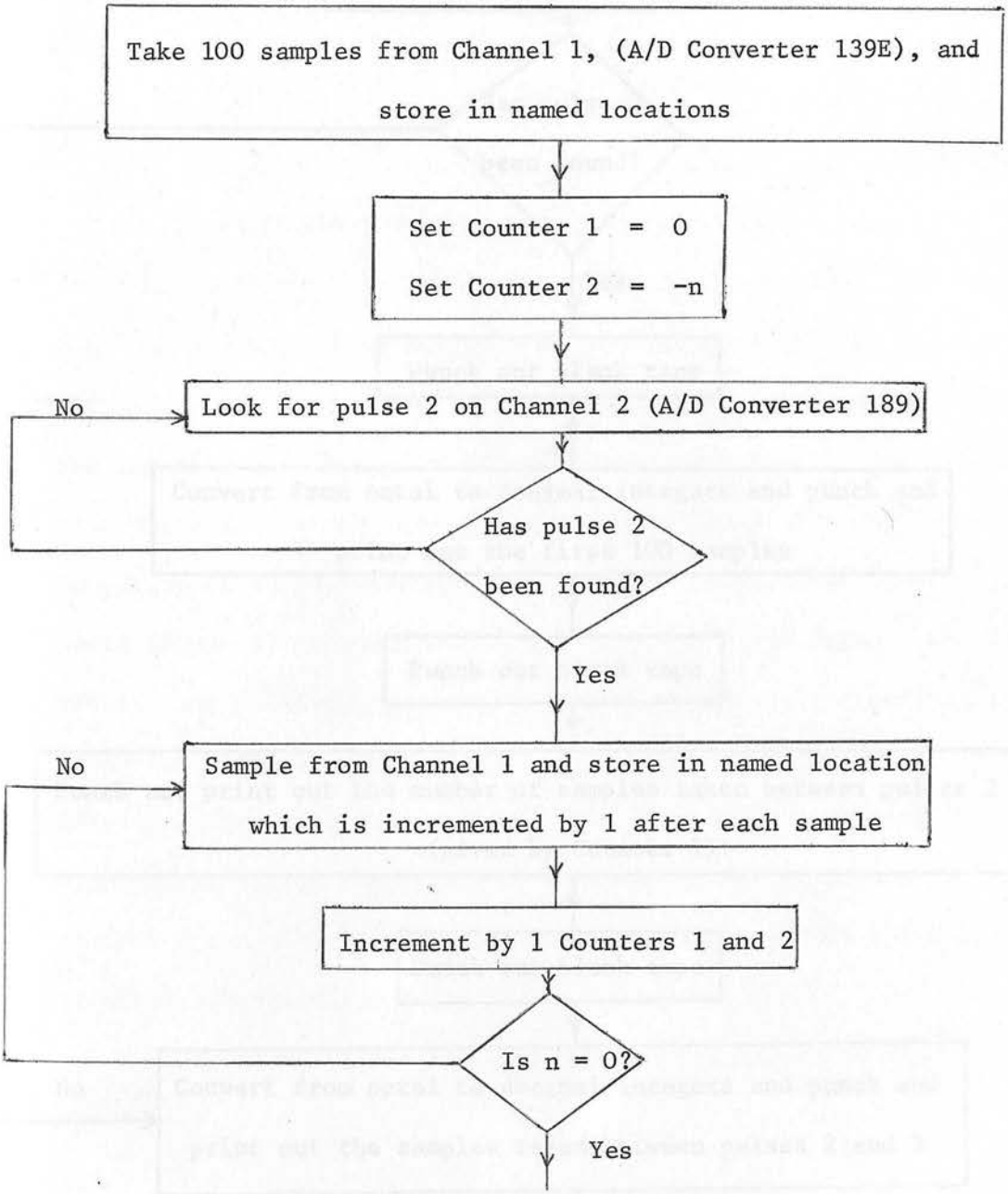

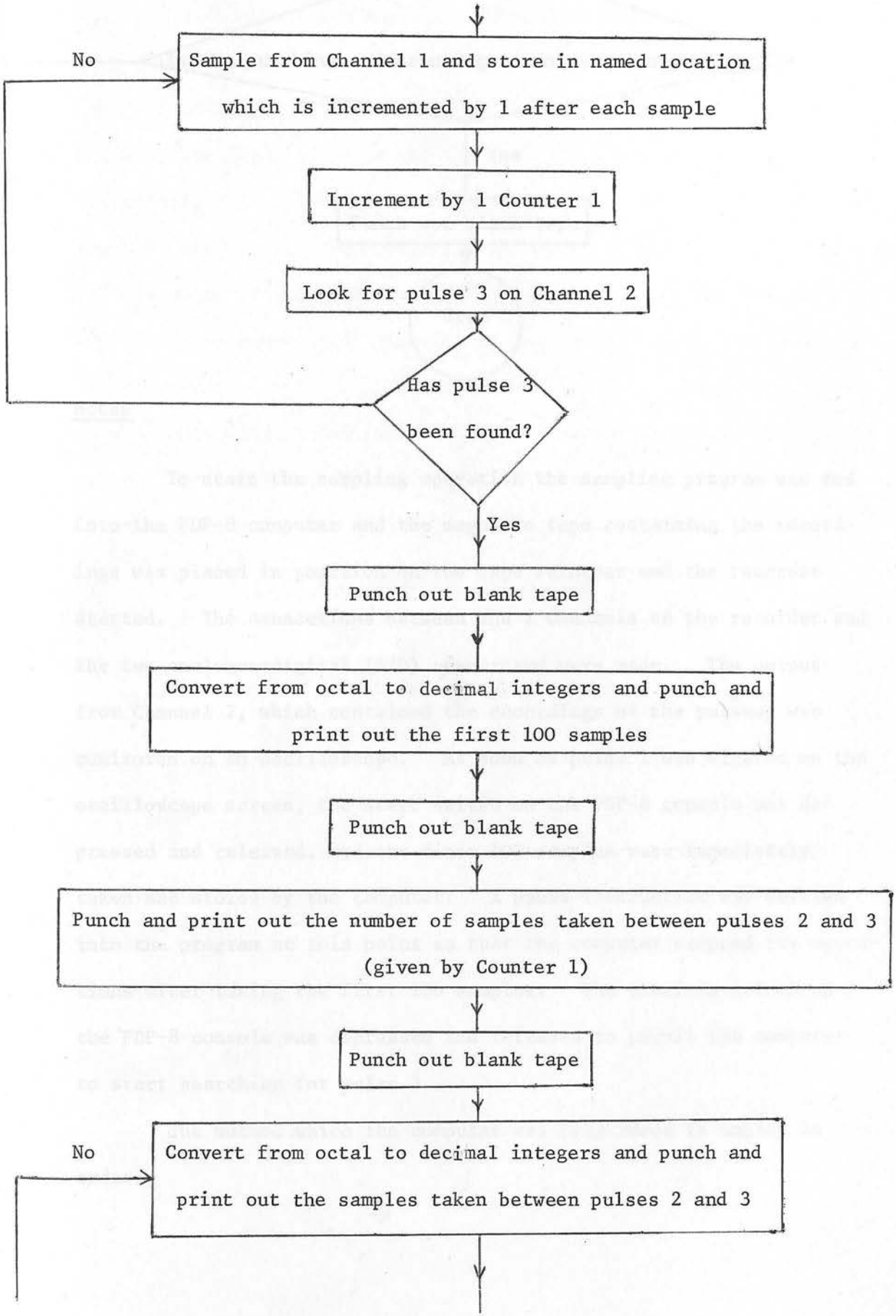
No
Sample from Channel 1 and store in named location which is incremented by 1 after each sample
Increment by 1 Counter 1
Look for pulse 3 on Channel 2
Has pulse 3 been found?
Yes
Punch out blank tape
Convert from octal to decimal integers and punch and print out the first 100 samples
Punch out blank tape
Punch and print out the number of samples taken between pulses 2 and 3 (given by Counter 1)
Punch out blank tape
No
Convert from octal to decimal integers and punch and print out the samples taken between pulses 2 and 3

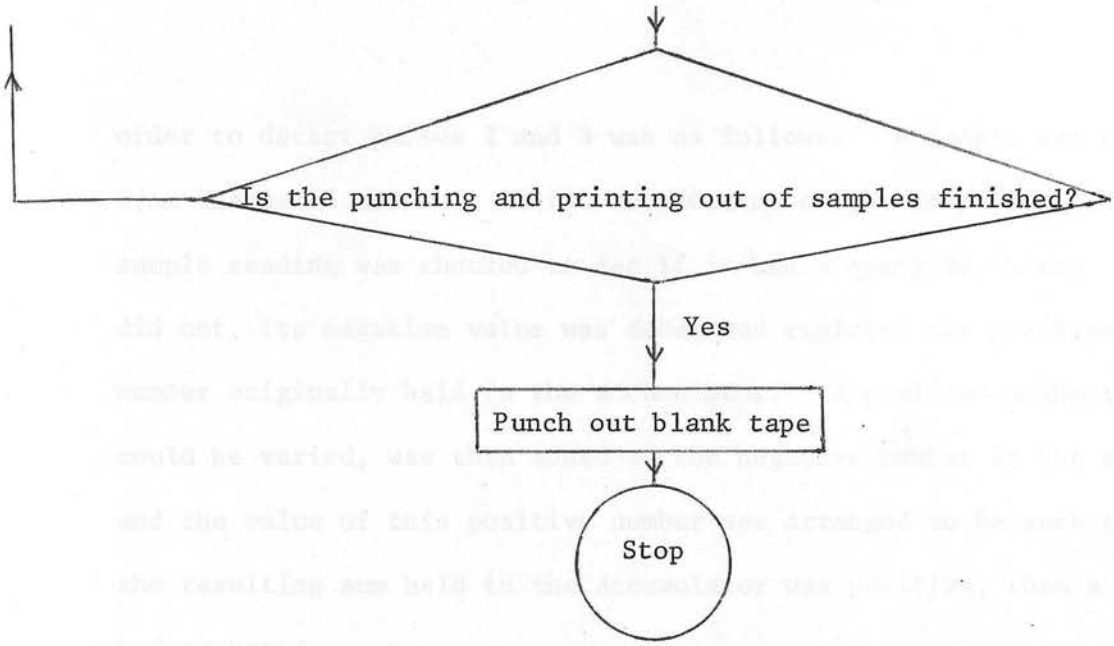

Notes

To start the sampling operation the sampling program was fed into the PDP-8 computer and the magnetic tape containing the recordings was placed in position on the tape recorder and the recorder started. The connections between the 2 Channels of the recorder and the two analogue-digital (A/D) converters were made. The output from Channel 2, which contained the recordings of the pulses, was monitored on an oscilloscope. As soon as pulse 1 was sighted on the oscilloscope screen, the start switch on the PDP-8 console was depressed and released, and the first 100 samples were immediately taken and stored by the computer. A pause instruction was written into the program at this point so that the computer stopped its operations after taking the first 100 samples. The continue switch on the PDP-8 console was depressed and released to permit the computer to start searching for pulse 2.

The method which the computer was programmed to employ in order/

order to detect pulses 2 and 3 was as follows. A sample was taken from Channel 2 and held in the accumulator of the computer. This sample reading was checked to see if it had a negative value; if it did not, its negative value was taken and replaced the positive number originally held in the accumulator. A positive number, which could be varied, was then added to the negative number in the accumulator; and the value of this positive number was arranged to be such that if the resulting sum held in the accumulator was positive, then a pulse had occurred.

After the second pulse had been detected and sampling recommenced, the number of samples taken before the programmed computer started looking for the third pulse, i.e. n samples, could be varied.

Timing loops were incorporated into the program so that all samples and the searches for pulses 2 and 3 occurred every $^{1}/_{100}$ second. As a consequence of this, pulse 2 had to take greater than $^{1}/_{100}$ seconds to reach its peak and less than $^{n}/_{100}$ seconds to reach its peak and fall off to its base value; and pulse 3 had to take greater than $^{1}/_{100}$ seconds to reach its peak.

The sampling program included instructions for the punched tape output to be equal parity, (and not non parity), binary coded punched tape, which could be fed directly into the KDF9 computer for further processing.

Programs (b), (c), (d), (e) and (f) given below were all written in/

in Atlas Autocode and processed on the KDF9 computer.

(b) Evaluating the Mean and Standard Deviation of a number of Measurements

Flow Diagram

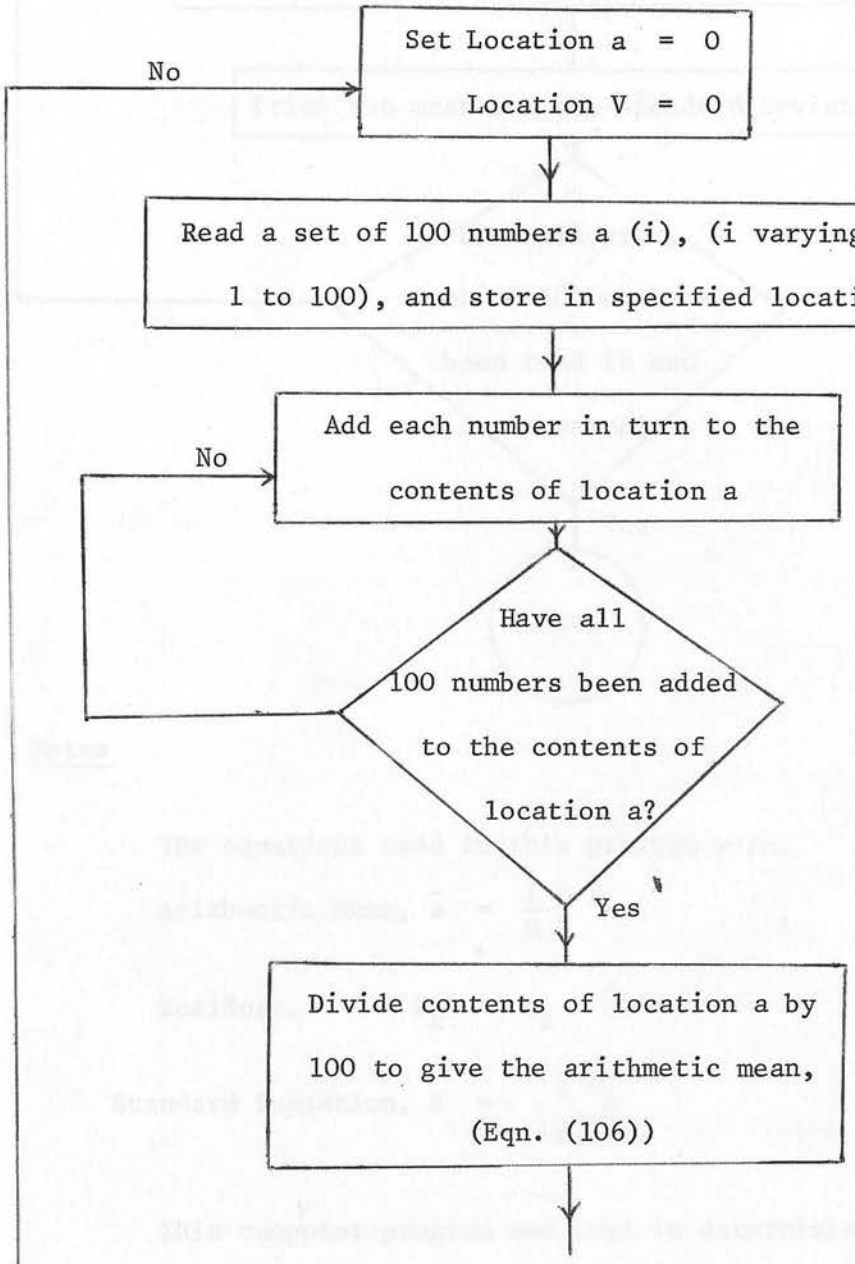

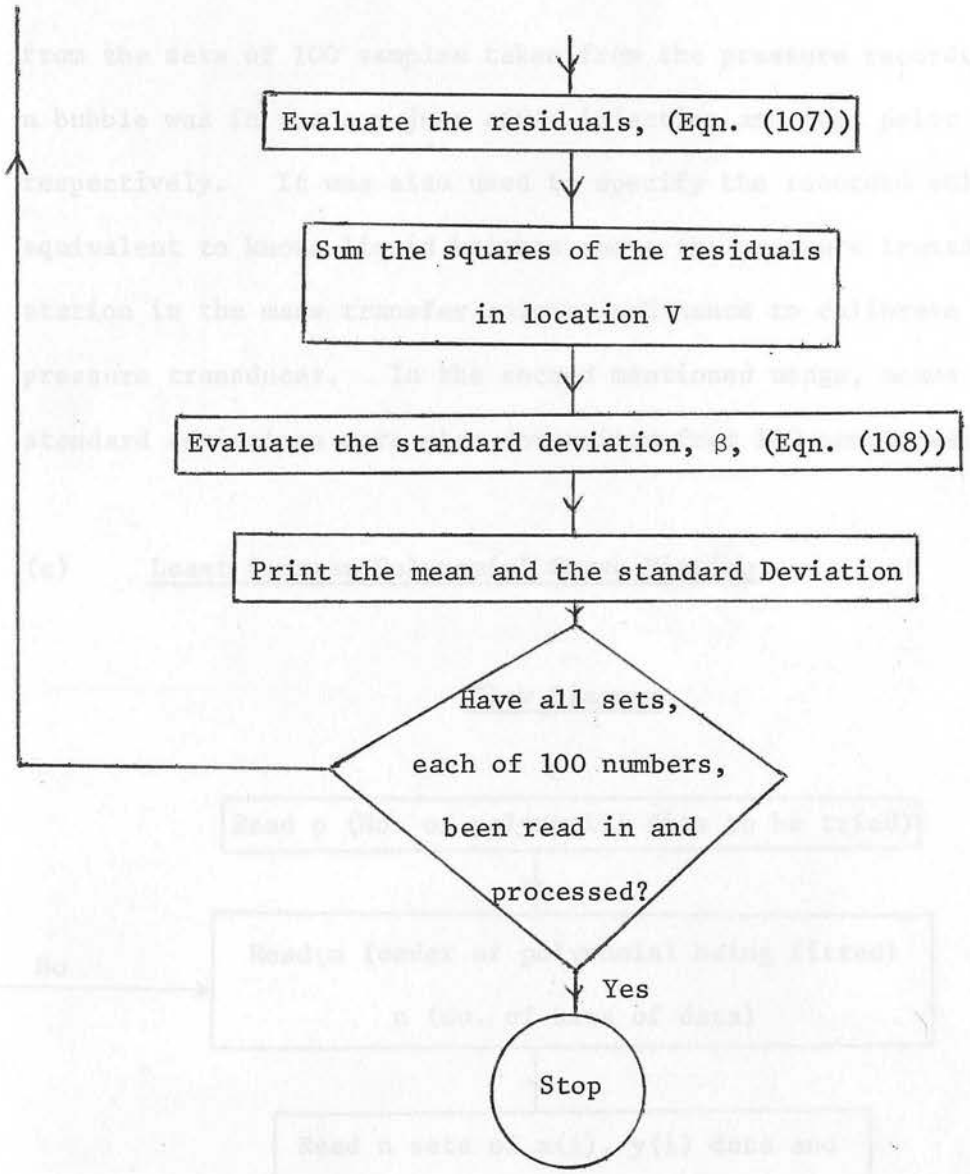

Notes

The equations used in this program were,

$$\text{Arithmetic Mean, } \bar{a} = \frac{1}{n}\sum_k a_k \qquad (106)$$

$$\text{Residual, } U_k = a_k - \bar{a} \qquad (107)$$

$$\text{Standard Deviation, } \beta = \frac{\sum U_k^2}{n(n-1)} \qquad (108)$$

This computer program was used in determining P_{T0} and P_{T1} from/

from the sets of 100 samples taken from the pressure recordings when a bubble was in the cup just after injection and just prior to release respectively. It was also used to specify the recorded values equivalent to known liquid heights above the pressure transducer station in the mass transfer column, and hence to calibrate the pressure transducer. In the second mentioned usage, means and standard deviations were also determined from 100 sample sets.

(c) Least Squares Polynomial Curve Fitting

Flow Diagram

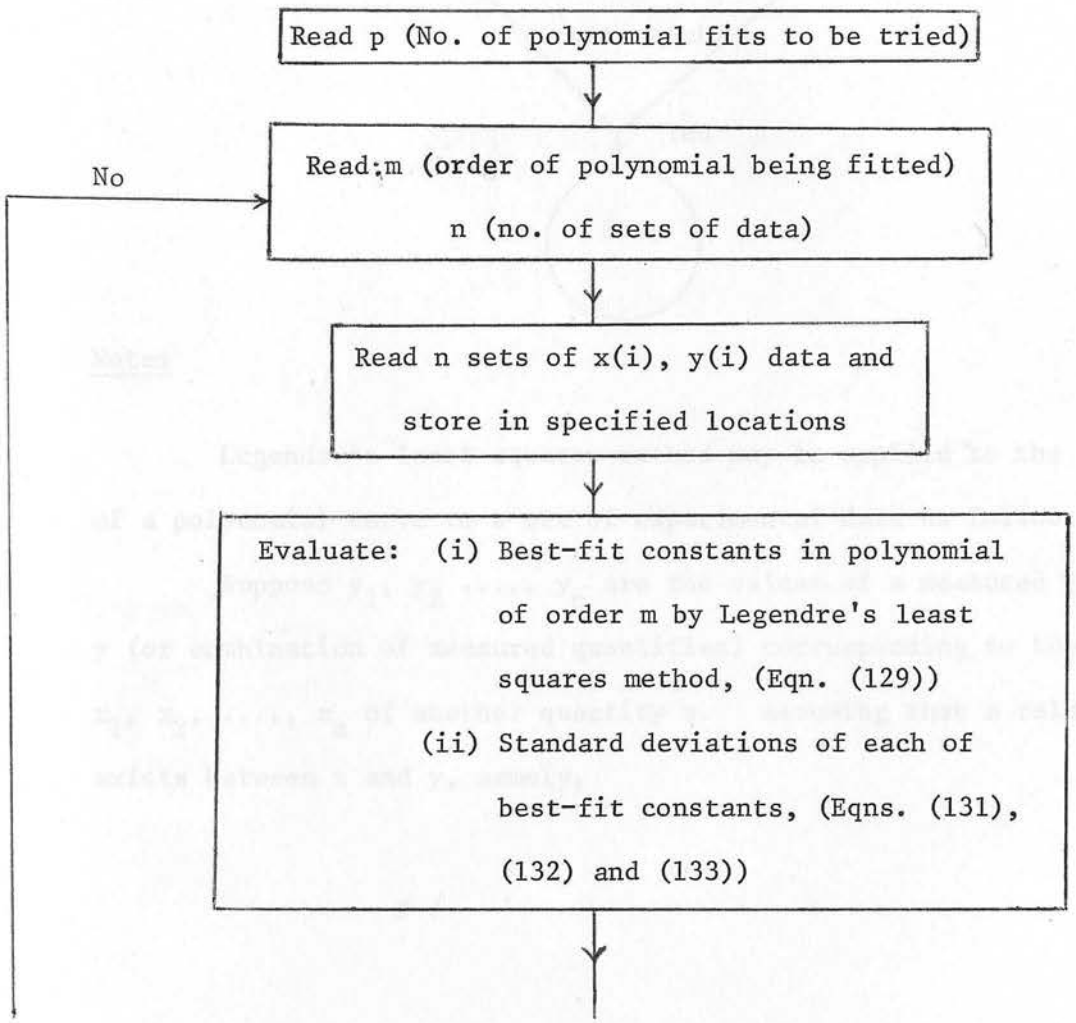

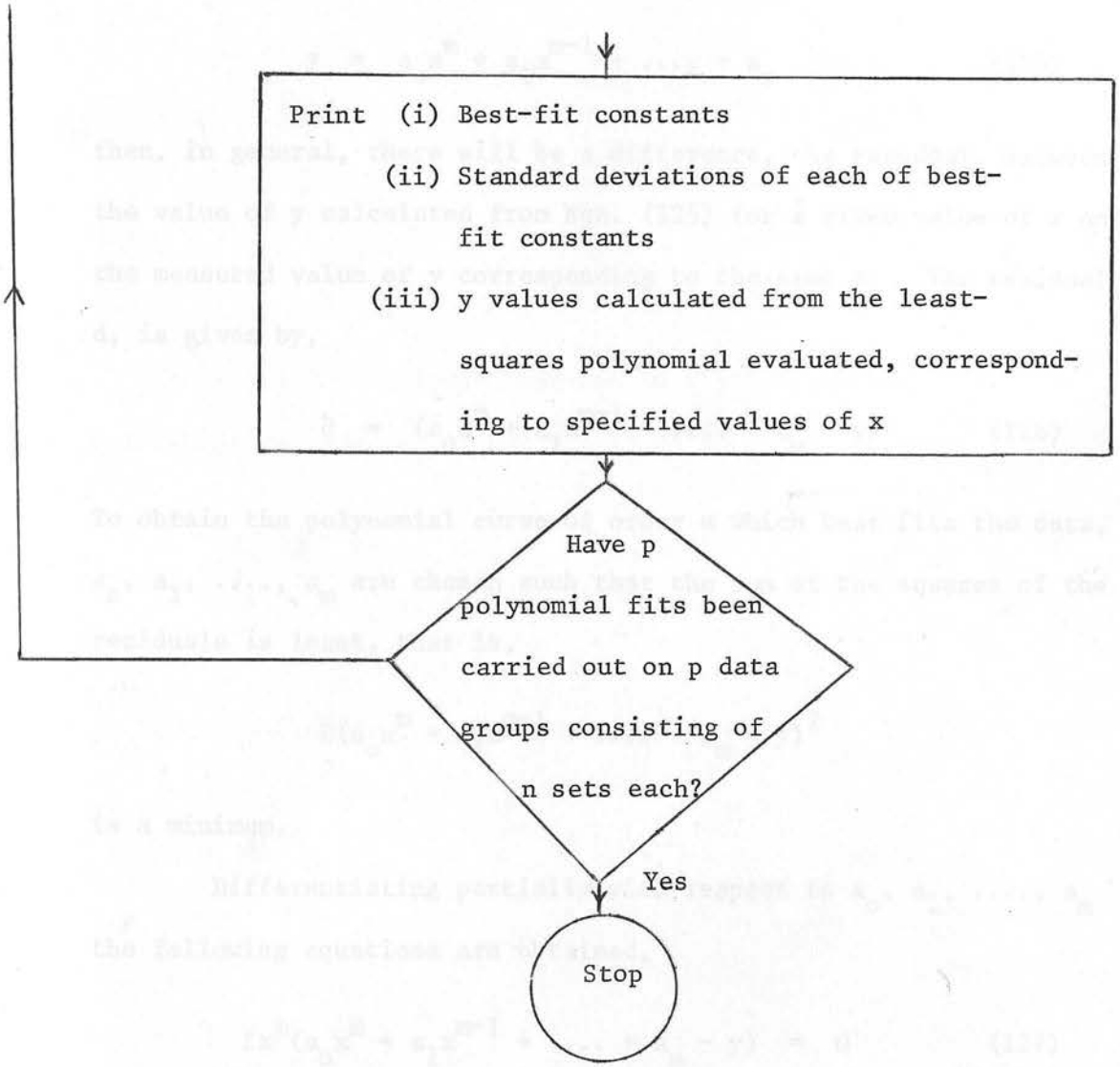

Notes

Legendre's least squares method may be applied to the fitting of a polynomial curve to a set of experimental data as follows.

Suppose y_1, y_2 ...., y_n are the values of a measured quantity y (or combination of measured quantities) corresponding to the values x_1, x_2, ..., x_n of another quantity x. Assuming that a relationship exists between x and y, namely,

y /

$$y = a_o x^m + a_1 x^{m-1} + ... + a_m \qquad (125)$$

then, in general, there will be a difference, the residual, between the value of y calculated from Eqn. (125) for a given value of x and the measured value of y corresponding to the same x. The residual, d, is given by,

$$d = (a_o x^m + a_1 x^{m-1} + ... + a_m - y) \qquad (126)$$

To obtain the polynomial curve of order m which best fits the data, a_o, a_1, ..., a_m are chosen such that the sum of the squares of the residuals is least, that is,

$$\Sigma(a_o x^m + a_1 x^{m-1} + ... + a_m - y)^2$$

is a minimum.

Differentiating partially with respect to a_o, a_1, ..., a_m the following equations are obtained,

$$\Sigma x^m(a_o x^m + a_1 x^{m-1} + ... + a_m - y) = 0 \qquad (127)$$

$$\Sigma x^{m-1}(a_o x^m + a_1 x^{m-1} + ... + a_m - y) = 0 \qquad (128)$$

$$\vdots \qquad\qquad \vdots$$

$$\Sigma(a_o x^m + a_1 x^{m-1} + ... + a_m - y) = 0 \qquad (129)$$

and so,

$$\frac{a_o}{\begin{vmatrix} \Sigma x^m y & \Sigma x^{2m-1} & ..... & \Sigma x^m \\ \vdots & \vdots & & \vdots \\ \Sigma y & \Sigma x^{m-1} & ..... & \Sigma 1 \end{vmatrix}} = \frac{a_1}{\begin{vmatrix} \Sigma x^{2m} & \Sigma x^m y & \Sigma x^{2m-2} & ..... & \Sigma x^m \\ \vdots & \vdots & \vdots & & \vdots \\ \Sigma x^m & \Sigma y & \Sigma x^{m-2} & ..... & \Sigma 1 \end{vmatrix}}$$

$$= /$$

$$= \ldots\ldots\ldots = \frac{1}{\begin{vmatrix} \Sigma x^{2m} & \Sigma x^{2m-1} & \ldots\ldots & \Sigma x^{m} \\ \cdot & \cdot & & \cdot \\ \cdot & \cdot & & \cdot \\ \cdot & \cdot & & \cdot \\ \Sigma x^{m} & \Sigma x^{m-1} & \ldots\ldots & \Sigma 1 \end{vmatrix}} \qquad (130)$$

The standard deviations of the best-fit constants of the polynomial of order m for the n sets of data is determined from (T6)

$$\frac{\beta^2_{a_o}}{\Sigma x^o} = \frac{\beta^2_{a_1}}{\Sigma x^2} = \ldots = \frac{\beta^2_{a_m}}{\Sigma x^{2m}} = \frac{\beta^2}{\Delta} \qquad (131)$$

where the determinant, Δ, is given by,

$$\Delta = \begin{vmatrix} \Sigma x^{2m} & \Sigma x^{2m-1} & \ldots\ldots & \Sigma x^{m} \\ \cdot & \cdot & & \cdot \\ \cdot & \cdot & & \cdot \\ \cdot & \cdot & & \cdot \\ \Sigma x^{m} & \Sigma x^{m-1} & \ldots\ldots & \Sigma x^{o} \end{vmatrix} \qquad (132)$$

$$\text{and } \beta^2 = \frac{\Sigma d^2}{(n - m - 1)} \qquad (133)$$

d is the residual and is defined by Eqn. (126)

In Eqns. (130), (131), (132),

$$\Sigma 1 = \Sigma x^o = n \qquad (134)$$

The elimination method of Gauss (F4) was employed to evaluate the polynomials in Eqns. (130) and (132).

Computer program (c) was used for smoothing the $K_L A$ vs D_e data/

data, the K_L vs D_e data, the U vs D_e data, the U(∞) vs D_e data and the E vs D_e data. It was also used for smoothing the pressure vs time sampling data, obtained from the recorded pressure trace, in order that P_T and dP_T/dt may be determined. In the last named usage, program (c) was extended to calculate dP_T/dt, since if

$$P = a_o t^m + a_1 t^{m-1} + ... + a_{m+1} t + a_m \qquad (135)$$

then

$$dP/dt = m a_o t^{m-1} + (m-1) a_1 t^{m-2} + ... + a_{m+1} \qquad (136)$$

In smoothing the K_L, $K_L A$, U, U(∞), and E vs D_e data, progressively higher order polynomials were fitted until the curve obtained was no longer smooth but oscillated. The highest order polynomial giving a smooth curve was taken to be the best fit for the data. Tests carried out on some of the pressure vs time data indicated that 1st or 2nd order polynomial fits over the 1 second time interval used, (0.5 seconds before the point where dP_T/dt and P_T were measured and 0.5 seconds after it, (see SECTION 3, INTRODUCTION)), provided smoothed curves as accurate as was possible with higher order polynomial fits before curve oscillation set in. This is to be expected from Eqn. (105), since if the volume and shape of a bubble did not change appreciably over a time interval of 1 second during its ascent through the liquid in the column and U_B and $K_L A$ also remained substantially constant over this time interval, then since $P_A >> (P_T - \frac{\rho_o}{\rho_{H_2O}} h)$, dP_T/dt would be expected to remain nearly constant.

This/

This would imply that pressure was almost a first order polynomial function of time over the 1 second time interval.

(d) Theoretical K_L vs D_e

Flow Diagram

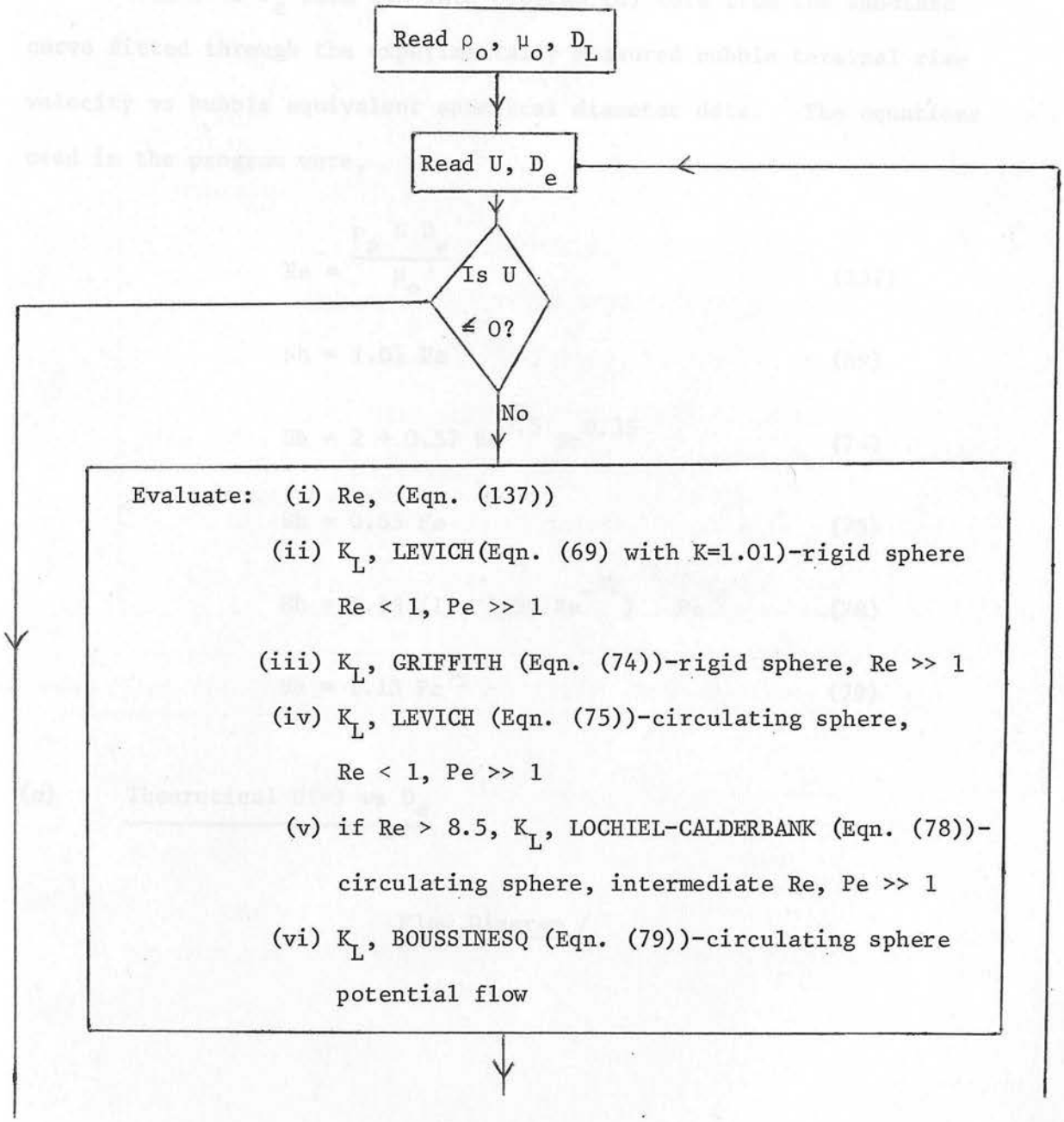

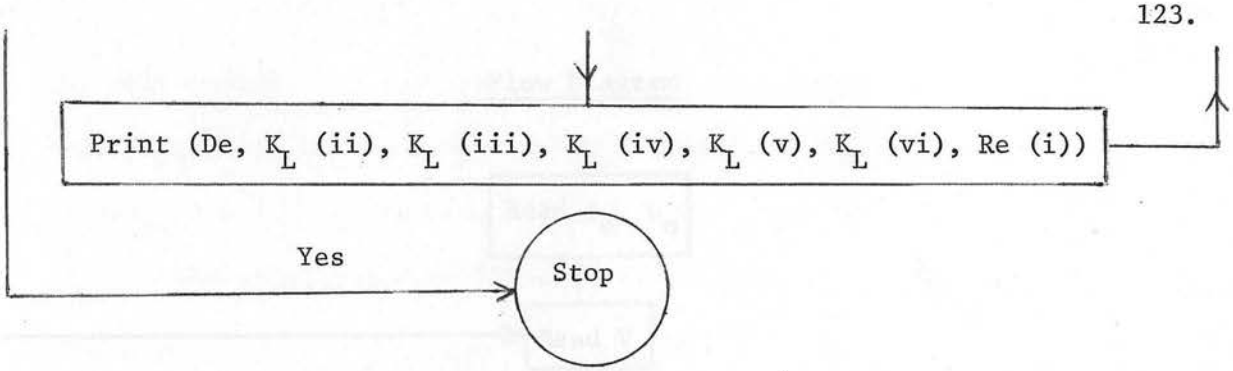

Notes

The U vs D_e data fed into program (d) were from the smoothed curve fitted through the experimentally measured bubble terminal rise velocity vs bubble equivalent spherical diameter data. The equations used in the program were,

$$Re = \frac{\rho_o U D_e}{\mu_o} \qquad (137)$$

$$Sh = 1.01\ Pe^{1/3} \qquad (69)$$

$$Sh = 2 + 0.57\ Re^{0.5}\ Sc^{0.35} \qquad (74)$$

$$Sh = 0.65\ Pe^{1/2} \qquad (75)$$

$$Sh = 1.13\ (1 - 2.90\ Re^{-1/2})^{1/2}\ Pe^{1/2} \qquad (78)$$

$$Sh = 1.13\ Pe^{1/2} \qquad (79)$$

(e) Theoretical U(∞) vs D_e

Flow Diagram /

Flow Diagram

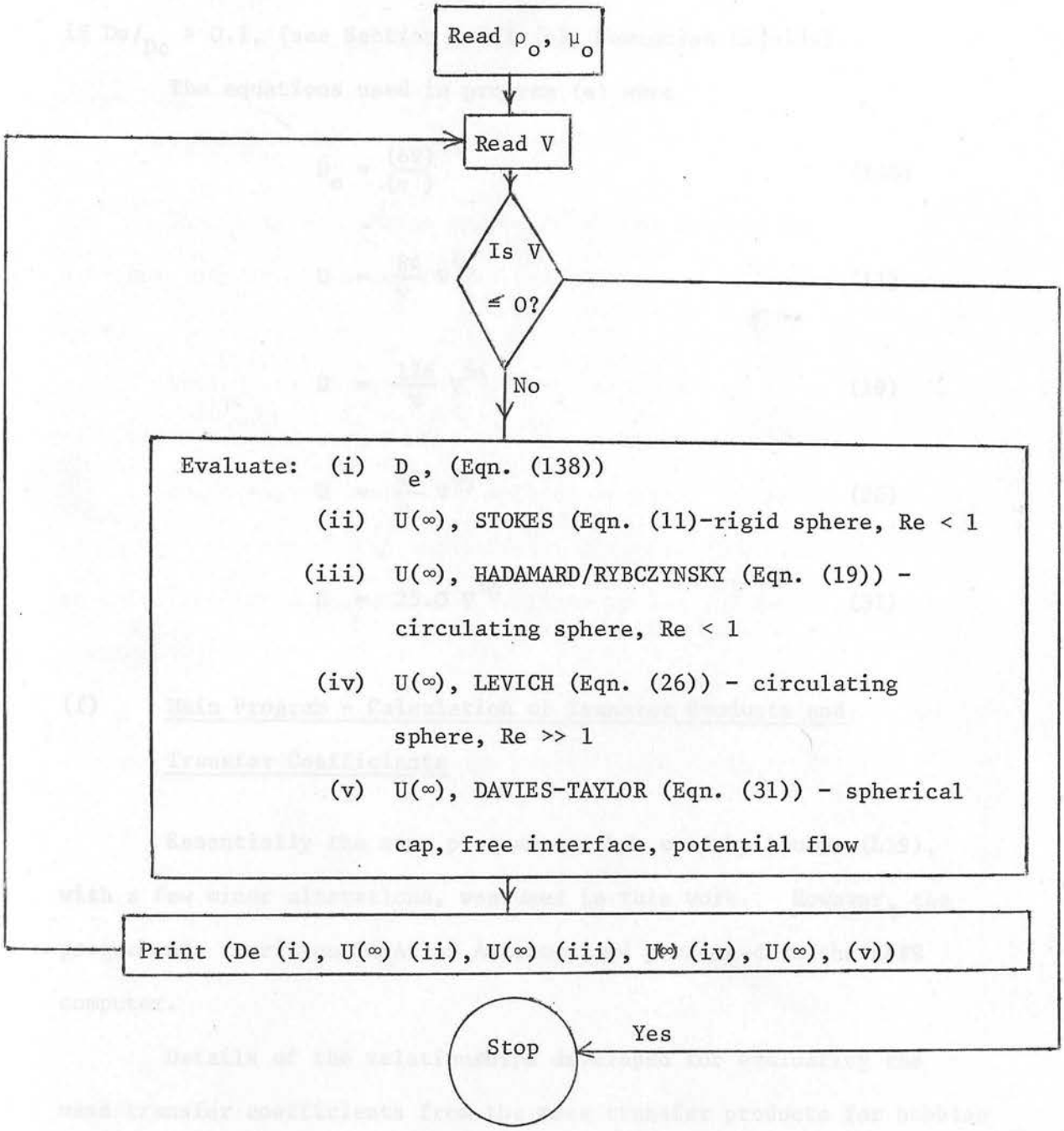

Notes

To evaluate U(∞), the bubble terminal rise velocity in an infinite/

infinite medium, the Uno-Kintner wall effect correction, (Eqn. (38)), need be applied to the measured bubble terminal rise belocities only if $De/_{Dc} > 0.1$, (see Section 1.2.1 (b), Newtonian Liquids).

The equations used in program (e) were

$$D_e = \frac{(6V)}{(\pi)}^{1/3} \qquad (138)$$

$$U = \frac{84}{\nu} V^{2/3} \qquad (11)$$

$$U = \frac{126}{\nu} V^{2/3} \qquad (19)$$

$$U = \frac{42}{\nu} V^{2/3} \qquad (26)$$

$$U = 25.0\, V^{1/6} \qquad (31)$$

(f) Main Program - Calculation of Transfer Products and Transfer Coefficients

Essentially the same program as that used by Loudon (L19), with a few minor alterations, was used in this work. However, the program was rewritten in Atlas Autocode and processed on the KDF9 computer.

Details of the relationships developed for evaluating the mass transfer coefficients from the mass transfer products for bubbles of different shapes may be found in ref. (L19) and are repeated in Appendix III of this thesis for the sake of completeness.

C H A P T E R 4

E X P E R I M E N T A L R E S U L T S

4. INTRODUCTION

Experimental data as processed by the methods described in the previous chapter are presented in graphical form in the following pages.

These data along with the other experimental parameters necessary to work out the data are tabulated in Appendix V.

Where appropriate, each section of graphical data is preceded by a summary of the magnitude of estimated experimental error as calculated by the procedures outlined in 3.1 and 3.2(c) of Chapter 3.

The physical properties of the gas-liquid systems used, and the means of determining them are specified in Appendix IV.

4.1 TERMINAL RISE VELOCITIES . CARBON DIOXIDE-DISTILLED WATER, AQUEOUS GLYCEROL SOLUTIONS AND AQUEOUS POLYOX SOLUTION

Terminal rise velocities of single carbon dioxide bubbles in free rise through distilled water, two aqueous Glycerol solutions and one aqueous Polyox solution contained in the 10.16 cm I.D. column are plotted against bubble equivalent spherical diameter in Figs. (15) to (18). Also included in Figs. (15), (16) and (17) are observed terminal rise velocity data corrected for the wall effects of the 10.16 cm I.D. column by Eqn. (38). These corrected bubble rise velocities are compared with the Mendelson equation, Eqn. (34), (Fig. (15)), and the Davies-Taylor equation, Eqn. (31), (Figs. (16) and (17)). The Hadamard/Rybczynsky equation, Eqn. (19), for circulating spheres in creeping flow is included in Figs. (16) and (17); and the Stokes equation, Eqn. (11), for rigid spheres in creeping flow is plotted in Fig. (17).

The experimental data shown in Figs. (15) to (18) is compared with the Dumitrescu equation, (Eqn. (36)), which gives the limiting velocity of a gas slug under potential flow conditions.

Bubble terminal rise velocity, U_B, was calculated according to Eqn. (122) given in Section 3.1(c), and bubble equivalent spherical diameter was found using Eqn. (120) contained in Section 3.1(b).

Standard deviations of the experimentally determined quantities, calculated by the methods outlined in Section 3.1 of Chapter 3, are summarised below.

(i)/

(i) Carbon Dioxide - Distilled Water

Run No.	D_e (cm)	U_B (cm/sec)
49	0.07 ± 0.01	9.40 ± 0.14
47	0.50 ± 0.004	23.15 ± 0.15
3	1.04 ± 0.001	23.88 ± 0.15
26	2.21 ± 0.001	30.74 ± 0.19
29	2.98 ± 0.001	33.61 ± 0.20
28	3.79 ± 0.001	34.35 ± 0.21

(ii) Carbon Dioxide - 90.6 per cent Aqueous Glycerol Solution

Run No.	D_e (cm)	U_B (cm/sec)
111	0.26 ± 0.01	3.02 ± 0.02
130	0.53 ± 0.004	12.34 ± 0.08
122	1.05 ± 0.001	21.17 ± 0.13
115	2.05 ± 0.001	28.32 ± 0.17
127	3.14 ± 0.001	32.46 ± 0.19
137	4.01 ± 0.001	33.56 ± 0.20
124	5.53 ± 0.002	34.45 ± 0.21

(iii)/

(iii) Carbon Dioxide - 99.0 per cent Aqueous Glycerol Solution

Run No.	D_e (cm)	U_B (cm/sec)
235	0.44 ± 0.004	2.38 ± 0.02
238	1.01 ± 0.001	11.44 ± 0.07
207	2.03 ± 0.001	23.04 ± 0.15
228	3.12 ± 0.001	30.30 ± 0.19
251	3.97 ± 0.001	31.65 ± 0.19
230	5.42 ± 0.001	33.99 ± 0.20

(iv) Carbon Dioxide - 1.0 per cent Aqueous Polyox Solution

Run No.	D_e (cm)	U_B (cm/sec)
316	0.26 ± 0.01	0.419 ± 0.004
340	0.53 ± 0.003	10.78 ± 0.07
327	1.01 ± 0.001	22.73 ± 0.14
334	2.18 ± 0.001	27.17 ± 0.16
360	3.02 ± 0.001	31.06 ± 0.19
354	4.06 ± 0.001	32.68 ± 0.20
312	5.62 ± 0.001	34.01 ± 0.20

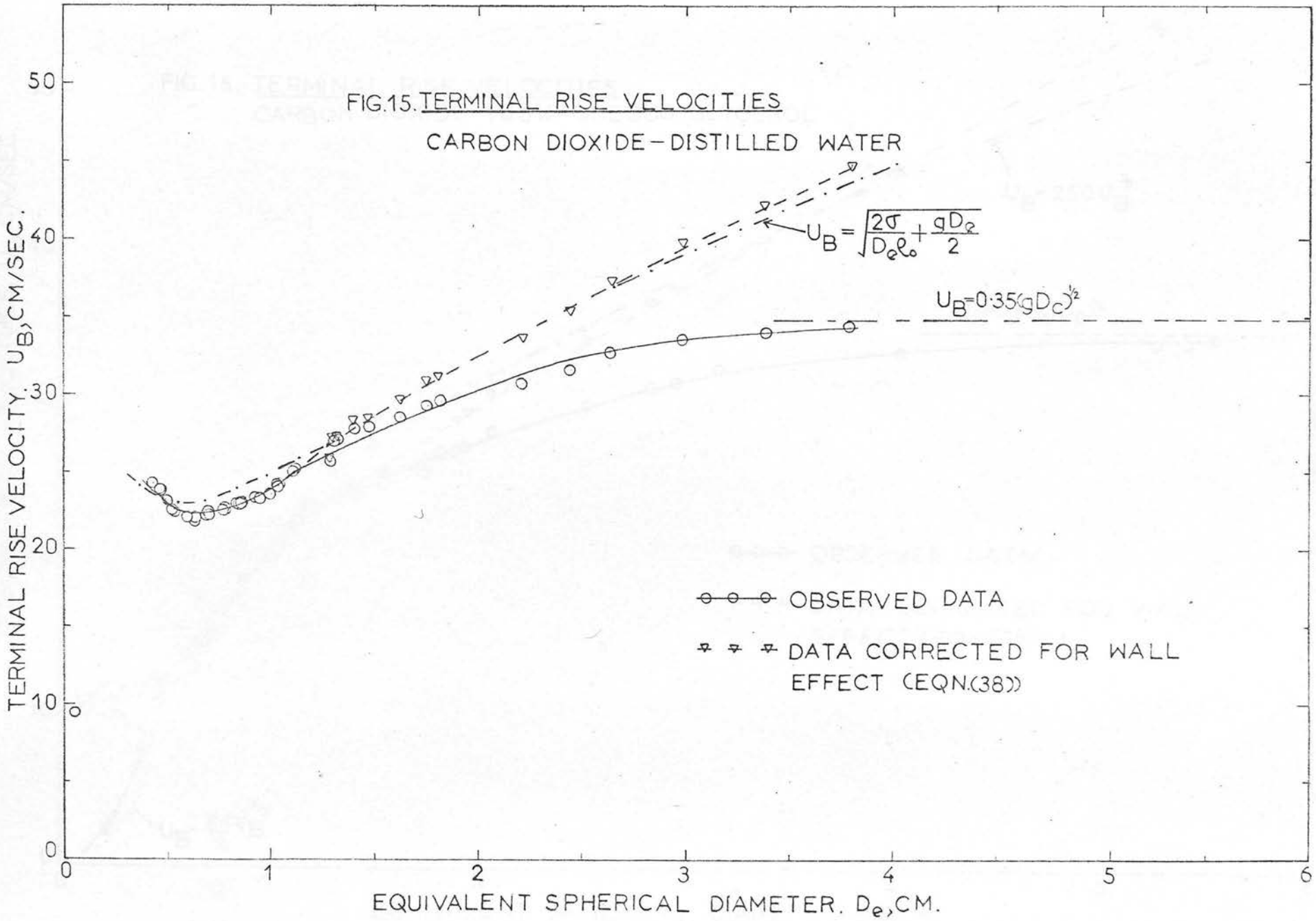
FIG.15. TERMINAL RISE VELOCITIES
CARBON DIOXIDE – DISTILLED WATER
$U_B = \sqrt{\frac{2\sigma}{D_e \rho_o} + \frac{g D_e}{2}}$
$U_B = 0.35 (g D_e)^{1/2}$
OBSERVED DATA
DATA CORRECTED FOR WALL EFFECT (EQN.(38))
TERMINAL RISE VELOCITY, U_B, CM/SEC.
EQUIVALENT SPHERICAL DIAMETER, D_e, CM.
0
10
20
30
40
50
0
1
2
3
4
5
6

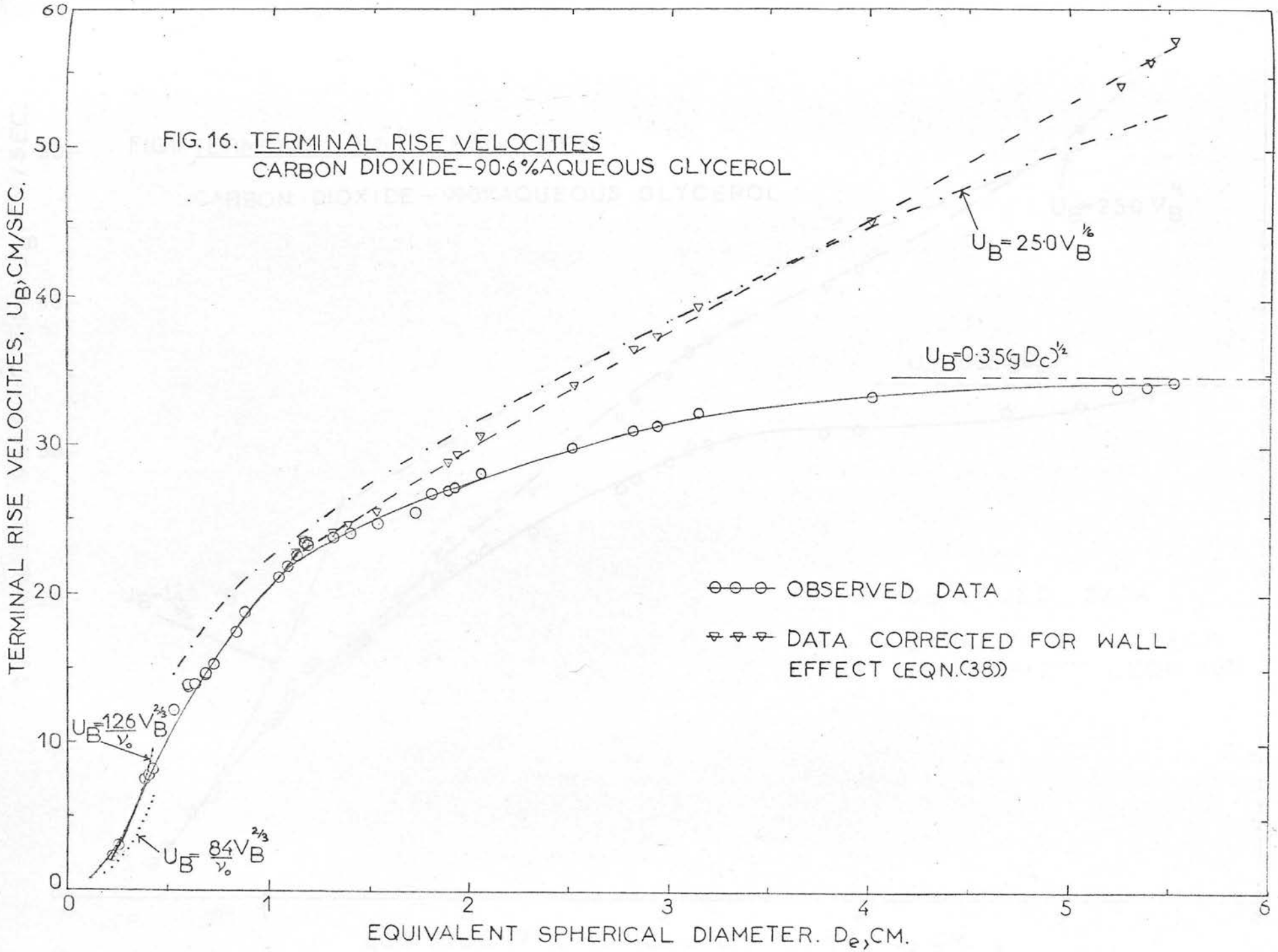
FIG. 16. TERMINAL RISE VELOCITIES
CARBON DIOXIDE–90·6% AQUEOUS GLYCEROL
$U_B = 25{\cdot}0 V_B^{1/6}$
$U_B = 0{\cdot}35 (g D_c)^{1/2}$
$U_B = \frac{126}{\nu_o} V_B^{2/3}$
$U_B = \frac{84}{\nu_o} V_B^{2/3}$
OBSERVED DATA
DATA CORRECTED FOR WALL EFFECT (EQN. (38))
TERMINAL RISE VELOCITIES, U_B, CM/SEC.
EQUIVALENT SPHERICAL DIAMETER. D_e, CM.
0
10
20
30
40
50
60
0
1
2
3
4
5
6

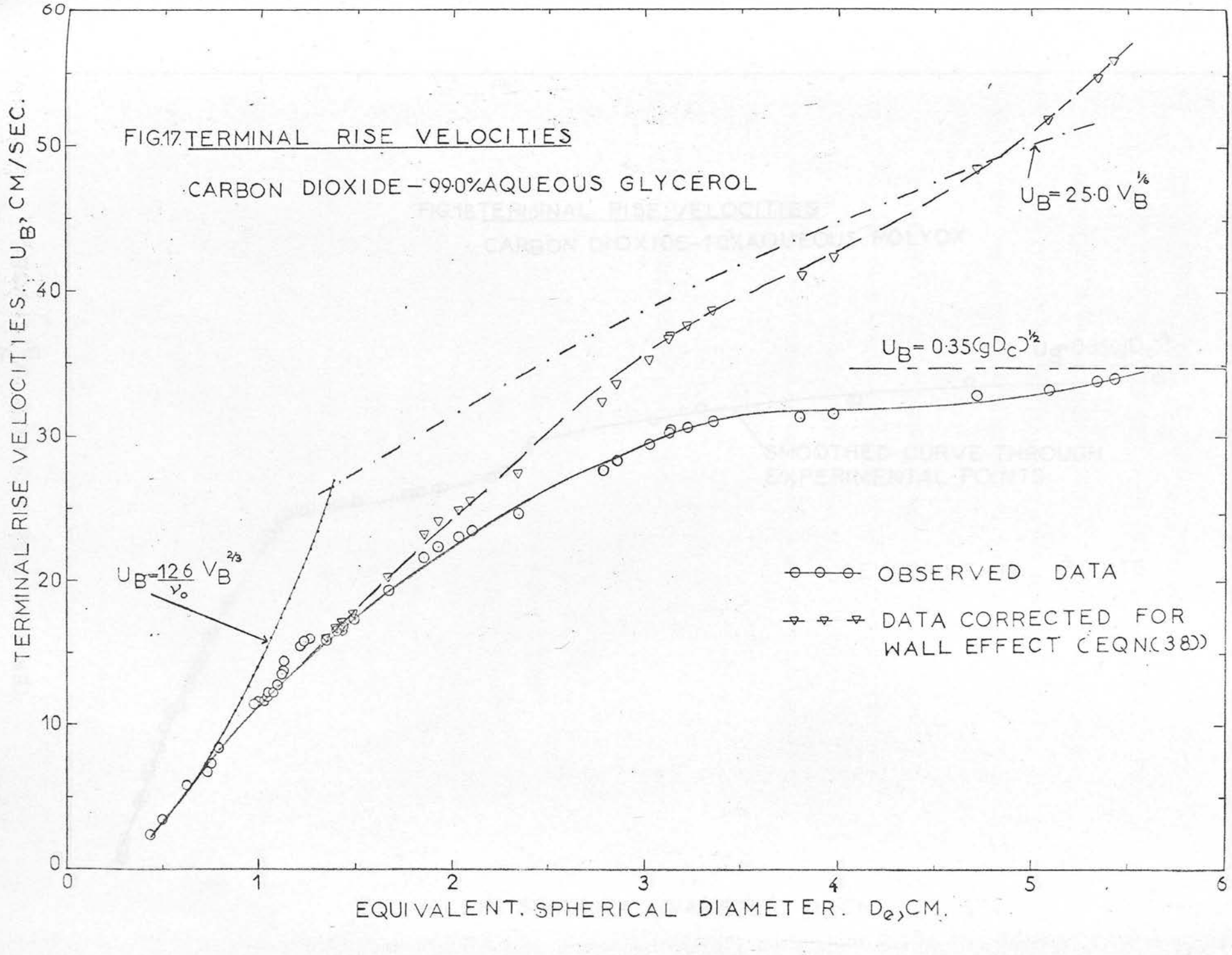
FIG.17. TERMINAL RISE VELOCITIES
CARBON DIOXIDE – 99·0% AQUEOUS GLYCEROL
$U_B = 25{\cdot}0\, V_B^{1/6}$
$U_B = 0{\cdot}35(gD_c)^{1/2}$
$U_B = \frac{12{\cdot}6}{\nu_o} V_B^{2/3}$
OBSERVED DATA
DATA CORRECTED FOR WALL EFFECT (EQN. (38))
TERMINAL RISE VELOCITIES, U_B, CM/SEC.
EQUIVALENT SPHERICAL DIAMETER, D_e, CM.
0
10
20
30
40
50
60
1
2
3
4
5
6

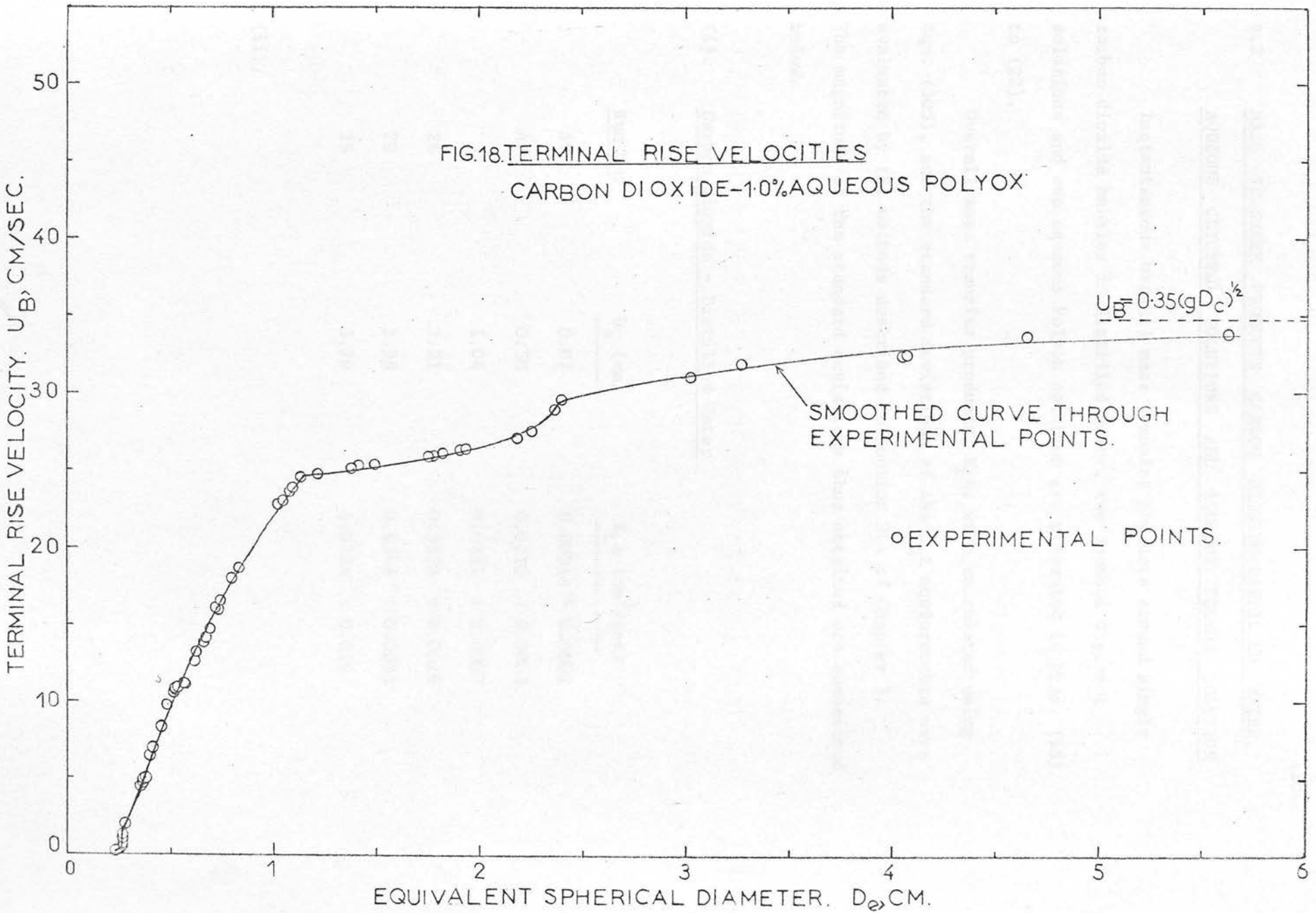
FIG.18. TERMINAL RISE VELOCITIES
CARBON DIOXIDE-1·0% AQUEOUS POLYOX
$U_B = 0.35(gD_e)^{1/2}$
SMOOTHED CURVE THROUGH EXPERIMENTAL POINTS.
○ EXPERIMENTAL POINTS.
TERMINAL RISE VELOCITY, U_B, CM/SEC.
EQUIVALENT SPHERICAL DIAMETER, D_e, CM.
0
10
20
30
40
50
0
1
2
3
4
5
6

4.2 MASS TRANSFER PRODUCTS CARBON DIOXIDE-DISTILLED WATER, AQUEOUS GLYCEROL SOLUTIONS AND AQUEOUS POLYOX SOLUTION

Instantaneous overall mass transfer products around single carbon dioxide bubbles in distilled water, two aqueous Glycerol solutions and one aqueous Polyox solution are presented in Figs. (19) to (22).

Overall mass transfer products, $K_L A$, were calculated using Eqn. (105), and the standard deviations of the $K_L A$ measurements were evaluated by the methods described in Section 3.1 of Chapter 3. The magnitude of the standard deviations thus obtained are summarised below.

(i) Carbon Dioxide - Distilled Water

Run No.	D_e (cm)	$K_L A$ (cm^3/sec)
49	0.07	0.00018 ± 0.0002
47	0.50	0.0210 ± 0.0003
3	1.04	0.0851 ± 0.0007
26	2.21	0.3559 ± 0.0019
29	2.98	0.6346 ± 0.0053
28	3.79	1.0124 ± 0.016

(ii)/

(ii) Carbon Dioxide - 90.6 per cent Aqueous Glycerol Solution

Run No.	D_e (cm)	$K_L A$ (cm^3/sec)
111	0.26	0.00069 ± 0.00007
130	0.53	0.0074 ± 0.0002
122	1.05	0.0398 ± 0.0002
115	2.05	0.1245 ± 0.0008
127	3.14	0.2300 ± 0.0021
137	4.01	0.2939 ± 0.0026
124	5.53	0.4212 ± 0.0060

(iii) Carbon Dioxide - 99.0 per cent Aqueous Glycerol Solution

Run No.	D_e (cm)	$K_L A$ (cm^3/sec)
235	0.44	0.00094 ± 0.0001
238	1.01	0.0106 ± 0.0002
207	2.03	0.0820 ± 0.0011
228	3.12	0.1568 ± 0.0018
251	3.97	0.2345 ± 0.0025
230	5.42	0.4777 ± 0.0081

(iv)/

(iv) Carbon Dioxide - 1.0 per cent Aqueous Polyox Solution

Run No.	D_e (cm)	$K_L A$ (cm^3/sec)
316	0.26	0.00035 ± 0.00005
340	0.53	0.0137 ± 0.0002
327	1.01	0.0396 ± 0.0003
334	2.18	0.1813 ± 0.0010
360	3.02	0.4907 ± 0.0024
354	4.06	0.9217 ± 0.0081
312	5.62	1.5946 ± 0.017

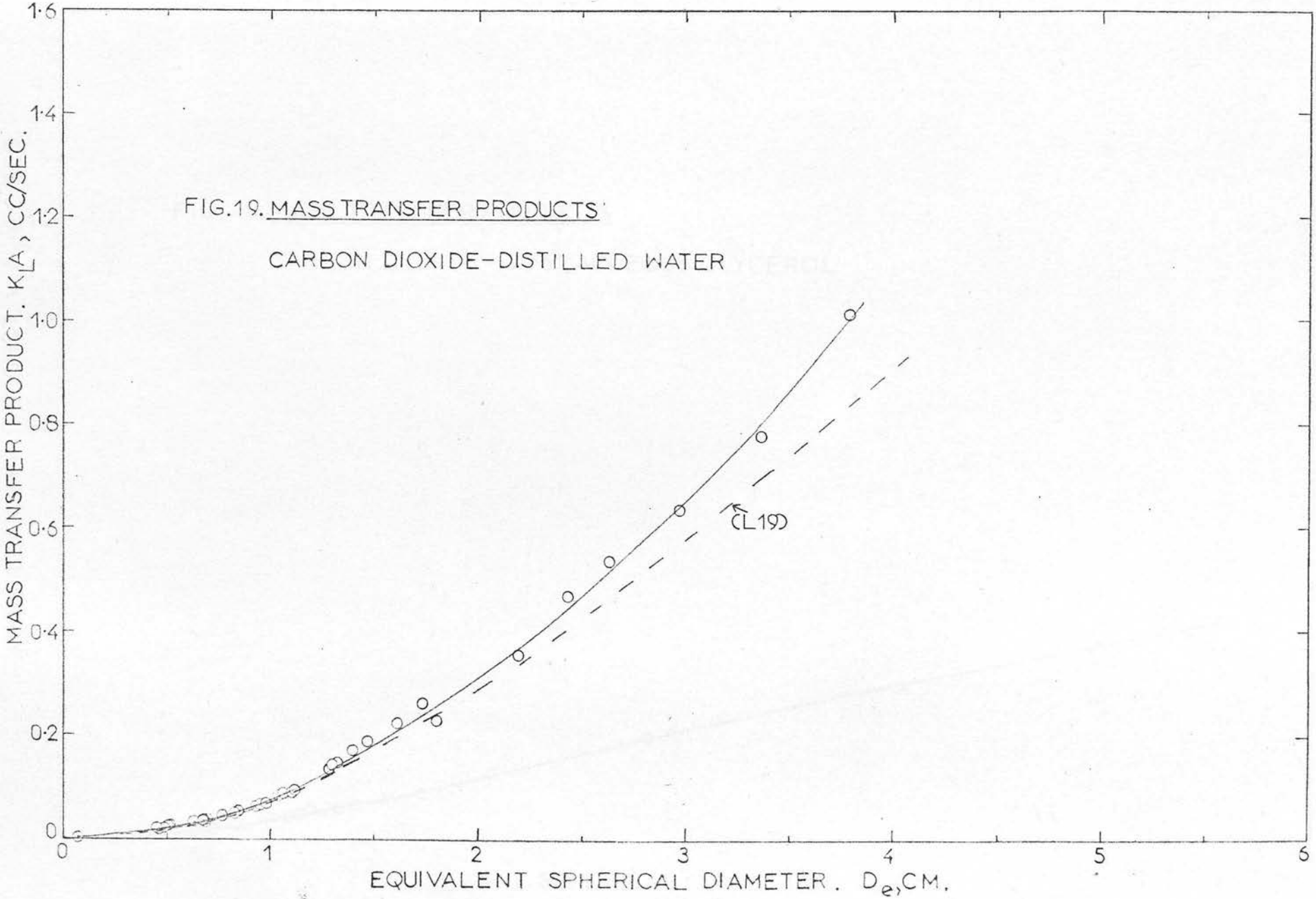
FIG.19. MASS TRANSFER PRODUCTS
CARBON DIOXIDE-DISTILLED WATER
MASS TRANSFER PRODUCT. K_LA, CC/SEC.
EQUIVALENT SPHERICAL DIAMETER. D_e, CM.
(L19)
1·6
1·4
1·2
1·0
0·8
0·6
0·4
0·2
0
0
1
2
3
4
5
6

FIG. 20. MASS TRANSFER PRODUCTS

CARBON DIOXIDE – 90·6% AQUEOUS GLYCEROL

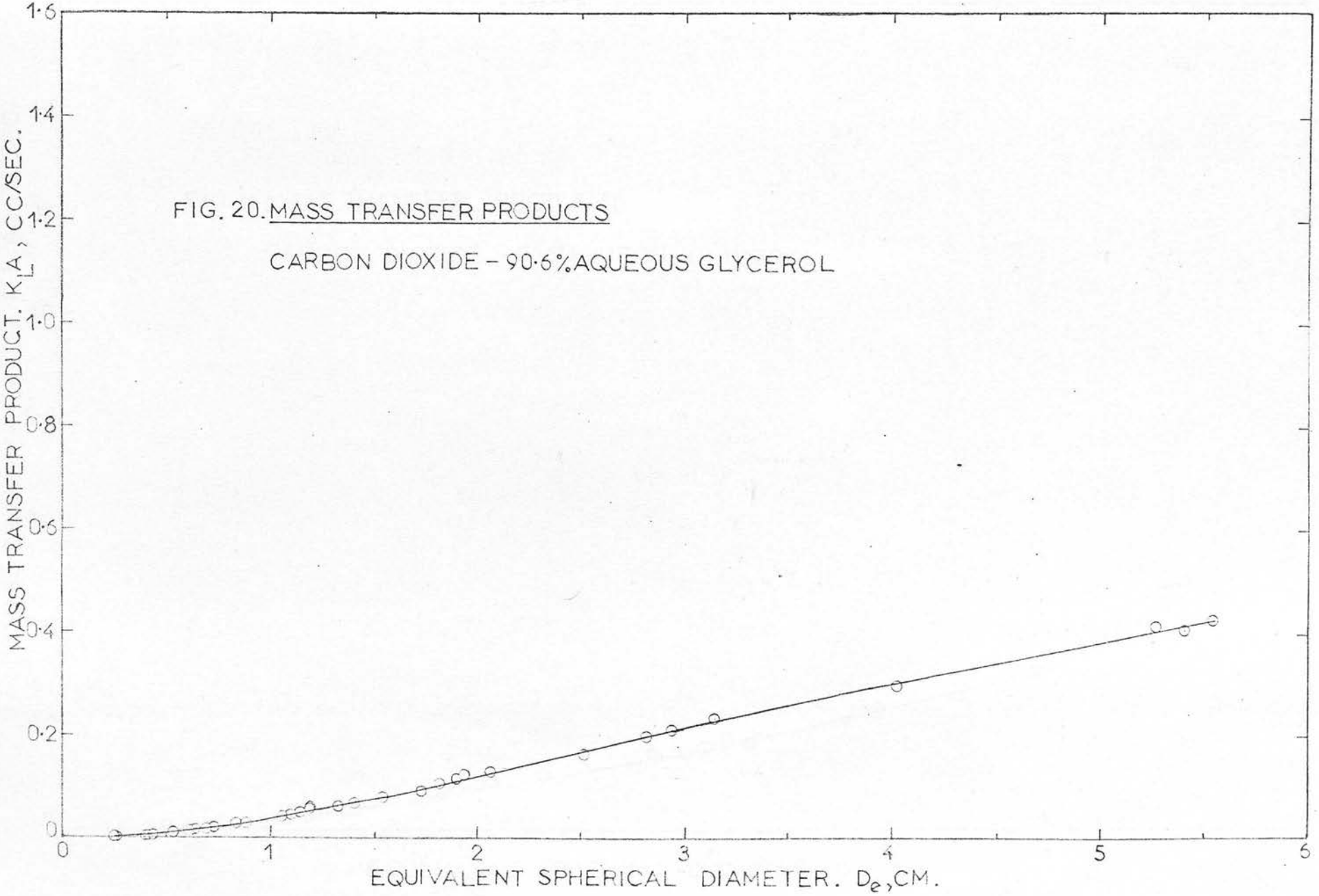

FIG. 21. MASS TRANSFER PRODUCTS

CARBON DIOXIDE – 99·0% AQUEOUS GLYCEROL

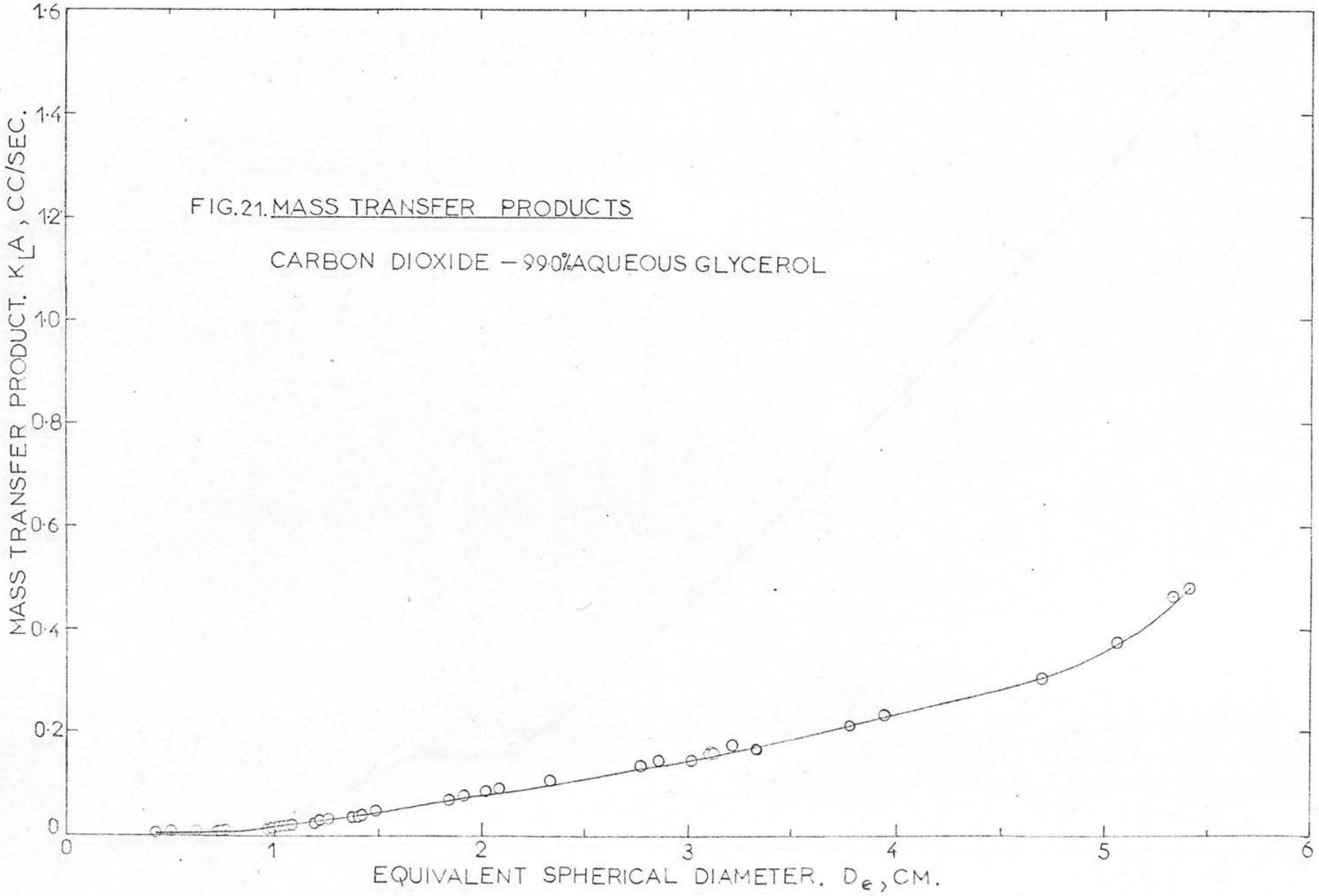

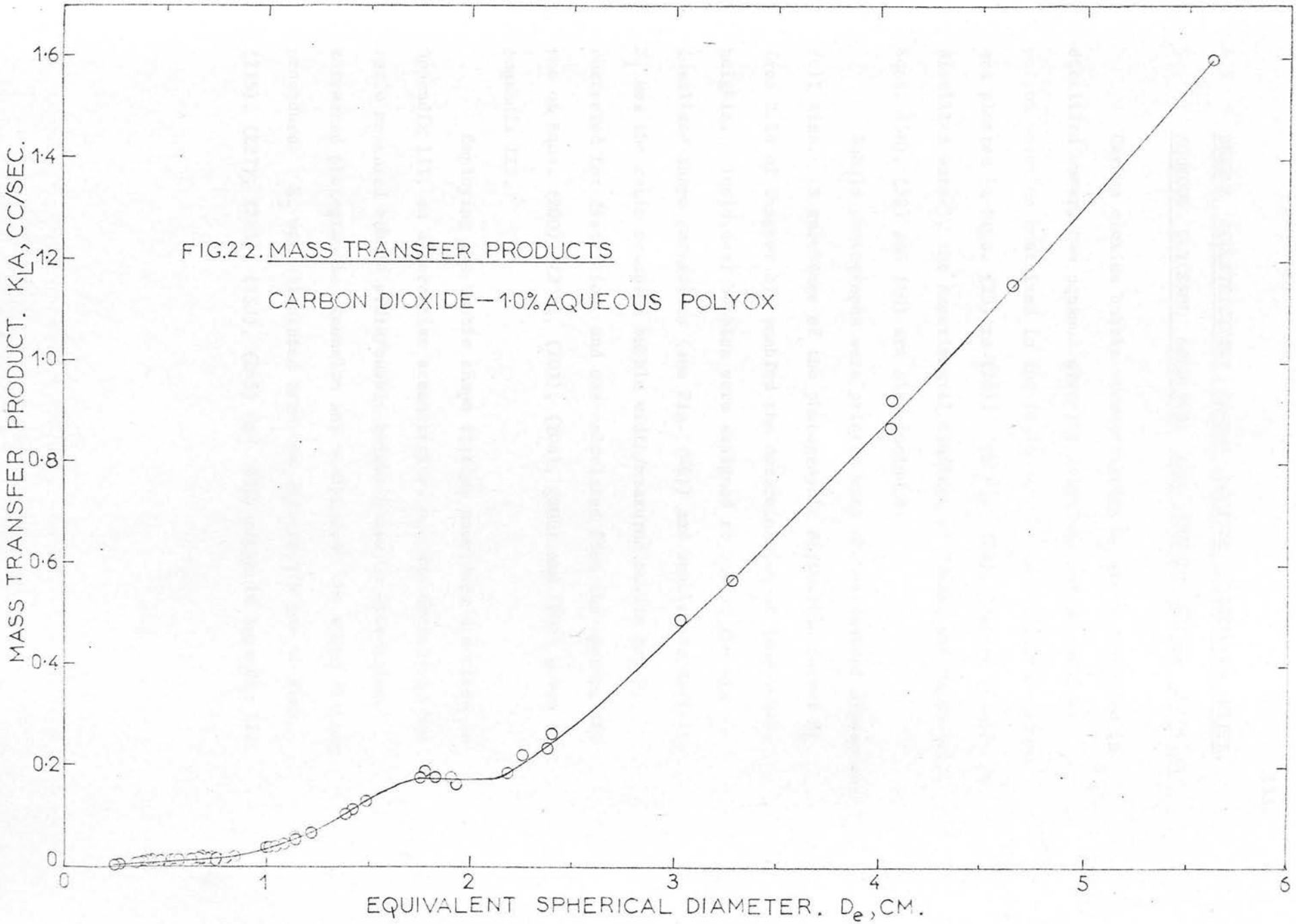
FIG.2 2. MASS TRANSFER PRODUCTS
CARBON DIOXIDE—1·0% AQUEOUS POLYOX
MASS TRANSFER PRODUCT. K_LA, CC/SEC.
EQUIVALENT SPHERICAL DIAMETER. D_e, CM.
0
0·2
0·4
0·6
0·8
1·0
1·2
1·4
1·6
1
2
3
4
5
6

4.3 BUBBLE ECCENTRICITIES. CARBON DIOXIDE - DISTILLED WATER, AQUEOUS GLYCEROL SOLUTIONS AND AQUEOUS POLYOX SOLUTION

Carbon dioxide bubble eccentricities E_1 and E_2 observed in distilled water, two aqueous glycerol solutions and one aqueous polyox solution contained in the 10.16 cm I.D. mass transfer column are plotted in Figs. (23) to (26). In Fig. (23), (carbon dioxide in distilled water), the experimental findings of Tadaki and Maeda (T1), Eqns. (58), (59) and (60) are also included.

Bubble photographs were printed with the horizontal dimensions full size. A knowledge of the photographic distortion factor M_R, (see 2.24 of Chapter 2), enabled the determination of true bubble heights. Individual bubbles were assigned to one of the six idealised shape categories (see Fig. (46)) and bubble eccentricity E_1 was the ratio measured bubble width/measured bubble height corrected for distortion, and was calculated from the appropriate one of Eqns. (200), (201), (203), (204), (206) and (208) given in Appendix III.

Employing the bubble shape fitting procedure described in Appendix III, an alternative eccentricity, E_2, was defined by the ratio measured bubble width/bubble height based on distortion - corrected photographic dimension and modified by the shape fitting procedure. E_2 was calculated from the appropriate one of Eqns. (215), (227), (245), (253), (265) and (281) given in Appendix III.

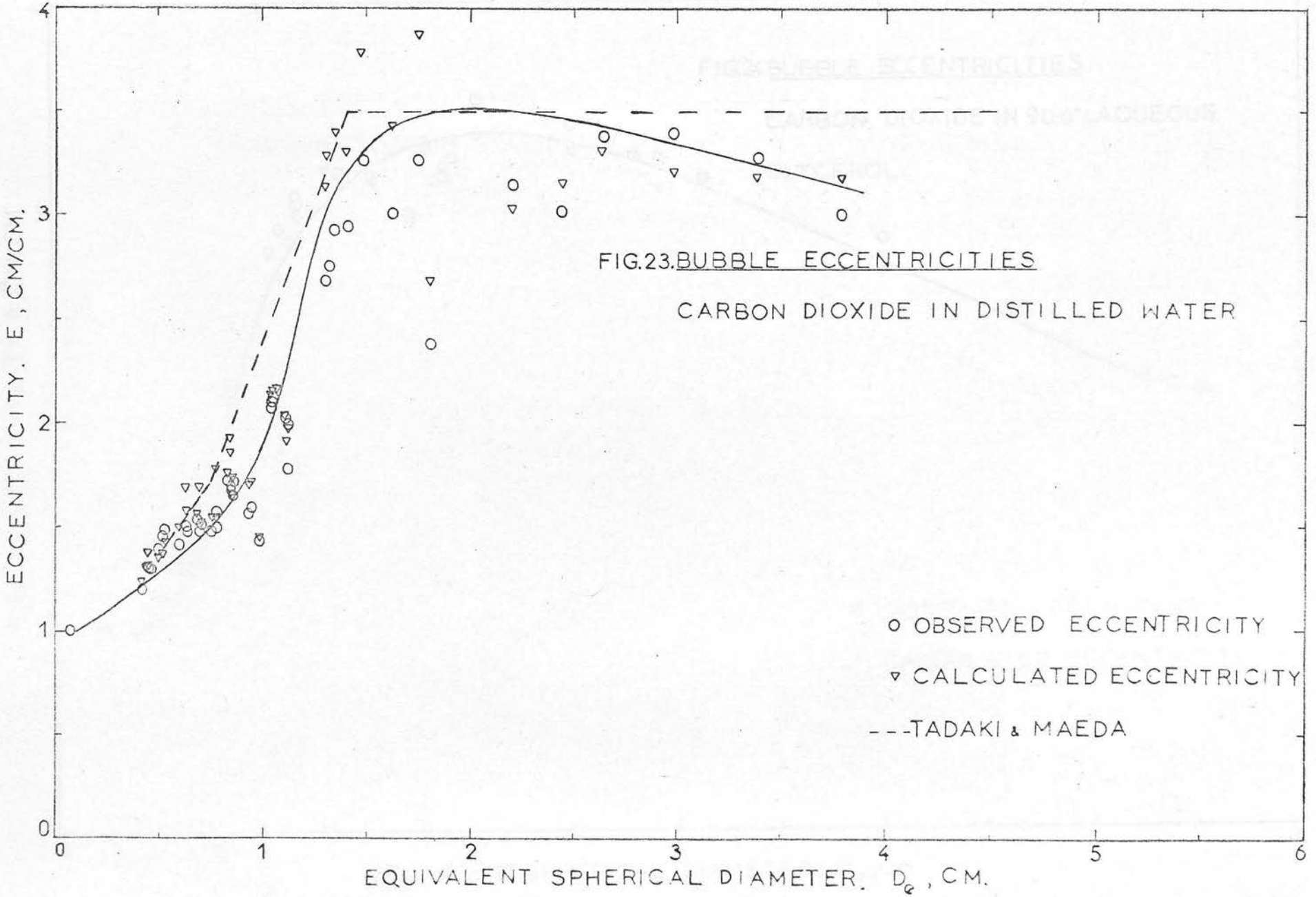

FIG.23. BUBBLE ECCENTRICITIES

CARBON DIOXIDE IN DISTILLED WATER

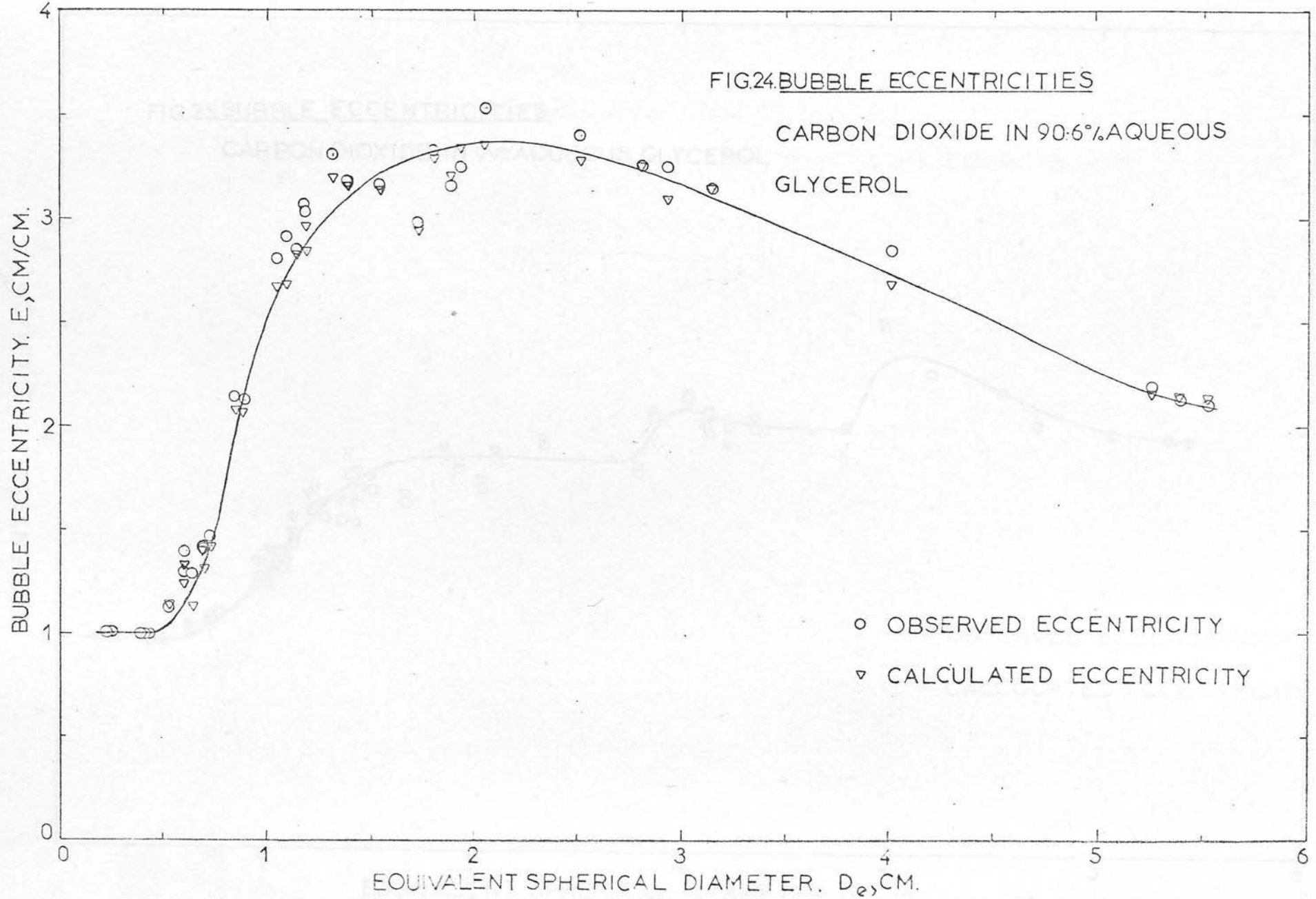
FIG.24. BUBBLE ECCENTRICITIES
CARBON DIOXIDE IN 90·6% AQUEOUS GLYCEROL
BUBBLE ECCENTRICITY, E, CM/CM.
EQUIVALENT SPHERICAL DIAMETER, D_e, CM.
OBSERVED ECCENTRICITY
CALCULATED ECCENTRICITY
0
1
2
3
4
5
6

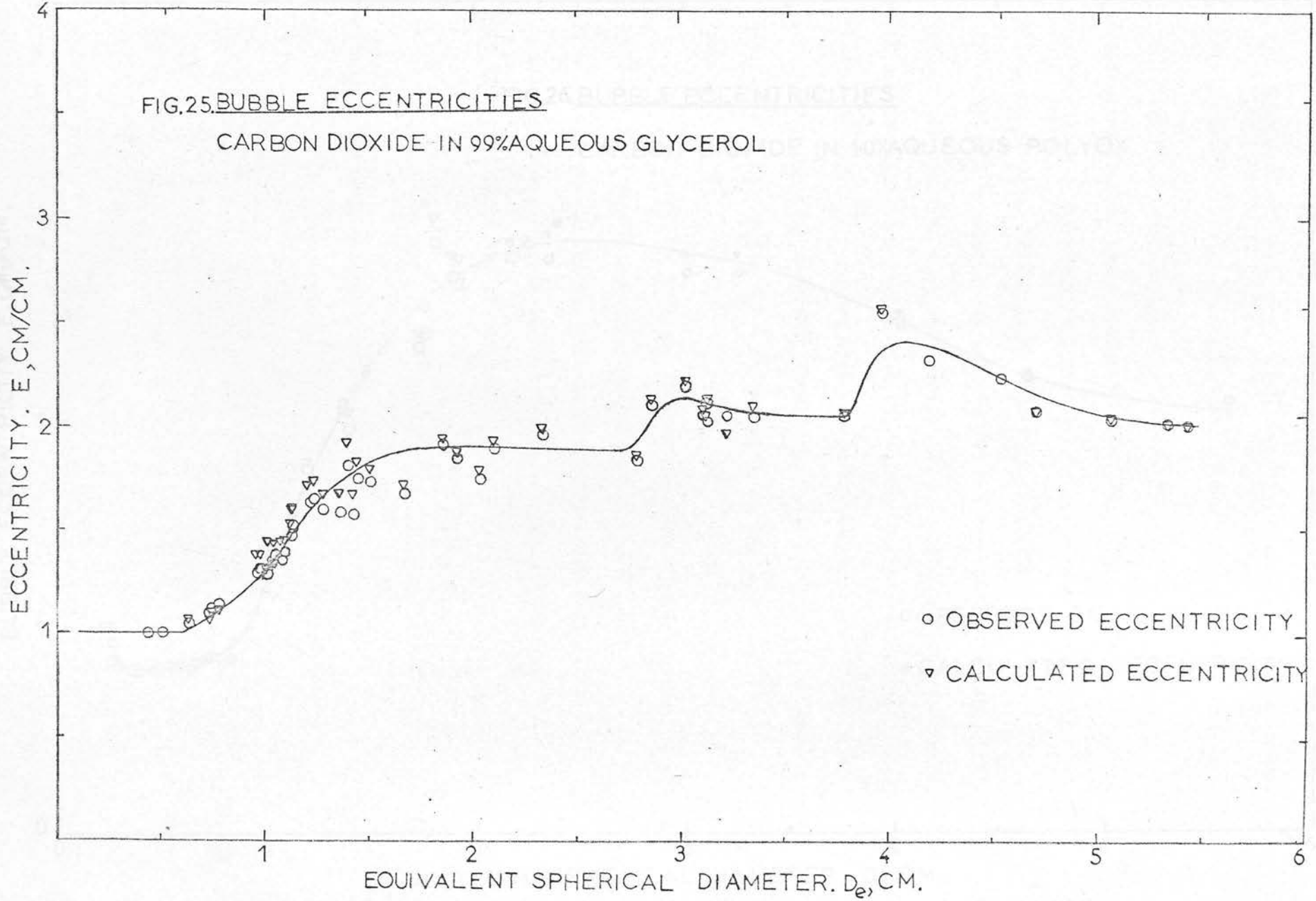
FIG. 25. BUBBLE ECCENTRICITIES
CARBON DIOXIDE IN 99% AQUEOUS GLYCEROL
ECCENTRICITY, E, CM/CM.
EQUIVALENT SPHERICAL DIAMETER, D_e, CM.
1
2
3
4
5
6
OBSERVED ECCENTRICITY
CALCULATED ECCENTRICITY

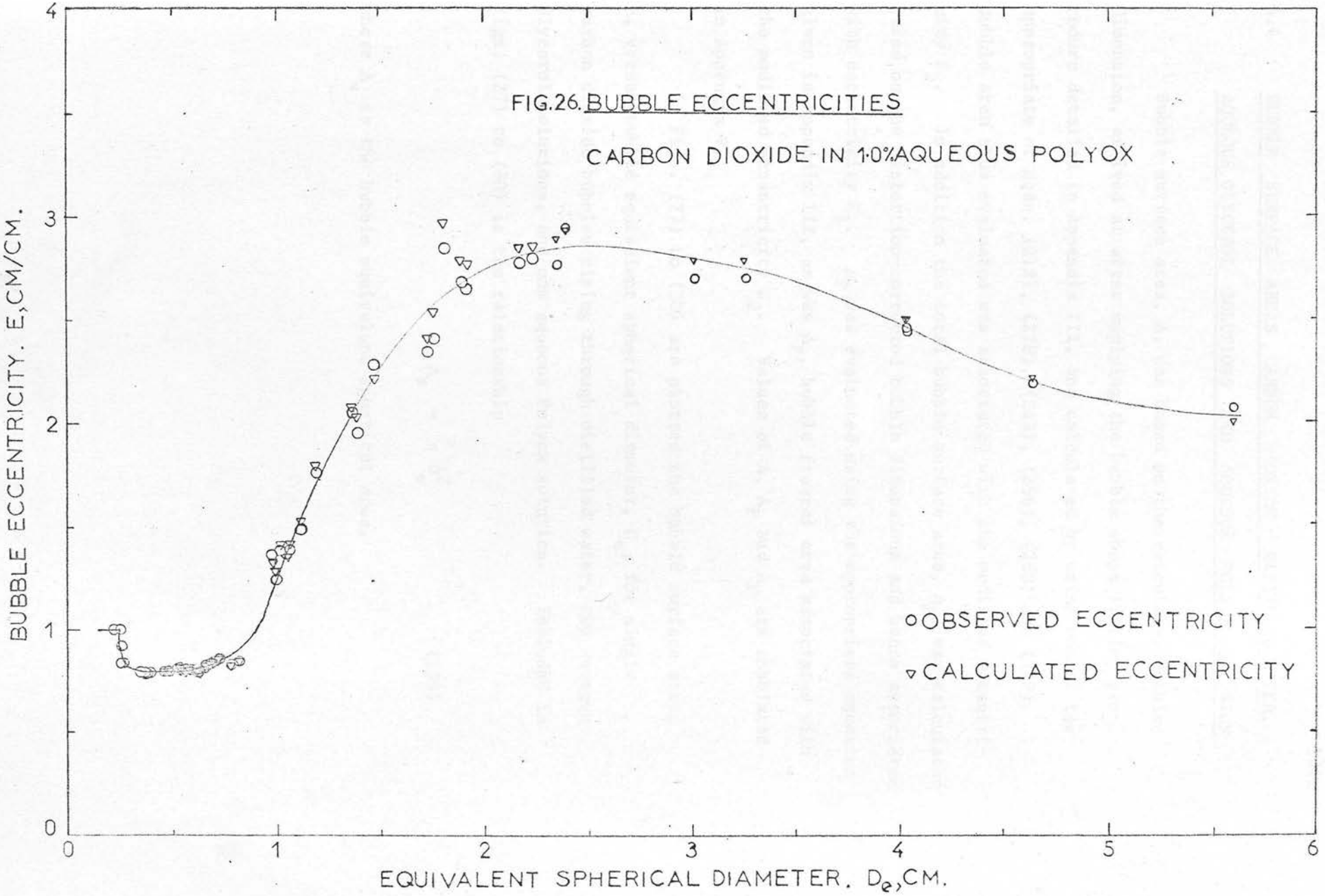
FIG.26. BUBBLE ECCENTRICITIES
CARBON DIOXIDE IN 1·0% AQUEOUS POLYOX
BUBBLE ECCENTRICITY. E, CM/CM.
EQUIVALENT SPHERICAL DIAMETER. D_e, CM.
0
1
2
3
4
5
6
OBSERVED ECCENTRICITY
CALCULATED ECCENTRICITY

4.4 BUBBLE SURFACE AREAS . CARBON DIOXIDE - DISTILLED WATER, AQUEOUS GLYCEROL SOLUTIONS AND AQUEOUS POLYOX SOLUTION

Bubble surface area, A, was based on the calculated bubble dimension, arrived at after applying the bubble shape fitting procedure detailed in Appendix III, and calculated by using one of the appropriate of Eqns. (212), (228), (243), (256), (268) and (282). Bubble area thus evaluated was associated with the modified eccentricity E_2. In addition the total bubble surface area, A_P, was calculated based on the distortion-corrected bubble dimensions and hence associated with eccentricity E_1. A_P was evaluated using the appropriate equation given in Appendix III, as was A_F, bubble frontal area associated with the modified eccentricity E_2. Values of A, A_P and A_F are tabulated in Appendix V.

In Figs. (27) to (30) are plotted the bubble surface area, A, versus bubble equivalent spherical diameter, D_e, for single carbon dioxide bubbles rising through distilled water, two aqueous Glycerol solutions, and one aqueous Polyox solution. Included in Figs. (27) to (30) is the relationship

$$A_s = \pi D_e^2 \qquad (139)$$

where A_s is the bubble equivalent spherical area.

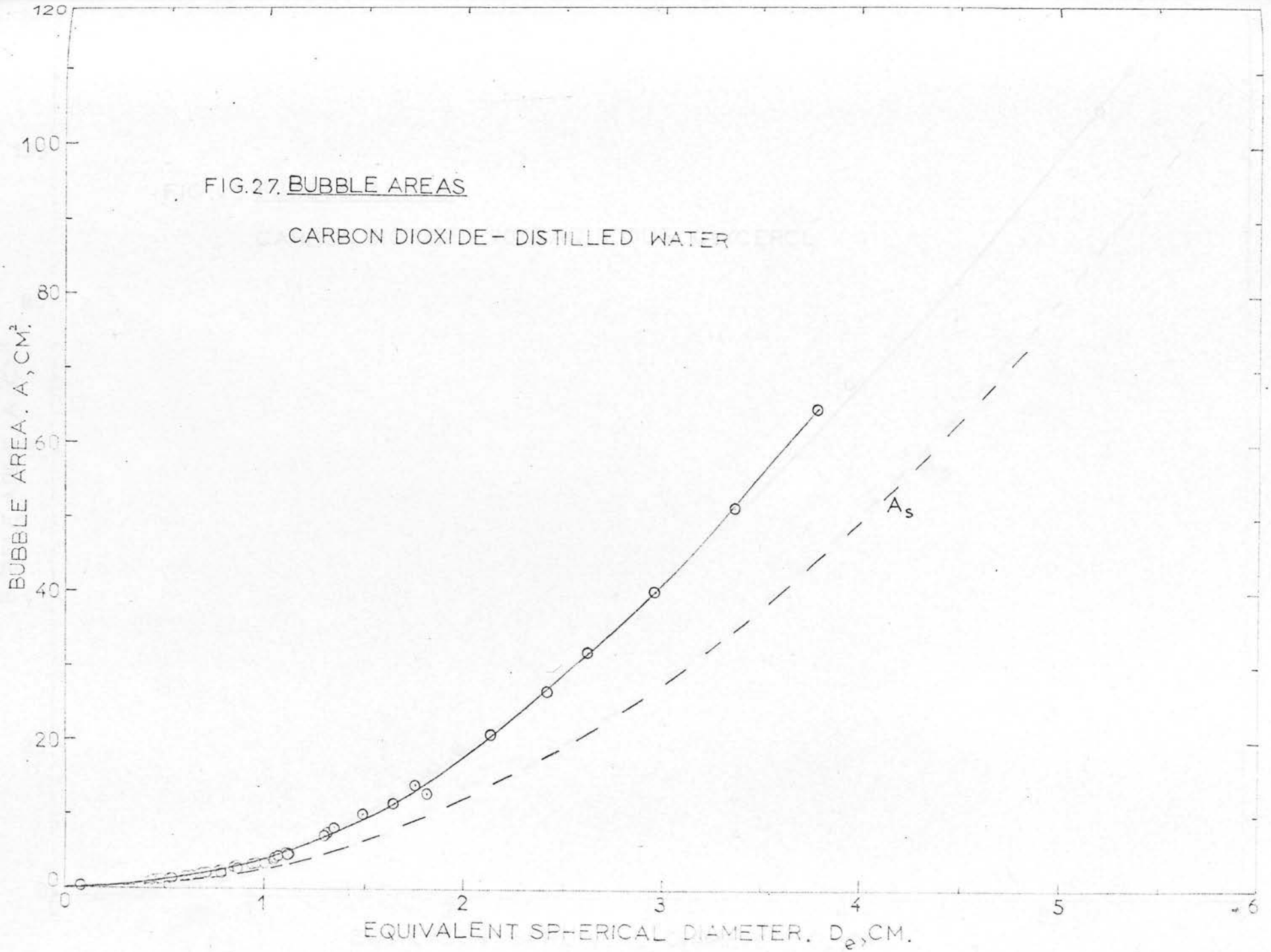
FIG. 27. BUBBLE AREAS
CARBON DIOXIDE – DISTILLED WATER
BUBBLE AREA, A, CM.²
EQUIVALENT SPHERICAL DIAMETER, D_e, CM.
A_s
0
20
40
60
80
100
120
1
2
3
4
5
6

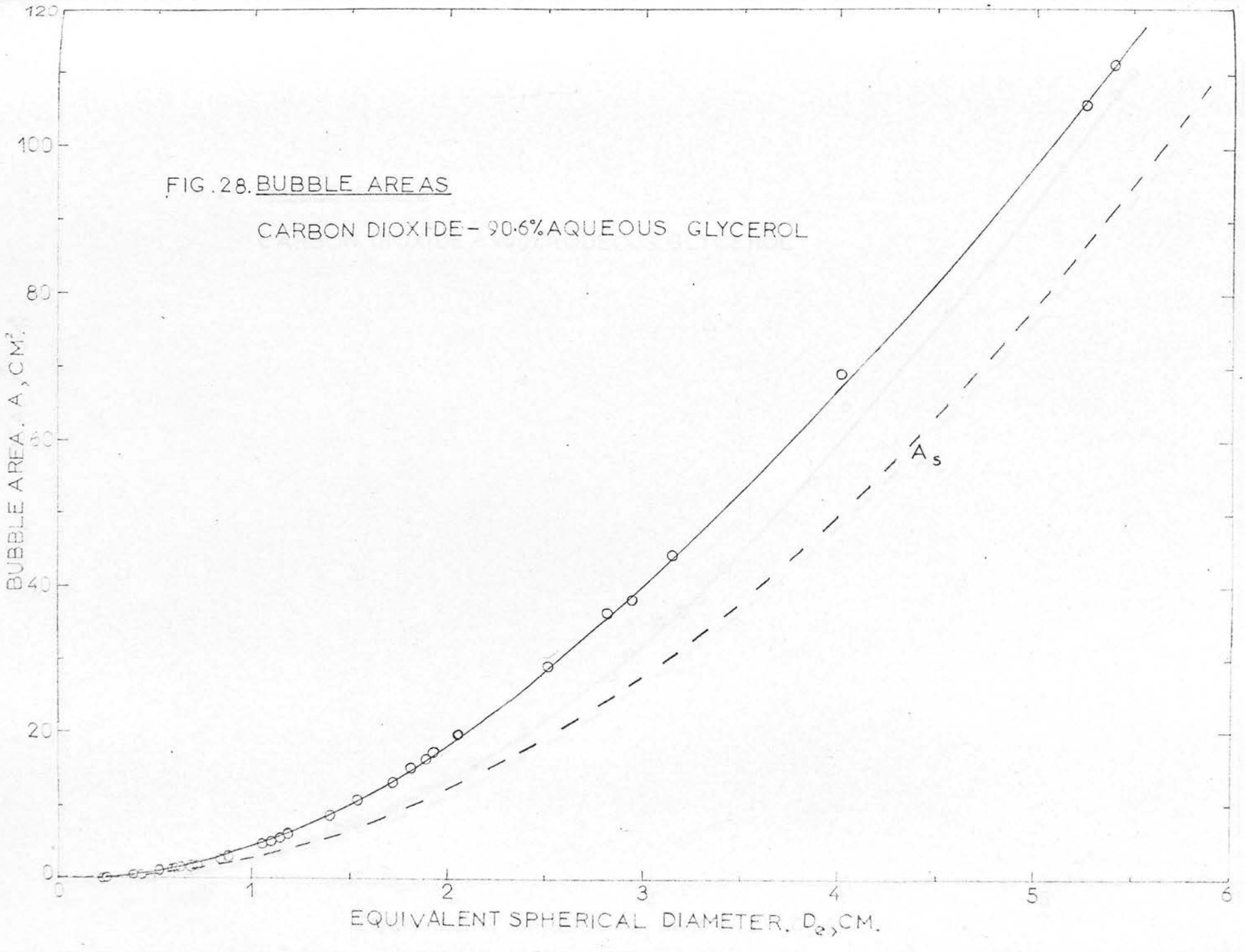
FIG. 28. BUBBLE AREAS
CARBON DIOXIDE – 90·6% AQUEOUS GLYCEROL
BUBBLE AREA, A, CM.²
EQUIVALENT SPHERICAL DIAMETER, D_e, CM.
A_s
0
20
40
60
80
100
120
1
2
3
4
5
6

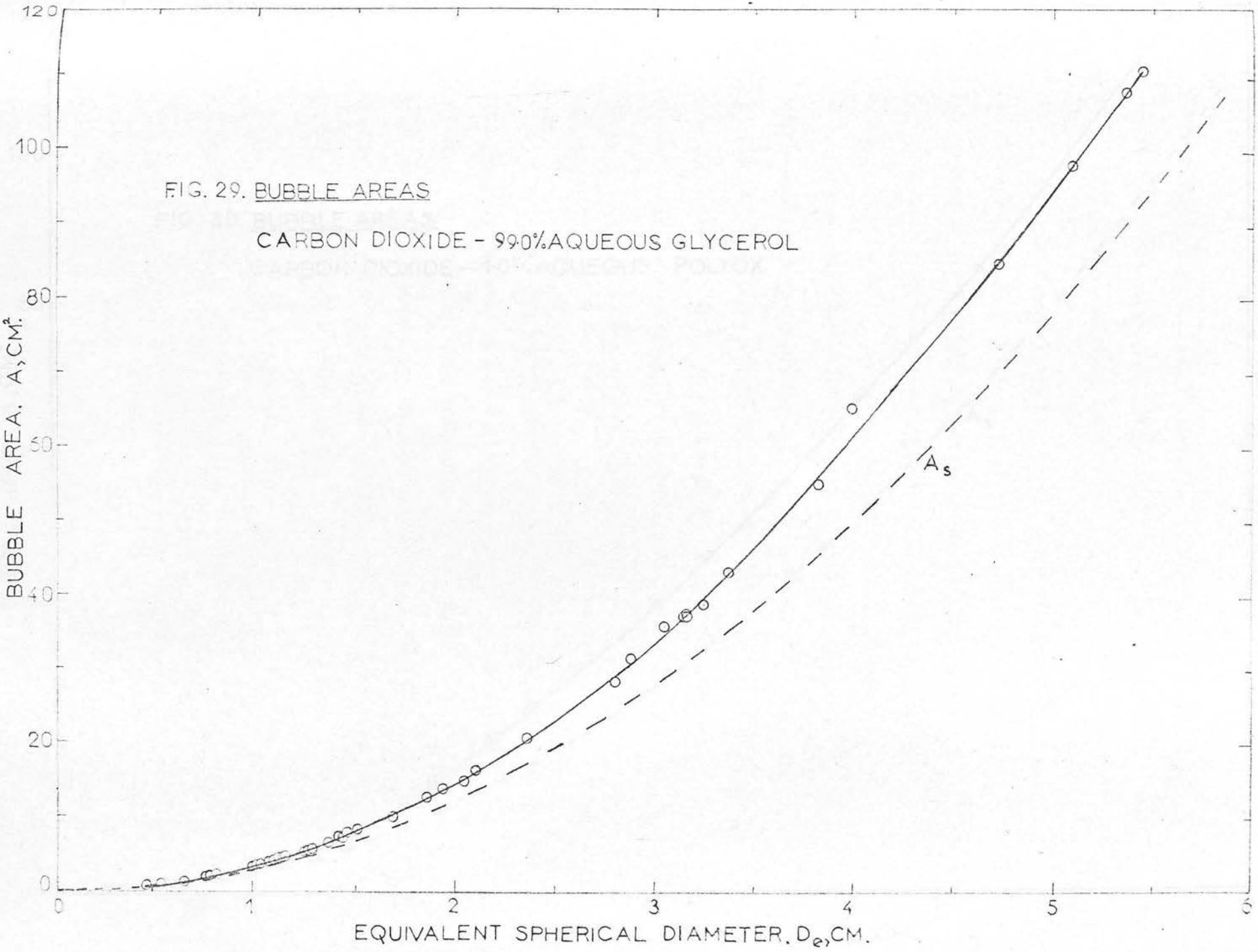

FIG. 29. BUBBLE AREAS

CARBON DIOXIDE - 99.0% AQUEOUS GLYCEROL

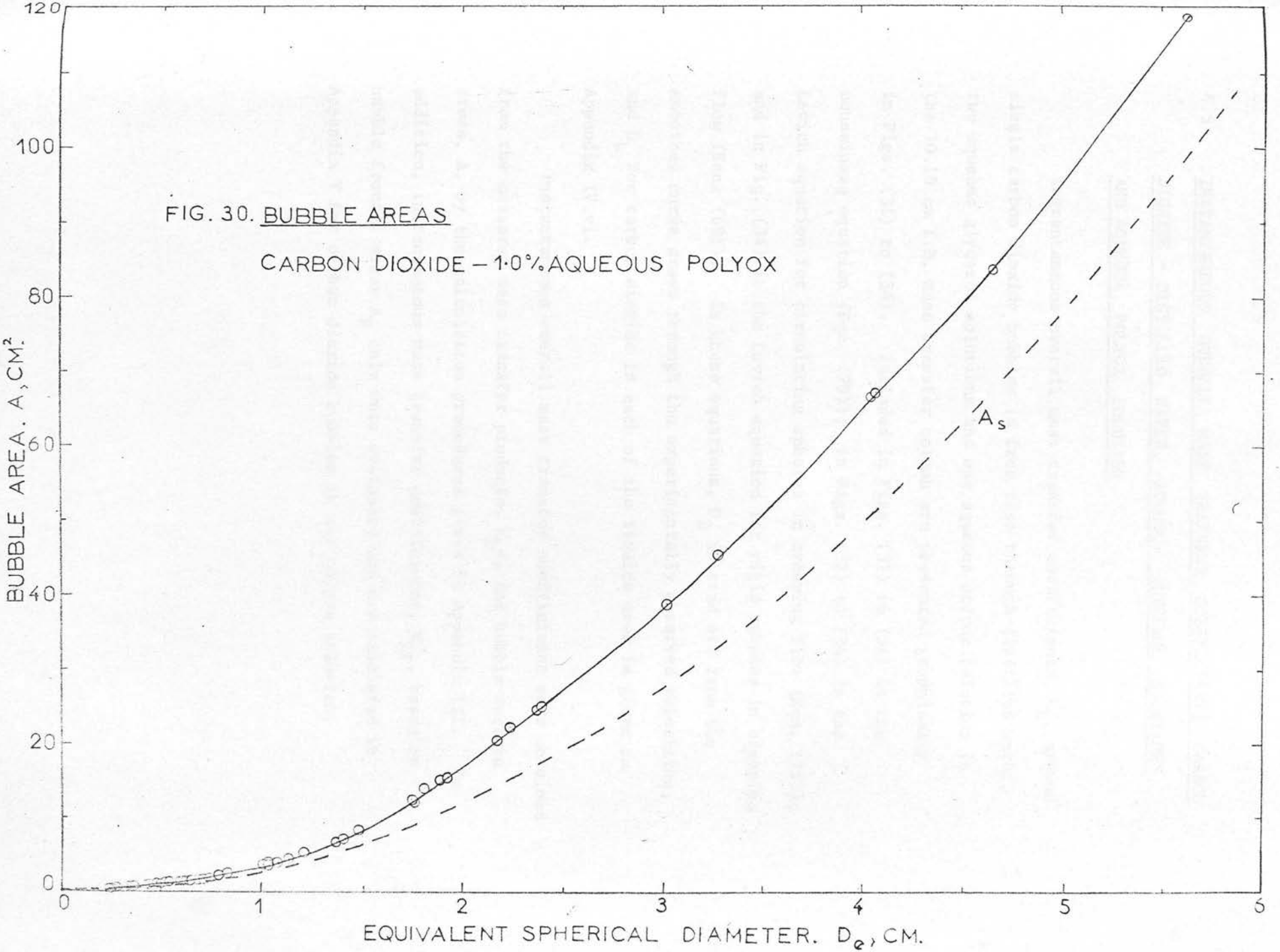

FIG. 30. BUBBLE AREAS

CARBON DIOXIDE – 1·0% AQUEOUS POLYOX

4.5 INSTANTANEOUS OVERALL MASS TRANSFER COEFFICIENTS. CARBON DIOXIDE - DISTILLED WATER, AQUEOUS GLYCEROL SOLUTIONS AND AQUEOUS POLYOX SOLUTION

Instantaneous overall mass transfer coefficients, K_L, around single carbon dioxide bubbles in free rise through distilled water, two aqueous glycerol solutions and one aqueous polyox solution in the 10.16 cm I.D. mass transfer column are presented graphically in Figs. (31) to (34). Included in Figs. (31) to (34) is the Boussinesq equation (Eqn. (79)); in Figs. (32) to (34) is the Levich equation for circulating spheres in creeping flow (Eqn. (75)); and in Fig. (34) is the Levich equation for rigid spheres in creeping flow (Eqn. (69)). In these equations, U_B is read off from the smoothed curve drawn through the experimentally observed velocities, and D_L for carbon dioxide in each of the liquids used is given in Appendix IV.vi.

Instantaneous overall mass transfer coefficients were obtained from the measured mass transfer products, $K_L A$, and bubble surface areas, A, by the calculation procedures given in Appendix III. In addition, instantaneous mass transfer coefficients, K_{LF}, based on bubble frontal areas A_F only were evaluated and are tabulated in Appendix V for carbon dioxide bubbles in the polyox solution.

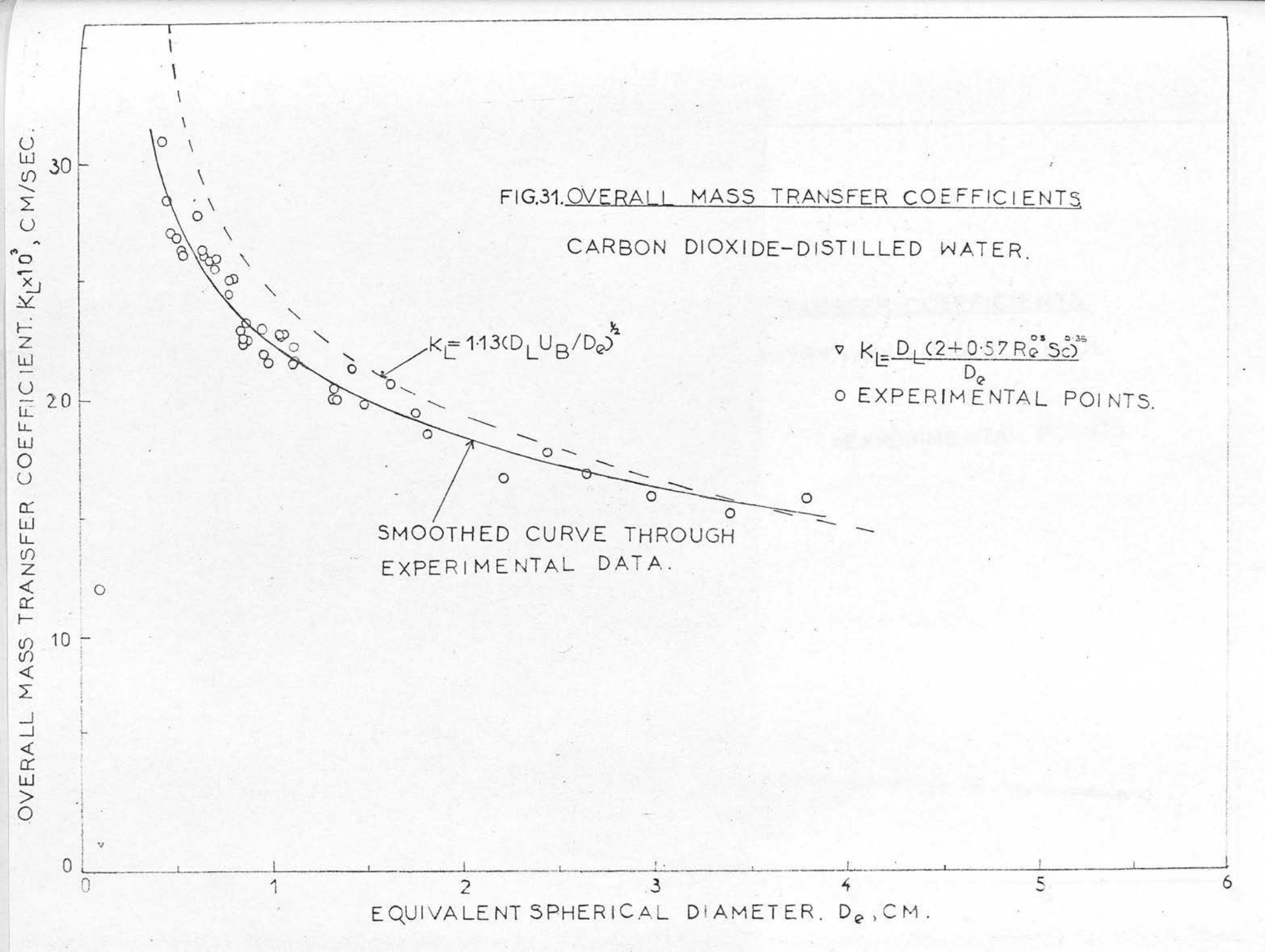
FIG.31. OVERALL MASS TRANSFER COEFFICIENTS
CARBON DIOXIDE-DISTILLED WATER.
$K_L = 1.13(D_L U_B / D_e)^{1/2}$
$K_L = \frac{D_L (2 + 0.57 R_e^{0.5} Sc^{0.35})}{D_e}$
EXPERIMENTAL POINTS.
SMOOTHED CURVE THROUGH EXPERIMENTAL DATA.
OVERALL MASS TRANSFER COEFFICIENT. $K_L \times 10^3$, CM/SEC.
EQUIVALENT SPHERICAL DIAMETER. D_e, CM.
0
10
20
30
0
1
2
3
4
5
6

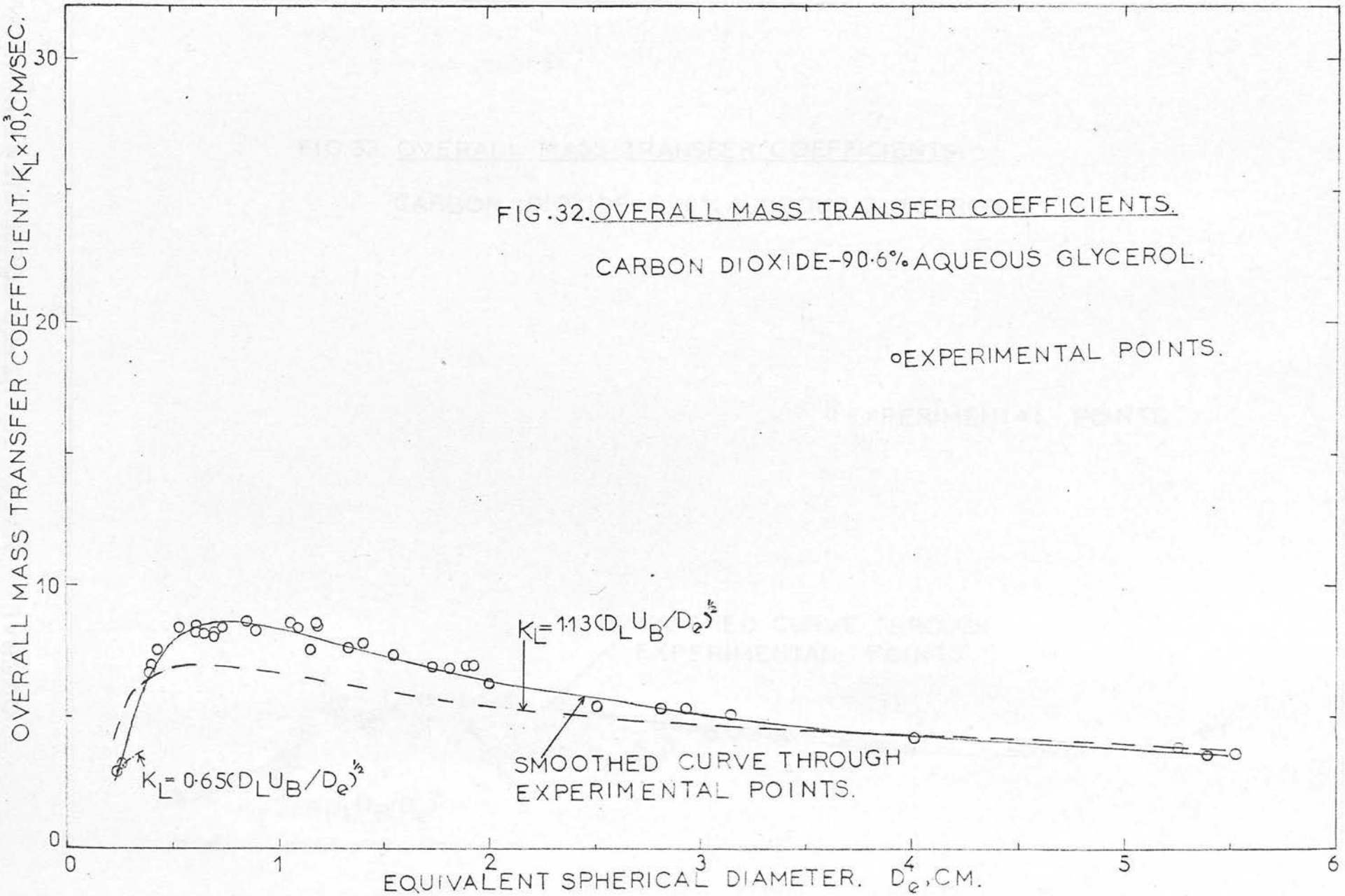
FIG. 32. OVERALL MASS TRANSFER COEFFICIENTS.
CARBON DIOXIDE-90·6% AQUEOUS GLYCEROL.
o EXPERIMENTAL POINTS.
OVERALL MASS TRANSFER COEFFICIENT. $K_L \times 10^3$, CM/SEC.
EQUIVALENT SPHERICAL DIAMETER. D_e, CM.
$K_L = 1.13 (D_L U_B / D_e)^{1/2}$
$K_L = 0.65 (D_L U_B / D_e)^{1/2}$
SMOOTHED CURVE THROUGH EXPERIMENTAL POINTS.
0
10
20
30
0
1
2
3
4
5
6

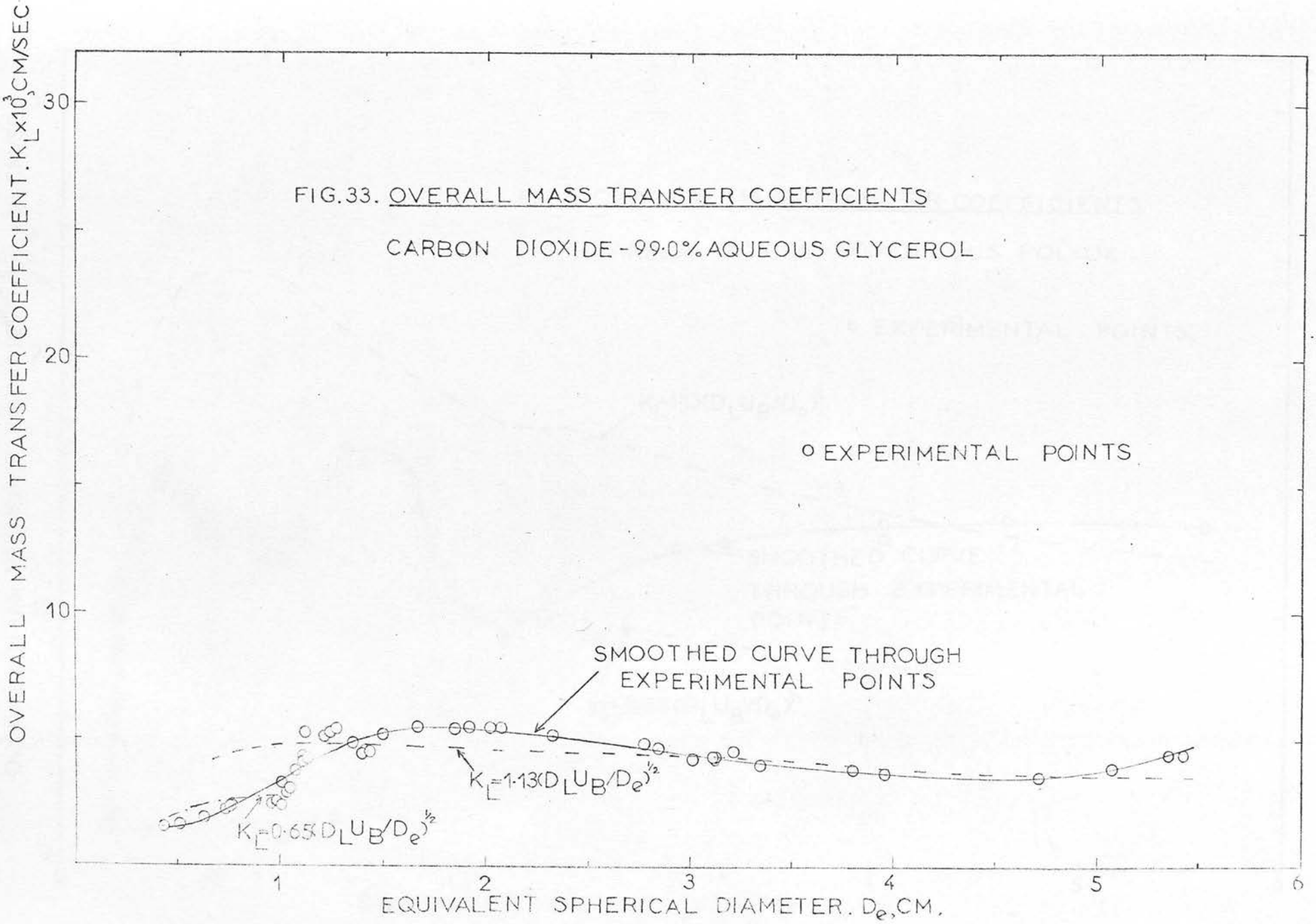
FIG. 33. OVERALL MASS TRANSFER COEFFICIENTS
CARBON DIOXIDE - 99·0% AQUEOUS GLYCEROL
OVERALL MASS TRANSFER COEFFICIENT. $K_L \times 10^3$, CM/SEC
30
20
10
o EXPERIMENTAL POINTS
SMOOTHED CURVE THROUGH EXPERIMENTAL POINTS
$K_L = 1{\cdot}13 (D_L U_B / D_e)^{1/2}$
$K_L = 0{\cdot}65 (D_L U_B / D_e)^{1/2}$
1
2
3
4
5
6
EQUIVALENT SPHERICAL DIAMETER. D_e, CM.

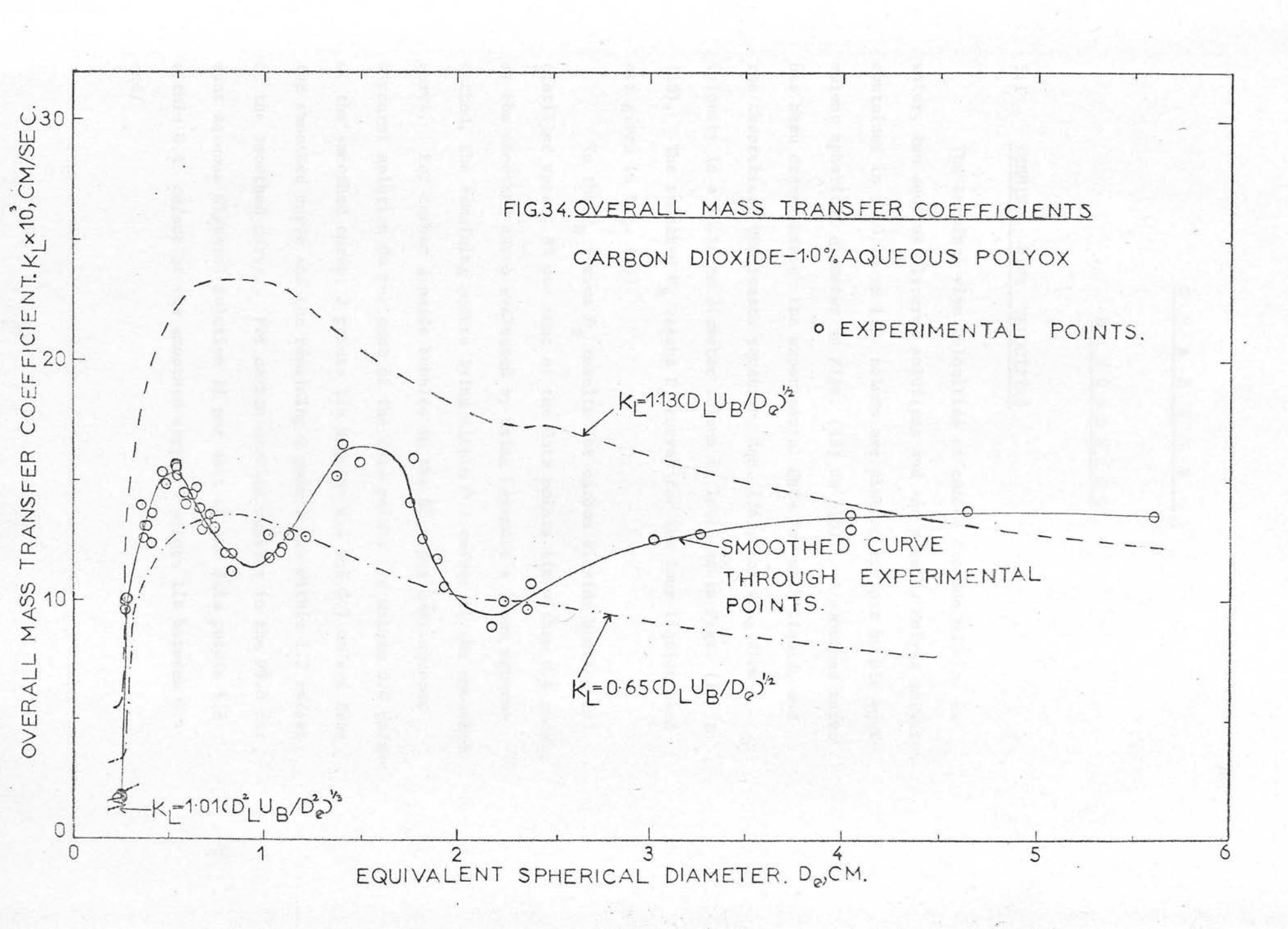
FIG.34. OVERALL MASS TRANSFER COEFFICIENTS
CARBON DIOXIDE-1·0% AQUEOUS POLYOX
o EXPERIMENTAL POINTS.
$K_L = 1.13 (D_L U_B / D_e)^{1/2}$
SMOOTHED CURVE THROUGH EXPERIMENTAL POINTS.
$K_L = 0.65 (D_L U_B / D_e)^{1/2}$
$K_L = 1.01 (D_L^2 U_B / D_e^2)^{1/3}$
OVERALL MASS TRANSFER COEFFICIENT, $K_L \times 10^3$, CM/SEC.
EQUIVALENT SPHERICAL DIAMETER, D_e, CM.
0
10
20
30
0
1
2
3
4
5
6

C H A P T E R 5

D I S C U S S I O N

5.1 TERMINAL RISE VELOCITIES

The terminal rise velocities of carbon dioxide bubbles in water, two aqueous Glycerol solutions and one aqueous Polyox solution contained in a 10.16 cm I.D. column are plotted against bubble equivalent spherical diameter in Figs. (15) to (18). A smoothed curve has been drawn through the experimental data for each liquid, and the theoretical Dumitrescu equation, Eqn. (36), for slug flow velocity in a 10.16 cm diameter column is included in Figs. (15) to (18). The smoothed U_B versus D_e curves for the four liquids used are given in Fig. (35).

In the U_B versus D_e results for carbon dioxide bubbles in distilled water, 88 per cent of the data points lie within 0.4 cm/sec of the smoothed curve evaluated by using Legendre's least squares method, the remaining points lying within 0.7 cm/sec of the smoothed curve. For carbon dioxide bubbles in the 90.6 per cent aqueous Glycerol solution 86 per cent of the data points lie within 0.4 cm/sec of the smoothed curve, 3 points lie between 0.4 and 0.7 cm/sec from the smoothed curve and the remaining 2 points lie within 1.2 cm/sec of the smoothed curve. For carbon dioxide bubbles in the 99.0 per cent aqueous Glycerol solution 71 per cent of the data points lie within 0.4 cm/sec of the smoothed curve, 9 points lie between 0.4 and/

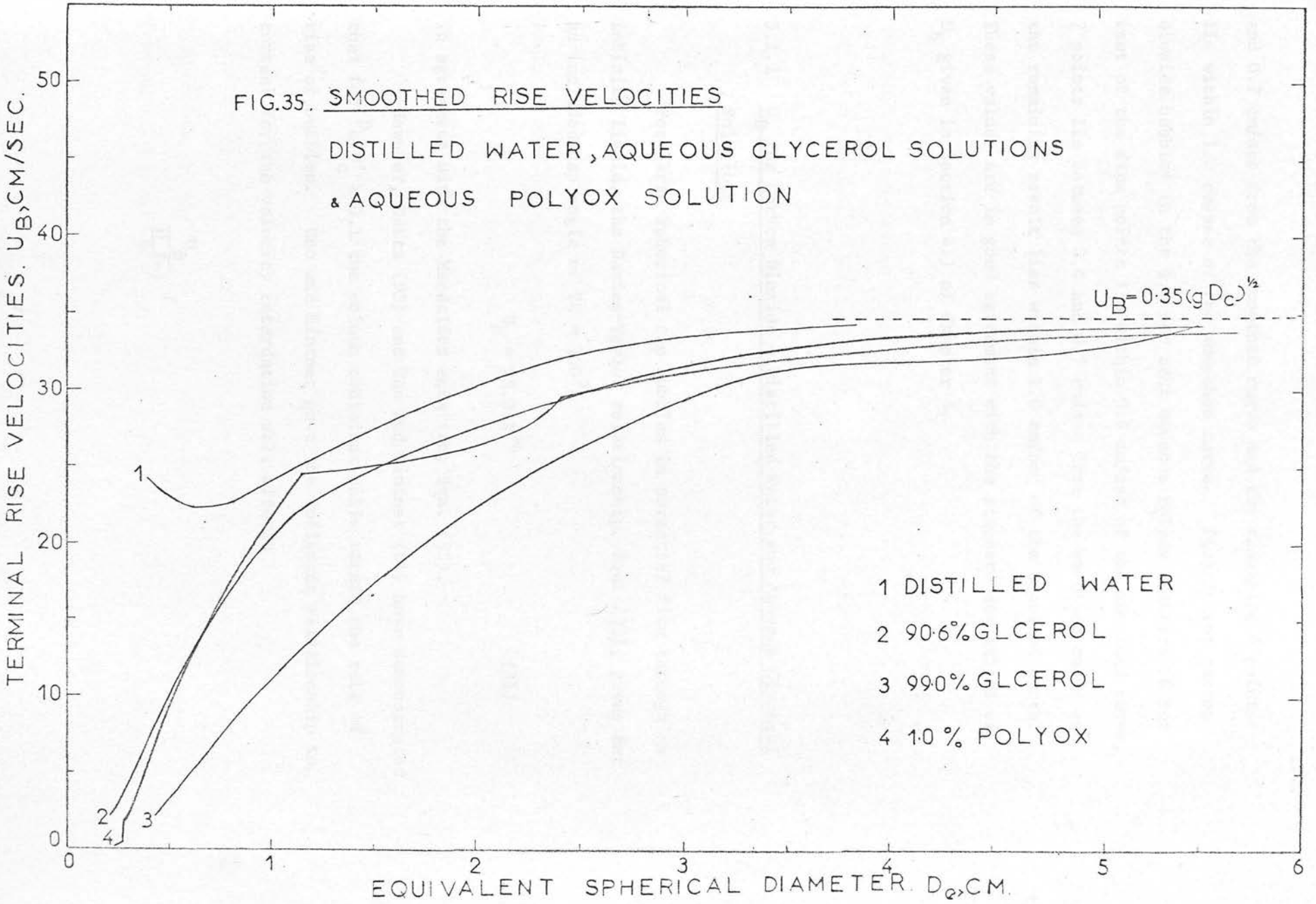
FIG.35. SMOOTHED RISE VELOCITIES
DISTILLED WATER, AQUEOUS GLYCEROL SOLUTIONS
& AQUEOUS POLYOX SOLUTION
TERMINAL RISE VELOCITIES. U_B, CM/SEC.
EQUIVALENT SPHERICAL DIAMETER. D_e, CM.
$U_B = 0.35 (g D_e)^{1/2}$
1 DISTILLED WATER
2 90·6% GLCEROL
3 99·0% GLCEROL
4 1·0 % POLYOX
0
10
20
30
40
50
0
1
2
3
4
5
6

and 0.7 cm/sec from the smoothed curve and the remaining 4 points lie within 1.0 cm/sec of the smoothed curve. Finally for carbon dioxide bubbles in the 1.0 per cent aqueous Polyox solution 86 per cent of the data points lie within 0.4 cm/sec of the smoothed curve, 7 points lie between 0.4 and 0.7 cm/sec from the smoothed curve and the remaining result lies within 1.0 cm/sec of the smoothed curve. These values are in good agreement with the standard deviations of U_B given in Section 4.1 of Chapter 4.

5.1.1 U_B for Carbon Dioxide - Distilled Water and Aqueous Glycerol Solutions

For large spherical cap bubbles in potential flow through an infinite liquid, the Davies-Taylor relationship, Eqn. (31), gives for an included cap angle of $2\Theta = 100^{\circ}$,

$$U_B = 25.0\ V^{1/6} \qquad (31)$$

in agreement with the Mendelson equation, Eqn. (35).

However, Datta (D3) and Uno and Kintner (U1) have demonstrated that for $D_e/D_c \geq 0.1$ the column container walls retard the rate of rise of bubbles. Uno and Kintner gave the following relationship to correct for the velocity retardation wall effects,

$$\frac{U_B}{U_{B(\infty)}} \ /$$

$$\frac{U_B}{U_B(\infty)} = \left(\frac{1}{b''} \left(1 - \frac{D_e}{D_c}\right)\right)^{0.765} \qquad (38)$$

b" appearing in Eqn. (38) was given in Ref. (U1) as a function of liquid surface tension and column diameter, and takes the value of 0.882 for distilled water and 0.892 for the two aqueous Glycerol solutions.

In Figs. (15) to (17), the measured terminal rise velocity data corrected for column wall effects by means of Eqn. (38) are included for comparison with the theoretical Mendelson or Davies-Taylor relationships given by Eqns. (34) and (31) respectively. From Figs. (15) to (17) it can be seen that column wall effects become significant at a value of D_e/D_c of 0.11 in distilled water (Fig. (15)), of 0.12 in the 90.6 per cent aqueous Glycerol solution (Fig. (16)), and of 0.11 in the 99.0 per cent aqueous Glycerol solution (Fig. (17)). These values are in good agreement with the value of D_e/D_c of 0.10, below which wall effects are negligible, indicated by Datta (D3) and by Uno and Kintner (U1).

It can be seen from Figs. (15) to (17) that at a sufficiently large bubble diameter, the velocity data corrected for wall effect rises above the Davies-Taylor equation predictions, and as bubble size is further increased, the amount by which the Davies-Taylor equation underpredicts the values of $U_B(\infty)$ become progressively larger. Thus the bubble equivalent spherical diameter at which $U_B(\infty)$ rises significantly above the theoretical Davies-Taylor value, (i.e. > 2 per cent above), in the 10.16 cm I.D. column used is 3.75 cm for water, 4.25 cm for the 90.6 per cent aqueous Glycerol solution, and 5.1 cm for the/

the 99.0 per cent aqueous Glycerol solution. These D_e values for distilled water and the 90.6 per cent aqueous Glycerol solution are in fairly good agreement with the findings of Davidson and Harrison (D10) who summarised the work of Uno and Kintner (U1) and showed that comparison of the experimental data with the ratio of limiting slug flow velocity, (Eqn. (36)), to the Davies-Taylor rise velocity, (Eqn. (31)), indicated the onset of slug flow at $D_e/D_c > 0.33$ approximately.

Figs. (15) to (17) and Fig. (35) show that at sufficiently large bubble diameters, the measured bubble rise velocity data, which approaches asymptotically the Dumitrescu equation, Eqn. (36), for the rise velocity of a gas slug of infinite length under potential flow conditions, lie within 5 per cent of the theoretical Dumitrescu predictions. The value of D_e at which the experimental curve approaches within 5 per cent of the Dumitrescu prediction is 2.65 cm in distilled water, Fig. (15); 3.5 cm (Re = 79) in the 90.6 per cent aqueous Glycerol solution, Fig. (16), and 5.1 cm (Re = 30) in the 99.0 per cent aqueous Glycerol solution, Fig. (17). It should be noted that Nicklin et al (N5) demonstrated experimentally that Eqn. (36) was applicable to a slug of finite length provided that viscosity effects were negligible.

From the foregoing discussion in this subsection, it can be seen that the approach to potential flow conditions occur at increasingly larger bubble equivalent spherical diameters and decreasing Re as Newtonian liquid viscosity is increased.

For/

For bubble sizes in the range 0.42 cm < D_e < 1.1 cm, in distilled water, (Figs. (15) and (35)), the terminal rise velocity data pass through a minimum, this minimum occurring at D_e = 0.51 cm which is in good agreement with the value of D_e = 0.505 cm predicted by the Mendelson equation, Eqn. (34). Mendelson (M7) divided the inviscid flow regime into two regions, the buoyancy dominated regime, D_e > 1.1 cm for distilled water, and the surface tension dominated regime, D_e less than 1.1 cm until viscous flow sets in. For distilled water the smoothed curve through the experimentally determined U_B data corrected for wall effect for D_e > 1.1 cm, always lies within 5 per cent of the theoretical Mendelson equation predictions over the bubble size range investigated, 0.42 cm < D_e < 3.79 cm. The measured values of U_B for D_e > 0.51 cm are in good agreement with the values obtained by Loudon (L19) for carbon dioxide bubbles in distilled water also contained in a 10.16 cm I.D. column. For 0.42 cm < D_e < 0.51 cm, the currently measured bubble rise velocities increase with decreasing bubble size and rise above the data of Loudon, which starts decreasing for D_e < 0.43 cm. Loudon's lower bubble rise velocity data for D_e < 0.51 cm is probably due to viscous flow setting in at a larger bubble size than in the present investigations. This may be explained in terms of a larger concentration of surface-active impurities in the bulk liquid used by Loudon, since as noted in Ref. (H1) this would result in an increase in bubble drag coefficient and a reduction in bubble rise velocity. As pointed out in Sections 2.1.2 (1) and 2.1.2 (2), two possible sources of liquid contamination in/

in Loudon's experimental work, (rust from the end plate of the column equal tee section, and petroleum jelly from stopcocks at the top and bottom of the mass transfer column), were eliminated in the present work. The present U_B data for carbon dioxide bubbles in distilled water in the size range (0.42 cm < D_e < 1.1 cm) is in good agreement with the U_B versus D_e data for nitrogen bubbles in distilled water obtained by Leonard and Houghton (L8 and L9) and the data of Haberman and Morton (H1) for air bubbles in distilled water. The value of U_B obtained for the 0.07 cm D_e bubble in distilled water is also in good agreement with the value experimentally obtained by Haberman and Morton (H1) for an air bubble at the same bubble size. For this bubble diameter, the spherical gas bubble behaves as if it were a solid sphere (M7, H1).

For small bubbles in the aqueous Glycerol solutions, (D_e < 0.4 cm (Re < 2) in the 90.6 per cent solution and D_e < 0.8 cm (Re < 1) in the 99.0 per cent solution), the experimental U_B versus D_e data are in agreement with Eqn. (19) which gives bubble velocities in the Hadamard/Rybczynsky regime, the regime for spherical circulating bubbles in creeping flow,

$$U_B = \frac{126}{\nu_o} V_B^{2/3} \qquad (19)$$

The predictions of Eqn. (19) are included in Figs. (16) and (17). In agreement with the findings of Haberman and Morton (H1) for liquids of high M ($M > 10^{-3}$), the velocity data for the 90.6 per cent and the 99.0 per cent aqueous Glycerol solutions increase steadily with increasing/

increasing bubble size. The rate of increase of U_B falls off at a fairly well-defined value of D_e (1.2 cm) for the 90.6 per cent Glycerol solution. No maxima or minima are encountered in the U_B versus D_e curves of the two Glycerol solutions, though the curve through the measured data for the 99.0 per cent aqueous Glycerol solution passes through a point of inflection at D_e = 3.5 cm, and more rapidly approaches the Dumitrescu equation predictions thereafter (see Figs. (17) and (35)). The point of inflection corresponds approximately to the point at which bubble skirting commences in the 99.0 per cent aqueous Glycerol solution.

5.1.2 U_B for Carbon Dioxide - Aqueous Polyox Solution

The terminal rise velocity data for carbon dioxide bubbles in the 1.0 per cent aqueous Polyox solution was found to be lower than that of distilled water, and to agree most closely with the data for the 90.6 per cent aqueous Glycerol solution of the three Newtonian liquids studied in this work (see Fig. (35)).

Fig. (36) is a log-log plot of bubble terminal rise velocity versus bubble volume for $D_e \leqslant 0.58$ cm ($V_B \leqslant 0.105$ cm^3). The data shows clearly that a critical bubble volume, 0.0105 cm^3 (D_e = 0.27 cm), exists at which there is an abrupt increase in velocity. This fact is also indicated in Figs. (18) and (35). At this critical bubble volume, the bubble velocity in the Polyox solution increases by a factor of/

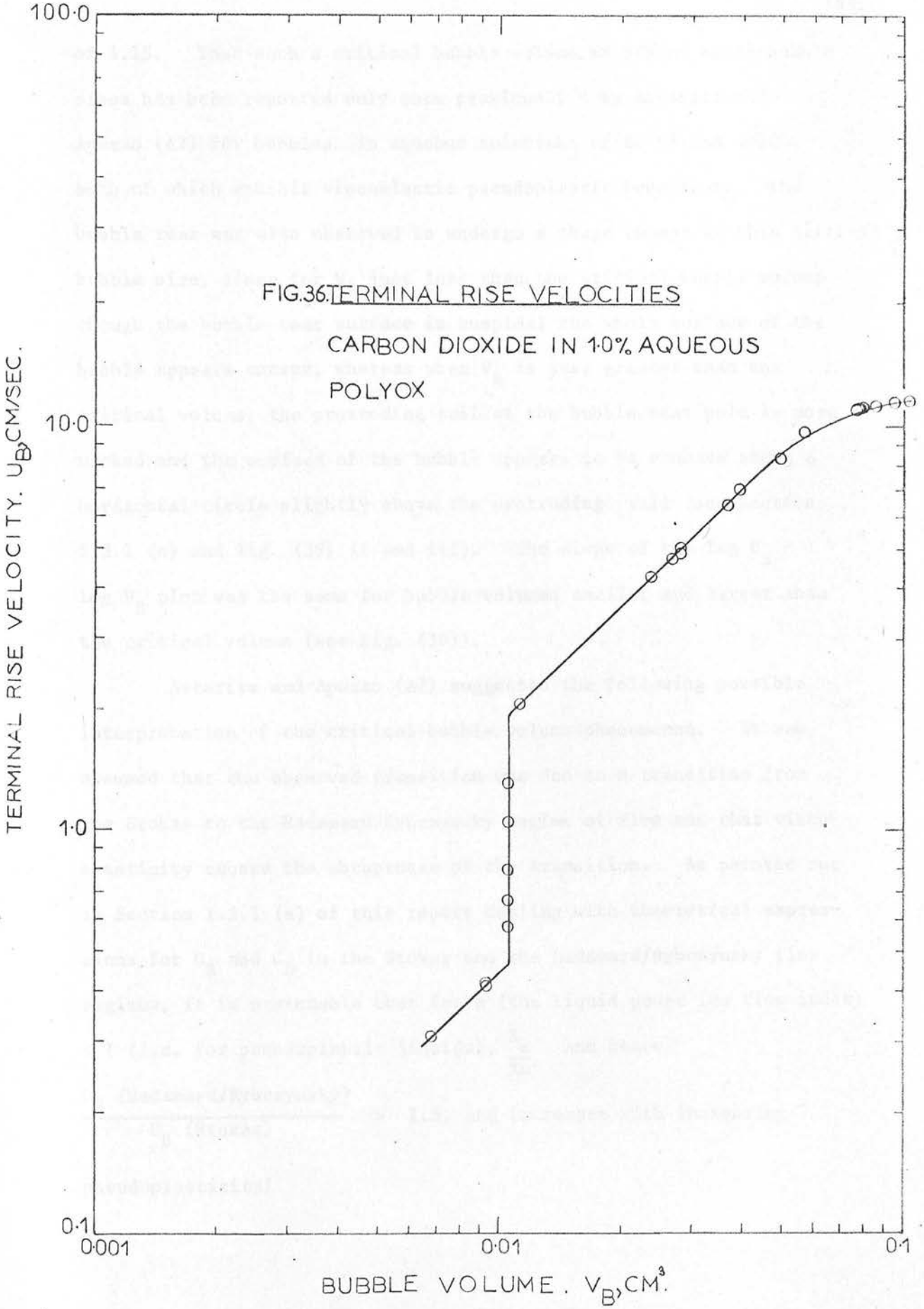

FIG.36. TERMINAL RISE VELOCITIES

CARBON DIOXIDE IN 1·0% AQUEOUS POLYOX

of 4.15. That such a critical bubble volume exists at small bubble sizes has been reported only once previously - by Astarita and Apuzzo (A7) for bubbles in aqueous solutions of ET497 and J-100, both of which exhibit viscoelastic pseudoplastic behaviour. The bubble rear was also observed to undergo a shape change at this critical bubble size, since for V_B just less than the critical bubble volume though the bubble rear surface is cuspidal the whole surface of the bubble appears convex, whereas when V_B is just greater than the critical volume, the protruding tail at the bubble rear pole is more marked and the surface of the bubble appears to be concave along a horizontal circle slightly above the protruding tail (see Section 5.3.1 (c) and Fig. (39) ii and iii). The slope of the log U_B - log V_B plot was the same for bubble volumes smaller and larger than the critical volume (see Fig. (36)).

Astarita and Apuzzo (A7) suggested the following possible interpretation of the critical bubble volume phenomenon. It was assumed that the observed transition was due to a transition from the Stokes to the Hadamard/Rybczynsky regime of flow and that viscoelasticity caused the abruptness of the transition. As pointed out in Section 1.2.1 (a) of this report dealing with theoretical expressions for U_B and C_D in the Stokes and the Hadamard/Rybczynsky flow regimes, it is presumable that for n (the liquid power law flow index) < 1 (i.e. for pseudoplastic liquids), $\frac{X_n}{Xn'}$ and hence $\frac{U_B \text{ (Hadamard/Rybczynsky)}}{U_B \text{ (Stokes)}} > 1.5$, and increases with increasing

pseudoplasticity/

pseudoplasticity. X_n and X_n' are given by Eqns. (15) and (20) respectively. From that section of this report it can also be seen from Eqn. (16) that in both the Stokes and the Hadamard/Rybczynsky regimes

$$\frac{(d \log U_B)}{(d \log V_B)} = \frac{1 + n}{3n} \qquad (140)$$

V_B = critical bubble volume

For the 1.0 per cent aqueous Polyox solution used, $\frac{(d \log U_B)}{(d \log V_B)}$ just before and after the critical bubble volume is 0.98 which from Eqn. (140) would give a value for n of 0.52. This value for n is in close agreement with the value of 0.540 (± 0.011), determined from the shear rate/shear stress measurements of the Ferranti-Shirley cone and plate rotational viscometer (see Appendix IV ii (2)).

The values obtained for the Polyox solution fit well into Table 3 below giving the values of the velocity increase factor at the critical bubble volume as well as local values of d log U_B/ d log V_B and the apparent non-Newtonian flow index calculated from Eqn. (140) for the solutions investigated by Astarita and Apuzzo.

Table 3

Solution	Ref.	$\frac{(d \log U_B)}{(d \log V_B)}$ critical volume	Velocity increase factor (presumably $\frac{U_B \text{ Hadamard/Rybczynsky}}{U_B \text{ Stokes}}$)	n (Eqn. (140))
Newtonian		0.667	1.500	1.00
0.30% ET497	(A7)	0.93	2.22	0.56
0.25% J-100	(A7)	0.94	2.35	0.55
1.0% Polyox	(Present work)	0.98	4.15	0.52
0.50% J-100	(A7)	1.06	5.55	0.46
0.70% ET497	(A7)	1.10	5.86	0.44

From Fig. (36) it can be seen that for $V_B > 0.056$ cm^3 ($D_e >$ 0.48 cm) the rate of increase of the bubble rise velocities with increasing bubble size starts gradually to decrease, though Figs. (18) and (35) indicate that bubble rise velocity continues to increase quite rapidly with increasing bubble D_e until $D_e = 1.1$ cm. At this point the shape of the curve changes noticeably and the rate of increase of U_B with increasing D_e falls sharply, and then starts to increase again until a bubble diameter of 2.4 cm is reached. At $D_e = 2.4$ cm dU_B/dD_e falls off sharply and the measured terminal rise velocities asymptotically approach the value predicted by the Dumitrescu equation, Eqn. (36). The data approaches within 5 per cent of the theoretical Dumitrescu prediction for $D_e > 4.1$ cm. As for the Newtonian liquids, it would be expected that for $D_e > 1.1$ cm, velocity retardation effects caused by the column wall would become significant.

The four regions into which the U_B versus D_e data can be divided, (0.24 cm $< D_e \leq 0.27$ cm, 0.27 cm $\leq D_e < 1.1$ cm, 1.1 cm $< D_e < 2.4$ cm, and 2.4 cm $< D_e < 5.62$ cm), also correspond approximately to four bubble shape regions and to four distinct regions in the K_L versus D_e curve for carbon dioxide bubbles in the Polyox solution (see Section 5.4.3).

Comparison of the present bubble rise velocity data with those of Loudon (L19) for carbon dioxide bubbles in aqueous CMC solutions which exhibit pseudoplastic behaviour, (given in Fig. (3)), reveals that the velocity data for the Polyox solution used in the present work are in closest agreement with the data for the 1.5 per cent aqueous CMC solution, (curve 4 of Fig. (3)), for $D_e > 0.5$ cm.

5.2 MASS TRANSFER PRODUCTS

Instantaneous mass transfer products around single carbon dioxide bubbles rising freely in distilled water, a 90.6 per cent and a 99.0 per cent aqueous Glycerol solution, and a 1.0 per cent aqueous Polyox solution contained in a 10.16 cm I.D. column are shown in Figs. (19) to (22). Fig. (37) contains a family of curves consisting of the smoothed curves drawn through the experimental $K_L A$ versus D_e data for each liquid.

In the $K_L A$ versus D_e results for carbon dioxide bubbles in distilled water, 91 per cent of the $K_L A$ results lie within 0.02 cm^3/sec of the smoothed curve drawn through the data, the remaining four data points lying within 0.03 cm^3/sec of the smoothed curve. For carbon dioxide bubbles in the 90.6 per cent aqueous Glycerol solution all the data points lie within 0.01 cm^3/sec of the smoothed curve, as do all the data points for the carbon dioxide bubbles in the 99.0 per cent aqueous Glycerol solution. For the 1.0 per cent aqueous Polyox solution 98.3 per cent of the $K_L A$ results lie within 0.02 cm^3/sec of the smoothed curve, the remaining single point lying wihtin 0.03 cm^3/sec of the smoothed curve value. These values are in good agreement with the standard deviations in $K_L A$ estimated by the methods described in Sections 3.1 and 3.2 (c) of Chapter 3 and given in Section 4.2 of Chapter 4.

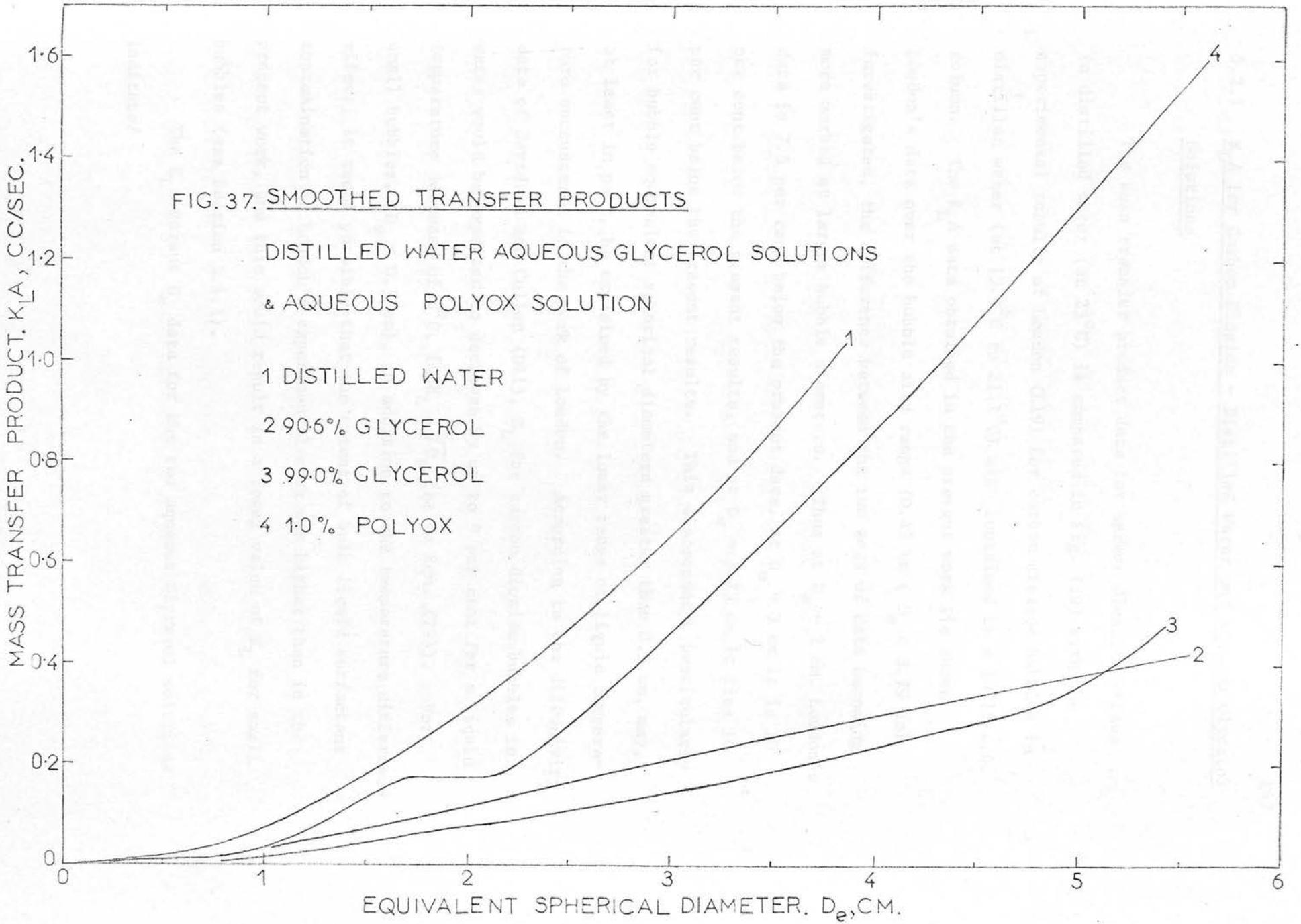
FIG. 37. SMOOTHED TRANSFER PRODUCTS
DISTILLED WATER AQUEOUS GLYCEROL SOLUTIONS
& AQUEOUS POLYOX SOLUTION
1 DISTILLED WATER
2 90·6% GLYCEROL
3 99·0% GLYCEROL
4 1·0% POLYOX
MASS TRANSFER PRODUCT, $K_L A$, CC/SEC.
EQUIVALENT SPHERICAL DIAMETER, D_e, CM.
0
0·2
0·4
0·6
0·8
1·0
1·2
1·4
1·6
1
2
3
4
5
6

5.2.1 $K_L A$ for Carbon Dioxide - Distilled Water and Aqueous Glycerol Solutions

The mass transfer product data for carbon dioxide bubbles in distilled water (at 25°C) is compared in Fig. (19) with the experimental results of Loudon (L19) for carbon dioxide bubbles in distilled water (at 15.1°C to 21.1°C) also contained in a 10.16 I.D. column. The $K_L A$ data obtained in the present work lie above Loudon's data over the bubble size range (0.42 cm $\leqslant D_e \leqslant$ 3.79 cm) investigated, the difference between the two sets of data becoming more marked at larger bubble diameters. Thus at D_e = 2 cm, Loudon's data is 7.5 per cent below the present data, at D_e = 3 cm it is 10 per cent below the present results, and at D_e = 3.75 cm it lies 16 per cent below the present results. This discrepancy, particularly for bubble equivalent spherical diameters greater than 0.5 cm, may, at least in part, be explained by the lower range of liquid temperature encountered in the work of Loudon. According to the diffusivity data of Davidson and Cullen (D11), K_L for carbon dioxide bubbles in water would be expected to decrease by up to 9 per cent for a liquid temperature decrease of 5°C, if $K_L \propto \sqrt{D_L}$ (as in Eqn. (79)). For small bubbles, (D_e < 0.5 cm), in addition to the temperature difference effect, it seems possible that the extent of bulk liquid surfactant contamination in Loudon's experimental work was higher than in the present work, and this would result in a lower value of K_L for small bubbles (see Section 5.4.1).

The $K_L A$ versus D_e data for the two aqueous Glycerol solutions indicate/

indicate that the mass transfer product progressively increases with increasing bubble size (Figs. (20), (21) and (37)). For $D_e > 3.9$ cm in the 99.0 per cent aqueous Glycerol solution the value of $d(K_LA)/dD_e$ shows a marked increase. The bubble size $D_e = 3.9$ cm corresponds to the onset of bubble skirting in the 99.0 per cent aqueous Glycerol solution (see Section 5.3.1 (b) and Fig.(38)).

5.2.2 K_LA for Carbon Dioxide - Aqueous Polyox Solution

The mass transfer product data for single carbon dioxide bubbles in the 1.0 per cent aqueous Polyox solution is shown in Figs. (22) and (37). The data show a small increase in K_LA with increasing bubble size over the range 0.24 cm $< D_e \leqslant$ 0.27 cm, a more marked increase over the bubble size range 0.27 cm $\leqslant D_e <$ 1 cm, and a still more rapid rate of increase over the bubble size range 1 cm $< D_e <$ 1.75 cm. Between $D_e = 1.75$ cm and $D_e = 2.2$ cm the value of K_LA remains almost constant at 0.18 cm^3/sec. For 2.2 cm $< D_e <$ 5.62 cm the value of K_LA increases sharply with increasing bubble size, and the K_LA versus D_e curve for the Polyox solution in this bubble size range lies displaced below that for distilled water and almost parallel to it (Fig. (37)).

From Section 5.4.3 and Fig. (39) it can be seen that for bubble equivalent spherical diameters $\leqslant$ 0.27 cm the bubble behaves as a solid particle, whereas over the bubble size range 0.27 cm $\leqslant D_e <$ 1 cm the bubble circulates and adopts a top shape. For $D_e >$ 1 cm the bubble/

bubble shape is that of an oblate spheroid with a tail until D_e = 2.2 cm when the bubble assumes a spherical cap shape. The observed $K_L A$ data for carbon dioxide bubbles in the Polyox solution can thus be explained in terms of bubble shape changes, (noting that in the region 1.75 cm < D_e < 2.2 cm the bubble shape is changing from oblate spheroidal with tail to spherical cap), and the transition from rigid to circulating sphere behaviour.

5.3 BUBBLE SHAPE AND SURFACE AREA

5.3.1 Bubble Shape and Eccentricity for Carbon Dioxide - Distilled Water, Aqueous Glycerol Solutions and Aqueous Polyox Solution

The various bubble shape configurations observed in distilled water and the two aqueous Glycerol solutions of solute concentrations 90.6 per cent and 99.0 per cent by weight are summarised in Fig. (38). Fig. (39) shows the various bubble shapes encountered in the 1.0 per cent aqueous Polyox solution. Bubble cross sections shown in Fig. (38) are not drawn to scale, although width to height ratios are representative of actual bubble photographs (after correction for optical distortion). Bubble horizontal dimensions in Fig. (39) are 96 per cent of full size, and so vertical dimensions are 0.96 M_R of full size, where M_R is the photographic distortion factor.

Bubble shapes have been characterised by a shape ratio, $S_R = {}^{D}e/2a$ (T1), which is tabulated in Appendix V, and also by an eccentricity parameter, $E = 2a/2b$ (the bubble width to height ratio) (C3). Bubble eccentricities E_1, calculated from optical distortion - corrected photographic dimensions, and E_2, evaluated after applying the bubble shape fitting procedure described in Appendix III, for bubbles in distilled water, the 90.6 per cent and the 99.0 per cent aqueous Glycerol solutions, and the 1.0 per cent aqueous Polyox solution contained in a 10.16 cm I.D. column are presented graphically versus D_e in Figs. (23) to (26). The smoothed curves through the experimental/

FIG. 38. BUBBLE SHAPES IN DISTILLED WATER AND AQUEOUS GLYCEROL SOLUTIONS

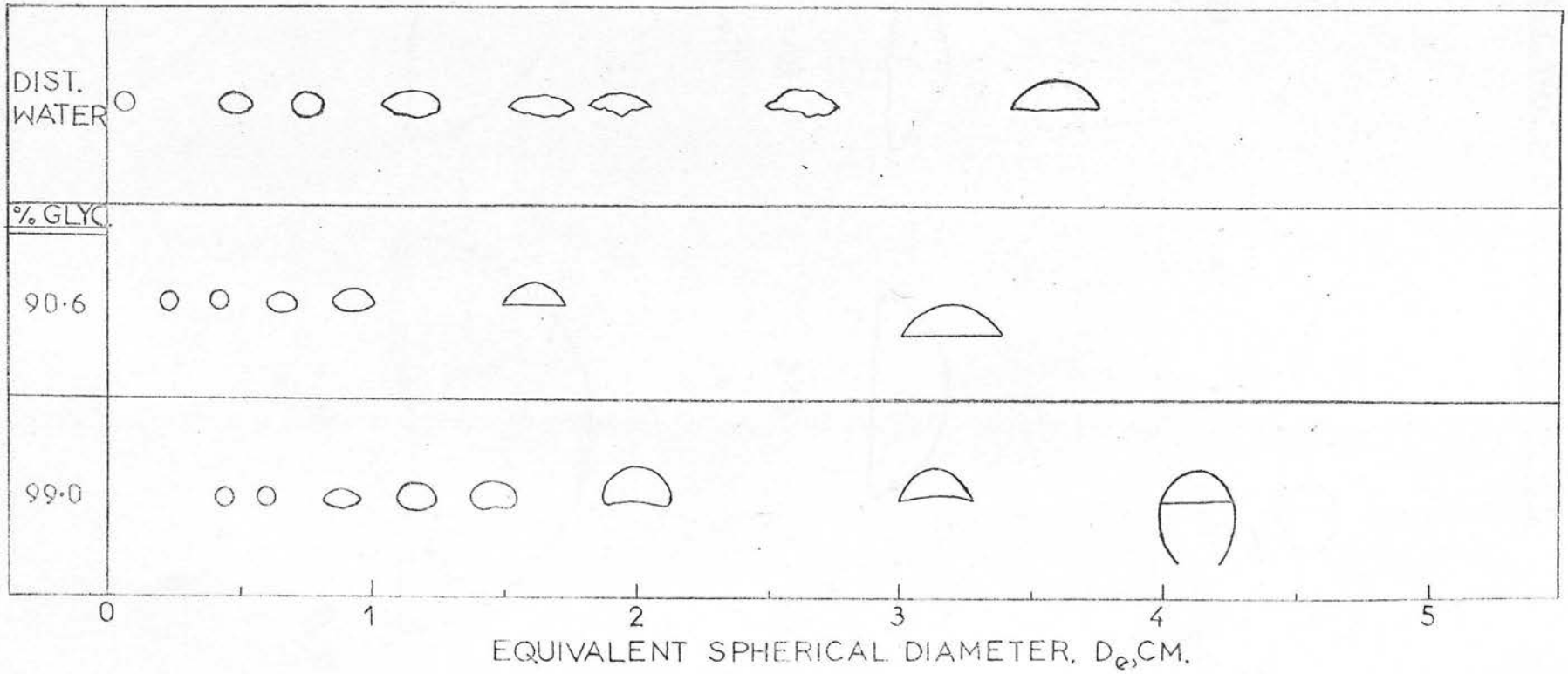

FIG. 39. BUBBLE SHAPES. CARBON DIOXIDE — 1·0% POLYOX

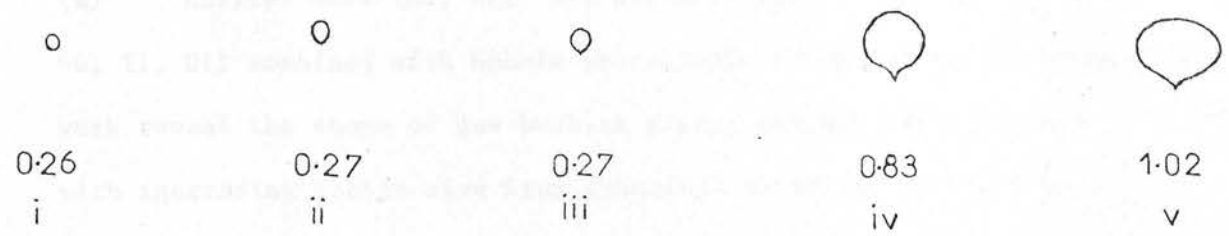

0·26 i | 0·27 ii | 0·27 iii | 0·83 iv | 1·02 v | D_e, CM.

1·37 vi | 1·82 vii | 1·93 viii | 2·18 ix | D_e, CM.

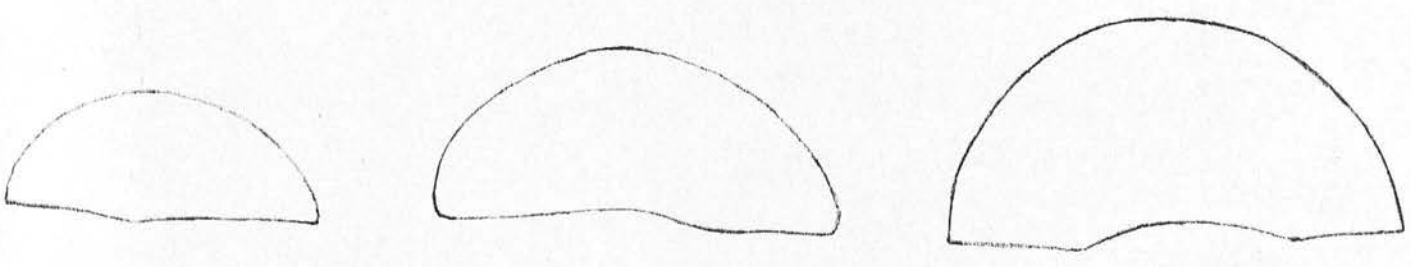

3·02 x | 4·05 xi | 4·65 xii | D_e, CM.

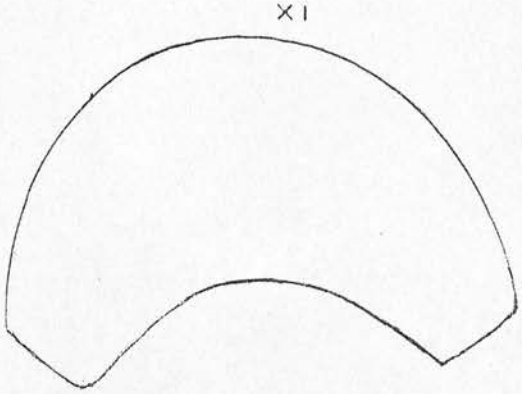

5·62 | D_e, CM.

experimental E versus D_e data for the four liquids are combined in Fig. (40).

(a) Earlier work (A3, C11, D4, D5, D7, D8, H1, L19, M9, R5, S1, S6, T1, U1) combined with bubble photographs taken during the present work reveal the shape of gas bubbles rising through water to vary with increasing bubble size from spherical to oblate spheroid to irregular ellipsoid to spherical cap. In the present work a spherical bubble shape was observed at $D_e = 0.07$ cm, an oblate spheroidal shape, (irregular for the larger bubble sizes in the size range), over the bubble size range $0.42 \leqslant D_e \leqslant 1.81$ cm, and a spherical cap shape over the bubble size range $1.81 \text{ cm} < D_e < 3.79$ cm, ($5900 < Re < 14500$). The 0.07 cm diameter bubble rose rectilinearly, while bubbles in the size range $0.42 \text{ cm} \leqslant D_e < 0.7$ cm rose with a zig-zag or spiral motion. Between bubble diameters of 0.7 cm, (Re = 1800), and 1.8 cm, an irregular ellipsoid shape was adopted and the bubble pulsated about a mean shape. These bubbles were also observed to rise rectilinearly with a rocking motion, and random bubble surface rippling started to develop in this size range. Over the bubble size range $1.8 \text{ cm} < D_e < 3$ cm a transition from irregular ellipsoid to spherical cap shape occurred, and over this size range bubble surface rippling was much in evidence. For $D_e = 3$ cm to $D_e = 3.67$ cm the bubbles adopted fully developed spherical cap shapes and exhibited little surface rippling, any which existed being mainly on the relatively planar bubble floor. These spherical caps rose rectilinearly/

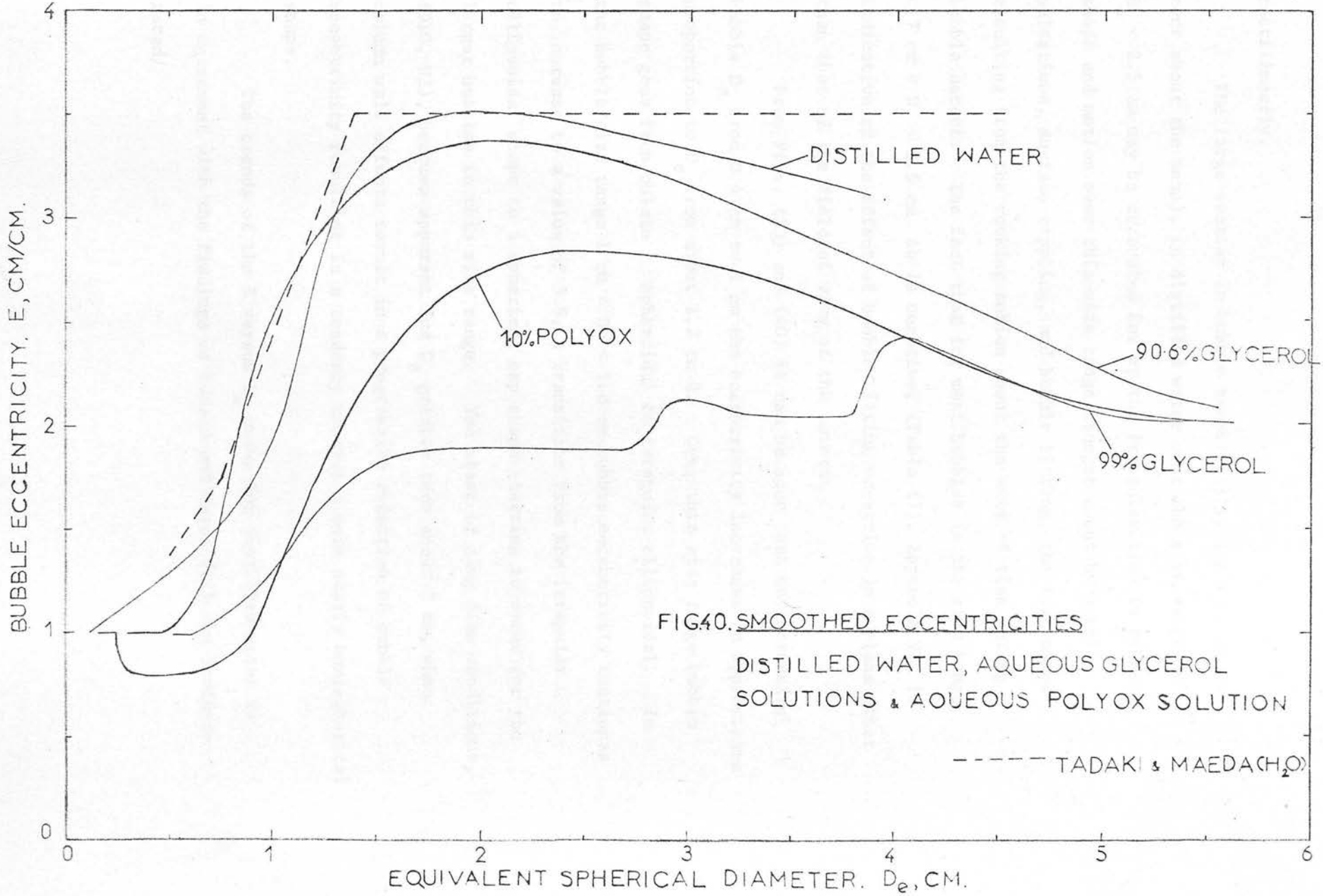

FIG.40. SMOOTHED ECCENTRICITIES

DISTILLED WATER, AQUEOUS GLYCEROL SOLUTIONS & AQUEOUS POLYOX SOLUTION

rectilinearly.

The large scatter in bubble eccentricity, (up to ± 30 per cent about the mean), in distilled water over the size range 0.7 cm < D_e < 2.5 cm may be accounted for by the irregularities in bubble shape and motion over this size range brought about by bubble pulsations, surface rippling, and bubble tilting, the last named resulting from the rocking motion about the axis of rise during bubble ascent. The fact that for most bubbles in the size range 0.7 cm < D_e < 2.5 cm Δb is negative, (Table (7), Appendix V), is indicative of the effect of bubble tilting occurring in a plane other than that of the field of view of the camera.

From Figs. (23) and (40) it can be seen that on increasing bubble D_e from 0.4 cm to 1 cm the eccentricity increases in approximate proportion to D_e from about 1.2 to 2. Over this size range bubble shape goes from oblate spheroidal to irregular ellipsoidal. In the bubble size range 1 cm < D_e < 1.8 cm bubble eccentricity continues to increase to a value of 3.5, a transition from the irregular ellipsoidal shape to a spherical cap shape starting to occur for the larger bubbles in this size range. The start of slug flow conditions, (D10, U1), becomes apparent for D_e greater than about 3 cm, when column wall effects result in a progressive reduction of bubble eccentricity resulting in a tendency towards a more nearly hemispherical shape.

The trends of the E versus D_e curve for distilled water is in agreement with the findings of Tadaki and Maeda (T1) who investi-

gated/

gated bubbles, (0.25 cm < D_e < 1.8 cm), in distilled water contained in a 10 cm I.D. column, and of Loudon for carbon dioxide bubbles, (0.2 cm < D_e < 4.8 cm), in distilled water contained in a 10.16 cm I.D. column.

(b) It is apparent from Fig. (38) that the random bubble surface rippling observed in distilled water for D_e > 0.9 cm was absent in the case of the more viscous 90.6 per cent and 99.0 per cent aqueous Glycerol solutions. Bubble shape configurations in the 90.6 per cent aqueous Glycerol solution were otherwise similar to those observed in distilled water. Thus for 0.23 cm ≤ D_e < 0.43 cm, the bubble was spherical in shape while for 0.43 cm < D_e < 0.53 cm the bubble underwent a shape transition resulting in an oblate spheroidal shape for 0.53 cm < D_e < 0.75 cm. Over the size range 0.75 cm < D_e < 1 cm a shape transition occurred resulting in a spherical cap shape for bubble diameters larger than 1 cm. Over the bubble size range investigated, 0.23 cm ≤ D_e ≤ 5.53 cm, the bubbles rose rectilinearly without noticeable rocking or pulsations in the 90.6 per cent aqueous Glycerol solution. In the 99.0 per cent aqueous Glycerol solution, the bubble was spherical for 0.44 cm ≤ D_e ≤ 0.60 cm. Over the size range 0.63 cm < D_e < 1 cm an oblate spheroidal shape was adopted. For 1 cm < D_e ≤ 1.8 cm a shape transition occurred, the bubble rear surface gradually flattening as bubble size was increased in this size range, and becoming slightly concave for bubble diameters near 1.8 cm. Over the bubble size range 1.8 cm < D_e ≤ 2.78 cm, the bubble adopted a > hemispherical shape with a concave rear surface, while for 2.78 cm < D_e /

$D_e \leqslant 5.42$ cm the bubble shape was that of a spherical cap. For bubbles in the spherical cap shape region in the 99.0 per cent aqueous Glycerol solution, the rear surface was concave until $3.9 \text{ cm} < D_e \leqslant 5.42$ cm when the spherical cap bubbles developed skirts around the peripheral edge of their rear surface, which was planar for these skirted bubbles. The lengths of skirts varied from about 4.8 cm to about 5.8 cm over the bubble size range $3.9 \text{ cm} < D_e \leqslant 5.42$ cm, and the skirts were symmetrical and stable. It was not possible to evaluate any generalised empirical criterion based on dimensionless groups for the onset of bubble skirting, as the conditions when skirting commences are known fully for only two liquids - a 6.1 per cent aqueous solution of Polyvinyl Alcohol (D5), and the 99.0 per cent aqueous Glycerol solution investigated in the present work. Over the bubble size range studied in the 99.0 per cent aqueous Glycerol solution, $0.44 \text{ cm} \leqslant D_e \leqslant 5.42$ cm, the bubble rose rectilinearly without pulsations or rocking.

The shape of the E versus D_e curve for the 90.6 per cent aqueous Glycerol solution is similar to that for distilled water (Fig. (40)). From Figs. (24) and (40) it can be seen that for bubbles going from a spherical to an oblate spheroidal shape, i.e. increasing the bubble D_e from 0.43 cm to 0.75 cm, the eccentricity increases almost proportionally to D_e from 1 to 1.5. Over the bubble size range $0.75 \text{ cm} < D_e < 2.1$ cm, which corresponds to bubble shape going from oblate spheroidal to spherical cap, the eccentricity continues to increase to a value of about 3.4. The onset of slug flow conditions/

conditions become apparent for D_e > about 3 cm and the eccentricity falls off to a value of about 2.1 at D_e = 5.5 cm. Fig. (40) indicates that the rate of fall off of the E versus D_e curve is greater for the more viscous 90.6 per cent aqueous Glycerol solution than for distilled water. From Figs. (24) and (38) it can be seen that in the absence of bubble surface rippling, bubble rocking, and bubble pulsations, the scatter of the eccentricity data about the smoothed curve is much less than for distilled water, the maximum deviation from the smoothed curve value being 10 per cent for this Glycerol solution (see Fig. (24)).

As for the 90.6 per cent solution, the scatter of the eccentricity data for bubbles in the 99.0 per cent aqueous Glycerol solution was considerably less than for distilled water and never exceeded an 8 per cent difference from the smoothed curve value (Fig. (25)). Fig. (40) shows the eccentricity values for bubbles in the 99.0 per cent aqueous Glycerol solution to lie much below those for either distilled water or the 90.6 per cent aqueous Glycerol solution. With reference to Fig. (25) it can be seen that from bubble D_e = 0.6 cm to D_e = 1.75 cm, the eccentricity increases in approximate proportion to D_e from 1 to 1.9. This size range corresponds to bubble shapes going from spherical to oblate spheroidal. Between D_e = 1.75 cm and D_e = 2.8 cm, i.e. for bubbles going from an oblate spheroidal to a > hemispherical shape, the eccentricity remains constant at 1.9. At D_e = 2.8 cm, the bubble adopts a spherical cap shape and the eccentricity rises to a value of 2.15, falling/

falling gradually to about 2.05 for D_e = 3.8 cm. At D_e = 3.9 cm, bubble skirting commences in the 99.0 per cent aqueous Glycerol solution and the eccentricity data rises to a value of about 2.4, falling to a value just above 2 at D_e = 5.5 cm. Fig. (40) shows that the E versus D_e curves for the two aqueous Glycerol solutions investigated tend to converge as D_e is increased above 4 cm.

(c) Fig. (39) shows that carbon dioxide bubbles in the 1.0 per cent aqueous Polyox solution were spherical for 0.24 cm $\leqslant D_e \leqslant$ 0.26 cm, prolate spheroidal for 0.26 cm $\leqslant D_e \leqslant$ 0.27 cm, and adopted a top shape for 0.27 cm $\leqslant D_e <$ 0.95 cm. For 0.95 cm $< D_e <$ 2.18 cm, the bubble shape was that of an oblate spheroid with a tail, though for 1.75 cm $< D_e <$ 2.18 cm, the bubble tail gradually disappeared and the bubble rear surface tended to flatten out. For 2.18 cm $\leqslant D_e \leqslant$ 5.62 cm, the bubbles adopted a spherical cap configuration. Over the size range, 1.75 cm $< D_e <$ 3 cm the bubble frontal surface exhibited a sharp change in radius of curvature in the vicinity of the lower edge of the bubble nose. For $D_e >$ 4 cm, a concave hole appeared in the centre of the bubble floor and became more pronounced with increasing bubble size. For $D_e >$ 4.5 cm, a circular lip of gas surrounding the concave hole in the bubble floor appeared, and this lip projected out below the bubble into its wake region (see Fig. (39) xiii). This bubble shape phenomenon has not been previously reported. Bubbles in the Polyox solution did not exhibit surface rippling and rose rectilinearly without rocking or pulsations.

The/

The tailing of the downstream surface of gas bubbles and liquid drops has been reported previously, (A7, B4, L19, M10, P7, W2), and is known to be peculiar to non-Newtonian fluid fields only. Tentative explanations of the tailing phenomenon observed in pseudo-plastic and thixotropic fluids (P7, W2) have been suggested in terms of fluid displaced by the bubble or drop failing to recover quickly enough, thereby resulting in a 'hole' at the rear of the bubble or drop. Astarita and Apuzzo (A7) suggested that viscoelasticity may play an important part in the appearance of unusual bubble shapes.

Figs. (26) and (40) show the eccentricity data to fall from a value of 1 at D_e = 0.26 cm to a value of 0.85 at D_e = 0.27 cm and a value of 0.8 at D_e = 0.3 cm. This corresponds to bubble configurations going from spherical, through prolate spheroidal to top shaped. The eccentricity remains constant at about 0.8 until D_e = 0.65 cm when it starts to rise gradually to a value of 0.85 at an equivalent spherical diameter of about 0.9 cm. This bubble size range corresponds to the top shaped bubble configuration. As D_e is increased above 0.95 cm, the eccentricity rises to a value of about 2.85 at D_e = 2.2 cm, the bubble adopting an oblate spheroid with tail shape over this size range. For $D_e > 3.5$ cm, the onset of slug flow conditions results in E falling off with increasing D_e to a value just above 2 at D_e = 5.5 cm. The scatter of the eccentricity data about the smoothed curve was always less than 8 per cent.

5.3.2 Bubble Surface Area for Carbon Dioxide - Distilled Water, Aqueous Glycerol Solutions and Aqueous Polyox Solution

The total surface areas, A, of single carbon dioxide bubbles rising through distilled water, a 90.6 per cent and a 99.0 per cent aqueous Glycerol solution, and a 1.0 per cent aqueous Polyox solution in a 10.16 cm I.D. column, are plotted versus bubble equivalent spherical diameter in Figs. (27) to (30). Included in Figs. (27) to (30) is the curve

$$A_s = \pi D_e^2 \qquad (139)$$

where A_s is the bubble equivalent spherical area.

Bubble surface area, A, was based on the calculated eccentricity E_2; i.e. the measured eccentricity, E_1, modified by the bubble shape fitting procedure described in Appendix III.

Loudon (L19) has shown that the percentage difference between E_1 and E_2 for a given bubble size results in a percentage difference only about one-third as large between A based on E_1 and A based on E_2. This lesser sensitivity of the surface areas of oblate spheroids and spherical caps to changes or errors in bubble height than to changes or errors in bubble width contributes to the A versus D_e plots, (Figs. (27) to (30)) exhibiting considerably less scatter than do the corresponding eccentricity versus D_e data. This is most noticeable for bubbles in distilled water (see Figs. (27) and (23)).

Table 4 below gives bubble surface areas taken from the smoothed A versus D_e data for carbon dioxide bubbles in distilled water, the/

the two aqueous Glycerol solutions and the one aqueous Polyox solution. Also included in Table 4 are bubble equivalent spherical areas, A_s.

Table 4

D_e (cm)	πD_e^2	Smoothed Bubble Surface Areas, cm^2			
		Water	90.6% Glycerol	99.0% Glycerol	1.0% Polyox
1.0	3.14	3.6	4.2	3.3	3.3
2.0	12.57	17.7	17.9	14.7	16.8
3.0	28.26	41.5	40.5	33.7	38.4
3.5	38.45	56.2	53.4	46.5	51.2
4.0	50.25		67.2	61.6	65.3
5.0	78.54		97.8	94.9	95.8

Inspection of Figs. (27) to (30) and Table 4 reveals the similarity between bubble surface areas observed in the distilled water and in the 90.6 per cent aqueous Glycerol solution. Bubble surface areas, A, in the 1.0 per cent aqueous Polyox solution and in the 99.0 per cent aqueous Glycerol solution were generally lower than for distilled water though for bubble $D_e > 3.5$ cm the values of A for all four solutions tended to converge. The bubble surface area data for the four solutions investigated also indicate that $(A - A_s)$ becomes progressively larger as bubble size is increased and the bubble shape becomes more distorted from the spherical shape. These/

These observations are in agreement with the variations of bubble shapes and eccentricities with equivalent diameter discussed in Section 5.3.1 of this Chapter.

5.4 INSTANTANEOUS OVERALL MASS TRANSFER COEFFICIENTS

Instantaneous overall mass transfer coefficients around single carbon dioxide bubbles ascending through distilled water (bubble size range: 0.42 cm $\leqslant D_e \leqslant$ 3.79 cm), a 90.6 per cent aqueous Glycerol solution (bubble size range: 0.23 cm $\leqslant D_e \leqslant$ 5.53 cm), a 99.0 per cent aqueous Glycerol solution (bubble size range: 0.44 cm $\leqslant D_e \leqslant$ 5.42 cm), and a 1.0 per cent aqueous Polyox solution (bubble size range: 0.24 cm $\leqslant D_e \leqslant$ 5.62 cm) contained in a 10.16 cm I.D. column are plotted versus D_e in Figs. (31) to (34). The smoothed K_L versus D_e curves through the experimental data for the four liquids studied are combined in Fig. (41). In all these graphs, K_L values have been evaluated on the basis of actual total bubble surface areas.

As the results of Loudon (L19) for carbon dioxide bubbles in distilled water and six aqueous CMC solutions, in which most possible means of contamination were avoided, exhibited no significant mass transfer coefficient time dependence, no attempt was made to ascertain the effect of bubble age on K_L in this work.

5.4.1 K_L for Carbon Dioxide - Distilled Water

In Fig. (31) the mass transfer coefficient data is compared with the Boussinesq equation, Eqn. (79), which describes transfer around circulating spheres in potential flow

$$Sh = 1.13\ Pe^{1/2}\ ; \quad K_L = 1.13\ (D_L U_B/De)^{1/2} \qquad (79)$$

The/

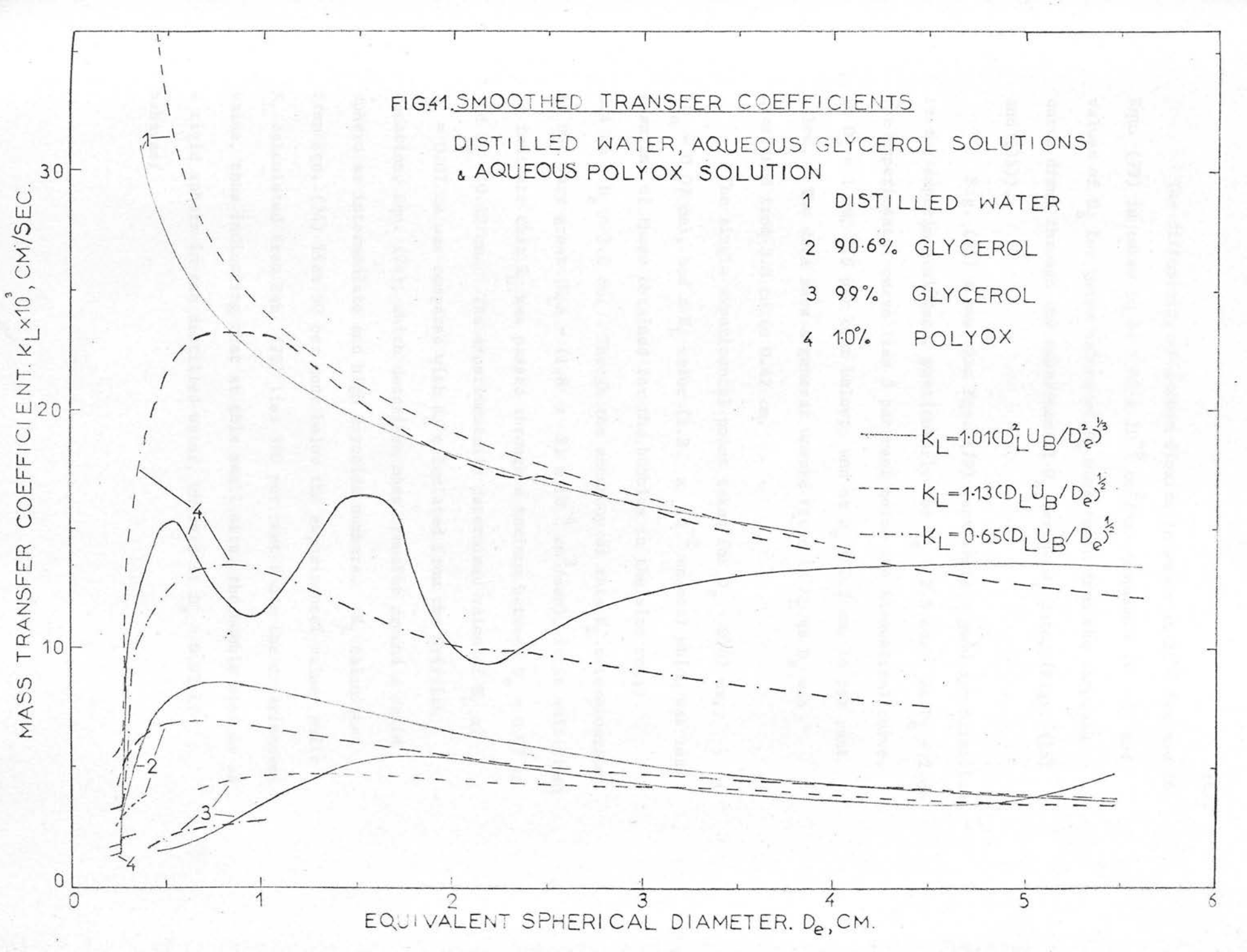
FIG.41. SMOOTHED TRANSFER COEFFICIENTS
DISTILLED WATER, AQUEOUS GLYCEROL SOLUTIONS & AQUEOUS POLYOX SOLUTION
1 DISTILLED WATER
2 90·6% GLYCEROL
3 99% GLYCEROL
4 1·0% POLYOX
$K_L = 1{\cdot}01 (D_L^2 U_B / D_e^2)^{1/3}$
$K_L = 1{\cdot}13 (D_L U_B / D_e)^{1/2}$
$K_L = 0{\cdot}65 (D_L U_B / D_e)^{1/2}$
MASS TRANSFER COEFFICIENT. $K_L \times 10^3$, CM/SEC.
EQUIVALENT SPHERICAL DIAMETER. D_e, CM.
0
10
20
30
0
1
2
3
4
5
6

The diffusivity of carbon dioxide in water at 25°C for use in Eqn. (79) is taken to be 1.92×10^{-5} cm^2/sec (Appendix IV vi) and values of U_B for given values of D_e were taken from the smoothed curve drawn through the experimental U_B versus D_e data, (Figs. (15) and (35)).

Fig. (31) shows that Eqn. (79) represents a good approximation to the experimental data, particularly for $D_e > 2.5$ cm. At $D_e = 2$ cm the experimental curve lies 5 per cent below the theoretical curve; at $D_e = 1$ cm, 7.5 per cent below; and at $D_e = 0.5$ cm, 16 per cent below. The data show a general upward trend in K_L as D_e was decreased from 3.8 cm to 0.42 cm.

The single experimental point taken for $D_e < 0.42$ cm, ($D_e = 0.07$ cm), had a K_L value (1.2×10^{-2} cm/sec) which was less than any of those obtained for the bubbles in the size range $0.4 \text{ cm} < D_e < 3.8$ cm. Though the accuracy of this K_L determination is not very great ($K_L A = (1.8 \pm 2) \times 10^{-4}$ cm^3/sec), it is sufficient to indicate that K_L has passed through a maximum between $D_e = 0.07$ cm and $D_e = 0.42$ cm. The experimentally determined value of K_L at $D_e = 0.07$ cm was compared with K_L calculated from the Griffith equation, Eqn. (74), which describes mass transfer around a solid sphere at intermediate and high Reynolds numbers. K_L calculated from Eqn. (74) lies 90 per cent below the experimental value, while K_L calculated from Eqn. (79) lies 380 per cent above the experimental value, thus indicating that at this small size, the bubble behaves as a rigid sphere in the distilled water, whereas at $D_e > 0.42$ it behaves/

behaves as a circulating bubble. This is also indicated by the U_B versus D_e data for carbon dioxide bubbles in distilled water, (Fig. (15)), and is in agreement with the data of Zieminski and Raymond (Z2) whose K_L results for carbon dioxide bubbles in distilled water at 25°C over the size range 0.27 cm to 0.38 cm is shown in Fig. (8). The results of Zieminski and Raymond show K_L to increase with decreasing bubble size from 0.044 cm/sec at D_e = 0.38 cm to a maximum value of 0.060 cm/sec at D_e = 0.30 cm; thereafter decreasing to a value of 0.055 cm/sec at D_e = 0.27 cm. In fact the data of Zieminski and Raymond could be inserted into the interval between D_e = 0.07 cm and D_e = 0.42 cm in Fig. (31). The data of Zieminski and Raymond fall some 33 per cent above the theoretical value predicted by Eqn. (79) at D_e = 0.30 cm, though at D_e = 0.38 cm the data fall only 5 per cent above the theoretical prediction. The maximum in K_L was attributed to a progressive transition between circulating and rigid bubble behaviour, in agreement with the observations in the present investigation.

Loudon (L19) found that for carbon dioxide bubble diameters below 1 cm the values of K_L in distilled water at 20°C remained approximately constant at 0.019 cm/sec until a bubble diameter of 0.45 cm was reached (Fig. (48) of Ref. (L19)), below which diameter the data fell sharply to a value of 0.009 cm/sec at D_e = 0.2 cm. Loudon considered interfacial contamination effects and/or the inability of the Visicorder method used for recording column pressure changes to give an accurate value of $^{dP}T/dt$ for such small bubbles, to/

to be responsible for the displacement of his K_L data around small bubbles below the values predicted by Eqn. (79). In this work a more accurate method of determining $^{dP}T/dt$ was used (Section 2.1.2 (7)), and two sources of column liquid contamination (rust from the end plate of the column equal tee section, and petroleum jelly from stopcocks at the top and bottom of the mass transfer column) were eliminated (Sections 2.1.2 (1) and 2.1.2 (2)). This probably explains the higher K_L values obtained in the present work for $D_e < 1$ cm even when the higher liquid temperature, (25^oC as compared with approximately 20^oC), is taken into account. For $D_e > 1$ cm, Eqn. (79) represents a good approximation to the results of Loudon (L19), as it does to the present data.

The general trend of the K_L versus D_e curve for carbon dioxide bubbles in distilled water over the bubble size range 0.42 cm $\leq D_e < 3.8$ cm is in agreement with the experimental observations of Hammerton (H5) for carbon dioxide bubbles in water, of Hammerton and Garner (H6) for carbon dioxide, ethylene, oxygen and hydrogen bubbles in distilled water, and of Coppock and Meiklejohn (C15) for oxygen bubbles in distilled water. The fact that many early investigators indicated a downward trend in the K_L value of soluble bubbles in water from equivalent spherical diameters as large as 2 cm may, in most cases, be explained by the effect of surfactants in the bulk liquid phase which progressively contaminate the gas-liquid interface and retard interfacial flow. This is discussed in greater detail in Section 1.3.1 (c) of this report.

5.4.2 K_L for Carbon Dioxide - Aqueous Glycerol Solutions

Instantaneous overall mass transfer coefficients around single carbon dioxide bubbles rising freely through two aqueous Glycerol solutions - a 90.6 per cent solution (ν = 1.46 cm^2/sec) and a 99.0 per cent solution (ν = 6.17 cm^2/sec) - are presented in Figs. (32), (33) and (41). In Figs. (32) and (33) the data is compared with the Boussinesq equation, Eqn. (79) and the Levich equation for circulating spheres in creeping flow, (Eqn. (75)).

$$Sh = 0.65\ Pe^{1/2}\ ;\quad K_L = 0.65\ (D_L U_B/D_e)^{1/2} \qquad (75)$$

The diffusivities of carbon dioxide in the 90.6 per cent and the 99.0 per cent aqueous Glycerol solutions at 25°C for use in Eqns. (75) and (79) are taken to be 1.7 x 10^{-6} cm^2/sec and 1.5 x 10^{-6} cm^2/sec respectively, (Appendix IV vi). The smoothed curves drawn through the observed rise velocity versus D_e data (Figs. (16), (17) and (35)) provided the U_B versus D_e values used in Eqns. (75) and (79).

For D_e > 3 cm, (Re > 65), in the 90.6 per cent aqueous Glycerol solution, the difference between the smoothed curve drawn through the experimental data and the theoretical curve of Eqn. (79) is always less than 6 per cent (see Fig. (32)). At D_e = 3 cm in the 99.0 per cent aqueous Glycerol solution the experimental and theoretical curves agree, (see Fig. (33)). As the bubble equivalent spherical diameter is increased above 3 cm, the experimental K_L curve falls below the theoretical curve of Eqn. (79) until at D_e = 3.9 cm, it lies 7 per cent below the theoretical curve. For D_e > 3.9 cm, the/

the rate of fall off of the measured overall mass transfer coefficient decreases markedly and at $D_e > 4.4$ cm K_L starts to increase, until at $D_e = 5.5$ cm, (Re = 40), the experimental curve lies some 20 per cent above the theoretical curve. The reason for this change in the downward trend of K_L with increasing D_e for $D_e > 3$ cm occurring at $D_e = 3.9$ cm is due to the commencement of bubble skirting, with its accompanying increase in bubble eccentricity (Fig. (25)), and flattening of the bubble rear surface (Fig. (38)), at this bubble size. As K_L for skirted bubbles was obtained from K_LA by dividing by A, the area of the spherical cap, (noting that only very small amounts of gas are contained in the skirts (D5, G15)), the enhancement in the Experimentally measured values of K_L for $D_e > 3.9$ cm in the 99.0 per cent aqueous Glycerol solution results from potential flow transfer from the outer surfaces and bubble wake transfer from the inner surfaces of the bubble skirts.

As D_e is decreased below 3 cm, the measured values of K_L in the 90.6 per cent aqueous Glycerol solution increase above those predicted by the theoretical Boussinesq equation, Eqn. (79), until a maximum is reached at $D_e = 0.75$ cm when the experimental curve lies 20 per cent above the theoretical curve. Below this bubble diameter, K_L decreases sharply, falling below the Boussinesq curve. For $D_e < 0.3$ cm the experimental K_L versus D_e curve rapidly approaches the values predicted by the Levich equation for circulating spheres in creeping flow, Eqn. (75).

From agreement between the theoretical and experimental K_L values/

values in the 99.0 per cent aqueous Glycerol solution at bubble D_e = 3 cm, the experimental curve rises above the theoretical Boussinesq curve as D_e is decreased below 3 cm. A maximum value of the experimental overall mass transfer coefficient occurs at D_e = 1.8 cm when the measured K_L value is 15 per cent greater than the theoretical Boussinesq value, and below this diameter the experimentally determined K_L values fall off sharply, decreasing below the Boussinesq curve for $D_e < 1.34$ cm. At D_e = 0.84 cm, the experimental curve agrees with the theoretical curve predicted by the Levich equation, Eqn. (75). As D_e is decreased below 0.84 cm, the experimental curve falls below the theoretical Levich curve until at D_e = 0.6 cm the measured K_L value lies 20 per cent below the theoretical value predicted by the Levich equation for circulating spheres in creeping flow. As D_e is decreased below 0.6 cm, the experimental curve approaches more closely the theoretical Levich curve, and at D_e = 0.44 cm, the experimental K_L value is only 10 per cent below the theoretical Levich value.

The reason for the observed shapes of the experimentally measured K_L versus D_e plots for carbon dioxide bubbles in the two aqueous Glycerol solutions may be explained as follows:

In the 90.6 per cent aqueous Glycerol solution, the maximum K_L value occurs at D_e = 0.75 cm. Inspection of Fig. (38) reveals that for 0.23 cm $\leq D_e < 0.43$ cm the carbon dioxide bubbles are spherical in the 90.6 per cent aqueous Glycerol solution, while for 0.43 cm $< D_e < 0.53$ cm a shape transition results until 0.53 cm $< D_e <$ 0.75 cm the bubbles adopt an oblate spheroidal shape. For 0.75 cm $<$ $D_e <$ /

D_e < 1 cm a shape transition occurs resulting in a spherical cap bubble shape for 1 cm < $D_e \leqslant$ 5.53 cm. Thus the maximum K_L value occurs at the transition from a spherical cap to an oblate spheroidal bubble shape. Fig. (38) also shows that for 0.44 cm $\leqslant D_e <$ 0.60 cm the carbon dioxide bubbles are spherical in the 99.0 per cent aqueous Glycerol solution, while for 0.63 cm < D_e < 1 cm the bubbles are oblate spheroidal in shape. Over the size range 1 cm < D_e < 1.8 cm a shape transition occurs resulting in a > hemisphere shape for 1.8 cm < D_e < 2.78 cm. When 2.78 cm < $D_e \leqslant$ 5.42 cm the bubbles adopt a spherical cap shape. The maximum K_L value for carbon dioxide bubbles in the 99.0 per cent aqueous Glycerol solution occurs at 1.8 cm, which again corresponds to the transition from a spherical cap shape with E < 2, (i.e. a > hemispherical bubble shape), to an oblate spheroidal shape. The sharp increase in Eccentricity at D_e = 2.8 cm, (see Fig. (25)), in the 99.0 per cent aqueous Glycerol solution corresponds to the experimental K_L versus D_e curve going from less than to greater than the theoretical Boussinesq prediction at that bubble size (see Fig. (33)).

Thus it is seen that shape transitions are reflected in the K_L versus D_e curves. The transition from spherical cap (with E > or < 2) to oblate spheroidal shape seems to be accompanied by instabilities in the liquid flow around the bubble, resulting in an increase in K_L above the theoretically predicted value. Part of this increase may, however, be explained by the application of the Lochiel-Calderbank equation, Eqn. (81), for oblate spheroids in potential flow, which/

which is shown in Fig. (6) and which predicts an enhancement in the theoretical mass transfer coefficient predicted by the Boussinesq equation, Eqn. (79), for bubbles in potential flow when the bubbles are oblate spheroidal and have eccentricities lying between 1 and 5.8. At bubble D_e = 0.75 cm in the 90.6 per cent aqueous Glycerol solution, the bubble eccentricity is just over 1.5 which would result in a 7 per cent increase in the theoretical K_L due to Boussinesq on the application of Eqn. (81), and at bubble D_e = 1.8 cm in the 99.0 per cent aqueous Glycerol solution, the bubble eccentricity is just over 1.9 which would result in an 8.5 per cent increase in the Boussinesq theoretical K_L.

Zieminski and Raymond (Z2) attribute the K_L maximum observed in their experimental K_L versus D_e data for carbon dioxide bubbles in distilled water as being due to a transition from circulating oblate spheroidal behaviour to rigid sphere behaviour. It is interesting to note that the K_L maximum found by Zieminski and Raymond for distilled water occurs with the experimental K_L value 33 per cent above the theoretical value predicted by the Boussinesq equation, Eqn. (79), whereas in the present work the maximum experimental K_L value is 20 per cent above the theoretical Boussinesq prediction for the 90.6 per cent aqueous Glycerol solution, and 15 per cent above for the 99.0 per cent aqueous Glycerol solution, indicating a progressive decrease with increasing Newtonian liquid viscosity.

For bubble sizes, $D_e < 0.3$ cm, in the 90.6 per cent aqueous Glycerol solution the bubbles are spherical and the experimental K_L values/

values rapidly approach from above the Levich equation for circulating spheres in creeping flow, i.e. Re of the order of 1 or less. At D_e = 0.4 cm, Re = 2 and at D_e = 0.31 cm, Re = 1, so the agreement between the Levich theory and experiment for carbon dioxide bubbles in the 90.6 per cent aqueous Glycerol solution is good. For bubble sizes, D_e < 1 cm, the experimental K_L versus D_e curve for the 99.0 per cent aqueous Glycerol solution approaches the Levich curve, falls below it, and, for D_e < 0.6 cm, converges towards the Levich curve from below. This is in agreement with the theoretical work of Sy and Lightfoot (S18) which predicts a K_L reduction of up to 20 per cent below the Levich theoretical predictions for circulating bubbles which are distorted from the spherical shape to an oblate spheroidal shape and are in the creeping flow regime. For 0.63 cm < D_e < 1 cm the carbon dioxide bubbles in the 99.0 per cent aqueous Glycerol solution are oblate spheroidal in shape, while for 0.44 cm < D_e < 0.60 cm the bubbles adopt a spherical shape; also, at D_e = 1.05 cm, Re = 2 and at D_e = 0.8 cm, Re = 1.

Thus the theoretical work for circulating bubbles in potential flow and for circulating bubbles in creeping flow, combined with probable external liquid flow instabilities produced by bubble shape transitions suitably explains the observed trends of the K_L versus D_e results for carbon dioxide bubbles in the two aqueous Glycerol solutions investigated. The trend of the present experimental K_L versus D_e curve for the small carbon dioxide bubbles in both aqueous Glycerol solutions are in agreement with the trend of the experimental curve for carbon dioxide bubbles, (0.2 cm < D_e < 0.7 cm), in Glycerol obtained/

obtained by Hammerton and Garner (H6) and shown in Fig. (9).

Both the rise velocity and the mass transfer coefficient results for the two aqueous Glycerol solutions indicate circulating bubbles for Re as low as 0.32, (D_e = 0.23 cm), in the 90.6 per cent solution, and as low as 0.16, (D_e = 0.44 cm), in the 99.0 per cent solution. This agrees with the findings of Garner and Hammerton (G2) and Hammerton and Garner (H6) which indicate a transfer from rigid to circulating bubble behaviour at Re = 0.023, (D_e = 0.3 cm), in Glycerol. This is also in agreement with the results of Redfield and Houghton (R2) for carbon dioxide bubbles in aqueous Dextrose solutions which indicate the persistence of circulating bubble behaviour down to Re as low as 0.02.

5.4.3 K_L for Carbon Dioxide - Aqueous Polyox Solution

Instantaneous overall mass transfer coefficients around single carbon dioxide bubbles rising through a 1.0 per cent aqueous Polyox solution are presented in Figs. (34) and (41). Included in Fig. (34) for comparison with the present data are the Boussinesq equation, Eqn. (79), the Levich equation for circulating spheres in creeping flow, Eqn. (75), and the Levich equation for rigid spheres in creeping flow, Eqn. (69),

$$Sh = 1.01\ Pe^{1/3}\ ; \quad K_L = 1.01\ (D_L^2\ U_B/D_e^2)^{1/3} \qquad (69)$$

The/

The diffusivity of carbon dioxide in the 1.0 per cent aqueous Polyox solution at 25°C for use in Eqns. (69), (75) and (79) is taken to be 1.92×10^{-5} cm^2/sec, (Appendix IV vi), and U_B versus D_e data was taken from the smoothed curve drawn through the experimental U_B versus D_e results, (Figs. (18) and (35)).

Inspection of Fig. (39) indicates that over the bubble size range $0.24 \leqslant D_e < 0.26$ cm the carbon dioxide bubbles in the Polyox solution are spherical in shape, while for $0.26 \text{ cm} \leqslant D_e \leqslant 0.27$ cm the bubble adopts a prolate spheroidal configuration. For $0.27 \text{ cm} \leqslant D_e < 0.95$ cm, the bubble is top shaped, and when $0.95 \text{ cm} < D_e < 2.18$ cm the shape is that of an oblate spheroid with a tail, though a shape transition starts occurring at $D_e = 1.75$ cm. Finally the spherical cap shape is adopted for $2.18 \text{ cm} \leqslant D_e \leqslant 5.62$ cm. A noticeable feature about the shape transitions in the viscoelastic pseudoplastic Polyox solution is the abruptness with which they occur at a given bubble size, compared with the shape transition regions observed in the Newtonian solutions investigated. As can be seen in Figs. (34) and (41), the experimental K_L versus D_e data can be divided into four regions corresponding to the shape regions, namely:

Region 1: $2.18 \text{ cm} \leqslant D_e \leqslant 5.62$ cm (Spherical Cap)

Region 2: $0.95 \text{ cm} < D_e < 2.18$ cm (Oblate Spheroid with tail)

Region 3: $0.27 \text{ cm} \leqslant D_e < 0.95$ cm (Top)

Region 4: $0.24 \text{ cm} \leqslant D_e \leqslant 0.27$ cm ("Solid" Prolate Spheroid and Sphere)

In/

In Region 1, the experimental K_L data rise from a value just below that predicted by the theoretical Levich equation, Eqn. (75) at D_e = 2.18 cm to a value 10 per cent above that of the theoretical Boussinesq equation, Eqn. (79), at D_e = 5.5 cm (see Fig. (34)); and approaches the measured K_L values for distilled water at these large bubble diameters. The data suggest that for sufficiently large bubbles, D_e > 4.25 cm, potential flow applies over the bubble frontal area of spherical cap bubbles in the 1.0 per cent aqueous Polyox solution. This is in agreement with the indications of the rise velocity data for bubbles in the 1.0 per cent Polyox solution, Figs. (18) and (35), and with the findings of Loudon (L19) for carbon dioxide bubbles in aqueous CMC solutions which exhibit pseudoplastic behaviour.

Regions 2 and 3 of the experimental K_L versus D_e data are characterised by K_L values rising from just below the theoretically predicted K_L values of the Levich equation, Eqn. (75), to a maximum, which lies below the theoretical predictions of the Boussinesq equation, and falling again to a value just below that predicted by the Levich equation. These maxima seem to be associated with bubble shape changes. The bubble shape transitions result from hydrodynamic effects which seem to markedly affect the liquid phase mass transfer coefficient. Existence of such maxima has been reported in only one previous publication (B4). Barnett et al (B4) followed the rise and dissolution rate of small carbon dioxide bubbles (D_e < 0.5 cm) in two aqueous CMC solutions, which exhibit pseudoplastic behaviour, contained/

contained in a constant pressure system. For each bubble a K_L versus D_e plot was presented over its time of rise through the liquid. It was noted that the mass transfer coefficients were high initially but tailed off rapidly with bubble age, though exceptions were found at specific bubble diameters where the bubble shape went through a transition. Thus a transition from the oblate spheroidal region to the solid sphere region was observed at an equivalent spherical diameter of about 0.2 cm. At a larger diameter, a second transition point occurred when the bubble shape changed from an oblate spheroid with tail shape to a top shape and finally to an oblate spheroid shape. A sudden increase of mass transfer coefficient was observed to occur at each of these two shape transition points.

In Region 4 of the K_L versus D_e data, the accuracy of the K_L measurements, (the standard deviation of $K_L A$ in this region is ± 15 per cent of the measured value, see Section 4.2), is sufficiently good to identify that for bubble $D_e \leqslant 0.27$ cm in the 1.0 per cent aqueous Polyox solution the prolate spheroidal and spherical bubbles exhibit solid body behaviour. Thus the K_L values predicted by the Levich equation for rigid spheres in creeping flow, Eqn. (69), lie on average 15 per cent below the K_L measurements in this region of bubble size, whereas the theoretical K_L predictions of the Levich equation for circulating spheres in creeping flow lie on average 130 per cent above them, and the Boussinesq equation predictions for circulating spheres in potential flow lie on average 300 per cent above them.

Thus/

Thus the mass transfer coefficient data confirm the evidence shown in Fig. (36) and discussed in Section 5.1.2 that at the critical bubble equivalent spherical diameter, 0.27 cm, a transition from rigid (Stokes regime) to circulating bubble behaviour occurs. Of the five bubbles with D_e = 0.27 cm, (V_B = 0.0105 cm^3), (see Fig. (36)), which undergo transition from circulating to rigid bubble behaviour between the bubble rise velocity measuring points, (photo-electric cell units P_1 and P_3, Fig. (11)), it is apparent that the three bubbles with the lowest velocities averaged over the distance between P_1 and P_3 undergo the transition to rigid sphere behaviour before reaching the mid-point between P_1 and P_3 and thus exhibit rigid bubble behaviour at this central measuring point. The other two bubbles with D_e = 0.27 cm undergo the transition after the central measurement point and so exhibit K_L values which indicate circulating bubble behaviour. For these two bubbles, the measured K_L values lie some 35 per cent above those indicated by the Levich equation for circulating spheres in creeping flow, (the Hadamard/ Rybczynsky regime), and this seems to be due to the U_B value used in Eqn. (75) being an average value over the distance P_1 to P_3 and being only about 50 per cent of the U_B at the central measuring point where K_L was determined, (see Fig. (36)). Since from Eqn. (75), $K_L \alpha \sqrt{U_B}$, this would result in the K_L value determined from Eqn. (75) for these two bubbles being about 30 per cent too low. Thus the mass transfer coefficient data confirm the theory of Astarita and Apuzzo (A7) discussed in Section 5.1.2 that at the critical bubble size/

size, D_e = 0.27 cm, for the 1.0 per cent aqueous Polyox solution, a transition from the Stokes to the Hadamard/Rybczynsky flow regime occurs.

The modified Reynolds number Re' defined by Eqn. (14), (with $m = K\,(8)^{n-1}$ (M14)), gives a value ≤ 1.1 in Region 1 and ≤ 2.3 for $D_e \leq 0.27$ thus indicating creeping flow conditions, and a value of 1393 when the bubble D_e = 5.5 cm.

As pointed out in Section 1.3.1 (a), Eqn. (79) which does not take into account the shape changes of large gas bubbles in free rise through liquids, represents only an approximation to mass transfer from bubbles in potential flow which adopt a spherical cap shape. For spherical cap bubbles, the Lochiel-Calderbank equation, Eqn. (87), more accurately represents bubble nose transfer, though no theoretical solution for transfer from the rear of spherical cap bubbles exists. This is discussed in more detail in the following sections of this report, Sections 5.5.1 and 5.5.2.

5.5 BUBBLE WAKE MASS TRANSFER

5.5.1 Theoretical Model for Bubble Wake Transfer

The photographic evidence of Slaughter and Wraith (S12) for spherical cap gas bubbles in an aqueous Glycerol solution (ν = 1.43 cm^2/sec), Davies and Taylor (D7) for spherical cap gas bubbles in nitrobenzene, and Collins (C12, C13) for two-dimensional cylindrical cap bubbles in water suggest the existence of a 3-dimensional wake containing a toroidal vortex behind a spherical cap bubble, and approximately completing the spheroid of which the bubble cap forms a part. The photographs of Crabtree and Bridgewater (C16) and Loudon (L19) suggest that in liquids of low viscosity such as water, turbulence develops in the wake region and the vortex is unstable. Crabtree and Bridgewater noted that clockwise rotation of the bubble release cup caused the first vortex to be shed to the right and vice versa in the low viscosity liquids in which vortex shedding was observed. This suggests that the dumping cup rotation to release the bubble may contribute to the instability which results in vortex shedding. At any given instant, nevertheless, the liquid flow near the gas bubble floor in the bubble wake, which is mainly responsible for bubble rear mass transfer, should, for the unstable wake with vortex shedding, be essentially the same as that in the case of the stable three-dimensional wake completing a spheroid with the gas bubble nose.

As/

As a result of this the following wake model was set up with a view to making a theoretical estimate of bubble rear mass transfer coefficients.

Assume a spherical cap bubble to rise in a free fluid field in potential flow at constant velocity U_B. The wake region immediately below the bubble is taken to complete the sphere of which the nose of the spherical cap bubble forms a part, and the bubble floor is taken to be essentially planar (see Fig. (5)).

The toroidal vortex in the bubble wake results in liquid elements, of which lines L and L' are part (see Fig. (42(a))), passing from the bulk liquid in the bubble wake to the centre of the bubble floor gas/liquid interface, flowing outwards to the edge of the bubble floor, and in so doing stretching,and streaming downwards following the streamlines in the bulk liquid outside the spheroid of which the bubble wake forms a part. These streamlines reach a point of stagnation at point C, (Fig. (42(a))), and then flow upwards to the centre of the bubble floor. During the time that each liquid element spends at the gas-liquid interface, a mass exchange with the gas in the bubble takes place, and the thickness of the liquid element into which significant mass transfer occurs during its time of contact with the bubble floor is taken to be so thin that any velocity variation occurs in the r-direction only and not the z-direction (see Fig. (42(c))). During its motion inside the bulk liquid of the bubble wake, a mass exchange occurs and it is assumed that this mass exchange results in each element of liquid arriving at the gas-liquid interface free of any gas solvent. This assumption seems/

SCHEMATIC DIAGRAMS OF SPHERICAL CAP BUBBLES AND THEIR WAKES FIG. 42.

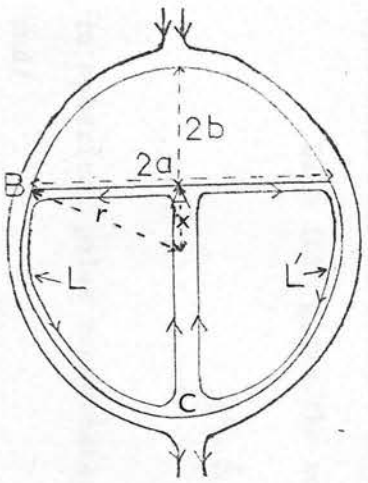

(a)

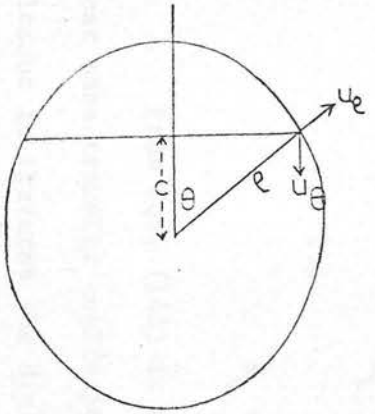

(b)

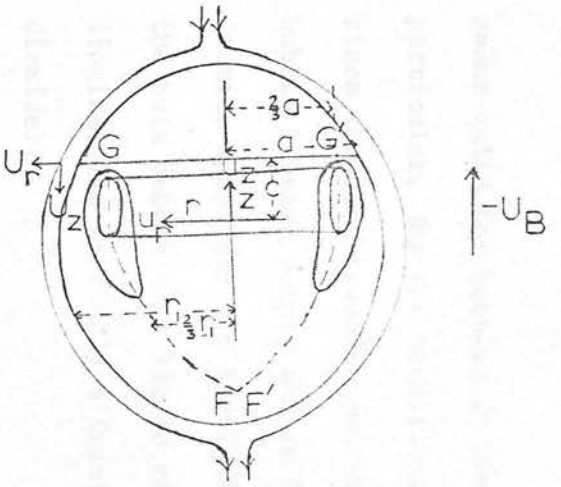

(c)

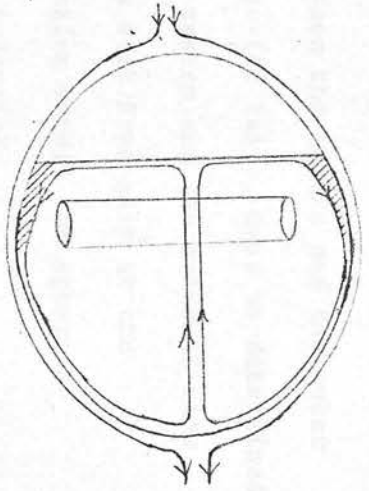

(d)

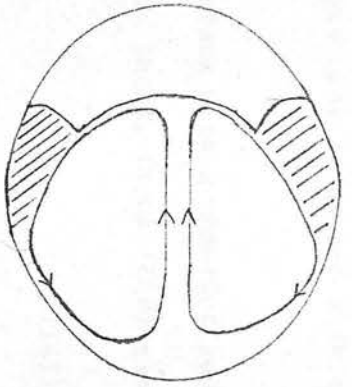

(e)

seems valid for bubbles in most gas-liquid contactors and, in particular, for the conditions prevailing in the current work, since the mass transfer measurement point is 65.5 cm above the bubble release point, and so for the short time taken by the carbon dioxide spherical cap bubble to traverse this distance, (2-3 seconds), the bulk bubble wake liquid remains almost completely void of carbon dioxide, (in fact only a fraction of 1 per cent saturated with carbon dioxide).

For diffusion from a plane interface with a constant surface concentration into a semi-infinite liquid phase, Crank (C18) gives

$$K_L = (D_L/\pi t)^{1/2} \qquad (141)$$

i.e.

$$K_L = 0.57\ (D_L/t)^{1/2} \qquad (142)$$

From Eqn. (142) it can be seen that to estimate the bubble rear mass transfer coefficient, K_{LR}, the time, t, taken by a liquid element to traverse the distance between the centre and the outer edge of the bubble floor, AB (see Fig. (42 (a))), must be determined.

Apply a velocity - U_B to the system and the external flow becomes flow over a stationary sphere with free slip at the spherical surface because of the rotation within the sphere.

Lamb (L2) gives the velocity potential

$$\phi'' = \frac{1}{2}\, U_B\, \frac{a^3}{\rho^2}\, \cos\theta \qquad (143)$$

in spherical polar coordinates for a moving sphere, with radius a

and/

and independent variables ρ, θ (Fig. (42 (b))

$$u\rho = - \frac{\delta\phi''}{\delta\rho} = U_B \frac{a^3}{\rho^3} \cos\theta \tag{144}$$

$$u_\theta = - \frac{1}{\rho} \frac{\delta\phi''}{\delta\theta} = \frac{1}{2} U_B \frac{a^3}{\rho^3} \sin\theta \tag{145}$$

Converting to cylindrical polar coordinates and applying the additional z-component of velocity - U_B (see Fig. (42 (c)))

$$u_z = u_\rho \cos\theta - u_\theta \sin\theta - U_B \tag{146}$$

i.e.

$$u_z = \frac{U_B a^3}{(r^2+z^2)^{5/2}} (z^2 - \frac{1}{2} r^2) - U_B \tag{147}$$

$$u_r = u_\rho \sin\theta + u_\theta \cos\theta \tag{148}$$

i.e.

$$u_r = \frac{3}{2} \frac{U_B a^3 rz}{(r^2+z^2)^{5/2}} \tag{149}$$

where

$$r = \rho\sin\theta \tag{150}$$

$$z = \rho\cos\theta \tag{151}$$

On the spherical surface

$$u_r = \frac{3}{2} U_B \sin\theta \cos\theta \tag{152}$$

$$u_z = - \frac{3}{2} U_B \sin^2\theta \tag{153}$$

Eqns. (152) and (153) provide two boundary conditions over the spherical/

spherical surface.

$u_z = 0$ at the plane $z = c$ (Fig. (42 (c)).

Fig. (5) shows the bubble wake to consist of a toroidal vortex moving with the bubble. The toroidal vortex equations in cylindrical polar coordinates are thus derived below. The independent variables are r and z, the velocities u_r and u_z, and there is no u_θ. The velocities in the wake are assumed not to vary with θ or t, i.e. the wake is taken to be symmetrical and stable with respect to time.

The continuity equation is, (Chap. III 12, (R7))

$$\text{div } \underline{u} = \frac{1}{r}\frac{\delta}{\delta r}(ru_r) + \frac{1}{r}\frac{\delta}{\delta z}(ru_z) \tag{154}$$

or

$$\frac{\delta u_r}{\delta r} + \frac{\delta u_z}{\delta z} = -\frac{u_r}{r} \tag{155}$$

Eqn. (154) is satisfied by a stream function ψ' such that

$$ru_r = \frac{\delta \psi'}{\delta z} \tag{156}$$

$$ru_z = -\frac{\delta \psi'}{\delta r} \tag{157}$$

The equations of motion are, (Chap. III 12, (R7))

$$u_r \frac{\delta u_r}{\delta r} + u_z \frac{\delta u_r}{\delta z} = -\frac{1}{\rho}\frac{\delta p}{\delta r} + \nu\left(\frac{1}{r}\frac{\delta}{\delta r} r \frac{\delta}{\delta r} u_r + \frac{\delta^2 u_r}{\delta z^2} - \frac{u_r}{r^2}\right) \tag{158}$$

u_r /

$$u_r \frac{\delta u_z}{\delta r} + u_z \frac{\delta u_z}{\delta z} = - \frac{1}{\rho} \frac{\delta p}{\delta z} + \nu \left(\frac{1}{r} \frac{\delta}{\delta r} r \frac{\delta u_z}{\delta r} + \frac{\delta^2 u_z}{\delta z^2} \right) \qquad (159)$$

p is eliminated by differentiating Eqn. (158) with respect to z and Eqn. (159) with respect to r,

$$\frac{\delta u_r}{\delta z} \left(\frac{\delta u_r}{\delta r} + \frac{\delta u_z}{\delta z} \right) + u_r \frac{\delta^2 u_r}{\delta r \delta z} + u_z \frac{\delta^2 u_r}{\delta z^2}$$

$$= - \frac{1}{\rho} \frac{\delta^2 p}{\delta r \delta z} + \nu \left(\frac{1}{r} \frac{\delta}{\delta r} r \frac{\delta^2 u_r}{\delta r \delta z} + \frac{\delta^3 u_r}{\delta z^3} - \frac{1}{r^2} \frac{\delta u_r}{\delta z} \right) \qquad (160)$$

$$\frac{\delta u_z}{\delta r} \left(\frac{\delta u_r}{\delta r} + \frac{\delta u_z}{\delta z} \right) + u_r \frac{\delta^2 u_2}{\delta r^2} + u_z \frac{\delta^2 u z}{\delta r \delta z}$$

$$= - \frac{1}{\rho} \frac{\delta^2 p}{\delta z \delta r} + \nu \left(\frac{\delta}{\delta r} \frac{1}{r} \frac{\delta}{\delta r} r \frac{\delta u_z}{\delta r} + \frac{\delta^3 u z}{\delta r \delta z^2} \right) \qquad (161)$$

Subtracting Eqn. (161) from Eqn. (160) and substituting Eqn. (155),

$$\left(u_r \frac{\delta}{\delta r} + u_z \frac{\delta}{\delta z} - \frac{u_r}{r} \right) \left(\frac{\delta u_r}{\delta z} - \frac{\delta u_z}{\delta r} \right)$$

$$= \nu \left(\frac{\delta}{\delta r} \frac{1}{r} \frac{\delta}{\delta r} r + \frac{\delta^2}{\delta z^2} \right) \left(\frac{\delta u_r}{\delta z} - \frac{\delta u_z}{\delta r} \right) \qquad (162)$$

where

$$\frac{\delta u_r}{\delta z} - \frac{\delta u_z}{\delta r} = w_2 \qquad (163)$$

is the vorticity, (Chap. III 1, (R7)).

Take/

Take

$$\psi(rz) = r\,\phi\,(rz) \tag{164}$$

then from Eqns. (156), (157), (163) and (164),

$$w_2 = \frac{\delta}{\delta z}\left(\frac{1}{r}\frac{\delta r}{\delta z}\,\phi\right) + \frac{\delta}{\delta r}\left(\frac{1}{r}\frac{\delta r}{\delta r}\,\phi\right) \tag{165}$$

i.e.

$$w_2 = \left(D^2 + \frac{\delta^2}{\delta z^2}\right)\phi \tag{166}$$

where

$$D^2 = \frac{\delta}{\delta r}\frac{1}{r}\frac{\delta}{\delta r}\,r \tag{167}$$

Therefore from Eqn. (162),

$$\left(u_r\, r\,\frac{\delta}{\delta r}\frac{1}{r} + u_z\frac{\delta}{\delta z}\right)\left(D^2 + \frac{\delta^2}{\delta z^2}\right)_{\phi} = \nu\left(D^2 + \frac{\delta^2}{\delta z^2}\right)^2\phi \tag{168}$$

since

$$u_r\, r\,\frac{\delta}{\delta r}\,\frac{1}{r} = u_r\frac{\delta}{\delta r} - \frac{u_r}{r} \tag{169}$$

The physical explanation of Eqn. (168) is:
The rate of convection of vorticity from the wake liquid/bulk external liquid interface into the bubble wake = viscous rate of dissipation of vorticity in the bubble wake.

The differential equation,

$$\frac{\delta^2 y}{\delta x^2} + \frac{1}{x}\frac{\delta y}{\delta x} + \left(\beta_1^2 - \frac{q^2}{x^2}\right)y = 0 \tag{170}$$

has/

has the Bessel function solution $J_q\ (\beta_1 x)$, (p. 150, Ref. (J1)).

Now, from Eqn. (167)

$$D^2\ \phi = \frac{\delta}{\delta r}\ \frac{1}{r}\ (r\ \frac{\delta \phi}{\delta r} + \phi) \tag{171}$$

i.e.

$$D^2\ \phi = \frac{\delta^2 \phi}{\delta r^2} + \frac{1}{r}\ \frac{\delta \phi}{\delta r}\ - \frac{\phi}{r^2} \tag{172}$$

Comparing Eqns. (170) and (172) it is seen that $q = 1$. β_1 (from Eqn. (170)) is possibly present in the solution of Eqn. (168) because of the presence of $\frac{\delta^2}{\delta z^2}$.

Hence try as a solution to Eqn. (168)

$$\phi = J_1\ (f(z)r) \tag{173}$$

The following mathematical relationships are given in Ref. (J1), p. 149:

$$\frac{d}{dx}\ (x^q\ Jq\ (\beta_1 x)) = \beta_1 x^q\ J_{q-1}\ (\beta_1\ x) \tag{174}$$

$$\frac{d}{dx}\ (Jq\ (x)) = -\ \frac{q}{x}\ Jq\ (x) + J_{q-1}\ (x) \tag{175}$$

$$\frac{d^2}{dx^2}\ J_1\ (\beta_1\ x) = -\ \beta_1^2\ J_1\ (\beta_1\ x) \tag{176}$$

$$\frac{d}{dx}\ (x^{-q}\ Jq\ (\beta_1\ x)) = -\beta_1\ x^{-q}\ J_{q+1}\ (\beta_1\ x) \tag{177}$$

From Eqns. (157), (173) and (174),

u_z = /

$$u_z = -\frac{1}{r}\frac{\delta}{\delta r}\, r\, J_1\,(f(z)r) \;=\; -\,f(z)\,J_o\,(f(z)r) \qquad (178)$$

From Eqns. (156), (173) and (175),

$$u_r = \frac{1}{r}\,\frac{\delta}{\delta z}\; r\, J_1\,(f(z)r) = \left(J_o\,(f(z)r) - \frac{1}{f(z)r}\; J_1\,(f(z)r)\right) rf'(z) \qquad (179)$$

From Eqns. (163), (176), (177), (178) and (179),

$$w_2 = \frac{f'(z)}{f(z)}\; J_2(f(z)r) - \left((f(z))^2 + rf'(z)\right)\; J_1(f(z)r) \qquad (180)$$

Thus the solution tried, (Eqn. (173)), satisfies the boundary conditions on the central vertical axis of the bubble wake, observed in Fig. (5), for vorticity and the two components of velocity since:

(i) Eqn. (178) gives u_z to be a maximum at $r = 0$, since $J_o(f(z)r)$ has its maximum value at $r = 0$

(ii) Eqn. (179) gives u_r to be zero at $r = 0$, since $J_1(f(z)r) = 0$ at $r = 0$

(iii) Eqn. (180) gives w_2 to be zero at $r = 0$, since $J_1(f(z)r) = 0$ at $r = 0$ and $J_2(f(z)r) = 0$ at $r = 0$.

As a first approximation to the solution, the non-linear terms of Eqn. (168) are not considered, i.e. the variables z and r are taken to be separable. Hence from Eqn. (179) the velocity distribution along the bubble floor, $z = c$, is given by

$$u_r = /$$

$$u_r = K_1 J_1 (r) \qquad (181)$$

where K_1 is a constant.

Thus the velocity of a thin liquid element flowing along the gas-liquid interface of the gas bubble floor is taken to follow the J_1 (r) distribution as it flows outwards from the centre of the bubble floor, r = 0, to the edge of the bubble floor, r = a.

The calibration of the x of the J_1 (x) function in terms of distances in centimetres was done as follows:

The points through the bubble wake at which u_z was zero, i.e. where the streamlines were horizontal in the bubble photograph of Fig. (5), were noted. These were found to follow a curved path as indicated by lines FG, F'G' of Fig. (42 (c)). At any given z, the distance from the central vertical axis of the bubble wake to the line FG or the line F'G' was two-thirds of the distance from the same central axis to the outer boundary of the bubble wake. This was found by direct measurements on Fig. (5) and bubble photographs in Refs. (C12, C13, L19). From Eqn. (178) u_z is zero if f(z) and/or J_o (f(z)r) = 0. u_z is zero along the planar gas bubble floor z = c, i.e. f(z) = 0; but for a given $z < c$, u_z is not zero for all values of r lying within the bubble wake. Consequently for $z < c$, f(z) cannot be zero, and so when u_z is zero, J_o (f(z)r) = 0. The first zero of the J_o(x) function is given by Watson (W5) to occur at x = 2.405 units and this would be expected to correspond to the surface forming part of a spheroid of which FG and F'G' in Fig. (42 (c)) are part. Extrapolating to the plane z = c, it is found that/

that at x = 2.405 units both f(z) and J_o (f(z)r) are zero, and the spherical cap gas bubble semi-major axis, a, is (1.5 x 2.405), i.e. 3.6, units of x.

Table 5 below, (W5), gives J_1 (x) versus x, and from this table it is seen that J_1 (x) is positive for x = 3.6 units and negative for a larger x, (x just greater than 3.8 units). The negative value would result in the improbable situation of liquid flowing inwards along the bubble floor from its edge to its centre. Thus the non-rigorous solution, Eqn. (181), seems to be in agreement with observed flow directions and flow patterns in the bubble wake.

Table 5

x	J_1 (x)	x	J_1 (x)
0	0.0	0.1	0.0499
0.2	0.0995	0.3	0.1483
0.4	0.1960	0.5	0.2423
0.6	0.2867	0.7	0.3290
0.8	0.3688	0.9	0.4059
1.0	0.4401	1.1	0.4709
1.2	0.4983	1.3	0.5220
1.4	0.5419	1.5	0.5579
1.6	0.5699	1.7	0.5778
1.8	0.5815	1.9	0.5812
2.0	0.5767	2.1	0.5683
2.2	0.5560	2.3	0.5399
2.4	0.5202	2.5	0.4971
2.6	0.4708	2.7	0.4416
2.8	0.4097	2.9	0.3754
3.0	0.3391	3.1	0.3009
3.2	0.2613	3.3	0.2207
3.4	0.1792	3.5	0.1374
3.6	0.0955	3.7	0.0538
3.8	0.0128		
4.0	-0.0660		

5.5.2 Comparison of Theoretically Determined and Experimentally Determined bubble rear mass transfer coefficients

After converting x units to centimetres as described in Section 5.5.1, it was necessary to calibrate the J_1 (x) function (given in Table 5) in terms of distance per unit time, cm/sec, (i.e. to determine the constant K_1 in Eqn. (181)). From Table 5 it can be seen that over an interval of 0.2 x-units J_1 (x) varies linearly with x within an accuracy of 0.3 per cent. Hence the 3.6 x-units representing the spherical cap gas bubble semi-major axis was divided into 18 intervals of 0.2 x-units each, and the time taken by a liquid element to traverse the 0.2 x-units distance calculated on the basis of J_1 (x) values in the middle of these intervals, (i.e. at x = 0.1, 0.3, ..., 3.3, 3.5). These times were summed over the 18 intervals to give t in Eqn. (142), hence permitting the calculation of K_L if D_L for the gas-liquid system under consideration is known. The velocity of the main stream liquid flowing over the spheroid, consisting of gas spherical cap and liquid wake, at the separation point, U, was resolved into its components U_r and U_z (see Fig. (42 (c))). The component U_r was matched with $u_{r\ (r=a)}$ and at any given distance, r_1, along the bubble floor from the centre.

$$u_{r(r=r_1)} = \frac{J_1\ (r_1).U_r}{0.0955} = \frac{J_1\ (r_1)\ u_{r(r=a)}}{0.0955} \qquad (182)$$

since J_1 (x) = 0.0955 at x = 3.6 (see Table 5).

As for u_r in Eqn. (152)

U_r = /

$$U_r = \frac{3}{2} U_B \sin\theta \cos\theta \qquad (183)$$

From Fig. (42 (a)),

$$2b + x = r \qquad (184)$$

$$\sin\theta = \frac{a}{r} \qquad (185)$$

$$r^2 = a^2 + x^2 = a^2 + 4b^2 - 4br + r^2 \qquad (186)$$

i.e.

$$4br = a^2 + 4b^2 \qquad (187)$$

i.e.

$$r = \frac{a^2 + 4b^2}{4b} \qquad (188)$$

The spherical cap eccentricity, E, is given by,

$$E = \frac{2a}{2b} \qquad (56)$$

so from Eqns. (188) and (56)

$$r = \frac{a(E^2 + 4)}{4E} \qquad (189)$$

From Eqns. (185) and (189),

$$\sin\theta = \frac{4E}{(E^2 + 4)} \qquad (190)$$

Now,

$$\cos\theta = (1 - \sin^2\theta)^{1/2} \qquad (191)$$

From Eqns. (190) and (191),

$$\cos\theta = \frac{(E^2 - 4)}{(E^2 + 4)} \qquad (192)$$

Therefore from Eqns. (183), (190) and (192),

$$U_r = \frac{6U_B E (E^2 - 4)}{(E^2 + 4)^2} = u_{r(r=a)} \qquad (193)$$

The/

The time t_i taken for a liquid element to traverse the 0.2 x-units interval, $(x_1 - 0.1)$ x-units to $(x_1 + 0.1)$ x-units, is obtained theoretically from Eqn. (194) which results from Eqns. (182) and (193),

$$t_i = \frac{0.0955\ a\ (E^2 + 4)^2}{108\ J_1(r_1) U_B\ E(E^2-4)} \qquad (194)$$

where E is taken to be E_2, measured bubble width/calculated bubble height, a is the bubble major semi-axis, and $^a/18$ cm is the length of a 0.2 x-units interval.

The time, t, for substitution into Eqn. (142) is given by,

$$t = \sum_{i=1}^{i=18} t_i \qquad (195)$$

i.e. t is a function of $\sum_{i=1}^{i=18} \frac{1}{J_1(0.2i - 0.1)}$

Bubble rear mass transfer coefficients were not experimentally measured directly during the course of this work, but were indirectly obtained from the instantaneous overall mass transfer coefficient data as follows:

For a given spherical cap bubble size the experimentally measured overall mass transfer coefficient, K_L, and the theoretical Boussinesq mass transfer coefficient, K_{Ls}, (Eqn. (79)), were read off from the smooth curves drawn through the experimental and theoretical K_L versus D_e data for each gas-liquid system investigated (see Figs. (31), (32), (33), (34) and (41)). The Lochiel-Calderbank equation/

equation for spherical cap bubbles, Eqn. (87), was then used to estimate transfer over the frontal area of the spherical cap bubble only,

$$\frac{Sh_{sc}}{Sh_s} = \frac{K_{Lsc}}{K_{Ls}} = \frac{1.58\ (3E^2 + 4)^{2/3}}{E^2 + 4} \qquad (87)$$

where subscripts sc and s refer to spherical cap frontal area and sphere respectively.

For the three Newtonian liquids used, (water and two aqueous Glycerol solutions), a spherical cap bubble was considered to be in potential flow if the wall-effect corrected, (Eqn. (38)), measured velocities lay within 5 per cent of the theoretical Davies-Taylor spherical cap bubble velocity,

$$U = 25.0\ V^{1/6} \qquad (31)$$

or the Mendelson velocity,

$$U = \sqrt{\frac{2\sigma}{D_e \rho_o} + \frac{gD_e}{2}} \qquad (34)$$

It is apparent from Figs. (18), (34), (35) and (41) that potential flow conditions over the entire spherical cap bubble frontal area is approached only for the largest bubble diameters investigated in the non-Newtonian aqueous Polyox solution, and for these large bubbles, as shown in Figs. ((39) xiii) and (42 (e)), the bubble floor is so distorted from a planar configuration that the velocity matching technique applied around the edge of the bubble floor/

floor and described in the early part of this Section of the report is inapplicable. Thus theoretical and experimental comparisons were carried out only for the three Newtonian liquids used.

The indirectly experimentally determined spherical cap rear transfer coefficient was given by,

$$K_{LR} = (K_L - \frac{K_{Lsc} \cdot A_F}{A}) \frac{A}{A_R} \qquad (196)$$

where K_L is the experimentally measured instantaneous overall mass transfer coefficient. Combining Eqns. (87) and (196),

$$K_{LR} = (K_L - \frac{1.58\ (3E^2 + 4)^{2/3} K_{Ls} A_F}{(E^2 + 4)A}) \frac{A}{A_R} \qquad (197)$$

where A, A_R and A_F have the usual meanings and E is taken to be E_2.

Eqns. (194), (195) and (142) for calculating the theoretical bubble rear transfer coefficients were programmed in Atlas Autocode for processing on the KDF9 computer, as was Eqn. (197) for estimating the experimental comparisons. The results from theory and experiment for water and the two aqueous Glycerol solutions are shown in Fig. (43), and the values of the ratio (K_{LR}/K_{Lsc}) experimental versus D_e are given in Table 6 below.

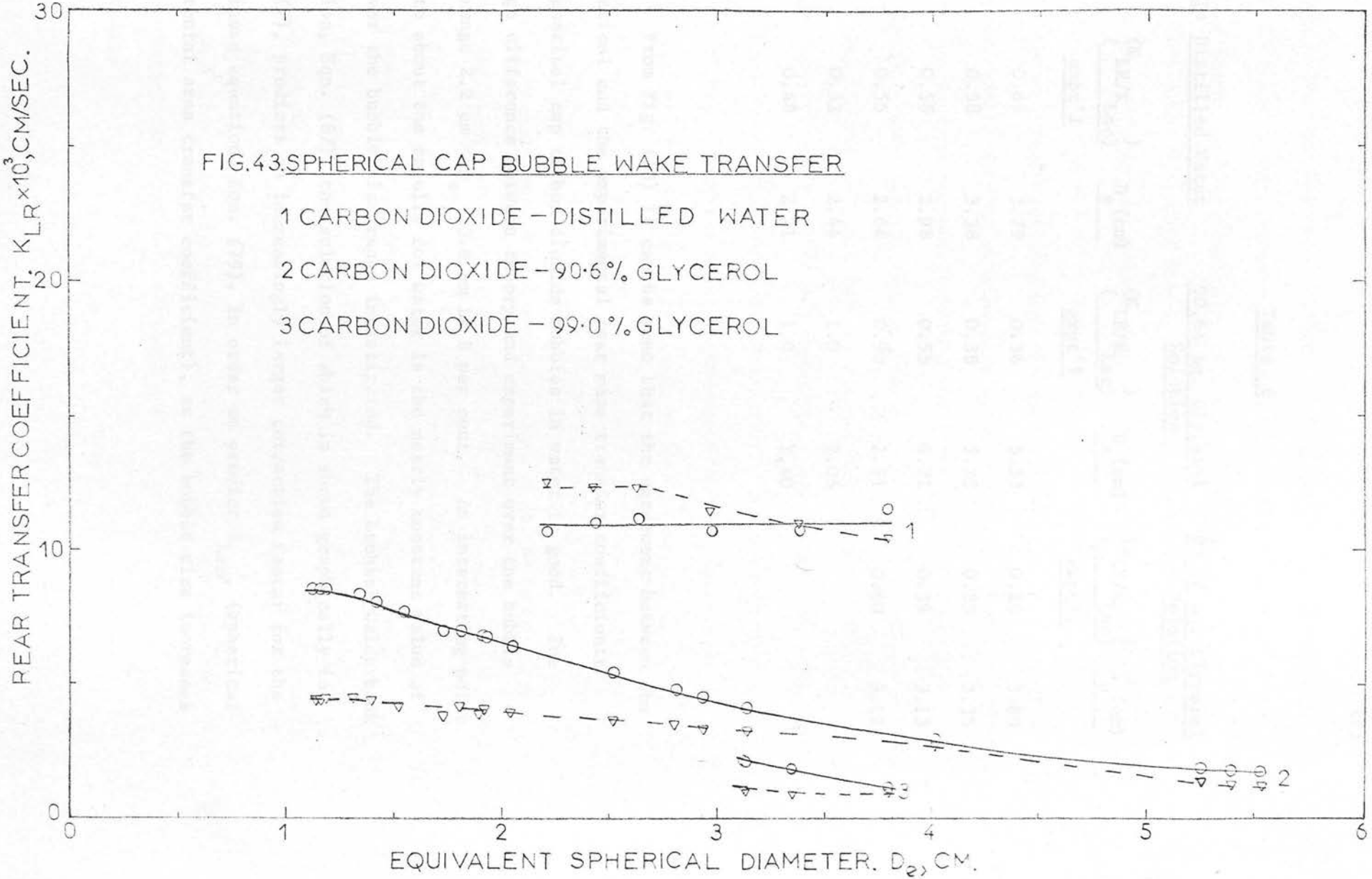
FIG. 43. SPHERICAL CAP BUBBLE WAKE TRANSFER
1 CARBON DIOXIDE – DISTILLED WATER
2 CARBON DIOXIDE – 90·6 % GLYCEROL
3 CARBON DIOXIDE – 99·0 % GLYCEROL
REAR TRANSFER COEFFICIENT, $K_{LR} \times 10^3$, CM/SEC.
EQUIVALENT SPHERICAL DIAMETER, D_e, CM.
0
10
20
30
1
2
3
4
5
6
1
2
3

Table 6

LIQUID: Distilled Water		90.6% aq. Glycerol Solution		99.0% aq. Glycerol Solution	
$\left(\frac{K_{LR}}{K_{Lsc}}\right)_{expt'l}$	D_e (cm)	$\left(\frac{K_{LR}}{K_{Lsc}}\right)_{expt'l}$	D_e (cm)	$\left(\frac{K_{LR}}{K_{Lsc}}\right)_{expt'l}$	D_e (cm)
0.65	3.79	0.36	5.53	0.28	3.80
0.58	3.38	0.38	5.25	0.35	3.35
0.55	2.98	0.55	4.01	0.39	3.13
0.55	2.64	0.90	2.51	0.40	3.12
0.52	2.44	1.0	2.05		
0.48	2.21	1.0	1.40		

From Fig. (43) it can be seen that the agreement between the theoretical and the experimental rear mass transfer coefficients for spherical cap carbon dioxide bubbles in water is good. The average difference between theory and experiment over the bubble size range 2.2 cm < D_e < 3.8 cm is 8 per cent. An interesting point to note about the results for water is the nearly constant value of K_{LR} over the bubble size range investigated. The Lochiel-Calderbank equation, Eqn. (87), the solution of which is shown graphically in Fig. (7), predicts an increasingly larger correction factor for the Boussinesq equation, Eqn. (79), in order to predict K_{Lsc}, (spherical cap frontal area transfer coefficient), as the bubble size increases and/

and wall effect becomes more pronounced, resulting in a reduction in bubble eccentricity. These two facts when combined counteract the Boussinesq equation prediction of a falling overall transfer coefficient with increasing bubble size at large bubble sizes, when U_B is nearly constant at a value near that predicted by the Dumitrescu equation, Eqn. (36), and D_e is increasing. The present work and that of Loudon (L19) both indicate the overall mass transfer coefficient of carbon dioxide bubbles in distilled water in a 10.16 cm I.D. column to remain nearly constant for 3 cm < D_e < 4.8 cm, the maximum bubble size investigated by Loudon.

The theoretical/experimental K_{LR} comparison for the two aqueous Glycerol solutions show a common tendency to decrease with increasing bubble size. The data for the 90.6 per cent aqueous Glycerol solution covers a wider size range than that for the 99.0 per cent aqueous Glycerol solution since the spherical cap shape is assumed by bubbles at a smaller size in the first mentioned solution, (see Fig. (38)), and from Figs. (16) and (17) the wall effect corrected bubble rise velocities indicate potential flow over the bubble nose at a smaller bubble size in the former solution. In addition, bubble skirting for D_e > 3.8 cm in the 99.0 per cent aqueous Glycerol solution made it impracticable to separate out K_{LR} from K_L for bubbles in this size range since mass transfer also occurred from the inner and outer surfaces of the skirt in addition to the bubble nose and floor.

The two aqueous Glycerol solutions indicate good agreement between theory and experiment for bubble D_e > 3.75 cm, the mean difference/

difference in this bubble size range between K_{LR} determined by the two methods being less than 20 per cent. The K_{LR} determinations for both theory and experiment indicate a tendency for K_{LR} to level out at a constant value at large bubble sizes, $D_e > 5$ cm, for the 90.6 per cent aqueous Glycerol solution, ($\nu = 1.46$ cm^2/sec, nearly the same as ν for the aqueous Glycerol solution in which the bubble in Fig. (5) was photographed (1.43 cm^2/sec)). As bubble sizes are decreased below $D_e = 3.5$ cm, the difference between the theoretical and the experimental curves for both aqueous Glycerol solutions increases. Both the theoretical and experimental curves level out at constant values for bubble $D_e < 1.5$ cm in the 90.6 per cent aqueous Glycerol solution. However, at these small bubble sizes, the theoretically predicted K_{LR} is only 55 per cent of the experimentally determined K_{LR}. It is suggested that this may be due to a thickening of the boundary layer between the liquid main stream flow and the gas bubble-liquid wake spheroid at and below the separation point for small spherical cap bubbles in viscous solutions, this region being shown hatched in Fig. (42 (d)). This would result in the velocity matching method used for U_r and u_r , which is described in the early part of this report Section, being inaccurate.

In general Eqn. (181) predicts the correct trends for bubble rear mass transfer coefficients for the three Newtonian liquids to which it was applied as bubble size is monotonically increased or decreased/

decreased . The orders of magnitude of K_{LR} predicted by Eqn. (37) are in good agreement with the indirectly experimentally determined values. When consideration of the inherent systematic errors in the determination of eccentricity values used in Eqns. (194) and (197), and the fact that a given percentage difference between K_{Lsc} as calculated from Eqn. (87) and K_{Lsc} in practice would result in a percentage difference between theoretically and experimentally determined K_{LR} approximately three times as large, the agreement between the approximate theoretical solution and experiment is encouraging.

Eqn. (194) predicts for E = 2 an infinite time, t, i.e. a stagnant liquid wake. Assuming conditions of potential flow, Guthrie and Bradshaw (G15) showed that if the gas in the skirt trailing a spherical cap bubble is in viscous flow, then the two limiting conditions for gas flow within the skirt resulting in stable bubble skirts are that,

$$\Delta = 2 \left(\frac{3 \mu_o U'}{\rho_o g} \right)^{\frac{1}{2}} \qquad (198)$$

for a circulating wake system in which the liquid velocity down the inside surface of the skirt is equal to that in the liquid flowing down the outside surface of the skirt, (where Δ is the skirt thickness and U' is the surface velocity of the liquid down the cylindrical skirt), and

Δ = /

$$\Delta = 2 \left(\frac{1.5\ \mu_o U'}{\rho_o g} \right)^{1/2} \qquad (199)$$

when the enclosed wake behind the bubble is completely stagnant.

Guthrie and Bradshaw's experimentally measured values of skirt thickness for large skirted spherical cap nitrogen bubbles (V_B = 53 cm^3) rising through an aqueous Glycerol solution (μ_o = 12 poises) gave a mean value for Δ of 41 μ having an accuracy of ± 30 per cent. The value of Δ predicted by Eqn. (199) using the stagnant wake model is 54μ and the value of Δ obtained from Eqn. (198) which uses the fully circulating wake model is 76μ. Thus Guthrie and Bradshaw (G15) concluded that for these large spherical cap bubbles (E = 2) the enclosed wake is relatively stagnant and the liquid moves freely down the outer gas-liquid interface of the skirt, in agreement with the predictions of Eqn. (194).

For E < 2, Eqn. (194) would result in a negative value for t. However, only very viscous solutions would be expected to reduce the bubble eccentricity below 2 at the high shear rates encountered when large bubbles rise through them. As a result the argument re a thickening of the boundary layer between the liquid main stream flow and the bubble wake region applied to smaller spherical cap bubbles in the two aqueous Glycerol solutions may be extended to larger spherical cap bubbles rising in these very viscous solutions. Thus Loudon's photographs (L19) of three-dimensional carbon dioxide bubbles with eccentricities less than 2, when particle tracers were used to outline the liquid flow patterns, indicate a marked boundary layer/

layer for the 3.0 per cent pseudoplastic aqueous CMC solution, which is non-existent in the low viscosity distilled water, and a weak toroidal vortex in the bubble wake. As a result the velocity matching method used to determine $u_{r(r=a)}$ may, here, also give values which are slightly too low, so the negative values of t which would be obtained in these cases need not be seriously considered. It is interesting to note that Loudon (L19) found $K_{LF}(= K_L \times \frac{A}{A_F})$ to agree approximately with the Boussinesq equation, (Eqn. (79), for spherical cap carbon dioxide bubbles in the 3.0 per cent aqueous CMC solution; signifying virtually no bubble rear transfer and hence a very weak or non-existent toroidal vortex in the wake region, which is in general agreement with the bubble rear transfer theory predictions for bubbles with eccentricities in the region of 2.

CONCLUSIONS

An experimental investigation was carried out into the motion and mass transfer of single carbon dioxide bubbles in free rise through three Newtonian liquids, (distilled water, a 90.6 per cent and a 99.0 per cent aqueous Glycerol solution), covering a wide range of liquid viscosity, (0.009 P to 7.75 P), and one non-Newtonian viscoelastic pseudoplastic liquid, (a 1.0 per cent aqueous Polyox solution), contained in a 10.16 cm I.D. column. A wide range of bubble sizes was investigated (0.2 cm < D_e < 6 cm).

In the present experimental work the equipment of Loudon (L19) was modified to reduce the possibilities of liquid phase contamination, and to ensure isothermal conditions in the mass transfer column. A novel data processing technique was used which allowed accurate measurement of the instantaneous rate of change of pressure of the constant volume system as the bubble rose through the liquid and dissolved. This was effected by recording the voltage variation, (corresponding to the column liquid pressure variation), from a pressure transducer on magnetic tape, and digitising the recording with the aid of an analogue-digital converter and a digital computer. The quantities evaluated in the experimental program were instantaneous values of bubble diameter, rise velocity, mass transfer product, eccentricity, surface area and overall mass transfer coefficient. An analysis was made of the experimental errors involved in the measurement of bubble diameter, rise velocity and mass transfer product/

product. A detailed comparison of the experimental data with the existing theoretical models relating to bubble rise velocity and overall mass transfer coefficient was carried out.

The terminal rise velocities of the carbon dioxide bubbles in the three Newtonian liquids confirmed previous findings with respect to wall proximity effects and the approach to slug flow conditions for sufficiently large bubbles; and also with respect to the general shapes of the bubble velocity versus diameter graphs. With increasing Newtonian liquid viscosity, the bubble terminal rise velocity data for a given bubble size decreased, this effect being most marked for bubble diameters, D_e, < 3 cm. Existing theories were found to adequately describe observed bubble rise velocity data for very small bubbles in creeping flow, which followed the Hadamard/Rybczynsky law (Eqn. (19)), large spherical cap shaped bubbles in potential flow which obeyed the Davies-Taylor equation (Eqn. (31)) and the Mendelson equation (Eqn. (34)), and oblate spheroidal bubbles in potential flow in the low viscosity distilled water, which followed the Mendelson equation predictions, (Eqn. (34)). The Dumitrescu equation for gas slugs in potential flow, (Eqn. (36)), was found to predict the upper limit for the rise velocity data of large bubbles in the Newtonian liquids contained in the 10.16 cm I.D. column. In the bubble size region intermediate between creeping flow and potential flow conditions no complete theoretical understanding of bubble rise velocity phenomena in Newtonian liquids at present exists.

The/

The rise velocity data of the carbon dioxide bubbles in the non-Newtonian 1.0 per cent aqueous Polyox solution was always lower than the data for distilled water. The terminal rise velocities of large spherical cap bubbles in the Polyox solution asymptotically approached the predictions of the Dumitrescu equation, Eqn. (36). A distinctive feature of the velocity data pertaining to the Polyox solution was the abrupt increase in velocity, by a factor of over 4, at a critical bubble size, D_e = 0.27 cm. A possible explanation of the existence of such a critical bubble size suggested by Astarita and Apuzzo (A7), was a transition from the Stokes (solid body) to the Hadamard/Rybczynsky (circulating body) regime of flow, the abruptness of the transition being due to viscoelasticity.

Bubble shapes were characterised by an eccentricity parameter (E = bubble width/bubble height), and by the shape ratio, $S_R = D_e$/ bubble width. Bubble shapes observed in distilled water varied through spherical to oblate spheroidal to spherical cap with increasing bubble size. Similar bubble shape configurations were observed in the 90.6 per cent aqueous Glycerol solution. As bubble size was increased in the 99.0 per cent aqueous Glycerol solution, the bubbles went from spheres to oblate spheroids to > hemispheres to spherical caps; the spherical caps developing stable symmetrical trailing skirts of gas for bubble D_e > 3.9 cm. The eccentricity data for the carbon dioxide bubbles in the three Newtonian liquids investigated decreased with increasing Newtonian liquid viscosity, though there was a tendency towards convergence at large bubble sizes.

Bubble/

Bubble shapes observed in the aqueous Polyox solution went from spherical to prolate spheroidal to that of a top (this last transition occurring at the critical bubble size), to that of an oblate spheroid with a tail, to that of a spherical cap. A previously unreported bubble floor configuration was observed for large spherical cap bubbles, $D_e > 4.5$ cm, in the aqueous Polyox solution.

Actual bubble surface areas were evaluated from the measured bubble photographic horizontal dimension, and the measured vertical dimension adjusted so that agreement was attained between the calculated bubble volume, (based on an idealised bubble shape configuration), and the measured bubble volume.

Instantaneous overall mass transfer coefficients, K_L, based on actual bubble surface areas were evaluated for carbon dioxide bubbles in each of the four solutions investigated. For carbon dioxide bubbles in water and for large carbon dioxide bubbles in the two aqueous Glycerol solutions, the mass transfer coefficient data were approximately predicted by the relationship due to Boussinesq (Eqn. (79)). Small spherical carbon dioxide bubbles in the Glycerol solutions followed closely the predictions of the Levich equation for circulating spheres in creeping flow; and when these small bubbles were oblate spheroidal in shape, the K_L versus D_e data agreed with the theoretical modifications of Sy and Lightfoot (S18) to the Levich equation predictions.

An interesting feature of the K_L versus D_e plot for each of the aqueous Glycerol solutions was the existence of a maximum K_L value/

value greater than that predicted by the Boussinesq equation. This maximum was found to occur shortly before the onset of creeping flow conditions and corresponded to a bubble shape transition from spherical cap, (with an eccentricity > or < 2), to oblate spheroid. It seems that this shape transition and the impending flow regime transition to creeping flow resulted in instabilities in the liquid flow around the bubble, resulting in an enhancement of the K_L value. An enhancement in the measured K_L value for the large skirted bubbles in the 99.0 per cent aqueous Glycerol solution, (D_e > 3.9 cm), was accounted for by mass transfer from the inner and outer surfaces of the skirt, noting that K_L for these skirted bubbles was obtained from K_LA by dividing by the surface area of the spherical cap.

The K_L versus D_e plot for carbon dioxide bubbles in the non-Newtonian Polyox solution had two maxima, these maxima being found to correspond to bubble shape transitions. The suggestion of Astarita and Apuzzo (A7) that at the critical bubble size in viscoelastic pseudoplastic liquids a transition occurred from Stokes (rigid body) behaviour to Hadamard/Rybczynsky (circulating body) behaviour was confirmed by the mass transfer coefficient data for carbon dioxide bubbles in the Polyox solution. This data indicated a transition from agreement with the Levich equation for rigid spheres in creeping flow (Eqn. (69)) to agreement with the Levich equation for circulating spheres in creeping flow (Eqn. (75)) at this bubble size. For large spherical cap bubbles, D_e > 4.0 cm, in the Polyox solution, the experimental K_L data were approximately predicted by the Boussinesq equation, Eqn. (79).

The/

The Boussinesq equation which predicts transfer from a sphere in potential flow represents only an approximation to transfer from spherical cap bubbles in potential flow. For these spherical cap bubbles the Lochiel-Calderbank equation, Eqn. (87), more accurately represents bubble nose transfer, but no theoretical model has previously been developed for the bubble wake transfer. Hence in Section 5.5 of Chapter 5 an approximate theoretical solution for mass transfer from the rear of spherical cap bubbles was derived; and the agreement between indirectly experimentally determined bubble rear transfer coefficients and the predictions of the approximate theoretical model for bubble wake transfer was found to be encouragingly good.

RECOMMENDATIONS FOR FUTURE WORK

1. The experimental study of single bubble mass transfer coefficient, terminal rise velocity and shape for bubbles in free rise through a stagnant liquid pool, could be extended to other non-Newtonian liquids, in particular dilatant liquids, (e.g. aqueous solutions of sodium silicate and of gum arabic (F10)), for which no published data exists.

2. A more rigorous experimental testing of the simplified bubble rear mass transfer theory developed in Section 5.5 of Chapter 5 could be carried out by measuring directly bubble rear transfer. A possible method of doing this is to note bubble shape, velocity of rise, and wake structure, (using some flow visualisation technique such as particle tracers), for a given bubble size in a liquid. The bubble nose shape could then be duplicated by a dumping cup under which a soluble gas is trapped. The appropriate liquid could then be passed over the cup with its gas bubble trapped below, at a suitable rate, and the wake structure checked to ensure that it remains the same as for the freely rising bubble. The rate of solution of the gas would then give a direct measure of bubble rear transfer, since only the bubble floor is exposed to the liquid.

3. A more rigorous solution of Eqn. (168) in Section 5.5.1 could be carried out in order to determine the liquid velocity distribution throughout the bubble wake. As this would probably require more detailed/

detailed knowledge of bubble wake structure, a photographic investigation, (using particle tracers), of the wake behind large three-dimensional spherical cap bubbles in various liquids could be carried out.

4. With certain modifications, the present experimental arrangement could be adapted to the study of mass transfer from bubbles immediately after coalescence, since if two bubbles rising through the column coalesce, the equations developed in Section 2 of Chapter 2 are applicable immediately a single bubble only exists. This would necessitate the design of a dumping cup to permit the collection of two bubbles, each of known volume, in the column, and to permit the release of these bubbles independently of each other to rise up the column central axis.

A P P E N D I X I

A.I. List of Electrical Circuitry and Equipment

A.I.i. OVERALL ELECTRICAL CIRCUITRY

A schematic circuit diagram showing the interconnections of all electrical equipment used is given in Fig. (44). In Fig. (44) are shown the supply sources and interconnections of the pressure transducer (Tr) and its zero balance circuit (C), the tape recorder (T.R.), photoelectric cell units P_1 and P_3 with their respective selector gates (SG1 and SG3), the electronic millisecond stopclock, photoelectric cell unit P_2 with its associated D.C. relay stage/ selector gate unit (RS/SG2) operating on the camera solenoid (S), and the manually operated pulse circuit (MP).

The illumination sources S1 and S3 associated with photo-electric cell units P_1 and P_3 respectively were controlled by the 0 - 260 V A.C. slide regulator V1; and a similar regulator V2 controlled the illumination source S2 of photoelectric cell unit P_2.

5 KΩ potentiometers R1 and R3 permitted the adjustment of the steady state voltages across the output terminals of P_1 and P_3 to within close proximity of the selector gate SG1 and SG3 trigger levels. A 0 - 1 mA D.C. moving coil meter (M) assisted the initial setting of P_1 and P_3 output voltages close to the trigger levels of SG1 and SG2, since a sudden deflection on the monitor meter, M, indicated that the selector gate switched into M had been triggered/

FIG. 44. ELECTRICAL CIRCUITRY

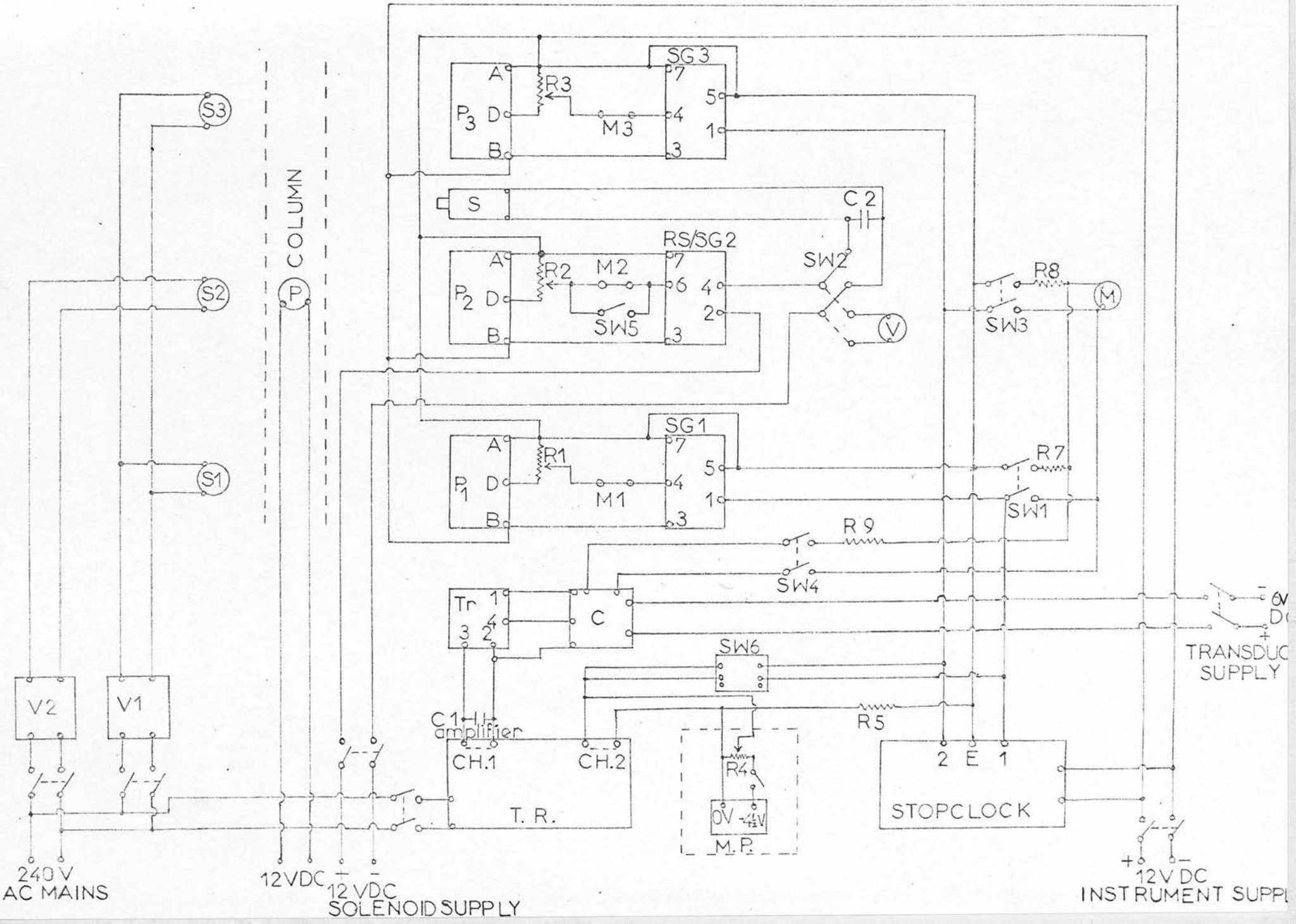

triggered. After setting R1 and R3 close to the trigger levels of SG1 and SG3, meter M was switched into circuit with the pressure transducer zero balance network by closing switch SW4. The transducer supply voltage could thus be monitored. The voltage inputs to M were suitably attenuated by resistors R7, R8 (15 KΩ) and R9 (10 KΩ). The steady state output voltage of P_2 was adjusted to within close proximity of the trigger level of the combined D.C. relay/selector gate unit RS/SG2 by means of a 20 KΩ linear potentiometer R2 connected across the output terminals of P_2. A 0 - 12 V D.C. voltmeter, V, wired to unit RS/SG2 via a double pole changeover switch SW2 assisted this operation, since a sudden full scale deflection on V indicated the closing of the relay at a particular setting of R2. After the setting of the steady state output voltage of P2, SW2 was switched to the solenoid S.

The keying arrangement to permit manual operation of the electronic stopclock and camera, (microswitches M1, M2 and M3 in conjunction with a single auto/manual switch SW5), was not used in the present work. For the small bubbles in the aqueous glycerol and aqueous polyox solutions which could not be detected by the photoelectric cell units P_1, P_2 and P_3, the manually operated pulse circuit (MP) was used and the camera shutter was operated manually.

A.I.ii. PRESSURE TRANSDUCER

Makers Solartron Limited

Type NT4-313 I-10

Serial/

Serial No.	F.2717		
Pressure Range	0-10 p.s.i.g.		
Excitation	5 V D.C./A.C. R.M.S.		
Diaphragm material	Stainless Steel F.V.520B		
Test Temperature ^{o}F	-65	+70	+250
Sensitivity mV F.S.	20.24	20.36	20.56
Linearity % F.S.	-1.19	-1.18	-1.36
Hysteresis % F.S.	less than 0.2		
Zero shift with temperature	+ 0.004% F.S./^{o}F		
Input Impedance	350Ω		
Output Impedance	350Ω		

Note

A circuit diagram of the pressure transducer pickup and zero balance network is shown in Fig. (45). The setting of potentiometer R11 (5 KΩ) controlled the transducer output voltage zero point; while potentiometer R10 (500Ω) adjusted the transducer supply voltage to 5.0 V. D.C.

The pressure transducer diaphragm was attached to a pair of strain gauge wires connected in a Wheatstone Bridge network. Deflection of the diaphragm produced an out of balance voltage which appeared at the transducer output terminals.

A.I.iii TAPE RECORDER

Make/

FIG .45 CIRCUIT DIAGRAM OF PRESSURE TRANSDUCER PICKUP AND ZERO BALANCE NETWORK

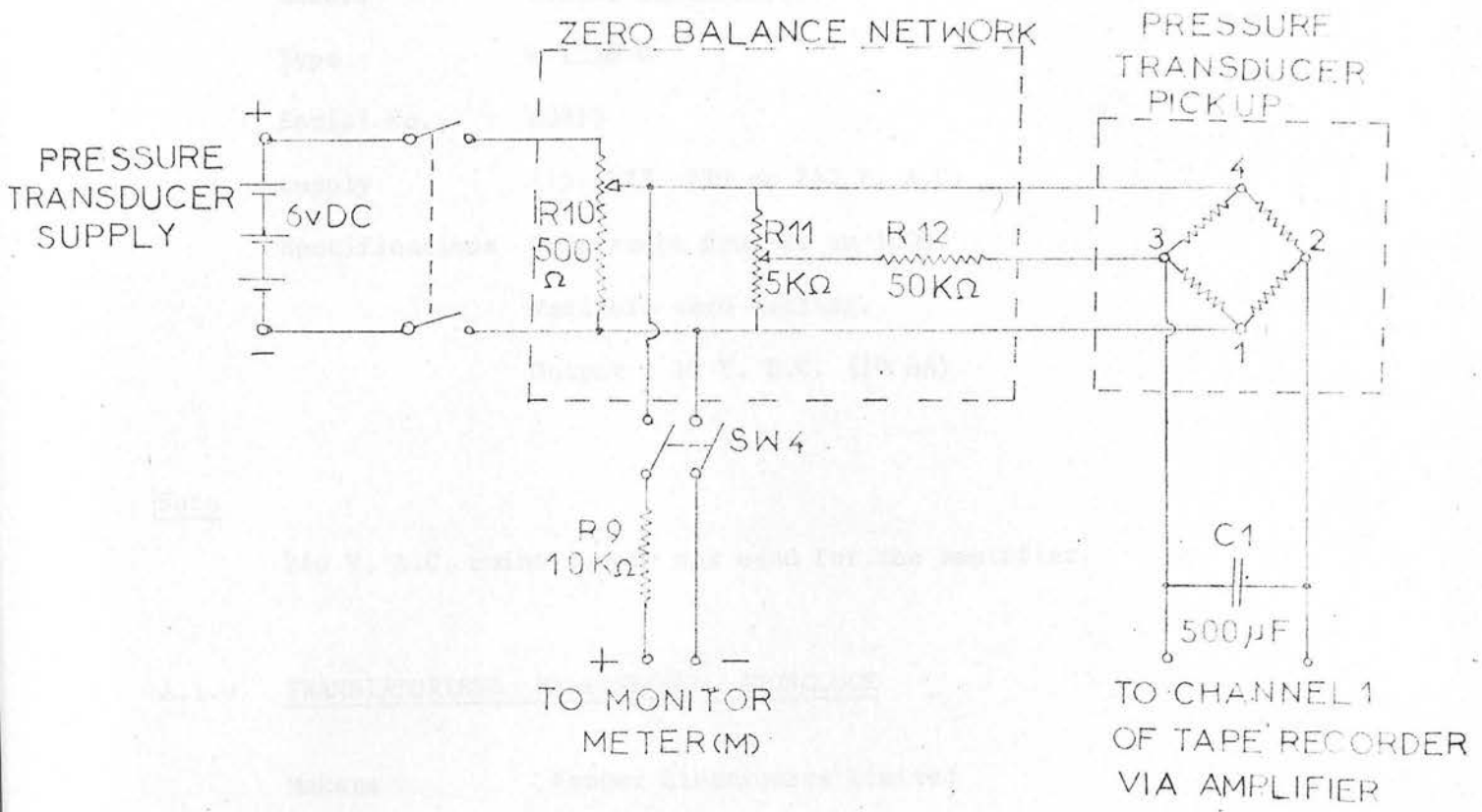

Make Elliott Tanberg

Type 64/E2

Serial No. 192

Specifications 3-speed ($1\frac{7}{8}$, $1\frac{3}{4}$, $7\frac{1}{2}$ i.p.s.)

2 Channel, adjustable gains on each channel.

A.I.iv VOLTAGE AMPLIFIER

Makers Rochar Electronique

Type A 1338 C

Serial No. 00915

Supply 115, 127, 220 or 240 V. A.C.

Specifications Gain range from 20 to 1000.

Variable zero setting.

Output ± 10 V. D.C. (10 mA)

Note

240 V. A.C. mains supply was used for the amplifier.

A.I.v. TRANSISTORISED MILLISECOND STOPCLOCK

Makers Venner Electronics Limited

Type T.S.A. 1014/BC

Serial No. G 6987

Time Range 0.0001 to 100,000 sec.

Pulse Trigger 4 V. positive going pulse having rise time of 2μs or less

Input Impedance 300 KΩ shunted by 80 pF

Supply 10-14 V. D.C.

A.I.vi PHOTOELECTRIC CELL UNITS P_1, P_2, P_3

Constructed according to T.S.12 circuit (Venner Electronics Ltd.)

Pin No.

A Supply positive (earthy)

B Supply negative

C Output I (Positive pulse when light beam broken)

D Output II (Positive pulse when light beam made)

Supply 6-12 V. D.C.

Note

Output II (Pin D) was used in all cases for correct triggering of the selector gates.

A.I.vii SELECTOR GATES (Associated with P_1 and P_3)

Makers	Venner Electronics Limited
Type	T.S. 6A
Triggering Potentials	ON - 1.2 V to -1.8 V)) for 10 V. D.C. supply OFF - 1.0 V to -1.6 V)
Differential	0.2 V
Impedance	Input 5KΩ Output 4.7KΩ
Supply	6-12 V. D.C.

Pin No.

1/

1 Output I Negative going

2 Output II Positive going

3 Supply negative

4 Input 2

5 Joined to pin no. 7 when using input 2

6 Input 1

7 Supply positive (earthy)

8 Not required

Notes

Input 2 (pin no. 4) and output 1 (pin no. 1) were used. Output 1 generated a negative going pulse when the selector gate was triggered to the ON condition and so the stopclock, which required positive going pulses for operation, was started and stopped when the selector gates were automatically reset to the OFF condition. This corresponded to a rising bubble having completely passed through the light beams associated with the photoelectric cell units P_1 and P_3.

A.I.viii COMBINED D.C. RELAY STAGE/SELECTOR GATE

(Associated with P_2)

Makers	Venner Electronics Limited	
Type	T.S.9	
Triggering Potential	- 1.25 V	for 10 V D.C. supply
Differential	0.2 V	

Impedance/

Impedance Input 10-15 KΩ

Supply 8-12 V D.C.

Pin No.

1	Normally closed contact)	Changeover common with pin no. 4
2	Normally open contact)	
3	Supply negative	
4	Common changeover contact	
5	Normally closed contact with pin no. 8	
6	Input	
7	Supply positive (earthy)	
8	Normally closed contact with pin no. 5	

Notes

Pin nos. 4 and 2 were used. This permitted connection of a normally open switch in series with the solenoid 12 V. D.C. power supply. Thus when a rising bubble was detected by P_2 the selector gate was triggered ON and pin nos. 4 and 2 were made common by the D.C. relay changeover, which caused energenisation of its solenoid.

A.I.ix SOLENOID

Makers Magnavox Limited

Type G 11A

Supply 24 V. D.C.

Note

In practice the solenoid operated satisfactorily on 12 V. D.C. supply.

A.I.x SLIDE REGULATORS

Makers	Matsunsga Mfg. Co. Limited
Input	230 V. A.C.
Output	0-260 V. A.C.
Maximum Rating	1 Ampere

A.I.xi PHOTOFLOOD

Makers	Lucas Limited
Type	Tungsten Iodine fog-spot lamp
Rating	12 V. D.C., 55 Watts

A.I.xii STRIPLIGHTS

Makers	Osram Limited
Type	Tubular striplight
Rating	240 V. A.C., 60 Watts

A.I.xiii MONITOR METER (M)

Makers	Sangmo-Weston Limited
Type	$4\frac{1}{2}$ in (11.4 cm) round
Rating	0-1 mA D.C. F.S.D.

APPENDIX II

A.II Estimation of Experimental Errors. Summary of Numerical Values Assigned to Experimental Errors in Measured Variables

Variable	Standard Deviation, β
h_1	0.3 cm
h_2	0.6 cm
L	0.3 cm
H	0.2 cm
M_L	0.0007 gm
ρ_o	0.00003 gm/cm^3
P_A	0.05 cm H_2O (25^oC)
T	0.1^oK
τ'	0.001 sec
Measured bubble dimensions	0.01 cm
P_{TO}	0.3 cm H_2O (25^oC)
P_{T1}	0.3 cm H_2O (25^oC)
P_T	0.4 cm H_2O (25^oC)
dP_T/dt (H_2O)	0.08 cm H_2O (25^oC)/sec
dP_T/dt (90.6% Aqueous Glycerol Soln.)	0.05 cm H_2O (25^oC)/sec
dP_T/dt (99.0% Aqueous Glycerol Soln.)	0.05 cm H_2O (25^oC)/sec
dP_T/dt (1.0% Aqueous Polyox Soln.)	0.06 cm H_2O (25^oC)/sec

The transducer calibration for each of the liquids used, and the standard deviations of the calibration constants are given in Appendix/

Appendix V. The column compressibility, α, and its standard deviation, for each liquid used, are also to be found in Appendix V.

The effect of the rotation of the dumping cup (to release a bubble) on the recorded pressure trace was checked by making recordings before and after rotating the cup, when it did not contain a bubble, in the column which contained a trapped gas space but was otherwise liquid filled. No detectable difference in the two pressure recordings was found.

A P P E N D I X III

A.III Calculation of Mass Transfer Products and Mass Transfer Coefficients

Mass transfer products were calculated from Eqn. (105)

$$-K_L A = \frac{1}{S}\left(\alpha \frac{dP_T}{dt} + \frac{\{V_{B1} + \alpha(P_T - P_{T1})\}\{dP_{T/dt} - \frac{\rho_o}{\rho_{H_2O}} U_B\}}{P_T - \frac{\rho_o}{\rho_{H_2O}} h + P_A}\right) \quad (105)$$

where $h = h_2$, the height of the bubble above the pressure transducer station when photographed.

A decision regarding bubble shape was made by the experimenter, and a 'shape number' = n_1 was assigned according to the following scheme:

Shape	n_1
Sphere	1
Top	2
Oblate spheroid	3
Oblate spheroid with tail	4
Spherical cap Spherical cap with skirt	5
⩾ hemisphere	6

With reference to Fig. (46) actual bubble eccentricity, E_1, was calculated from photograph measurements by means of relationships specific/

FIG. 46. IDEALISED REPRESENTATIONS OF ACTUAL BUBBLE SHAPES INDICATING DIMENSIONS MEASURED FROM PHOTOGRAPHS

NOTE

Horizontal dimensions denote bubble widths at photographic magnification of unity

Vertical dimensions denote bubble heights corrected for photographic distortion

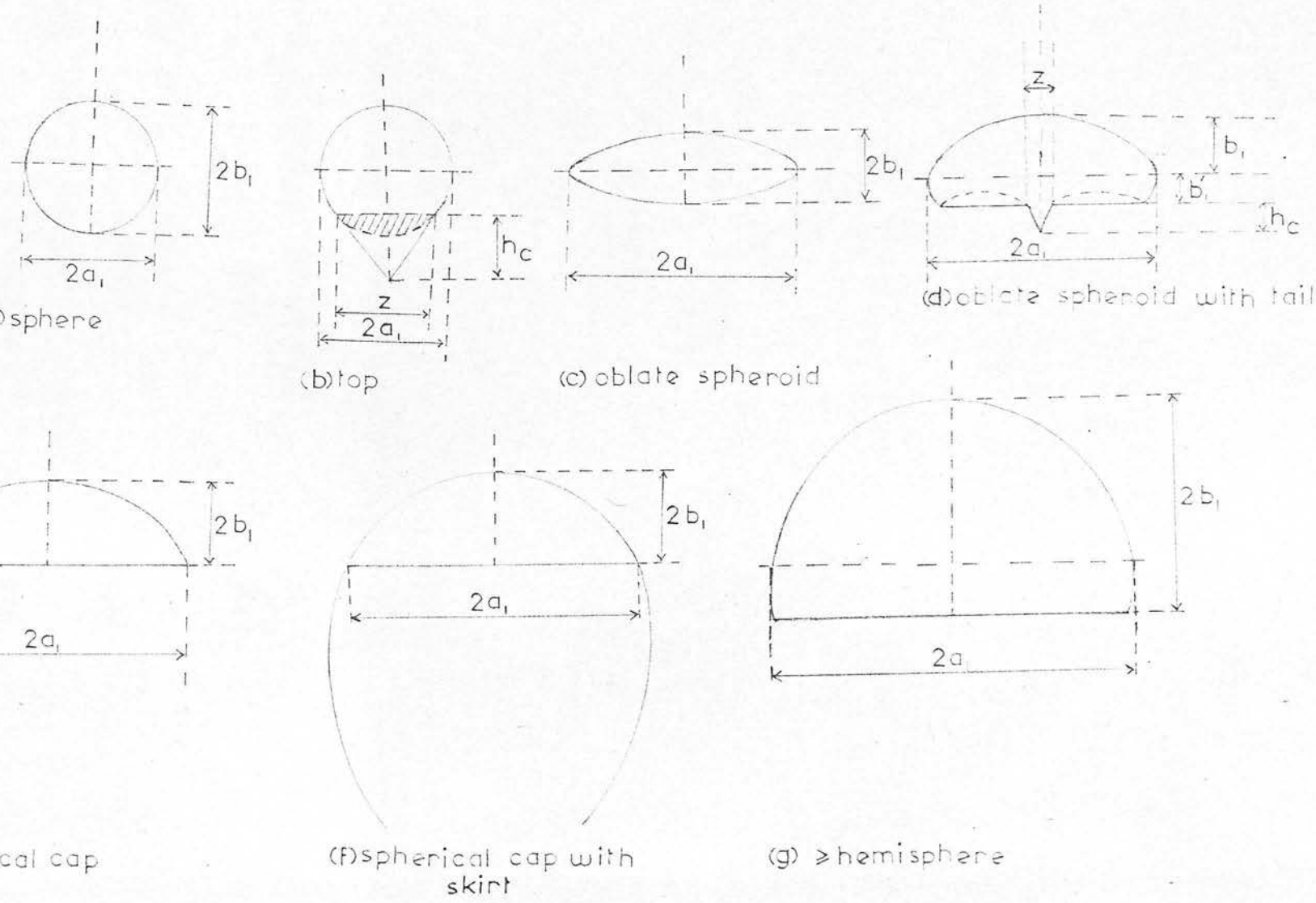

specific to each of the six shape categories within which a particular bubble fell. The appropriate relationships employed in each of the six possible cases were,

(a) Fig. (46 a) Sphere

$$E_1 = {}^{2a}1/_{2b_1} \tag{200}$$

(b) Fig. (46 b) Top

$$E_1 = {}^{2a}1/_{(2a_1 + h_c - 2y)} \tag{201}$$

where 2y represents the height of the hatched segment in Fig. (46 b) and is given by

$$2y = (a_1 - \tfrac{1}{2}(4a_1 - z^2)^{1/2}) \tag{202}$$

The dimension 2y did not therefore require direct measurement.

(c) Fig. (46 c) Oblate spheroid

$$E_1 = {}^{2a}1/_{2b_1} \tag{203}$$

(d) Fig. (46 d) Oblate Spheroid with Tail

$$E_1 = {}^{2a}1/_{(b_1(1 + {}^{1}/_{n_R}) + h_c)} \tag{204}$$

where the parameter n_R is defined by the ratio

$$n_R = {}^{b}1/_{b_1'} \tag{205}$$

(e) Fig. (46 e) Spherical Cap

$$E_1 = {}^{2a}1/_{2b_1} \tag{206}$$

(f) Fig. (46 f) Spherical Cap with Skirt

$$E_1 = {}^{2a}1/_{2b_1} \tag{207}$$

(g) Fig. (46 g) ⩾ Hemisphere

$$E_1 = {}^{2a}1/_{2b_1} \tag{208}$$

Thus/

Thus all eccentricity measurements were based on the maximum horizontal bubble dimension and the vertical dimension through the central vertical axis of the rising bubble.

Actual bubble dimensions were adjusted slightly in order to secure an exact shape fit to one of Figs. (46 a) through (46 g) on a bubble volume basis. Bubble surface areas were then calculated in terms of the adjusted bubble dimensions.

Data requirements for the shape fitting and surface area calculation procedures, and hence the instantaneous mass transfer coefficient determinations were,

M_R (photographic distortion ratio)

n_1 Run No. D_e $K_L A$ (Sphere routine, $n_1 = 1$)

n_1 Run No. D_e $K_L A$ $2a_1$ h_c z (Top routine, $n_1 = 2$)

n_1 Run No. D_e $K_L A$ $2a_1$ $2b_1$ (Oblate spheroid routine, $n_1 = 3$)

n_1 Run No. D_e $K_L A$ $2a_1$ b_1 b_1' h_c z (Oblate spheroid with tail routine, $n_1 = 4$)

n_1 Run No. D_e $K_L A$ $2a_1$ $2b_1$ (Spherical cap and spherical cap with skirt routine, $n_1 = 5$)

n_1 Run No. D_e $K_L A$ $2a_1$ $2b_1$ ($\geqslant$ Hemisphere routine, $n_1 = 6$)

0 (included to terminate program)

In the computer program n_1 served to specify the appropriate subroutine to be entered.

As a result of the experimental technique employed, two independent methods of bubble volume determination were available,

(a) the relation $V_B = V_{B1} + \alpha (P_T - P_{T1})$ (103)

$$= \frac{\pi D_e^3}{6} \qquad (209)$$

(b) direct calculation from photograph measurements on the basis of an assumed shape.

For a given bubble, agreement between V_B determined by methods (a) and (b) was seldom realised, since a systematic error was introduced by the assignment of an assumed shape in (b). Consequently the scheme adopted for bubble surface area, A, determination was:

Calculate V_B by method (a) given above, then taking the bubble measurement in the horizontal plane ($2a_1$) determine bubble height such that the volume calculated from the assumed shape was in agreement with V_B. Bubble surface area was then based on the measured bubble width and calculated bubble height (measured bubble height/ M_R).

The advantage of this method lay in the fact that in most cases bubble width was the largest characteristic length on the photograph, and in the case of a tilting bubble, the measured bubble width was always substantially correct, but the measured height was subject to error.

If the percentage difference between measured and calculated bubble dimension, (usually height), was < 15% then the initial shape assignment was considered relevant and the ideal shape equations were taken to fit the actual case to a sufficiently close approximation.

It should be noted that in the Top routine ($n_1 = 2$), bubble width, and not height, was calculated, and spherical cap bubbles with skirts (Fig. (46 f)) are known to contain only very small amounts/

amounts of gas in their skirts (D5, G15) and so were treated as spherical caps, ($n_1 = 5$).

The computer program printout included the following,

Run No.

Shape No. (n_1)

D_e, cm

E_1 = bubble eccentricity, measured width/measured height

E_2 = bubble eccentricity, measured width/calculated height

A, cm^2 = total bubble surface area based on measured width and calculated height

A_P, cm^2 = total bubble surface area based on measured width and measured height

A_S, cm^2 = equivalent spherical area

A_F, cm^2 = bubble frontal area, based on calculated height of bubble nose above horizontal plane containing maximum bubble width

A_R, cm^2 = $A - A_F$ = area of bubble rear

$\Delta a, b$ = percentage difference between measured and calculated bubble dimensions

$K_L A$, cm^3/sec = mass transfer product

K_L, cm/sec = $K_L A/A$ = overall instantaneous mass transfer coefficient

K_{LF}, cm/sec = $K_L A/A_F$ = mass transfer coefficient based on frontal area only

S_R /

S_R = Shape Ratio, measured width/equivalent spherical diameter

$U_B(\infty)$, cm/sec = Uno-Kintner (Eqn. (38)) corrected measured terminal bubble rise velocity.

The calculations executed in the sub-routines are described below. Fig. (46) should be referred to. V_B in all the following equations was calculated from Eqn. (103).

(a) Spheres routine, $n_1 = 1$

$$V_B = \frac{\pi}{6} D_e^3 = \frac{\pi}{6} (2a_2)^3 \tag{210}$$

From Eqn. (210), D_e and the calculated bubble dimension/2, a_2, were found.

$$\Delta a = (a_2 - a_1) \frac{100}{a_1} \tag{211}$$

$$A = A_S = \pi(2a_2)^2 \tag{212}$$

$$A_F = A_R = \pi(2a_2)^2/2 \tag{213}$$

$$A_P = \pi (2a_1)^2 \tag{214}$$

$$E_1 = E_2 = 1 \tag{215}$$

$$S_R = 1 \tag{216}$$

$$K_{LF} = K_L A/A_F \tag{217}$$

$$K_L = K_L A/A \tag{218}$$

The volumes of small spherical bubbles, (D_e < approx. 0.4 cms), rising through and dissolving in the solutions used were determined/

determined from bubble photograph dimensions and the assumed spherical shape. This was because a discrepancy was found to exist between instantaneous bubble volume, V, as calculated on the basis of bubble photograph dimensions and the assumed spherical shape, and the bubble volume, V_B, calculated from Eqn. (103). This was also found in the work of Loudon (L19). Loudon carried out a graticule traverse of the mass transfer column in order that the influence of bubble migration from the column central axis on photographic distortion could be determined. It was found that this had little effect on the measured bubble photograph dimensions and so bubble photograph measurements were considered the more reliable measure of bubble size. Thus in Eqns. (210) to (214), a_2 was set equal to a_1 and

$$\frac{\pi(2a_1)^3}{6} = \frac{\pi D_e^3}{6} \qquad (219)$$

replaced Eqn. (210).

The possible factors affecting the discrepancy between V and V_B are listed and discussed in ref. (L19). Probably the most important are:

(i) liquid losses when wiping into a weighing bottle the liquid remaining suspended from the liquid displacement line terminal nozzle.

(ii) slight thermal expansion and contraction of the liquid filling the mass transfer column.

(b) Tops routine, $n_1 = 2$

Let/

Let the spherical segment contained by the cone have volume V_h and curved surface area A_h (2x, 2y are not measured from the photograph).

$$x = z/2 \tag{220}$$

$$y = \frac{1}{2}\left(a_1 - \frac{1}{2}\left(4a_1^2 - z^2\right)^{1/2}\right) \tag{221}$$

$$V_h = \frac{\pi y}{3}\left(3x^2 + 4y^2\right) \tag{222}$$

$$A_h = \pi(x^2 + 4y^2) \tag{223}$$

$$E_1 = 2a_1/(2a_1 + h_c - 2y) \tag{201}$$

The cone volume, $V_c = \pi z^2 h_c/12$ (224)

The cone area, $A_c = \frac{\pi z}{2}\left(h_c^2 + z^2/4\right)^{1/2}$ (225)

$$V_B = \frac{\pi}{6} D_e^3 = \frac{4}{3}\pi a_2^3 + V_c - V_h \tag{226}$$

From Eqn. (226), D_e and the calculated bubble width/2, a_2, were found.

y', based on a_2, was calculated from Eqn. (221). If $\frac{y' - y}{y} > 0.01$, then $y = y'$ and V_h, A_h and hence a_2 (Eqns. (221), (222) and (226)), were re-estimated. This was repeated until $\frac{y' - y}{y} < 0.01$.

$$E_2 = 2a_2/(2a_2 + h_c - 2y) \tag{227}$$

$$A = 4\pi a_2^2 + A_c - A_h \tag{228}$$

$$A_F = 2\pi a_2^2 \tag{229}$$

$$A_R = A - A_F \tag{230}$$

$$\Delta a = (a_2 - a_1)\frac{100}{a_1} \tag{231}$$

$$A_S = \pi D_e^2 \tag{232}$$

$$K_{LF} = /$$

$$K_{LF} = K_L A/A_F \tag{233}$$

$$K_L = K_L A/A \tag{234}$$

$$A_P = 4\pi a_1^2 + A_c - A_h \tag{235}$$

$$S_R = 2a_1/D_e \tag{236}$$

(c) Oblate spheroid routine, $n_1 = 3$

$$E_1 = 2a_1/2b_1 \tag{203}$$

Defining

$$e_1 = \frac{1}{a_1}\,(a_1^2 + b_1^2)^{1/2} \tag{237}$$

then,

$$A_P = 2\pi a_1^2 + \frac{\pi b_1^2}{e_1}\ln\left(\frac{(1 + e_1)}{(1 - e_1)}\right) \tag{238}$$

$$V_B = \frac{\pi}{6} D_e^3 = \frac{4}{3}\pi a_1^2 b_2 \tag{239}$$

From Eqn. (239), D_e and the calculated height/2, b_2, were found

$$\Delta b = (b_2 - b_1)\frac{100}{b_1} \tag{240}$$

$$A_S = \pi D_e^2 \tag{241}$$

Defining

$$e_2 = \frac{1}{a_1}(a_1^2 + b_2^2)^{1/2} \tag{242}$$

then,

$$A = 2\pi a_1^2 + \frac{\pi b_2^2}{e_2}\ln\left(\frac{1 + e_2}{1 - e_1}\right) \tag{243}$$

A_R = /

$$A_R = A_F = A/2 \tag{244}$$

$$E_2 = 2a_1/2b_2 \tag{245}$$

$$K_{LF} = K_L A/A_F \tag{246}$$

$$K_L = K_L A/A \tag{247}$$

$$S_R = 2a_1/D_e \tag{248}$$

(d) Oblate spheroid with tail routine, $n_1 = 4$

$$\text{Let } b_1/b_1' = b_2/b_2' = n_R \tag{249}$$

$$E_1 = 2a_1/(b_1 (1 + {}^1/n_R) + h_c) \tag{204}$$

The radius of the rear plane surface,

$$R' = a_1 \left(1 - \frac{1}{n_R^2}\right)^{1/2} \tag{250}$$

Defining

$$e_1 = \frac{1}{a_1} (a_1^2 - b_1^2)^{1/2} \tag{237}$$

then,

$$A_P = \pi(R'^2 - z^2/4) + \frac{\pi z}{2} \left(h_c^2 + \frac{z^2}{4}\right)^{1/2}$$

$$+ \pi a_1^2 \left(1 + \frac{1}{n_R^2} \sqrt{e_1^2 + n_R^2 (1 - e_1^2)}\right)$$

$$+ \frac{\pi b_1^2}{e_1} \ln \left(\frac{e_1 + \sqrt{e_1^2 + n_R^2 (1 - e_1^2)}}{n_R (1 - e_1)} \right) \tag{251}$$

$$V_B = /$$

$$V_B = \frac{\pi D_e^3}{6} = \pi a_1^2 b_2 \left(\frac{2}{3} + \frac{1}{n_R} - \frac{1}{3n_R^3}\right) + \frac{\pi z^2 h_c}{12} \qquad (252)$$

From Eqn. (252), D_e and the calculated height of bubble nose above plane of maximum width, b_2, were found

$$E_2 = 2a_1/\left(b_2\left(1 + \frac{1}{n_R}\right) + h_c\right) \qquad (253)$$

$$\Delta b = (b_2 - b_1)\frac{100}{b_1} \qquad (254)$$

$$A_S = \pi D_e^2 \qquad (255)$$

Defining

$$e_2 = \frac{1}{a_1}\left(a_1^2 + b_2^2\right)^{1/2} \qquad (242)$$

then,

$$A = \pi\left(R'^2 - \frac{z^2}{4}\right) + \frac{\pi z}{2}\left(h_c^2 + \frac{z^2}{4}\right)^{1/2}$$

$$+ \pi a_1^2\left(1 + \frac{1}{n_R^2}\sqrt{e_2^2 + n_R^2(1 - e_2^2)}\right)$$

$$+ \frac{\pi b_2^2}{e_2} \ln\left(\frac{e_2 + \sqrt{e_2^2 + n_R^2(1 - e_2^2)}}{n_R(1 - e_2)}\right) \qquad (256)$$

$$A_F = \frac{1}{2}\left(2\pi a_1^2 + \frac{\pi b_2^2}{e_2} \ln\left(\frac{1 + e_2}{1 - e_2}\right)\right) \qquad (257)$$

$$A_R = A - A_F \qquad (258)$$

$$K_{LF} = K_L A/A_F \qquad (259)$$

$$K_L = K_L A/A \qquad (260)$$

$$S_R = /$$

$$S_R = 2a_1/D_e \tag{261}$$

(e) Spherical Cap, $n_1 = 5$

$$E_1 = 2a_1/2b_1 \tag{206}$$

$$A_P = 2\pi\ (a_1^{\ 2} + 2b_1^{\ 2}) \tag{262}$$

$$V_B = \frac{\pi}{6} D_e^{\ 3} = \frac{\pi b_2}{3} (3a_1^{\ 2} + 4b_2^{\ 2}) \tag{263}$$

From Eqn. (263), D_e was found, and the calculated height/2, b_2, was obtained by solving

$$b_2^{\ 3} + \frac{3a_1^{\ 2}}{4} b_2 - \frac{D_e^{\ 3}}{8} = 0 \tag{264}$$

The appropriate real root of Eqn. (264) was determined by means of an analytical approach presented in (P5).

$$E_2 = 2a_1/2b_2 \tag{265}$$

$$\Delta b = (b_2 - b_1) \frac{100}{b_1} \tag{266}$$

$$A_S = \pi D_e^{\ 2} \tag{267}$$

$$A = 2\pi\ (a_1^{\ 2} + 2b_2^{\ 2}) \tag{268}$$

$$A_R = \pi a_1^{\ 2} \tag{269}$$

$$A_F = A - \pi a_1^{\ 2} \tag{270}$$

$$K_{LF} = K_L A/A_F \tag{271}$$

$$K_L = K_L A/A \tag{272}$$

$$S_R = /$$

$$S_R = 2a_1/D_e \tag{273}$$

(f) $\geqslant$ Hemisphere routine, $n_1 = 6$

$$E_1 = 2a_1/2b_1 \tag{208}$$

$$A_P = 4\pi b_1 (2a_1 - b_1) \tag{274}$$

$$V_B = \frac{\pi}{6} D_e^3 = \frac{4\pi b_2^2}{3} (3a_1 - 2b_2) \tag{275}$$

From Eqn. (275), D_e was found; and, if b_2 is written as b, then calculated bubble height/2, b_2, was obtained by solving

$$F(b) = b^3 - 1.5a_1 b^2 + \frac{D_e^3}{16} = 0 \tag{276}$$

by using the Newton-Raphson iteration,

$$b_{n+1} = b_n - F(b_n)/F'(b_n) \tag{277}$$

with

$$F'(b) = 3b(b - a_1) \tag{278}$$

The starting point of the iteration was conveniently taken as $2b_1/2$, and with this starting point, the iteration converged to the appropriate root of the three possible roots of the cubic equation (276).

$$\Delta b = (b_2 - b_1) \frac{100}{b_1} \tag{279}$$

$$A_S = \pi D_e^2 \tag{280}$$

$$E_2 = 2a_1/2b_2 \tag{281}$$

A /

$$A = 4\pi b_2 (2a_1 - b_2) \quad (282)$$

$$A_F = 2\pi a_1^2 \quad (283)$$

$$A_R = A - A_F \quad (284)$$

$$K_{LF} = K_L A/A_F \quad (285)$$

$$K_L = K_L A/A \quad (286)$$

$$S_R = 2a_1/D_e \quad (287)$$

Safety instructions were written into the program allowing it to continue with the next set of data should one of the following occur in carrying out the subroutine for a given set of data:

(1) Oblate spheroid routine - (i) Bubble becomes spherical or prolate as a result of calculated height exceeding measured width.

(ii) Calculated upper half of oblate spheroid with tail becomes greater than or equal to measured width/2.

(2) Spherical cap routine - Bubble becomes greater than or equal to a hemisphere as a result of calculated height exceeding measured width/2.

(3) $\geqslant$ Hemisphere routine - Bubble becomes less than hemisphere as a result of calculated height becoming less than measured width/

width/2.

(4) Negative or zero operand in log.

(5) Negative or zero operand in square root.

A P P E N D I X IV

A.IV Physical Properties of Gas-Liquid Systems

A.IV.i LIQUID DENSITY, ρ_o

Liquid (25°C)	ρ_o (gm/cc)
Distilled Water	0.9971
90.6% Aqueous Glycerol Solution	1.2336
99.0% Aqueous Glycerol Solution	1.2555
1.0% Aqueous Polyox Solution	0.9991

Density measurements were carried out using a 50 cc specific gravity bottle. The density of distilled water at 25°C, 0.9971 gm/cc, was obtained from Ref. (P6), and this compared with the measured value using the specific gravity bottle, served as a means of checking the accuracy of the specific gravity bottle. The density measurements served to specify the concentrations of the aqueous Glycerol solutions used, by comparison with the tabulated density data for aqueous Glycerol solutions contained in Ref. (P6).

A.IV.ii LIQUID VISCOSITY, μ_o

(1) Newtonian Liquids

Liquid (25°C)	μ_o (poises)
Distilled Water	0.00894
90.6% Aqueous Glycerol Solution	1.80
99.0% /	

99.0% Aqueous Glycerol Solution 7.75

The viscosities assigned to each of the three Newtonian liquids was obtained from Ref. (H11).

(2) Non-Newtonian Liquid

Aqueous Polyox solutions are known to be elastic and to display pseudoplastic behaviour in steady shear (B1). The viscous properties of the 1.0% aqueous Polyox solutions were studied on a Ferranti-Shirley cone-and-plate viscometer. This instrument is described in Ref. (W9). Elastic behaviour cannot be detected on a conventional cone-and-plate viscometer.

The Ferranti-Shirley viscometer operates on the principle of an accurately machined rotating cone of large apex angle subjecting to shear a small sample of fluid between the cone face and a stationary precision-ground flat plate. The torque exerted on the rotating cone is balanced by a torque spring and indicated on a moving coil meter by means of an electro-mechanical dynamometer system. A gear train and electronic control permit accurately controlled continuously variable cone speeds within the range 0-1000 R.P.M. A thermostatically controlled water bath permits the plate and hence sample temperature to be maintained constant during sample shearing operations. Three thermocouples located at different plate radii monitor the sample temperature.

Relationships Employed

(a)/

(a) Shear Stress, τ

$$\tau = 3\ T_c \Delta' / 2\pi R_c^{\ 3} \text{ dyne/cm}^2 \quad (288)$$

where

T_c = torque spring constant, dyne. cm/division

(= 2011 dyne cm/division, instrument No. F.S.236)

Δ' = indicator meter deflection, divisions

R_c = cone radius, cm

(= 3.5 cm, large cone No. F.S.178)

i.e. $$\tau = \frac{(3 \times 2011\Delta')}{(2\pi \times 3.5^3)} \text{ dyne/cm}^2 = 22.4\ \Delta' \text{ dyne/cm}^2 \quad (289)$$

(b) Shear Rate, $\dot{\gamma}$

$$\dot{\gamma} = \omega/\psi \text{ sec}^{-1}$$

where

ω = cone angular velocity, radians/sec

ψ = cone angle, radians

(= 0.00611 radians, large cone No. F.S.178)

i.e. $$\dot{\gamma} = \frac{2\pi N}{60\psi} \quad (291)$$

where N = rotational velocity of cone, R.P.M.

i.e. $$\dot{\gamma} = \frac{(2\pi N)}{(60 \times 0.00611)} \text{ sec}^{-1} = 17.14\ N \text{ sec}^{-1} \quad (292)$$

(c) Apparent viscosity, μ_a

$$\mu_a = (\tau/\dot{\gamma}) \text{ poise} \quad (293)$$

i.e. $$\mu_a = (1.307\ \Delta'/N) \text{ poise} \quad (294)$$

Results/

Results

The following are the results obtained for the 1.0% aqueous Polyox solution at 25°C using the Ferranti-Shirley cone-and-plate rotational viscometer No. F.S.236 fitted with large cone No. F.S.178.

N	$\dot{\gamma}$	Δ'_I	τ_I	μ_{a_I}	Δ'_D	τ_D	μ_{a_D}
R.P.M.	sec^{-1}	divisions	$dyne/cm^2$	poise	divisions	$dyne/cm^2$	poise
5	85.7	3.8	85.1	0.993	3.5	78.4	0.915
10	171.4	5.6	125.4	0.732	5.5	123.2	0.719
25	428.5	9.0	201.6	0.470	8.4	188.2	0.439
50	857.0	13.2	295.7	0.345	12.1	271.0	0.316
75	1285.5	16.3	365.1	0.284	15.3	342.7	0.267
100	1714.0	20.7	463.7	0.271	20.7	463.7	0.271
200	3428.0	27.8	622.7	0.182	28.7	642.9	0.188
300	5142.0	31.2	698.9	0.136	32.0	716.8	0.139
400	6856.0	32.8	734.7	0.107	32.7	732.5	0.107
500	8570.0	34.3	768.3	0.090	34.2	766.1	0.089

These results are presented graphically in Figs. (47) and (48).

Notes

(a) Subscript I refers to $\dot{\gamma}$ increasing while subscript D refers to $\dot{\gamma}$ decreasing.

(b) Values of Δ'_I and Δ'_D are averages of three separate determinations, using in each case fresh samples of the 1.0% aqueous Polyox solution.

(c) The data indicate an apparent slight discontinuity at a $\dot{\gamma}$ of about/

FIG. 4.7. SHEAR STRESS SHEAR RATE

1·0 % AQUEOUS POLYOX AT 25°C

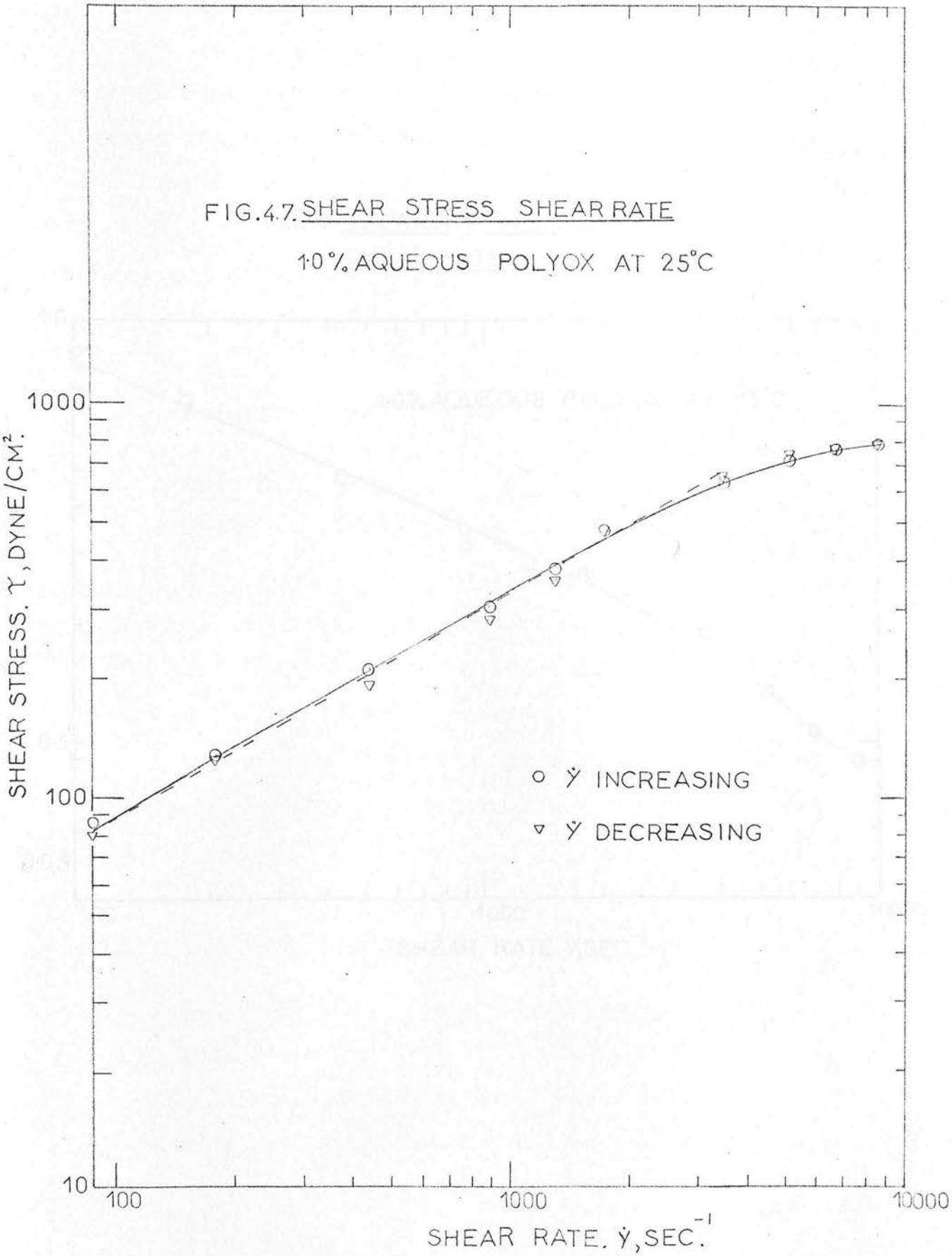

FIG.48. APPARENT VISCOSITY – SHEAR RATE

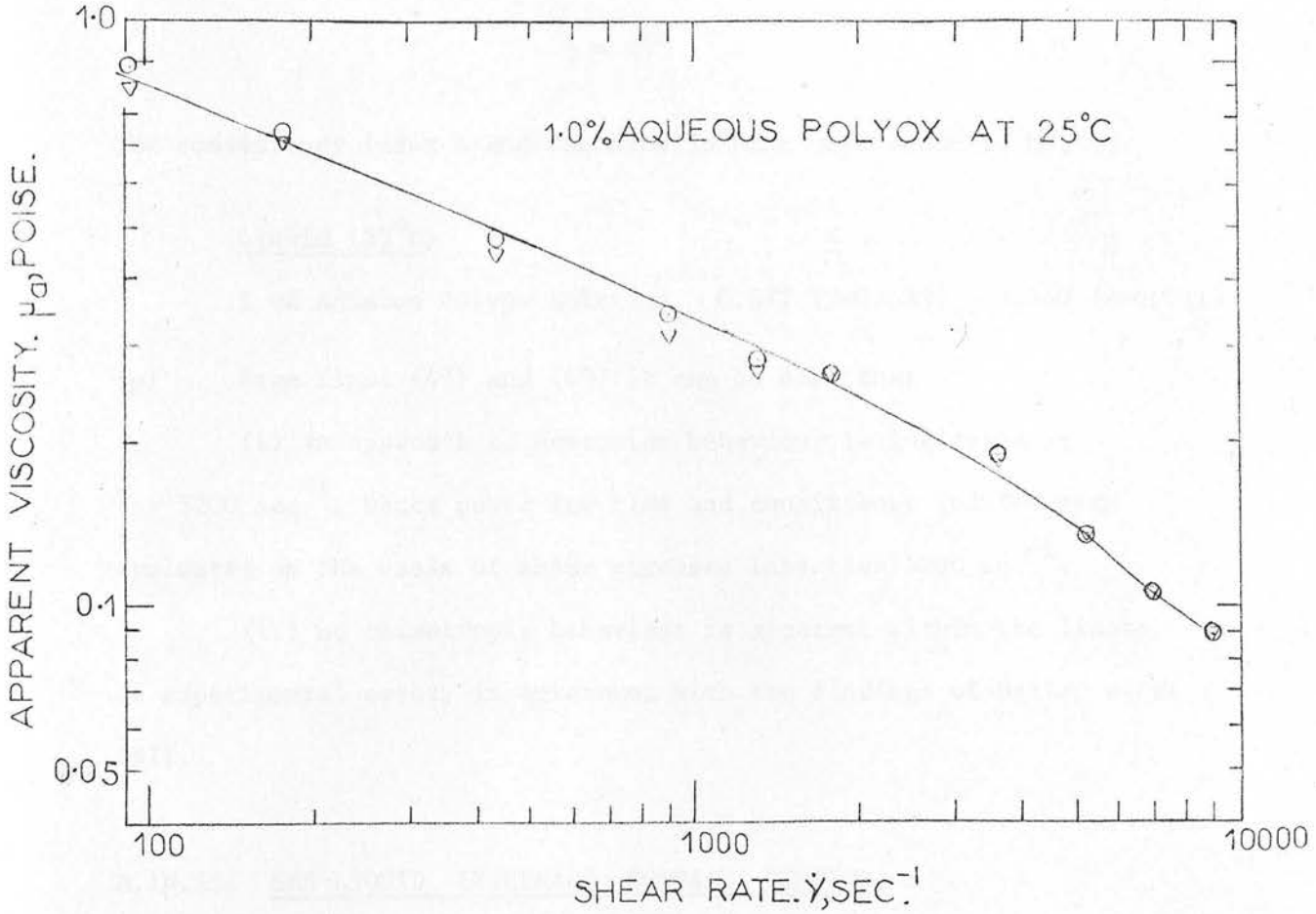

about 1300 sec^{-1}, possibly due to the fact that in this region of shear rate gear changes between the 0-100 R.P.M. and 0-1000 R.P.M. viscometer ranges were necessary.

(d) Included on the plot of the shear stress - shear rate curve, Fig. (47), is a line representing an approximate fit to the viscometric data according to the power law model, Eqn. (3),

$$\tau = K\dot{\gamma}^n \qquad (3)$$

The consistency index K and the flow index n were found to be,

Liquid (25°C)	K	n
1.0% Aqueous Polyox Solution	0.877 (β=0.033)	0.540 (β=0.011)

(e) From Figs. (47) and (48) it can be seen that

(i) an approach to Newtonian behaviour is indicated at $\dot{\gamma} > 5200\ sec^{-1}$, hence power law flow and consistency indices were evaluated on the basis of shear stresses less than 5200 sec^{-1}.

(ii) no thixotropic behaviour is apparent within the limits of experimental error, in agreement with the findings of Bailey et al (B1).

A.IV.iii GAS-LIQUID INTERFACE SURFACE TENSION, σ

Liquid (25°C)	σ (dynes/cm)
Distilled Water	72.0 ± 0.05
90.6% Aqueous Glycerol Solution	63.8 ± 3.0
99.0% Aqueous Glycerol Solution	62.5 ± 3.0
1.0% Aqueous Polyox Solution	71.9 ± 0.1

The surface tension of water was obtained from Ref. (W3). The differences between the surface tensions of aqueous Glycerol solutions of various concentrations and that of pure water, $\Delta\sigma$, were also listed in Ref. (W3), and from this list

$\Delta\sigma$ (90.6% Aqueous Glycerol Solution, $25^{o}C$) = -8.2 ± 3.0 dynes/cm

$\Delta\sigma$ (99.0% Aqueous Glycerol Solution, $25^{o}C$) = -9.5 ± 3.0 dynes/cm

A Wilhelmy surface tension balance, (Fig. (49)), was used to determine $\Delta\sigma$ for the 1.0% aqueous Polyox solution. This balance consisted of a rectangular glass slide, (cleaned with chromic acid, rinsed with distilled water and dried with filter paper), suspended from the end of the extended beam of a balance and counterpoised with the slide partially immersed in distilled water contained in a glass trough. When the water was replaced by exactly the same volume of the aqueous Polyox solution, the slide took up a new position of equilibrium attained when the change of the downward pull F_d of the surface tension was compensated by the change in buoyancy F_u of the submerged portion of the slide, i.e.

$$\Delta F_d = \Delta F_u \tag{295}$$

$$\text{or } 2(w + t')\Delta\sigma = g\rho_o wt'\Delta h \tag{296}$$

where $\Delta\sigma$ = difference between surface tension of solution and that of water, w = width of slide, t' = thickness of slide, Δh = change in length of submerged part of slide, g = gravitational acceleration, and ρ_o = density of water (the density of the solution was taken to differ/

FIG. 49. WILHELMY SURFACE TENSION BALANCE

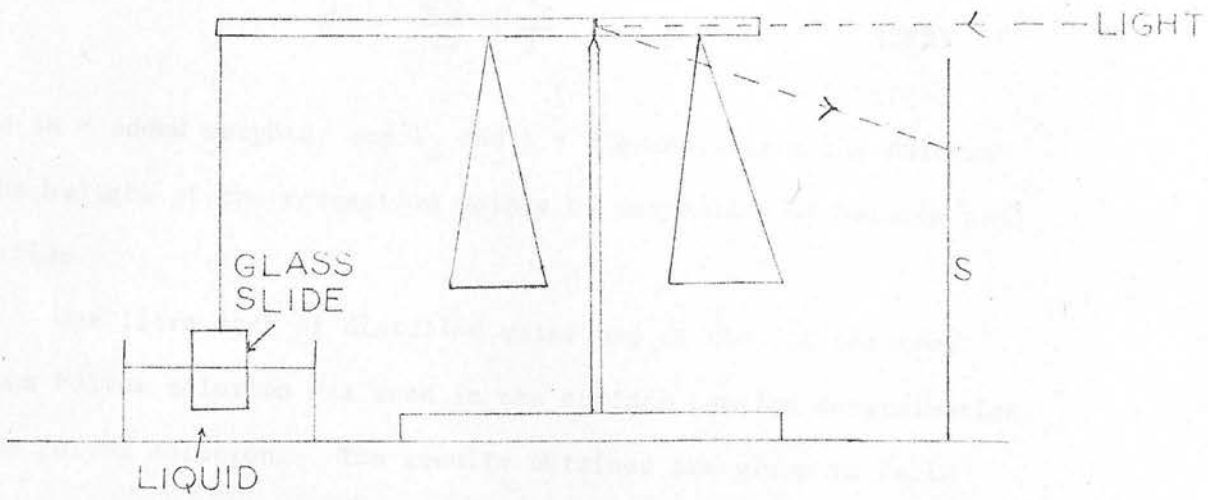

differ negligibly from that of water).

For small displacements of the slide Δh was proportional to Δs, the change in reading on the vertical scale S, or

$$-2(w + t')\Delta\sigma = K''\Delta s \qquad (297)$$

The value of the constant K''was determined by observing the values of Δs associated with different weights on the balance pan (R.H.S.) with the slide immersed in water, the relation being

$$K'' = \frac{g\Delta W}{\Delta s} \cdot \frac{1_o}{1} \qquad (298)$$

where ΔW = added weights, and 1_o and 1 = distances from the fulcrum of the balance of the respective points of suspension of balance pan and slide.

One litre each of distilled water and of the 1.0 per cent aqueous Polyox solution was used in the surface tension determination of the Polyox solution. The results obtained are given in Table (6) below.

Table 6

Added Wts. (gm)	Reading on Scale S (cm ± 0.025 cm)	
	Distilled Water	1.0 per cent Polyox Solution
30.50 (Balanced)	28.00	27.85
30.60	26.25	26.30
30.70	24.55	24.55
30.80	22.80	22.75

Using/

Using Eqn. (298) it is found that K''= -8.92. From Table (6) the maximum value of Δs is -0.15, which from Eqn. (297) corresponds to $\Delta\sigma = -0.3 \pm 0.05$ dynes/cm. The value of $\Delta\sigma$ averaged over the four points is -0.08 ± 0.05 dynes/cm.

A.IV.iv MOLECULAR WEIGHT, M'

The mean molecular weight, M' of a solution of A in B was given by

$$M' = \frac{100}{\frac{\text{Wt\% A}}{\text{Mol.wt.A}} + \frac{\text{Wt\% B}}{\text{Mol.wt.B}}} \qquad (299)$$

The molecular weight of water is 18, that of Polyox approximately 3,000,000 (B1), and that of Glycerol, $C_3H_5(OH)_3$, 92. Hence

Liquid	M'
Distilled Water	18
1.0 per cent Aqueous Polyox	18
90.6 per cent Aqueous Glycerol	66.4
99.0 per cent Aqueous Glycerol	88.4

A.IV.v HENRY'S CONSTANT, He

Liquid ($25^{\circ}C$)	He (cm H_2O)
Distilled Water	1.70×10^6
1.0 per cent Aqueous Polyox	1.70×10^6
90.6 per cent Aqueous Glycerol	1.39×10^6
99.0 per cent Aqueous Glycerol	1.07×10^6

The Henry's Constant for water at 25°C was obtained from Ref. (W3), (noting that 1 atmosphere = 1034 cm H_2O = 760 mm Hg). The Henry's Constant for the 1.0 per cent Aqueous Polyox Solution was taken to be substantially the same as that for pure water.

The Henry's Constants for the aqueous Glycerol solutions were obtained from, (W3),

$$\text{He (cm } H_2O) = \frac{17.0324 \times 10^6 \times \rho_o}{M'\alpha''} \times \frac{1034}{760} \qquad (300)$$

where α'' is the Bunsen absorption coefficient and is defined as the volume of gas (reduced to 0°C, 760 mm Hg) which, at the temperature of the experiment, is dissolved in one volume of the solvent when the partial pressure of the gas is 760 mm Hg. α'' for carbon dioxide in a 90.6 per cent aqueous Glycerol solution and in a 99.0 per cent aqueous Glycerol solution was given to be 0.414 and 0.412 respectively at 15°C (W3). No data was available at the temperature of 25°C. Hence the scaling up factor used in order to determine $^1/\alpha''$ at 25°C in each case was 1.34. This was the ratio He (water at 25°C)/He (water at 15°C), (W3), and was also the ratio He (≃ 20 per cent aqueous Glycerol solution at 25°C)/He (≃ 20 per cent aqueous Glycerol solution at 15°C), (W3), the ≃ 20 per cent aqueous Glycerol solution being the highest concentration at which data at both 15°C and 25°C was available.

A.IV.vi CARBON DIOXIDE - LIQUID DIFFUSION COEFFICIENT, D_L

Liquid (25°C)	D_L (cm^2/sec)
Distilled Water	1.92×10^{-5}
1.0 per cent Aqueous Polyox	1.92×10^{-5}
90.6 per cent Aqueous Glycerol	1.7×10^{-6}
99.0 per cent Aqueous Glycerol	1.5×10^{-6}

Water and Aqueous Polyox Solution

The diffusion coefficient of carbon dioxide in distilled water at 25°C was obtained from the measurements of Davidson and Cullen (D11); and the diffusion coefficient of carbon dioxide in the 1.0 per cent aqueous Polyox solution was taken to be substantially the same.

Aqueous Glycerol Solutions

Ratcliff and Holdcroft (R1) used Eyring's lattice model of a liquid, which is based on the similarity between diffusion and the viscous transfer of momentum to predict diffusion coefficients. Ratcliff and Holdcroft found their theory to hold for relatively small solute molecules, such as carbon dioxide, diffusing in electrolyte solutions containing relatively small ions, and at concentrations that were not too high. For concentrations of Glycerol in water of up to 5 g mole/l ($\simeq$ 45 per cent by weight) it was found that

$$\frac{d}{dc}\left(\frac{D_L}{D_{LO}}\right) = -0.132 \qquad (301)$$

where/

where D_{LO} is the diffusivity of carbon dioxide in pure water.

At increasingly higher glycerol concentrations Ratcliff and Holdcroft noted that Eqn. (301) would be expected to give increasingly too low a value of diffusivity. Redfield and Houghton (R2) pointed out that D_L would be expected to settle out to a constant value as the solution viscosity was increased. Redfield and Houghton (R2) found the liquid diffusivity of carbon dioxide in aqueous dextrose solutions to decrease with increasing viscosity until in the liquid viscosity range 3.5 - 32 poises the diffusion coefficient was 1.7×10^{-6} cm^2/sec and independent of viscosity. This was qualitatively explained by extension of the quasi-crystalline "cell-model" for liquid diffusion proposed by Houghton (H14), in that as viscosity increased, the behaviour would eventually approach that of a solid where the diffusing molecule spent much more of its time oscillating about its equilibrium position than it did in moving from one site to another.

Calderbank (C2) measured diffusion coefficients for carbon dioxide in aqueous Glycerol solutions of concentrations ranging between 9.5 per cent and 70.4 per cent wt/wt at a temperature of $25^{o}C$. The Ratcliff/Holdcroft straight line relationship, (Eqn. (301)), was thus drawn through the Calderbank diffusion coefficient data for Glycerol concentrations of 0 per cent wt/wt (0 gm mole/1)-40 per cent wt/wt (5 gm mole/1), (see Fig. (50)). A smoothed curve was then fitted to the Calderbank diffusion coefficient data over the concentration range 40 per cent wt/wt (5 gm mole/1) - 70.4 /

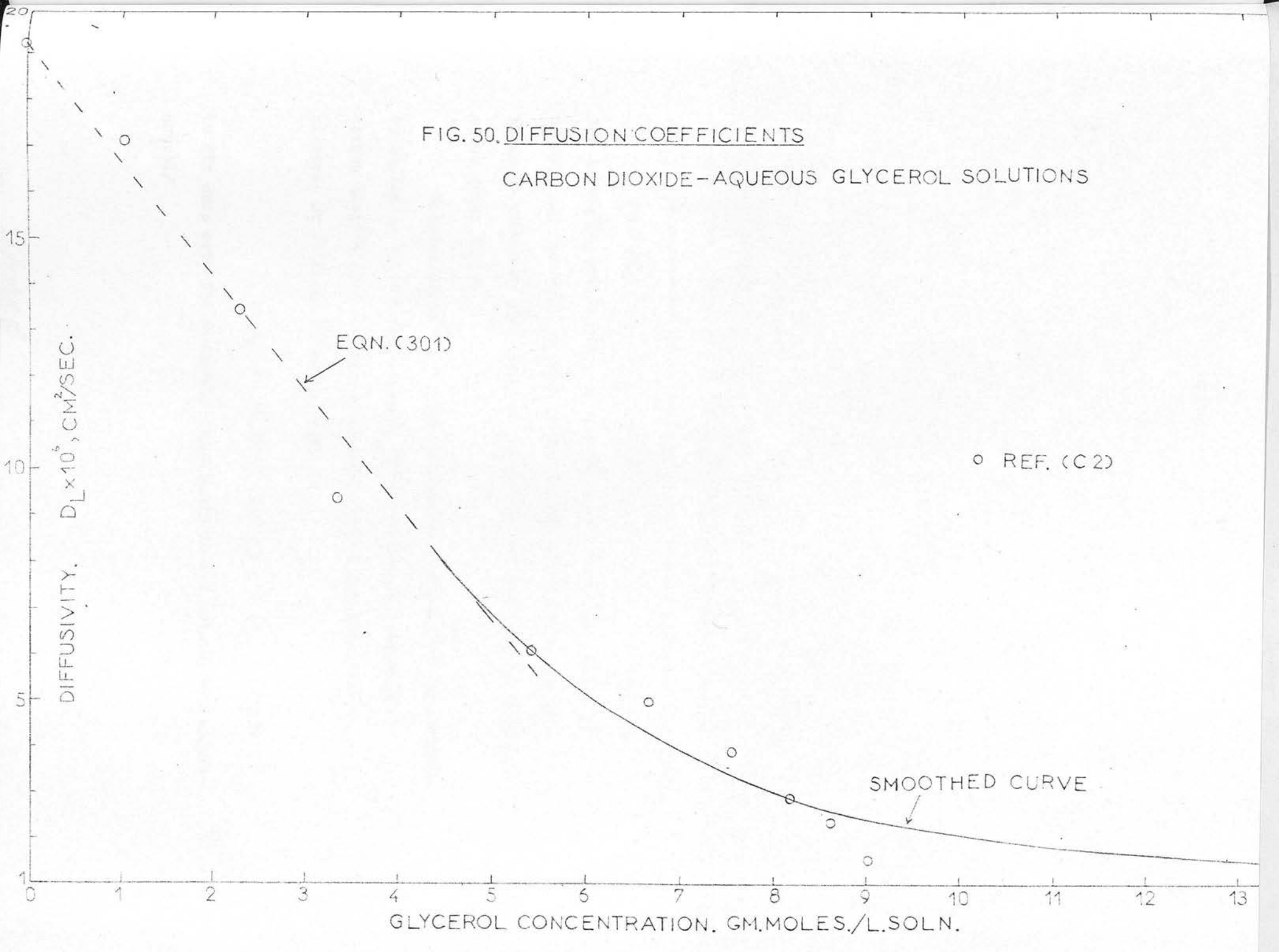
FIG. 50. DIFFUSION COEFFICIENTS
CARBON DIOXIDE – AQUEOUS GLYCEROL SOLUTIONS
EQN. (301)
REF. (C 2)
SMOOTHED CURVE
DIFFUSIVITY, $D_L \times 10^5$, CM²/SEC.
GLYCEROL CONCENTRATION, GM. MOLES/L. SOLN.
20
15
10
5
1
0
1
2
3
4
5
6
7
8
9
10
11
12
13

70.4 per cent wt/wt (9.03 gm mole/l) using the least squares method, and the curve extrapolated to a 99.0 per cent wt/wt (13.50 gm mole/l) aqueous Glycerol solution. The curve was found to give values of D_L which decreased and became progressively more nearly independent of liquid viscosity with increasing liquid viscosity, as predicted by Redfield and Houghton.

Ratcliff and Holdcroft (R1) pointed out that the scatter of the experimentally measured diffusion coefficients of Calderbank suggested that the average deviation (± 8 per cent) over the range of applicability of their equation was due to experimental error. The average deviation of the experimental data over the Glycerol concentration range through which the smoothed curve was fitted was of the same order (± 13 per cent), and may be similarly explained.

The values 1.7×10^{-6} cm^2/sec and 1.5×10^{-6} cm^2/sec for the diffusion coefficients of the 90.6 per cent wt/wt (12.15 gm mole/l) and the 99.0 per cent wt/wt (13.50 gm mole/l) aqueous Glycerol solutions respectively, were read off from the extrapolated curve (Fig. (50)).

Further support for these diffusion coefficients was provided by Davies et al (D6) who measured the diffusion coefficients of carbon dioxide into a range of organic liquids and hydrocarbon mixtures at 25^oC and found the equation

$$\ln D_L = -0.50 \ln (100 \mu_o) - 4.47 \qquad (302)$$

to fit data over the viscosity range 0.004 to 1.1 poises, the experimental/

mental data lying within ± 30 per cent of the values predicted by Eqn. (302). Eqn. (302) predicts a value of 2.4×10^{-6} cm^2/sec for the 90.6 per cent wt/wt aqueous Glycerol solution (μ = 1.80 poises), and a value of 1.3×10^{-6} cm^2/sec for the 99.0 per cent wt/wt aqueous Glycerol solution (μ = 7.75 poises). These values are within acceptable limits of the values used, when consideration of the accuracy of Eqn. (302) is taken into account.

APPENDIX V

A.V. Tabulated Results

Experimental results for the carbon dioxide - distilled water, carbon dioxide - aqueous Glycerol solutions and carbon dioxide - aqueous Polyox solution presented in graphical form in Chapter 4 of the text are tabulated in Tables (7) through (10) overleaf. Other relevant experimental parameters are also included.

TABLE (7) TERMINAL RISE VELOCITY AND MASS TRANSFER RUNS. CARBON DIOXIDE IN DISTILLED WATER

Transducer Calibration: $P = (-0.260\ (\pm 0.0015)x + 148.3\ (\pm 0.6))$ cm H_2O (25^oC) where x is the PDP 8 digitised transducer voltage (0-2000, positive; 2000-4095, negative)

α = 0.002557 ± 0.000025 $cm^3/cm\ H_2O$ (25^oC)

L = 50.0 ± 0.2 cm

h_1 = 1.0 ± 0.3 cm

h_2 = 66.5 ± 0.6 cm

H = 50.0 ± 0.2 cm

M_R = 1.1333

b" (Eqn. (38)) = 0.882

T = 25.0 ± 0.1^oC

Run No.	D_e (cm)	U_B (cm/sec)	U(∞) (cm/sec)	E_1	E_2	S_R	Δa,b	A(cm^2)	A_P(cm^2)	A_F(cm^2)	K_LA (cm^3/sec)	$K_L \times 10^2$ (cm/sec)
2	2.44	31.60	35.41	3.02	3.16	1.55	- 4.7	26.93	27.38	15.71	0.4735	1.759
3	1.04	23.88	23.88	2.11	2.16	1.29	- 2.6	3.78	3.81	1.89	0.0851	2.255
4	0.71	22.19	22.19	1.52	1.52	1.15	0.2	1.65	1.65	0.83	0.0426	2.578
5	0.78	22.81	22.81	1.58	1.78	1.21	-11.2	2.05	2.17	1.03	0.0496	2.416
6	0.86	22.95	22.95	1.72	1.73	1.20	- 0.8	2.45	2.46	1.22	0.0564	2.303
7	0.63	22.12	22.12	1.50	1.59	1.17	- 5.2	1.28	1.32	0.64	0.0334	2.610
8	0.68	22.16	22.16	1.54	1.56	1.16	- 1.1	1.51	1.52	0.76	0.0387	2.558

TABLE (7) (Contd.)

Run No.	D_e (cm)	U_B (cm/sec)	$U(\infty)$ (cm/sec)	E_1	E_2	S_R	$\Delta a,b$	$A(cm^2)$	$A_P(cm^2)$	$A_F(cm^2)$	$K_L A$ (cm^3/sec)	$K_L \times 10^2$ (cm/sec)
9	0.70	22.33	22.33	1.49	1.69	1.19	-11.4	1.61	1.71	0.80	0.0408	2.533
10	0.77	22.49	22.49	1.48	1.55	1.16	- 4.0	1.93	1.97	0.96	0.0479	2.482
11	0.85	22.95	22.95	1.68	1.86	1.23	-10.0	2.46	2.58	1.23	0.0545	2.214
12	0.95	23.21	23.21	1.60	1.72	1.20	- 7.2	3.01	3.12	1.50	0.0655	2.177
13	0.84	22.90	22.90	1.68	1.92	1.24	-12.2	2.39	2.53	1.19	0.0534	2.241
14	0.78	22.77	22.77	1.50	1.55	1.16	- 3.0	1.97	2.00	0.99	0.0491	2.488
15	0.86	22.90	22.90	1.65	1.65	1.18	0.2	2.46	2.45	1.23	0.0548	2.234
16	0.63	22.09	22.09	1.49	1.69	1.19	-11.6	1.31	1.40	0.66	0.0339	2.585
17	0.46	23.72	23.72	1.31	1.37	1.11	- 3.8	0.68	0.69	0.34	0.0190	2.817
18	0.47	23.65	23.65	1.31	1.31	1.10	- 0.4	0.72	0.72	0.36	0.0193	2.685
19	0.52	22.47	22.47	1.46	1.36	1.11	7.1	0.88	0.84	0.44	0.0228	2.604
20	0.53	22.41	22.41	1.49	1.42	1.12	4.8	0.89	0.87	0.44	0.0229	2.588
21	0.99	23.54	23.54	1.44	1.45	1.13	- 0.2	3.16	3.17	1.58	0.0676	2.137
22	1.12	25.17	25.17	2.00	1.99	1.26	0.2	4.32	4.31	2.16	0.0924	2.141
23	1.40	27.86	28.35	2.96	3.31	1.49	-10.7	8.09	8.32	4.04	0.1706	2.109
24	1.31	26.95	27.21	2.76	3.28	1.49	-15.8	7.05	7.38	3.53	0.1429	2.026
25	1.81	29.56	31.21	2.38	2.68	1.39	-11.2	12.43	12.91	6.22	0.2283	1.837
26	2.21	30.74	33.68	3.15	3.03	1.52	3.8	21.60	21.32	15.30	0.3559	1.648
27	1.04	23.91	23.91	2.08	2.14	1.29	- 2.9	3.79	3.83	1.90	0.0849	2.241
28	3.79	34.35	44.60	3.01	3.18	1.55	- 5.5	65.25	66.55	38.00	1.0124	1.552
29	2.98	33.61	39.82	3.40	3.22	1.56	5.7	40.53	39.84	23.55	0.6346	1.566
30	2.64	32.67	37.37	3.38	3.31	1.58	2.1	32.32	32.11	18.66	0.5370	1.662
32	0.42	24.16	24.16	1.21	1.25	1.08	- 3.1	0.55	0.56	0.28	0.0169	3.064
33	1.34	27.03	27.37	2.93	3.40	1.50	-13.7	7.51	7.79	3.75	0.1486	1.979
34	1.12	25.15	25.15	1.79	1.92	1.24	- 6.9	4.26	4.39	2.13	0.0938	2.204
35	0.94	23.22	23.22	1.57	1.71	1.20	- 8.6	2.91	3.03	1.45	0.0661	2.275
37	1.06	24.50	24.50	2.13	2.17	1.29	- 1.8	3.95	3.97	1.97	0.0887	2.249
38	1.11	25.05	25.05	2.02	2.03	1.27	- 0.4	4.28	4.29	2.14	0.0913	2.131
39	1.75	29.35	30.80	3.27	3.87	1.57	-15.4	13.45	13.94	6.73	0.2588	1.924

TABLE (7) (Contd.)

Run No.	D_e (cm)	U_B (cm/sec)	$U(\infty)$ (cm/sec)	E_1	E_2	S_R	$\Delta a,b$	$A(cm^2)$	$A_P(cm^2)$	$A_F(cm^2)$	K_LA (cm^3/sec)	$K_L \times 10^2$ (cm/sec)
40	1.62	28.56	29.63	3.01	3.43	1.51	-12.3	10.93	11.29	5.47	0.2228	2.037
41	1.48	27.90	28.60	3.27	3.77	1.56	-13.3	9.61	9.91	4.80	0.1884	1.961
42	1.30	25.63	25.85	2.69	3.14	1.46	-14.2	6.77	7.06	3.39	0.1350	1.994
45	0.83	22.83	22.83	1.72	1.76	1.21	- 2.6	2.29	2.32	1.14	0.0519	2.270
46	0.60	22.15	22.15	1.42	1.50	1.14	- 5.2	1.18	1.21	0.59	0.0324	2.752
47	0.50	23.15	23.15	1.39	1.35	1.11	2.6	0.79	0.78	0.40	0.0210	2.658
49	0.07	9.40	9.40	1.00		1.00			0.015	0.008	0.00018	1.196
50	3.38	34.02	42.11	3.29	3.19	1.56	3.1	51.98	51.47	30.25	0.7797	1.500

TABLE (8) TERMINAL RISE VELOCITY AND MASS TRANSFER RUNS. CARBON DIOXIDE IN 90.6% AQUEOUS GLYCEROL SOLUTION

Transducer Calibration: $P = (-0.258\ (\pm 0.0010)x + 152.0\ (\pm 0.6))$ cm H_2O (25^oC) where x is the PDP-8 digitised transducer voltage (0-2000, positive, 2000-4095, negative)

α = 0.002370 ± 0.000021 $cm^3/cm\ H_2O$ (25^oC)

L = 50.0 ± 0.2 cm

h_1 = 1.0 ± 0.3 cm

h_2 = 66.5 ± 0.6 cm

H = 50.0 ± 0.2 cm

M_R = 1.0500

b" (Eqn. (38)) = 0.892

T = 25.0 ± 0.1°C

Run No.	D_e (cm)	U_B (cm/sec)	U(∞) (cm/sec)	E_1	E_2	S_R	Δa,b	A(cm^2)	A_P(cm^2)	A_F(cm^2)	K_LA (cm^3/sec)	$K_L \times 10^2$ (cm/sec)
102	2.93	31.58	37.52	3.25	3.09	1.53	5.3	38.31	37.66	22.48	0.2067	0.539
103	1.93	27.38	29.48	3.25	3.34	1.58	- 2.9	17.34	17.50	9.99	0.1219	0.703
105	1.14	22.76	22.85	2.86	2.83	1.48	1.3	5.61	5.58	3.37	0.0430	0.766
106	1.32	23.91	24.36	3.31	3.20	1.56	3.6	7.89	7.81	4.59	0.0607	0.769

TABLE (8) (Contd)

Run No.	D_e (cm)	U_B (cm/sec)	$U(\infty)$ (cm/sec)	E_1	E_2	S_R	$\Delta a,b$	$A(cm^2)$	$A_P(cm^2)$	$A_F(cm^2)$	K_LA (cm^3/sec)	$K_L \times 10^2$ (cm/sec)
107	0.73	15.37	15.37	1.46	1.42	1.12	2.8	1.71	1.69	0.86	0.0144	0.842
108	0.69	14.77	14.77	1.41	1.31	1.09	7.5	1.50	1.44	0.75	0.0120	0.803
109	2.81	31.22	36.64	3.26	3.26	1.57	- 0.1	36.28	36.30	21.01	0.1946	0.536
110	1.40	24.15	24.79	3.16	3.17	1.55	- 0.1	8.87	8.87	5.17	0.0691	0.779
111	0.26	3.02	3.02	1.00		1.00			0.212	0.106	0.00069	0.325
112	0.23	2.30	2.30	1.00		1.00			0.160	0.080	0.00045	0.284
113	0.64	14.04	14.04	1.28	1.13	1.04	13.1	1.30	1.21	0.65	0.0107	0.819
114	2.51	30.06	34.23	3.40	3.28	1.57	3.7	29.07	28.75	16.81	0.1596	0.549
115	2.05	28.32	30.84	3.53	3.36	1.59	5.0	19.65	19.38	11.30	0.1245	0.634
116	1.81	26.86	28.60	3.32	3.29	1.58	1.0	15.12	15.07	8.74	0.1046	0.692
117	0.43	8.25	8.25	1.00		1.00			0.58	0.29	0.0044	0.758
118	1.89	27.01	28.98	3.16	3.20	1.56	- 1.2	16.34	16.41	9.51	0.1134	0.694
119	1.54	24.86	25.83	3.16	3.14	1.55	0.6	10.70	10.68	6.25	0.0793	0.741
120	1.19	23.51	23.69	3.03	2.96	1.51	2.3	6.18	6.13	3.66	0.0524	0.848
121	1.18	23.63	23.80	3.06	2.84	1.48	7.9	6.01	5.84	3.60	0.0513	0.855
122	1.05	21.17	21.17	2.80	2.67	1.44	4.9	4.65	4.56	2.83	0.0398	0.857
123	1.09	21.96	21.96	2.91	2.68	1.44	8.5	5.01	4.85	3.05	0.0424	0.847
124	5.53	34.45	57.57	2.11	2.12	1.30	- 0.4	116.53	116.85	76.26	0.4212	0.361
125	5.25	34.01	54.34	2.19	2.15	1.31	1.8	105.64	104.55	68.79	0.4080	0.386
126	5.39	34.20	55.91	2.12	2.13	1.30	- 0.7	111.19	111.70	72.60	0.3995	0.359
127	3.14	32.46	39.45	3.14	3.14	1.55	0.0	44.43	44.43	25.95	0.2300	0.518
128	1.73	25.62	27.09	2.98	2.95	1.51	0.8	13.15	13.11	7.80	0.0911	0.693
129	0.84	17.57	17.57	2.14	2.08	1.29	2.8	2.68	2.63	1.76	0.0232	0.866
130	0.53	12.34	12.34	1.13	1.14	1.04	- 0.4	0.88	0.88	0.44	0.0074	0.847
131	0.69	14.72	14.72	1.42	1.40	1.12	1.5	1.52	1.51	0.76	0.0126	0.826
132	0.60	13.95	13.95	1.39	1.33	1.10	4.5	1.15	1.12	0.58	0.0097	0.839
133	0.61	13.94	13.94	1.29	1.23	1.07	4.3	1.16	1.14	0.58	0.0099	0.847
134	0.88	18.89	18.89	2.12	2.06	1.28	2.7	2.95	2.90	1.95	0.0245	0.833
135	0.40	7.79	7.79	1.00		1.00			0.503	0.251	0.00353	0.703
136	0.39	7.51	7.51	1.00		1.00			0.488	0.244	0.00329	0.674
137	4.01	33.56	45.15	2.69	2.85	1.48	- 5.5	69.30	70.95	41.50	0.2939	0.424

TABLE (9) TERMINAL RISE VELOCITY AND MASS TRANSFER RUNS. CARBON DIOXIDE 99.0% AQUEOUS GLYCEROL SOLUTION

Transducer Calibration: $P = (-0.210\ (\pm 0.0010)x + 188.9\ (\pm 0.5))$ cm H_2O (25^oC) where x is the PDP-8 digitised transducer voltage (0-2000, positive, 2000-4095 negative)

α = 0.002622 ± 0.000022 $cm^3/cm\ H_2O$ (25^oC)

L = 50.0 ± 0.2 cm

h_1 = 1.0 ± 0.3 cm

h_2 = 66.5 ± 0.6 cm

H = 50.0 ± 0.2 cm

M_R = 1.0279

b" (Eqn. (38)) = 0.892

T = 25.0 ± 0.1°C

Run No.	D_e(cm)	U_B (cm/sec)	U(∞) (cm/sec)	E_1	E_2	S_R	Δa,b	A(cm^2)	A_P(cm^2)	A_F(cm^2)	K_LA (cm^3/sec)	$K_L \times 10^2$ (cm/sec)
201	1.44	16.61	17.11	1.74	1.82	1.20	- 4.8	7.57	7.80	4.76	0.0338	0.447
202	1.13	14.41	14.45	1.51	1.60	1.14	- 5.7	4.42	4.56	2.57	0.0233	0.527
203	1.40	16.25	16.68	1.81	1.91	1.23	- 5.1	7.26	7.51	4.70	0.0317	0.436
205	1.24	15.79	15.99	1.65	1.73	1.17	- 4.4	5.51	5.66	3.35	0.0288	0.522

TABLE (9) (Contd.)

Run No.	D_e (cm)	U_B (cm/sec)	$U(\infty)$ (cm/sec)	E_1	E_2	S_R	$\Delta a,b$	$A(cm^2)$	$A_P(cm^2)$	$A_F(cm^2)$	K_LA (cm^3/sec)	$K_L \times 10^2$ (cm/sec)
206	0.99	11.49	11.49	1.30	1.36	1.07	- 4.5	3.22	3.28	1.73	0.0079	0.244
207	2.03	23.04	25.04	1.74	1.79	1.19	- 2.7	14.87	15.12	9.24	0.0820	0.551
208	1.42	16.34	16.80	1.57	1.65	1.15	- 4.8	7.06	7.26	4.17	0.0315	0.447
209	1.36	15.74	16.10	1.58	1.66	1.15	- 4.6	6.53	6.70	3.87	0.0313	0.480
210	1.05	12.29	12.29	1.37	1.33	1.10	2.9	3.51	3.46	1.76	0.0106	0.302
211	1.12	13.63	13.66	1.46	1.53	1.11	- 4.6	4.32	4.42	2.45	0.0175	0.404
212	1.13	14.08	14.11	1.52	1.59	1.13	- 4.9	4.40	4.52	2.55	0.0232	0.528
213	1.27	16.05	16.28	1.59	1.68	1.16	- 5.3	5.68	5.85	3.39	0.0309	0.543
214	1.22	15.55	15.72	1.63	1.71	1.17	- 4.4	5.32	5.46	3.21	0.0272	0.511
215	1.04	12.26	12.26	1.35	1.42	1.08	- 5.1	3.66	3.74	2.01	0.0102	0.279
216	0.97	11.31	11.31	1.29	1.36	1.06	- 4.9	3.10	3.16	1.67	0.0075	0.241
219	3.35	31.06	38.66	2.05	2.10	1.29	- 2.4	42.78	43.45	28.05	0.1661	0.388
220	1.67	19.27	20.25	1.67	1.71	1.17	- 2.5	9.87	10.02	5.97	0.0540	0.547
221	1.01	11.76	11.76	1.33	1.43	1.09	- 7.0	3.42	3.53	1.88	0.0077	0.226
222	1.50	17.18	17.79	1.73	1.80	1.20	- 3.9	8.17	8.37	5.09	0.0424	0.519
225	1.85	21.65	23.14	1.91	1.94	1.23	- 1.8	12.71	12.86	8.31	0.0689	0.542
226	1.92	22.32	24.01	1.85	1.90	1.23	- 2.5	13.57	13.80	8.75	0.0743	0.548
228	3.12	30.30	36.74	2.06	2.08	1.28	- 1.1	36.78	37.03	24.21	0.1568	0.426
229	4.71	32.82	48.45	2.08	2.08	1.29	- 0.4	84.25	84.45	55.40	0.3045	0.361
230	5.42	33.99	55.82	2.02	2.02	1.27	- 0.3	110.36	110.56	73.29	0.4777	0.433
231	5.34	33.73	54.67	2.03	2.03	1.27	- 0.3	107.19	107.38	72.21	0.4596	0.429
232	2.78	27.62	32.31	1.84	1.86	1.22	- 1.3	28.20	28.43	17.95	0.1346	0.477
233	3.22	30.67	37.60	2.05	1.97	1.25	3.9	38.48	37.51	25.39	0.1745	0.453
234	2.34	24.63	27.58	1.96	1.99	1.26	- 1.9	20.55	20.81	13.67	0.1040	0.506
235	0.44	2.38	2.38	1.00		1.00			0.615	0.307	0.00094	0.153
236	1.08	12.35	12.35	1.35	1.43	1.08	- 5.3	3.92	4.01	2.15	0.0148	0.379
237	3.13	30.49	37.05	2.04	2.06	1.28	- 1.1	37.13	37.39	24.50	0.1567	0.422
238	1.01	11.44	11.44	1.28	1.31	1.05	- 2.1	3.33	3.36	1.77	0.0106	0.319
239	1.10	12.76	12.77	1.39	1.44	1.09	- 4.0	4.10	4.17	2.26	0.0178	0.435
241	0.74	6.70	6.70	1.09	1.06	1.02	2.5	1.70	1.68	0.85	0.0039	0.230

TABLE (9) (Contd.)

Run No.	D_e (cm)	U_B (cm/sec)	$U(\infty)$ (cm/sec)	E_1	E_2	S_R	$\Delta a,b$	$A(cm^2)$	$A_p(cm^2)$	$A_F(cm^2)$	K_LA (cm^3/sec)	$K_L \times 10^2$ (cm/sec)
242	0.75	7.32	7.32	1.11	1.09	1.03	1.3	1.78	1.77	0.89	0.0043	0.240
243	2.09	23.38	25.55	1.89	1.93	1.24	- 2.2	16.18	16.41	10.54	0.0887	0.548
244	3.80	31.25	40.98	2.05	2.06	1.28	- 0.6	54.58	54.80	36.02	0.2140	0.392
245	0.79	8.22	8.22	1.13	1.10	1.03	2.7	1.94	1.91	0.97	0.0048	0.244
246	0.63	5.71	5.71	1.04	1.07	1.02	- 2.7	1.23	1.25	0.61	0.0024	0.194
248	2.86	28.41	33.53	2.10	2.13	1.30	-- 1.3	31.33	31.59	20.46	0.1445	0.461
249	0.51	3.39	3.39	1.00		1.00			0.811	0.405	0.0013	0.160
250	3.13	30.49	37.04	2.12	2.14	1.30	- 1.0	37.58	37.81	24.51	0.1601	0.426
251	3.97	31.65	42.38	2.54	2.56	1.41	- 0.7	64.80	65.00	39.99	0.2345	0.362
252	5.08	33.21	51.75	2.03	2.04	1.27	- 0.3	97.36	97.55	64.48	0.3737	0.384
253	3.02	29.41	35.31	2.19	2.21	1.32	- 1.1	35.41	35.64	22.85	0.1444	0.408

TABLE (10) TERMINAL RISE VELOCITY AND MASS TRANSFER RUNS. CARBON DIOXIDE IN 1.0% AQUEOUS POLYOX SOLUTION

Transducer Calibration: $P = (0.292\ (\pm 0.0011)x + 187.6\ (\pm 0.5))$ cm H_2O ($25^\circ C$) where x is the PDP-8 digitised transducer voltage (0-2000, positive; 2000-4095, negative)

α = 0.001210 ± 0.000013 cm H_2O ($25^\circ C$)

L = 50.0 ± 0.2 cm

h_1 = 1.0 ± 0.3 cm

h_2 = 66.5 ± 0.6 cm

H = 50.0 ± 0.2 cm

M_R = 1.1042

T = 25.0 ± 0.1°C

Run No.	D_e (cm)	U_B (cm/sec)	E_1	E_2	S_R	$\Delta a,b$	$A(cm^2)$	$A_P(cm^2)$	$A_F(cm^2)$	K_LA (cm^3/sec)	$K_L \times 10^2$ (cm/sec)	$K_{LF} \times 10^2$ (cm/sec)
301	3.27	31.85	2.70	2.77	1.47	- 2.7	45.41	45.92	27.39	0.5720	1.260	2.089
303	4.65	33.78	2.19	2.21	1.32	- 1.0	83.76	84.24	54.05	1.1498	1.373	2.127
304	1.08	23.70	1.39	1.34	1.16	5.2	3.85	3.76	1.91	0.0460	1.196	2.411
305	0.62	12.56	0.81	0.81	0.99	- 1.7	1.21	1.25	0.58	0.0173	1.432	2.961
307	0.48	9.65	0.80	0.80	0.99	- 1.3	0.719	0.737	0.345	0.0106	1.480	3.082

TABLE (10) (Contd.)

Run No.	D_e (cm)	U_B (cm/sec)	E_1	E_2	S_R	$\Delta a,b$	$A(cm^2)$	$A_P(cm^2)$	$A_F(cm^2)$	K_LA (cm^3/sec)	$K_L \times 10^2$ (cm/sec)	$K_{LF} \times 10^2$ (cm/sec)
308	1.77	26.05	2.41	2.53	1.36	- 5.3	11.80	12.01	5.95	0.1883	1.597	3.164
309	0.35	4.25	0.80		0.99			0.401	0.192	0.0056	1.400	2.919
310	1.49	25.51	2.28	2.21	1.33	3.9	8.24	8.13	4.17	0.1301	1.580	3.124
311	0.27	0.57	0.92		1.00			0.231	0.115	0.00041	0.177	0.355
312	5.62	34.01	2.06	2.00	1.26	2.7	118.26	116.21	78.78	1.5946	1.348	2.024
313	1.13	24.39	1.49	1.53	1.20	- 3.3	4.36	4.42	2.18	0.0550	1.263	2.527
314	2.37	29.07	2.76	2.89	1.49	- 4.5	24.40	24.86	14.56	0.2366	0.970	1.625
315	0.79	17.92	0.83	0.83	0.99	- 6.7	1.98	2.27	0.96	0.0237	1.198	2.461
316	0.26	0.419	1.00		1.00			0.212	0.106	0.00035	0.168	0.335
317	1.21	24.75	1.77	1.79	1.25	- 1.2	5.17	5.20	2.61	0.0652	1.260	2.495
318	0.69	14.62	0.84	0.84	0.99	0.2	1.49	1.49	0.73	0.0196	1.313	2.684
319	0.38	5.05	0.79		0.99			0.449	0.215	0.00589	1.310	2.738
320	0.28	2.05	0.86		0.99			0.242	0.119	0.00242	1.000	2.038
321	0.63	13.12	0.80	0.80	0.99	- 0.7	1.26	1.27	0.61	0.0184	1.470	3.049
323	1.03	22.94	1.38	1.40	1.17	- 2.3	3.52	3.55	1.75	0.0409	1.164	2.336
324	0.53	10.94	0.80	0.80	0.99	- 1.1	0.90	0.92	0.43	0.0138	1.540	3.204
325	1.08	23.58	1.36	1.41	1.17	- 4.1	3.88	3.96	1.93	0.0473	1.220	2.447
327	1.01	22.73	1.37	1.32	1.14	4.8	3.38	3.30	1.68	0.0396	1.173	2.354
329	1.90	26.32	2.68	2.79	1.42	- 4.3	14.87	15.08	7.87	0.1737	1.168	2.206
330	1.41	25.26	1.96	2.03	1.29	- 4.2	7.19	7.31	3.64	0.1162	1.617	3.194
331	0.37	4.86	0.80		0.99			0.448	0.215	0.00586	1.309	2.726
332	1.75	26.04	2.60	2.65	1.43	- 2.4	12.40	12.50	6.31	0.1745	1.407	2.763
333	0.27	0.662	0.92		1.00			0.231	0.115	0.00041	0.178	0.358
334	2.18	27.17	2.78	2.85	1.48	- 2.5	20.41	20.62	12.22	0.1813	0.888	1.484
335	2.25	27.62	2.80	2.87	1.49	- 2.5	21.92	22.14	13.10	0.2192	1.000	1.672
336	1.37	25.13	2.05	2.07	1.30	- 1.3	6.84	6.88	3.47	0.1039	1.519	2.996
337	0.37	4.70	0.80		0.99			0.436	0.209	0.00548	1.258	2.620
338	0.57	11.19	0.80	0.79	0.99	- 0.5	1.03	1.04	0.50	0.0148	1.441	2.989
339	1.02	22.42	1.24	1.28	1.13	- 4.3	3.36	3.43	1.67	0.0395	1.176	2.370

TABLE (10) (Contd.)

Run No.	D_e (cm)	U_B (cm/sec)	E_1	E_2	S_R	$\Delta a,b$	$A(cm^2)$	$A_P(cm^2)$	$A_F(cm^2)$	K_LA (cm^3/sec)	$K_L \times 10^2$ (cm/sec)	$K_{LF} \times 10^2$ (cm/sec)
340	0.53	10.78	0.80	0.80	0.99	- 1.2	0.89	0.91	0.43	0.0137	1.542	3.210
342	0.83	18.66	0.85	0.85	0.99	1.2	2.21	2.16	1.08	0.0264	1.194	2.434
343	0.54	11.06	0.81	0.81	0.94	- 1.1	0.99	0.96	0.46	0.0144	1.521	3.143
344	0.74	16.67	0.85	0.85	0.99	- 2.6	1.76	1.85	0.86	0.0228	1.300	2.656
345	0.83	18.66	0.85	0.85	0.99	- 1.2	2.21	2.26	1.08	0.0247	1.119	2.283
346	0.42	7.04	0.79		0.99			0.56	0.27	0.0077	1.365	2.848
347	0.27	1.03	0.86		0.99			0.234	0.114	0.00222	0.953	1.946
348	0.58	11.44	0.80	0.80	0.99	0.5	1.07	1.06	0.52	0.0150	1.401	2.904
349	0.66	13.70	0.84	0.83	0.99	- 1.8	1.38	1.43	0.67	0.0190	1.379	2.834
350	0.41	6.42	0.79		0.99			0.54	0.26	0.0067	1.236	2.580
351	0.67	14.16	0.83	0.84	0.99	0.8	1.43	1.41	0.70	0.0183	1.285	2.637
352	0.46	8.36	0.80		0.99			0.66	0.32	0.0101	1.530	3.182
353	0.24	0.308	1.00		1.00			0.174	0.087	0.00029	0.170	0.339
354	4.06	32.68	2.44	2.52	1.41	- 3.2	67.33	68.41	41.72	0.9217	1.369	2.209
355	2.39	29.59	2.93	2.89	1.49	1.5	24.81	24.67	14.80	0.2648	1.067	1.789
356	1.82	26.18	2.85	2.97	1.46	- 4.7	13.93	14.12	7.23	0.1753	1.259	2.426
357	1.93	26.46	2.65	2.76	1.41	- 4.2	15.27	15.48	8.19	0.1612	1.056	1.969
358	4.05	32.57	2.46	2.51	1.40	- 2.0	66.80	67.46	41.46	0.8668	1.298	2.091
359	0.27	0.786	0.92		1.00			0.231	0.115	0.00041	0.179	0.360
360	3.02	31.06	2.70	2.78	1.47	- 2.9	38.81	39.29	23.40	0.4907	1.264	2.097
361	0.26	0.409	1.00		1.00			0.212	0.106	0.00035	0.165	0.331
362	0.72	16.08	0.85	0.85	0.99	- 4.6	1.65	1.80	0.80	0.0223	1.354	2.770
363	0.27	1.30	0.86		1.00			0.234	0.115	0.0023	0.986	2.007
364	0.74	16.08	0.85	0.85	0.99	- 3.3	1.71	1.83	0.84	0.0222	1.299	2.655
365	0.53	11.04	0.82	0.81	0.99	- 1.0	0.91	0.93	0.44	0.0141	0.1546	3.198

N O M E N C L A T U R E*

A	bubble surface area
A_1, A_2 etc.	coefficients in Eqn. (22)
A_c	surface area of cone defined by Eqn. (225)
A'_c	cross sectional area of body perpendicular to direction of motion
A_F	bubble frontal area
A_R	area of bubble rear
A_s	bubble equivalent spherical area
A_P	bubble surface area calculated from distortion-corrected photographic measurements
a	bubble semi-width
a'''	constant in Eqn. (5)
a_1	horizontal photographic dimension defined in Fig. (46)
a_2	value assumed by a_1 following bubble shape fitting procedure
B_1, B_2 etc.	coefficients in Eqn. (22)
b	bubble semi-height
b''	experimental parameter, $f(D_c, \sigma)$
b'''	constant in Eqn. (5)
b_1	vertical photographic dimension defined in Fig. (46)
b'_1	vertical photographic dimension defined in Fig. (46)
b_2	value assumed by b_1 following bubble shape fitting procedure
b'_2	value assumed by b'_1 following bubble shape fitting procedure

* Unless otherwise specified, symbols have the following meanings

N O M E N C L A T U R E (Contd.)

C^*	solute gas interfacial equilibrium concentration
C_0	solute gas bulk phase concentration
C_1	constant in Eqns. (36) and (37)
C_2	function of bubble velocity and velocity profile of liquid, given in Eqn. (37)
C_D	drag coefficient defined by Eqn. (8)
c	concentration of Glycerol in water (g mole/l)
D	characteristic dimension
D_c	column diameter
D_e	bubble equivalent spherical diameter
D_L	molecular diffusivity of solute (disperse phase) in continuous phase
D_{LO}	diffusivity of carbon dioxide in pure water, Eqn. (301)
d	residual, difference between value of a measured quantity calculated from best-fit polynomial equation and the measured value, defined by Eqn. (126)
E	bubble eccentricity, width/height
E_1	bubble eccentricity, distortion-corrected measured width/ measured height
E_2	bubble eccentricity, measured width/calculated height
Eo	Eotvos Number, $g\rho_o D^2/\sigma$
e_1	parameter defined by Eqn. (237)
e_2	parameter defined by Eqn. (242)
F	$= V\Delta\rho g$, drag force
F'	two dimensional pressure
Fr	Froude Number, $U/(gD)^{1/2}$
G	rigidity modulus of the fluid
g	gravitational acceleration

N O M E N C L A T U R E (Contd.)

H	column liquid pressure reference level above pressure transducer
He	Henry's constant
h	height above pressure transducer
h_1	height above pressure transducer of bubble in dumping cup
h_2	height of bubble above pressure transducer when photographed
h_c	vertical photographic dimension defined in Fig. (46)
K	constant in Power Law Eqn. (3)
K'	$= {}^{\mu}i/\mu_o$
K''	calibration constant defined by Eqn. (298)
K_1, K_2	constants in Ellis model, Eqn. (4)
K_3, K_4	constants in Oldroyd model, Eqn. (6)
K_5	$^{\mu}/G$, constant in Maxwell model, Eqn. (7)
K_n	function of n, defined by Eqn. (28)
K_L	overall liquid film mass transfer coefficient
K_LA	overall mass transfer product
K_{LF}	liquid film mass transfer coefficient based on bubble frontal area
K_{LR}	bubble rear liquid film mass transfer coefficient
k	constant
L	vertical separation of velocity timing photoelectric cell units P_1 and P_3
l	distance from fulcrum of Wilhelmy balance to point of suspension of the slide
l_o	distance from fulcrum of Wilhelmy balance to point of suspension of the balance pan
M	dimensionless group, $g\mu_o^4/\rho_o\sigma^3$

N O M E N C L A T U R E (Contd.)

M'	molecular weight of continuous phase
M_L	mass of displaced liquid
M_R	photographic distortion ratio, $\frac{\text{magnification in vertical plane}}{\text{magnification in horizontal plane}}$, the denominator was set = 1
m	non-Newtonian fluid consistency, Eqn. (14)
N	speed of rotation
n	flow index, Eqn. (3)
n'	number of moles
n_1	bubble shape number, see Appendix III
n_R	bubble dimension ratio defined by Eqn. (249)
P_A	atmospheric pressure
P_B	bubble internal pressure
P_{BO}	bubble internal pressure on termination of bubble injection
P_{B1}	bubble internal pressure just prior to its release
Pe	continuous phase Peclet Number, $^{DU}/_{D_L}$
P_n	Legendre polynomials of order n, see Eqn. (62)
P_T	column liquid gauge pressure at pressure transducer station
P_{TO}	column liquid gauge pressure on termination of bubble injection
P_{T1}	column liquid gauge pressure just prior to bubble release
p	pressure
R	gas constant
R'	radius of bubble floor
R''	curvature radius of a spherical cap
R_c	viscometer cone radius
Re	Reynolds Number, $^{\rho UD}/_{\mu}$

N O M E N C L A T U R E (Contd.)

Re'	generalised Reynolds Number defined by Eqn. (14)
Re''	generalised Reynolds Number defined by Eqn. (50)
r	the geometric interface of a bubble or drop, see Eqn. (62)
S	solubility parameter defined by Eqn. (98)
S'	fractional rate of surface renewal
Sc	continuous phase Schmidt Number, $\mu_o/\rho_o D$
Sh	continuous phase Sherwood Number, $K_L D/D_L$
S_R	bubble shape ratio, measured width/equivalent spherical diameter
T	temperature, ^oK
T_c	viscometer torsion spring constant
t	time
t'	thickness of slide
t_e	phase contact time
U	translational velocity
U'	surface velocity of liquid down the inside of the bubble skirt
$U(\infty)$	translational velocity in infinite medium
U_B	bubble terminal rise velocity
U_k	residual, difference between most probable value of a measured quantity and the measured value, defined by Eqn. (107)
$U_{o/U}$	bubble equatorial interfacial velocity ratio
u	velocity
V	bubble volume calculated from optical distortion-corrected photographic dimensions
V_B	bubble volume
V_{BO}	bubble volume as injected into column
V_{Bl}	bubble volume just prior to bubble release

N O M E N C L A T U R E (Contd.)

V_c	cone volume defined by Eqn. (224)
We	Weber Number, $D\rho_o U^2/\sigma$
w	width of slide
w_2	vorticity, see Eqn. (163)
X_n	function of n, see Eqn. (15)
X'_n	function of n, see Eqn. (20)
x	variable defined in text
y	variable defined in text
z	horizontal photographic dimension defined in Fig. (46)
α	column specific compressibility
α'	constant in Ellis model Eqn. (4)
α''	Bunsen absorption coefficient
β	standard deviation
Δa	percentage change in bubble dimension (horizontal) caused by shape fitting
Δb	percentage change in bubble dimension (vertical) caused by shape fitting
ΔF_d	change in downward pull of surface tension on slide
ΔF_u	change in buoyancy of submerged portion of slide
Δh	change in length of submerged part of slide
ΔP_T	change in column pressure indicated by pressure transducer
Δs	change in reading on scale S of Wilhelmy balance
ΔV_S	change in system volume
$\Delta\rho$	$= (\rho_o - \rho_i)$
$\Delta\sigma$	surface tension of solution - surface tension of pure water
$\Delta\phi$	increase in logarithmic damping decrement
Δ	bubble skirt thickness

N O M E N C L A T U R E (Contd.)

Δ'	viscometer indicator meter deflection
Δ_1	column liquid gauge pressure with valve V_2 at top of column open, see Fig. (11)
Δ_2	column liquid gauge pressure with valves V_5 and V_6 open, see Fig. (11)
θ	half-angle of a spherical cap, see Fig. (42 (b))
λ	parameter defined by Eqn. (85)
ℓ	$= \rho_i/\rho_o$
μ	Newtonian viscosity
μ_a	non-Newtonian apparent viscosity
μ_i	disperse phase Newtonian viscosity
μ_o	continuous phase Newtonian viscosity
ν	kinematic viscosity, μ/ρ
ν_o	$= \mu_o/\rho_o$
$\dot{\gamma}$	shear rate
$\dot{\gamma}_a$	non-Newtonian fluid apparent rate of shear
ρ	density
ρ_i	gas or disperse phase density
ρ_{H_2O}	density of water at 25^oC
ρ_o	liquid or continuous phase density
σ	surface tension
τ	shear stress
τ'	time taken by ascending bubble to traverse the distance between photoelectric cell units P_1 and P_3
τ_o	yield stress
ψ	viscometer cone angle
ψ'	stream function, see Eqns. (156) and (157)

N O M E N C L A T U R E (Contd.)

ϕ	function of two independent variables, see Eqn. (164)
ϕ'	volume concentration of the solute in a non-Newtonian solution, see Eqn. (5)
ϕ''	velocity potential defined by Eqn. (143)
ω	angular velocity of viscometer cone

Subscripts

os	oblate spheroid
ps	prolate spheroid
s	spheroid
sc	spherical cap
z) r)	independent variables, see Fig. (42 (c))
ρ) θ)	independent variables, see Fig. (42 (b))

BIBLIOGRAPHY

A1 Akselrud, G.A., Zh. Fiz. Khim., 1953, 27, 1445.

A2 Allen, H.S., Phil. Mag., 1900, 50, 323.

A3 Angelino, H., Chem. Engng. Sci., 1966, 21, 541.

A4 Angelo, J.B., Lightfoot, E.N. & Howard, D.W., Amer. Inst. Chem. Engrs. J., 1966, 12, 751.

A5 Arnold, H.D., Phil. Mag., 1911, 22, 755.

A6 Ashare, E., Bird, R.B. & Lescaboure, J.A., Amer. Inst. Chem. Engrs. J., 1965, 11, 910.

A7 Astarita, G. & Apuzzo, G., Amer. Inst. Chem. Engrs. J., 1965, 11, 815.

A8 Astarita, G. & Marrucci, G., Rend. Cl. Sci. Fis. Mat. Natl. Accad. Luicei, 1964, 8-36, 836.

A9 Avetisyan, R.A. & Trapeznikov, A.A., Russian J. Phys. Chem., 1964, 38, 1660.

B1 Bailey, F.E. Jr., Powell, G.M. & Smith, K.L., Ind. & Engng. Chem., 1958, 50, 8.

B2 Baird, M.H.I. & Davidson, J.F., Chem. Engng. Sci., 1962, 17, 87.

B3 Baird, M.H.I. & Hamielec, A.E., Can. J. Chem. Engng., 1962, 40, 119.

B4 Barnett, S.M., Humphrey, A.E. & Litt, M., Amer. Inst. Chem. Engrs. J., 1966, 12, 253.

B5 Birkhoff, G., "Hydrodynamics", 1st Ed., 1955, 10, Dover Publ. Inc. (N.Y.).

B6 Bizzell, G.D. & Slattery, J.C., Chem. Engng. Sci., 1962, 17, 777.

B7 Boltze, E., Grenschichten an Rotation Körpern, Göttingen dissertation, 1908.

B8 Bond, W.N. & Newton, D.A., Phil. Mag., 1928, 5, 794.

B9 Boussinesq, J., J. Math., 1905, 6, 285.

B10 Bowman, C.W. & Johnson, A.I., Can. J. Chem. Engng., 1962, 40, 139.

B11 Bowman, C.W., Johnson, A.I., Ward, D.M. & Trass, O., Can. J. Chem. Engng., 1961, 39, 9.

B12 Bryn, T., Forsch. Geb. Ing., 1933, 4, 27.

C1 Calderbank, P.H. & Korchinski, I.J.O., Chem. Engng. Sci., 1956, 6, 65.

C2 Calderbank, P.H., Trans. Instn. Chem. Engrs., 1959, 37, 173.

C3 Calderbank, P.H. & Lochiel, A.C., Chem. Engng. Sci., 1964, 19, 485.

C4 Calderbank, P.H., Trans. Instn. Chem. Engrs., 1967, 45, CE 209.

C5 Chao, B.F., Phys. Fluids, 1962, 5, 69.

C6 Cheh, H.Y. & Tobias, C.W., Ind. & Engng. Chem., 1968, 7, 48.

C7 Chou, C.H. & Charles, M.E., Can. J. Chem. Engng., 1968, 46, 143.

C8 Clarke, D.S., Ph.D. Thesis, Univ. of Birmingham, 1953.

C9 Cohen, L.S. & Hanratty, T.J., Amer. Inst. Chem. Engrs. J., 1965, 11, 138.

C10 Cole, R., Amer. Inst. Chem. Engrs. J., 1967, 13, 403.

C11 Collins, R., Chem. Engng. Sci., 1965, 20, 788.

C12 Collins, R., Chem. Engng. Sci., 1965, 20, 851.

C13 Collins, R., J. Fluid Mech., 1966, 25, 469.

C14 Collins, R., Chem. Engng. Sci., 1967, 22, 89.

C15 Coppock, P.D. & Meiklejohn, G.T., Trans. Instn. Chem. Engrs., 1951, 29, 75.

C16 Crabtree, J.R., & Bridgwater, J., Chem. Engng. Sci., 1967, 22, 1517.

C17 Conkie, W.R. & Savic, P., Nat. Res. Counc. of Canada, 1953, Report MT-22.

C18 Crank, J., "The Mathematics of Diffusion", 1957, Oxford: Clarendon Press.

D1 Danckwerts, P.V., Ind. Eng. Chem., 1950, 42, 2077.

D2 Danckwerts, P.V., Chem. Engng. Sci., 1965, 20, 785.

D3 Datta, R.L., Trans. Indian Instn. Chem. Engrs., 1960, 13, 69.

D4 Datta, R.L., Napier, D.H. & Newitt, D.M., Trans. Instn. Chem. Engrs., 1950, 28, 14.

D5 Davenport, W.G., Richardson, F.D. & Bradshaw, A.V., Chem. Engng. Sci., 1967, 22, 1221.

D6 Davies, G.A., Ponter, A.B. & Craine, K., Can. J. Chem. Engrs., 1967, 45, 372.

D7 Davies, R.M. & Taylor, G.I., Proc. Roy. Soc., 1950, A200, 375.

D8 Deindoerfer, F.H. & Humphrey, A.E., Ind. Engng. Chem., 1961, 52, 755.

D9 Dumitrescu, D.T., Z. Angew. Math. Mech., 1943, 23, 139.

D10 Davidson, J.F. & Harrison, D., "Fluidised Particles", 1963, Cambridge Univ. Press.

D11 Davidson, J.F. & Cullen, E.J., Trans. Instn. Chem. Engrs., 1957, 35, 51.

E1 Einstein, A., Ann. Physik., 1906, 19, 289; 1911, 34, 591.

E2 Ernst., W.D., Amer. Inst. Chem. Engrs. J., 1965, 11, 940.

F1 Fararoui, A. & Kintner, R.C., Trans. Soc. Rheol., 1961, 5, 369.

F2 Fidleris, V. & Whitmore, R.L., Brit. J. Appl. Phys., 1961, 12, 490.

F3 Fieser, L.F. & Fieser, M., "Organic Chemistry", 1963, Rheinhold Publishing Corp.

F4 Fox, L., "An Introduction to Numerical Linear Algebra", Chapter 3, 1964, Clarendon Press.

F5 Frederickson, A.G., "Principles & Applications of Rheology", 1964, Prentice-Hall (N.J.)

F6 Friedlander, S.K., Amer. Inst. Chem. Engrs. J., 1957, 3, 43.

F7 Friedlander, S.K., Amer. Inst. Chem. Engrs. J., 1961, 7, 347.

F8 Fröhlich, H. & Sack, R., Proc. Roy. Soc., 1946, A 185, 415.

F9 Frössling, N., Gerlands Beitr. Geophys., 1938, 52, 170.

F10 Foust, A.S., Wenzel, L.A., Clump, C.W., Maus, L. & Anderson, L.B., "Principles of Unit Operations", p. 100, 1960, John Wiley & Sons, Inc.

G1 Garabedian, P.R., Proc. Roy. Soc., 1957, A241, 423.

G2 Garner, F.H. & Hammerton, D., Chem. Engng. Sci., 1954, 3, 1.

G3 Garner, F.H. & Skelland, A.H.P., Ind. Engng. Chem., 1954, 46, 1255.

G4 Garner, F.H. & Skelland, A.H.P., Chem. Engng. Sci., 1955, 4, 149.

G5 Godoretskaya, A., Zh. Fiz. Khim., 1949, 23, 71.

G6 Goldsmith, M.L. & Mason, S.G., J. Fluid Mech., 1962, 14, 42.

G7 Goldstein, S., "Modern Developments in Fluid Dynamics", 1938, 2, 550, Oxford Univ. Press.

G8 Goldstein, S. "Modern Developments in Fluid Dynamics", 1938, 1, 64, Oxford Univ. Press.

G9 Gorring, R.L. & Katz, D.L., Amer. Inst. Chem. Engrs. J., 1962, 8, 123.

G10 Grace, J.R. & Harrison, D., Chem. Engng. Sci., 1967, 22, 1337.

G11 Griffith, R.M., Chem. Engng. Sci., 1960, 12, 198.

G12 Griffith, P. & Wallis, G.B., J. Heat Transfer, 1961, 83, 307.

G13 Guyer, A. & Pfister, X., Helv. Chim. Acta, 1946, 29, 1173.

G14 Griffith, R.M., Chem. Engng. Sci., 1962, 17, 1057.

G15 Guthrie, R.I.L. & Bradshaw, A.V., Chem. Engng. Sci., 1969, 24, 913.

H1 Haberman, W.L. & Morton, R.K., Trans. Amer. Soc. Civil Engrs., 1956, 121, 227.

H2 Hadamard, J., Compt. Rend., 1911, 152, 1735.

H3 Hamielec, A.E. & Johnson, A.I., Can. J. Chem. Engng., 1962, 40, 41.

H4 Hamielec, A.E., Johnson, A.I. & Houghton, W.T., Amer. Inst. Chem. Engrs. J., 1967, 13, 220.

H5 Hammerton, D., Ph.D. Thesis, Univ. of Birmingham, 1953.

H6 Hammerton, D. & Garner, F.H., Trans. Instn. Chem. Engrs., 1954, 32, S-18.

H7 Hanratty, T.J. & Engin, J.M., Amer. Inst. Chem. Engrs. J., 1957, 3, 299.

H8 Hartunian, R.A. & Sears, W.R., J. Fluid Mech., 1957, 3, 27.

H9 Harriott, P., Can. J. Chem. Engng., 1962, 40, 60.

H10 Higbie, R., Amer. Inst. Chem. Engrs. J., 1935, 31, 365.

H11 Hodgman, C.D. (ED.), "Handbook of Chemistry and Physics", 37th Ed., 2025, 1955-56, Chem. Rubber Pub. Co., U.S.A.

H12 Houghton, G., Ritchie, P.D. & Thomson, J.A., Chem. Engng. Sci., 1957, 7, 111.

H13 Hu, S. & Kintner, R.C., Amer. Inst. Chem. Engrs. J., 1955, 1, 42.

H14 Houghton, G., J. Chem. Phys., 1964, 40, 1628.

J1 Jahnke-Emde (ED.), "Tables of Higher Functions", 1948, Teubner, Leipzig.

J2 Johnson, A.I. & Braida, L., Can. J. Chem. Engng., 1957, 35, 165.

J3 Johnson, A.I. & Hamielec, A.E., Amer. Inst. Chem. Engrs. J., 1960, 6, 145.

K1 Klee, A.J. & Treybal, R.E., Amer. Inst. Chem. Engrs. J., 1956, 2, 444.

L1 Ladenburg, R., Ann. Physik, 1907, 23, 447.

L2 Lamb, H., "Hydrodynamics", 6th Ed., 1932, Cambridge Univ. Press.

L3 Langmuir, I., Phys. Rev., 1918, 12, 368.

L4 Ledig, P.G., Ind. Engng. Chem., 1924, 16, 1231.

L5 Ledig, P.G. & Weaver, E.R., J. Am. Chem. Soc., 1924, 46, 650.

L6 Leibermann, L., J. Appl. Phys., 1957, 28, 205.

L7 Leonard, J.H., Ph.D. Thesis, Univ. of Pittsburgh, 1961.

L8 Leonard, J.H. & Houghton, G., Nature, 1961, 190, 687.

L9 Leonard, J.H. & Houghton, G., Chem. Engng. Sci., 1963, 18, 133.

L10 Lewis, W.K. & Whitman, W.G., Ind. Engng. Chem., 1924, 16, 1215.

L11 Levich, V.G., "Physicochemical Hydrodynamics", Chap. 8, 1962, Prentice-Hall (N.J.).

L12 Li, P.S., Ph.D. Thesis, Univ. of Washington, 1953.

L13 Li, P.S., West F.B., Vance, W.H. & Moulton, R.W., Amer. Inst. Chem. Engrs. J., 1965, 11, 581.

L14 Licht, W. & Pansing, W.F., Ind. Engng. Chem., 1953, 45, 1885.

L15 Licht, W. & Narasimhamurthy, G.S.R., Amer. Inst. Chem. Engrs. J., 1955, 1, 366.

L16 Lochiel, A.C., Ph.D. Thesis, Univ. of Edinburgh, 1963.

L17 Lochiel, A.C., Can. J. Chem. Engng., 1965, 43, 40.

L18 Lochiel, A.C. & Calderbank, P.H., Chem. Engng. Sci., 1964, 19, 471.

L19 Loudon, J.R., Ph.D. Thesis, Univ. of Edinburgh, 1968.

L20 Loudon, J.R., Calderbank, P.H. & Coward, I., Chem. Engng. Sci., 1966, 21, 614.

L21 Luchak, G. & Langstroth, G.S., Can. J. Research, 1950, 28A, 580.

L22 Lindland, K.P. & Terjesen, S.G., Chem. Engng. Sci., 1956, 5, 1.

M1 Magarvey, R.H. & Bishop, R.L., Can. J. Phys., 1961, 39, 1418.

M2 Magarvey, R.H. & Maclatchy, C.S., Amer. Inst. Chem. Engrs. J., 1968, 14, 260.

M3 Manley, D.M.J.P., Brit. J. Appl. Phys., 1960, 11, 38.

M4 Marrucci, G., Ind. Engng. Chem., 1965, 4, 224.

M5 Maxwell, J.C., Phil. Trans., 1867, 49, 157.

M6 Maxworthy, T., J. Fluid Mech., 1967, 27, 367.

M7 Mendelson, H.D., Amer. Inst. Chem. Engrs., 1967, 13, 250.

M8 McGary, C.W. Jr., J. Polymer Sci., 1960, 46, 51.

M9 Miyagi, O., Phil. Mag., 1925, 50, 112.

M10 Mhatre, M.V. & Kintner, R.C., Ind. Engng. Chem., 1959, 51, 865.

M11 Moore, D.W., J. Fluid Mech., 1959, 6, 113.

M12 Moore, D.W., J. Fluid Mech., 1963, 16, 161.

M13 Morse, H.W., Proc. Am. Acad. Arts and Sci., 1910, 45.

M14 Metzner, A.B. & Reed, J.C., Amer. Inst. Chem. Engrs. J., 1955, 1, 434.

N1 Nate, T. & Himmelblau, D.M., Amer. Inst. Chem. Engrs. J., 1967, 13, 697.

N2 Nernst, W., Zh. Fiz. Khim., 1904, 47, 52.

N3 Nicolitsas, A.J. & Murgatroyd, W., Chem. Engng. Sci., 1968, 23, 934.

N4 Noordsij, P. & Rotte, J.W., Chem. Engng. Sci., 1967, 22, 1475.

N5 Nicklin, D.J., Wilkes, J.O. & Davidson, J.F., Trans. Instn. Chem. Engrs., 1962, 40, 61.

O1 O'Brien, M.P. & Gosline, I.E., Ind. Engng. Chem., 1935, 27, 1436.

O2 Oldroyd, J.G., Proc. Roy. Soc., 1950, A200, 523.

O3 Oseen, C.W., Arkiv. Mat. Astron. Fysik., 1910, 6, 75; 1913, 9, 1.

P1 Pan, F.Y. & Acrivos, A., Ind. & Engng. Chem., 1968, 7, 227.

P2 Pasveer, A., Sewage Ind. Wastes, 1955, 27, 1130.

P3 Pattle, R.E., Trans. Instn. Chem. Engrs., 1950, 28, 27.

P4 Peebles, F.N. & Garber, H.J., Chem. Engng. Progr., 1953, 49, 88.

P5 Perry, J.H. (ED.), "Chemical Engineers' Handbook", 3rd Ed., 1950, McGraw-Hill.

P6 Perry, J.H. (ED.), "Chemical Engineers' Handbook", 4th Ed., 1963, 3, 86, McGraw-Hill.

P7 Philopoff, W., Rubber Chem. Technol., 1937, 10, 76.

P8 Pilpel, N., C.P.E., 1966, October,57.

R1 Ratcliff, G.A. & Holdcroft, J.G., Trans. Instn. Chem. Engrs., 1963, 41, 315.

R2 Redfield, J.A. & Houghton, G., Chem. Engng. Sci., 1965, 20, 131.

R3 Rippin, D.W.T. & Davidson, J.F., Chem. Engng. Sci., 1967, 22, 217.

R4 Rose, P.M. & Kintner, R.C., Amer. Inst. Chem. Engrs. J., 1966, 12, 530.

R5 Rosenberg, B., David Taylor Model Basin, Rept. 727, 1950.

R7 Rosenhead, L. (ED.), "Laminar Boundary Layers", 1st Ed., 1963, Oxford Univ. Press.

R8 Rozen, A.M. & Krylov, V.S., Int. Chem. Engng., 1966, 6, 429.

R9 Ruckenstein, E., Rev. Chim., 1961, 6, 221.

R10 Ruckenstein, E., Chem. Engng. Sci., 1964, 19, 131.

R11 Ruckenstein, E., Chem. Engng. Sci., 1964, 19, 505.

R12 Ruckenstein, E., Int. J. Heat Mass Transfer, 1967, 10, 1785.

R13 Rybczynsky, W., Bull. Acad. Sci. (Cracovie), 1911, 1, A40.

S1 Saffman, P.G., J. Fluid Mech., 1956, 1, 249.

S2 Sato, T., Taniyama I. & Shimokawa, S., Kagaku Kōgaku, 1966, 4, 215.

S3 Schlichting, H., "Boundary Layer Theory", 1960, 71, McGraw-Hill.

S4 Schwerdtfeger, K., Chem. Engng. Sci., 1968, 23, 937.

S5 Sibree, J.O., Trans. Farad. Soc., 1930, 26, 26; 1931, 27, 161.

S6 Siemes, W., Chem. Ing. Tech., 1954, 26, 614.

S7 Siddique, Q.M., Ph.D. Thesis, Univ. of Wisconsin, 1959.

S8 Sih, P.H. & Newman, J., Int. J. Heat Mass Transfer, 1967, 10, 1749.

S9 Skelland, A.H.P. & Wellek, R.M., Amer. Inst. Chem. Engrs. J., 1964, 10, 491.

S10 Slattery, J.C., Amer. Inst. Chem. Engrs. J., 1962, 8, 663.

S11 Slattery, J.C. & Bird, B.R., Chem. Engng. Sci., 1961, 16, 231.

S12 Slaughter, I. & Wraith, A.E., Chem. Engng. Sci., 1968, 23, 932 .

S13 Smoluchowski, M. von, Bull Acad. Sci. (Cracovie), 1903, 182.

S14 Sternling, C.V. & Scriven, L.E., Amer. Inst. Chem. Engr. J., 1959, 5, 514.

S15 Stewart, W.E., Angelo, J.B. & Lightfoot, E.N., Chem. Engng. Sci., (To be published).

S16 Stokes, G.G., "Mathematical and Physical Papers", 1880, 1, Cambridge Univ. Press.

S17 Stuke, B., Naturwiss, 1952, 39, 325.

S18 Sy, F. & Lightfoot, E.N., Amer. Inst. Chem. Engrs. J., 1968, 14, 835.

S19 Shoemaker, P.D. & Marc de Chazal, L.E., Chem. Engng. Sci., 1969, 24, 795.

T1 Tadaki, T. & Maeda, S., Chem. Engng. (Japan), 1961, 25, 254.

T2 Tanner, R.I., Chem. Engng. Sci., 1964, 19, 349.

T3 Taylor, T.D. & Acrivos, A., J. Fluid Mech., 1964, 18, 466.

T4 Timson, W.J. & Dunn, C.G., Ind. Engng. Chem., 1960, 52, 799.

T5 Topley, B. & Whytlaw-Gray, R.W., Phil. Mag., 1927, 4, 873.

T6 Topping, J., "Errors of Observation and their Treatment", 1966, Chapman & Hall Ltd.

T7 Torobin, L., Can. J. Chem. Engng., 1959, 37, 129, 167, 224.

U1 Uno, S. & Kintner, R.C., Amer. Inst. Chem. Engrs. J., 1956, 2, 420.

V1 Von Bogdandy, L., Von Rutsch, W. & Stranski, J.N., Chem. Ing. Tech., 1959, 31, 580.

W1 Ward, D.M., Can. J. Chem. Engng., 1962, 40, 164.

W2 Warshay, M.E., Bogusz, E., Johnson, M. & Kintner, R.C., Can. J. Chem. Engng., 1959, 37, 29.

W3 Washburn, E.W. (ED.), "International Critical Tables of Numerical Data, Physics, Chemistry and Technology", 1st Ed., 447, 467, 1928, McGraw-Hill.

W4 Wassermann, M.L. & Slattery, J.C., paper presented at A.I.Ch.E. Houston Meeting, 1963.

W5 Watson, G.N., "Theory of Bessel Functions", 2nd Ed., 1952, Cambridge Univ. Press.

W6 Weissenberg, K., Nature, 1947, 159, 310.

W7 Wellek, R.M., Agrawal, A.K. & Skelland, A.H.P., Amer. Inst. Chem. Engrs. J., 1966, 12, 854.

W8 White, E.T. & Beardmore, R.H., Chem. Engng. Sci., 1962, 17, 351.

W9 Wilkinson, W.L., "Non-Newtonian Fluids", 1960, 1, Pergamon.

W10 Winnikow, S., Chem. Engng. Sci., 1967, 22, 477.

W11 Woodland, D.J. & Mack, E. Jr., J. Amer. Chem. Soc., 1933, 55, 3/49.

Z1 Zdonik, S.B., M.S. Thesis, Mass. Inst. Technol., 1942.

Z2 Zieminski, S.A. & Raymond, D.R., Chem. Engng. Sci., 1968, 23, 17.